THE UNIVERSITY *of* EDINBURGH

Modelling of High Pressure Instruments and Experiments using Finite Element Methods

Juan Carlos Fallas Chinchilla

A thesis submitted in fulfilment of the requirements for the degree of Doctor of Philosophy to the School of Engineering

University of Edinburgh

2018

Declaration

This thesis has been composed by myself and it has not been submitted in any previous application for a degree. The work reported within was executed by me, unless otherwise stated.

Juan Carlos Fallas Chinchilla

March 2018

Acknowledgements

First and foremost, I would like to express my immense gratitude to my supervisor Prof. Konstantin Kamenev. He has always been patient and helpful during the completion of my PhD. I greatly acknowledge the moral, intellectual and financial support that he has provided. He has given me the independence to implement innovative solutions and to pursue things that interest me.

This PhD thesis would not have been possible without the incredible collaboration of staff and fellow students from the Centre for Science at Extreme Conditions (CSEC), the School of Engineering and the University of Edinburgh. I certainly appreciate all the technical and administrative support, exchange of knowledge, friendship, and willingness to help. Special thanks to Prof. John Loveday for his help in understanding compressed water properties, Dr. Jane Blackford for sharing her enormous expertise in materials science and engineering, and Dr. Frank Mill for his help in my professional development. Additionally, I would like to express my gratitude with Prof. Peter Higgs for his kind words and encouragement every time we had the opportunity to see each other. His achievements and humility are truly inspirational.

The financial support granted by the University of Edinburgh has been extremely important. I am thankful for receiving both Principal's Career Development PhD Scholarship and Global Research Scholarship, as they provided me with the opportunity of pursuing my PhD. I am also grateful for the financial support I received from The Institution of Mechanical Engineers (IMechE) during the writing of this thesis.

Personnel at ISIS Neutron Source (Rutherford Appleton Laboratory, UK) have been also of great help during the elaboration of this project. Special thanks to Christopher Ridley and Dr. Craig Bull for their support with information regarding high pressure neutron devices and accessories.

My gratitude also goes to my friends and people who have been a positive influence throughout the years. I would like to thank Prof. Dhanesh Chandra for his guidance through my formative years in research. Prof. Chandra served as my supervisor during

my MSc. in Materials Science and Engineering. His level of scientific and technical skills, work ethics and humanism have given me an example to try to emulate.

My friend Ana Brión-Martínez was key during my transition to the University of Edinburgh. I am thankful for her support and encouragement. I would also like to thank my friend and fellow student Laurence Dresch for her kind and selfless help proofreading this thesis. I greatly appreciate her time and patience.

Last but not least I am most grateful to my parents and my sister for their support over the years. I could never have made it this far without them.

Abstract

The study of matter at extreme conditions has been of great importance for modern society. A correct understanding of materials and environments subject to high pressures and temperatures enabled the development of car and jet engines, manufacture of goods, energy production and space travels among other human milestones. Discoveries in magnetism, geology, chemistry, and crystallography have been reported in literature as well, illustrating relevant contributions of this research area. Science at extreme conditions constantly requires to innovate instruments and characterisation methods. Sophisticated proficiencies are needed to explore and reproduce conditions of interest for this field.

Since the 1990s, high pressure instruments for neutron scattering have boosted the study of compressed matter. The design and subsequent improvement of the Paris-Edinburgh (PE) press and toroidal anvils successfully impacted this area, currently being the most extensively used instrument for high pressure neutron scattering, commonly used for pressures of the order of 10 GPa. Recent incorporation of toroidal anvils made of Zirconia Toughened Alumina (ZTA) has opened new experimental possibilities. Neutron transparency and mechanical resistance are key properties of this ceramic material. At this point it is essential to understand ZTA anvils design and working conditions in order to increase experimental capabilities and access new frontiers in compressed matter.

Computer-based modelling technique Finite Element Analysis (FEA) has been a recent ally for instrumentation design and optimisation. Phenomena such as mechanical stress, deformations, and thermal distributions can be modelled in an object, gathering information regarding its mechanical stability, behaviour and failure. Although this method is popular in industrial and engineering design and applications, it has not been widely employed in high pressure research due to scarce information in material properties under extreme conditions, as well as in innovative ceramics and metallic alloys introduced in these types of scientific devices.

The FEA method is an accessible alternative, able to provide key information in high pressure devices prior their manufacture. Furthermore, it has also the potential to model a compressed sample behaviour, being a promising low-cost alternative for high pressure experiments.

This PhD thesis has two main objectives:

1- To produce an FEA model and methodology, evaluating stress distributions and integrity of an existing ZTA toroidal anvil design in a PE press experimental assembly. The model includes ZTA toroidal anvils, gaskets, binding ring, supporting platens, and a water sample. For accurate results, relevant parameters such as friction coefficients, gasket's tangent moduli, and binding ring's lateral stress were investigated and included. This high pressure set is of routine use in neutron facilities for loads from 0 to 75 tonnes and sample volumes of tens of cubic millimetres.
2- To simulate and analyse via FEA the performance of the water sample included in the model developed. For a range of 0 – 6.7 GPa, aspects such as pressure versus load, molar volume, and phase transitions are assessed and benchmark with literature and experimental data to observe the accuracy of the obtained results.

Implementation of the FEA model in this thesis yielded a comprehensive stress and failure analysis in the high pressure set described, quantifying and locating peak stresses. Their link with ZTA anvils' failure is confirmed by extensive laboratory evidence available, validating FEA results gathered. Furthermore, a series of optimisations have been introduced towards reducing stress accumulation in critical areas, enhancing the anvils lifetime. Results and methodology obtained here can be employed as a guideline for the analysis of other anvil geometries and their design, aiming to reach higher pressures and larger sample capacity.

FEA versatility also proved successful assessing sample behaviour at static pressure steps. Water properties such as Poisson's ratio and bulk moduli were estimated at high pressure. This complex task is difficult to obtain experimentally and has not been reported in literature.

Index

Index of Figures

Index of Tables

Chapter 1

Introduction

Since the 1950's, the scientific community has increased efforts towards the development of high pressure technology. Advances in experimental techniques and devices have boosted the field of materials at extreme conditions. Hence, it is worthwhile to study how arrangements of atoms transform under high pressure and how the properties of a determined substance are altered.

Advances in high pressure instruments has led to multiple achievements in physics, chemistry, and geology among others. Today it is possible to apply and control pressure accurately on a small volume sample (single crystal or powder). Data is collected and analysed in a practical amount of time, determining its structure.

Chapter 1 introduces the topics of experimental high pressure, crystallography, and neutron diffraction experiments. The FEA method is also described as it has a major role in this project. An outline of the instrumentation and modelling challenges that this PhD thesis aims to improve is provided.

1.1 High Pressure

Around the world, scientists and engineers are interested in the study of matter at extreme conditions. Parameters such as high temperature, pressure, and magnetic or electrical field may cause dramatic interferences on the structure and macroscopic properties of a determined compound. This scientific field dates back to 1909, when Percy Williams Bridgman started his research on properties of matter under extreme pressures[1–3]. By developing an anvil-opposed high pressure apparatus, he revolutionised research in this area. In 1946, Bridgman won the Nobel Prize in Physics for his contributions to high pressure[4,5]. After further improvements of Bridgman's device, Lawson and Tang[6] were to first to employ diamond anvils for high pressure in 1950. Today, there exist two main laboratory methods for high pressure generation: static and dynamic.

1.1.1 Static High Pressure Generation

On static pressure generation, the diamond anvil cell (DAC) has revolutionized how high pressure studies are performed. This device is shown in Figure 1.1. The DAC is based on the essential definition of pressure (equal to force divided by area). To accomplish enormous pressures, it is not necessary to significantly increase the force when the area of application is reduced to square micrometres. This apparatus includes two diamonds aligned to match each other on a polished flat tip (commonly known as culet), where a sample is introduced. A metallic gasket material is used to enclose the sample and to provide support to the anvils. Pressure calibrants such as ruby chips are also sited with the sample[6].

The culets usually have a diameter between 50 µm – 1 mm. By applying axial load, the sample is encapsulated by diamonds and gasket and compressed[4]. The maximum static pressure reachable in a laboratory environment is over 600 GPa[7]. While Weir achieved the first infrared absorption experiments with samples at high pressure[8], Jamieson obtained the first high-pressure x-ray diffraction patterns for Bismuth[9] using a DAC. Those experiments were performed without gaskets. Incorporation of gaskets was significant as it allowed reduction of pressure gradients by filling the sample chamber with a hydrostatic or quasi-hydrostatic pressure medium[4].

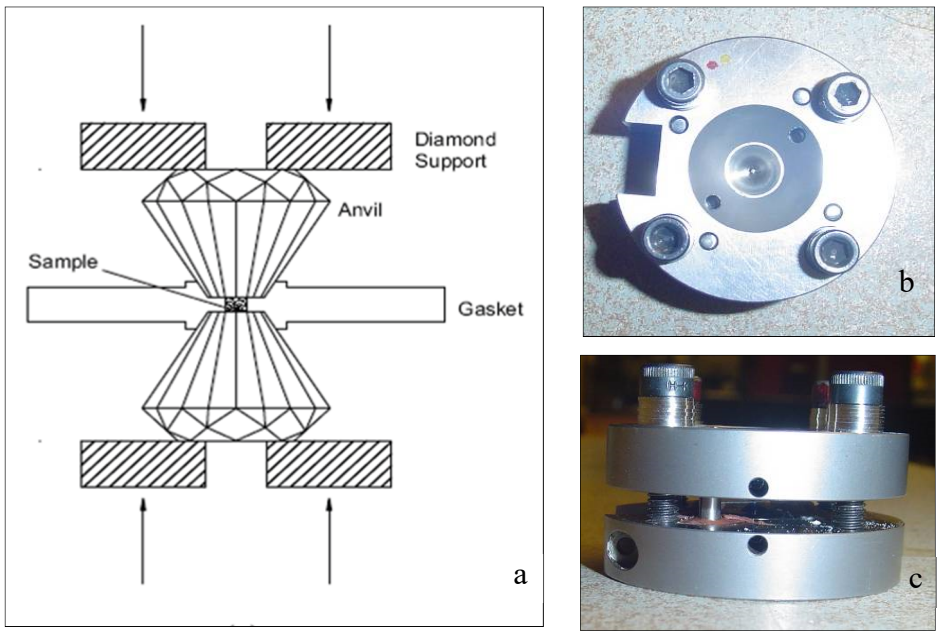

Figure 1.1. Diamond anvil cell operation principle and external body configuration. Scheme (a) explains how diamond anvils operate, compressing a sample encapsulated by a metallic layer (gasket). As the diamonds compressive surfaces (culets) have an extremely small area (square micrometres), pressures to the order of GPa can be generated with relatively reduced forces. At the external body (b and c), it is visible a set of screws which can be easily tightened to administrate high pressure.

A key advantage of diamond anvils is their transparency to electromagnetic and neutron radiation beams for characterisation studies such as x-rays, neutrons, and lasers for Raman and IR spectroscopy. Due to hardness, diamonds experience extremely low deformation upon the application of high pressure. Other advantages of this device are its compact size, portability, and adaptability to other apparatuses. It can be employed in a variety of experiments as the cell body can be properly adjusted to investigate particular problems. These aspects deliver exceptional experimental properties, being especially reliable for laboratory work.

There are remarkable publications on general high pressure methods and their effects in materials. A paper by Hemley and Aschcroft[10] as well as a review by Block and Piermarini[11] are relevant to this topic. Details, technical information, and applications are available in a book written by Eremets[6]. A general explanation of the DAC can be found

in a publication by Jayaraman[4]. Bassett[12] wrote an interesting piece on the 50th anniversary of the diamond anvil cell.

High costs associated with diamonds limits their size when used as anvils. Therefore, sample volumes in high pressure experiments are extremely small. Hard and transparent gems such as Sapphire and Cubic Zirconia offers an alternative, reaching pressures up to 25.8 GPa and 16.7 GPa respectively[13]. Sapphire anvils were introduced for neutron diffraction research at the end of the 1980s, providing lower pressures but larger sample volumes than diamonds[14]. Synthetic single crystal Moissanite (6h-SiC) has been studied as well for enlarging volume capacity in high pressure anvils. These alternative materials have been implemented in facilities around the world, proving their usefulness in science at extreme conditions.

1.1.2 Dynamic High Pressure Generation

High pressure dynamic techniques (also known as shock compression) create conditions of extreme pressure and temperature on microseconds or even picoseconds time scales. Pressures from 5 to 500 GPa are reachable, with a consequent increase in temperature as the process is adiabatic (compression occurs extremely fast).

Among complex tools to generate shock compression, light gas guns are of common use. This instrument accelerates a metallic projectile until reaching velocities of 4 – 7 Km/s with Helium or Hydrogen as a driving gas. Shock compression is produced when the projectile impacts a target capsule where a sample is located. A light gas gun approximate dimensions are 6.5 m length and a bore diameter of 20 mm. Sample dimensions are commonly 10 – 20 mm diameter and 0.001 – 1 mm thick[15,16]. Figure 1.2 illustrates this device.

Explosives, high electrical pulsed currents, and pulsed lasers are also employed for shock compression experiments. As alterations in sample's crystal structure are expected, characterisation methods as flash x-ray diffraction and Raman spectroscopy are generally employed. Properties such as electric resistivity can be measured by electrodes placed at the sample[15].

Shock compression is used to study a broad variety of research topics such as films, synthesis of new materials, bond strength, shock induced defects, and chemical reactions. One of the most popular cases of a commercial material produced by dynamic compression is diamond powder for abrasives. Carbon and metal powders are positioned on a cylinder where an explosive creates pressure and temperature conditions to transform Carbon into diamond particles[15]. Shock compression is also key for comprehending the performance bulletproof vests and armours, aerospace propulsion, and explosives[16]. The most extreme case of shock compression in a technological application is a nuclear weapon. Nellis[15,17] provides good insights on dynamic compression experiments and theory.

Figure 1.2. An example of dynamic pressure generation – light gas gun[18]. In general, the impactor and the target are considerably small compared to the piston. Hot gas is created in a short period and expands to accelerate the piston and then the impactor.

In high pressure literature the units preferred are the Pascal (Pa) where 1 Pa is equal to 1 N/m^2. The bar is also frequently employed, where 1 bar is equal to 100000 Pa (also equivalent to 1 atmosphere). Therefore:

- 1 GPa = 10^9 Pa, 1 MPa = 10^6 Pa.
- 1 bar = 0.1 MPa, 1 kbar = 0.1 GPa, 1 Mbar = 100 GPa.

1.1.3 High Pressure Research Examples

Current high pressure devices allow to increase sample pressure in a well-regulated manner, providing scientists with a powerful tool to generate knowledge in multiple research areas, where some of the main are described in the following paragraphs.

1.1.3.1 Chemistry and Materials Science

High pressure is a powerful technique in synthesis and characterization of new materials. Outstanding effects in magnetic, thermal and optical properties can be identified and studied in detail. High pressure studies have been conducted in almost every element of the periodic table[19]. However, many complex materials with potential applications remain to be considered.

Examples of high pressure research in materials science and engineering are provided by a variety of Lithium based complex hydrides, due to their potential utilisation in hydrogen storage. Compounds such as borohydrides and alanates (complex alkali metal aluminohydrides) are part of this group, for example, $Ca(BH_4)_2$ and $LiAlH_4$ have 11.4 wt% and 10.5 wt% of hydrogen respectively[20], making them suitable candidates in hydrogen storage applications. Generally, hydrogen desorption can be reached in metallic hydrides under controlled settings. It is crucial to understand the behavior of these materials under high pressure. Air pollution, global warming, and climate change are factors stimulating these investigations, as more efficient on-board hydrogen systems for vehicles would decrease dependence on fossil fuels.

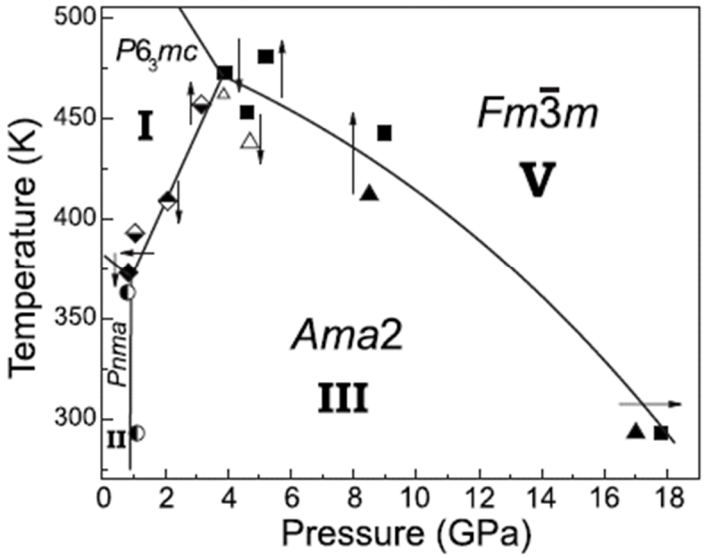

Figure 1.3. Pressure Temperature (PT) phase diagram of $LiBH_4$. This diagram is an example of a hydrogen storage material studied at extreme conditions of pressure and temperature[21]. It is possible to observe the structural changes $LiBH_4$ suffers at a pressure range of 0 – 18 GPa and room temperature – 500 K.

High pressure conditions can also create compounds which do not form under other circumstances. Helium (nature's most inert atom) combines with the most stable simple molecule (N_2) to form $He(N_2)_{11}$. A variety of compounds as these have been observed, such as $Ar(O_2)_3$, $Ar(H_2)_2$, and multiple compounds in the CH_4-H_2 system[10].

1.1.3.2 Astrophysics and Geosciences

In the universe, most of the matter is under extreme conditions of pressure and temperature. Pressure at the core of a neutron star is estimated to be 10^{26} GPa. Inside our planet, pressure at the inner core reaches up to 361.7 GPa, at the outer core 328.1 GPa, and at the mantle 135.2 GPa[22]. Astrophysicists and geoscientist are interested in devices to approximate these conditions in a laboratory, increasing knowledge on minerals and different phenomena at the Earth's interior. Substantial efforts have been completed to improve techniques on heating minerals (via lasers) at conditions of the deep mantle in a DAC.

Geoscientist rely on high pressure investigations to understand the formation or occurrence of minerals, Carbon fuels, earthquakes, volcanoes, masses of land and a broad variety of phenomena happening in the Earth.

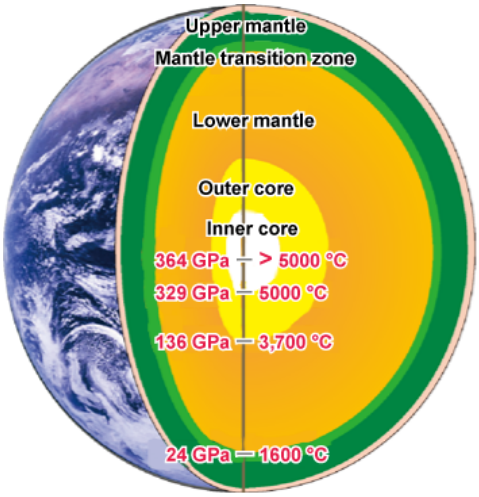

Figure 1.4. Illustration of high pressure and temperature conditions at the Earth's lower mantle, outer core, and inner core. High pressure experiments aim to recreate these conditions in laboratories, to study the composition and structure of materials at those extreme conditions. Image from JAMSTEC[23].

High pressure experiments on H_2O have led to the detection of dense cage (clathrate) structures. These high pressure compounds could form and condense in clouds of dense atmospheres within large planets or as ice on their moons[10].

1.1.3.3 Biology

According to Balny[24], high pressure in biological systems started with early observations by Bridgman in 1914, stating that:

"if the white of an egg is subject to hydrostatic pressure at room temperature, it becomes coagulated, presenting an appearance much like of a hard-boiled egg".

The following examples show how high pressure has impacted research in biology.

- The influence of high pressure on inactivation of viruses, enzymes, antibodies, antigens, microorganisms, cells, and tissues has been reported by Basset and Macheboeuf[25].
- In Japan, the first study on the pressure and temperature effects on ovalbumin and haemoglobin was published with the data reported as a phase diagram[26].
- At high pressures and low temperatures, negative activation energies have been detected and understood as the pressure-induced penetration of water into the protein. This is the first stage in the denaturation process according to Wu's theory of protein denaturation[27].

In the 1990s, high pressure found new fields of industrial applications after recommendations made by Hayashi and his co-workers in Japan. Although potential applications of high pressure for vaccine development and for the treatment of milk have been studied, it was in Japan were the first products were placed on the market. This was followed by several studies involving various opportunities in food science[28], medical, and pharmaceutical applications[24,29].

1.1.3.4 Energetic Materials

Exploration into energetic materials has encouraged many static high pressure and shock compression experiments. In an explosive, pressures of the order of 50 GPa and temperatures around 5500 K can be achieved[30,31]. These materials are commonly mixed with polymers as a binder. Polymers are also significant in energetic materials research

as they increase the total energy output of an explosive. Although the addition of a small amount of polymeric material to an explosive may lower the risk to accidental detonation, it also increases its machinability. Polymers utilised for this purpose include Kel-F 800, and Estane[32,33].

An example of a propellant which contains a polymeric binder, is ammonium perchlorate composite propellant. This is often used as a solid rocket fuel in space vehicles, being a mixture of ammonium perchlorate with hydroxyl terminated polybutadiene as a binder[34,35]. To investigate about the molecular bonds of energetic polymers such as glycidyl azide polymer, nitrocellulose, and poly (vinyl nitrate), Moore and McGrane performed experiments on vibrational spectroscopy[36]. Fabbiani and Pulham[30] offer a good review on the effect of pressure on energetic materials.

1.2 Crystallography

A major focus in high pressure science concerns the study of how atoms rearrange and form new structures when compressed. Crystallography represents the science which studies highly ordered microscopic structures (or arrangement of atoms, ions or molecules) mainly in a solid state. Crystal structure plays a major role in physical, chemical, or biological properties of materials, such as optical transparency, mechanical resistance, and magnetism.

Crystallographic experiments describe the unique distribution of molecules, atoms or ions mainly in solids, exposing symmetric patterns due to the nature of its constituents. These arrays repeating on the three dimensions are named crystal lattice, being a unit cell the minimum unit of volume which contains all the symmetric and structural information. The unit cell concept is illustrated in Figure 1.5. To discover these individual units that macroscopically create a crystal, an incident beam (electromagnetic radiation, neutron, electron or even a proton beam for example) is passed through a sample. The beam is scattered by the sample's electrons or nuclei creating a diffraction pattern and containing information about, among other things, atomic positions, unit cell volume[37].

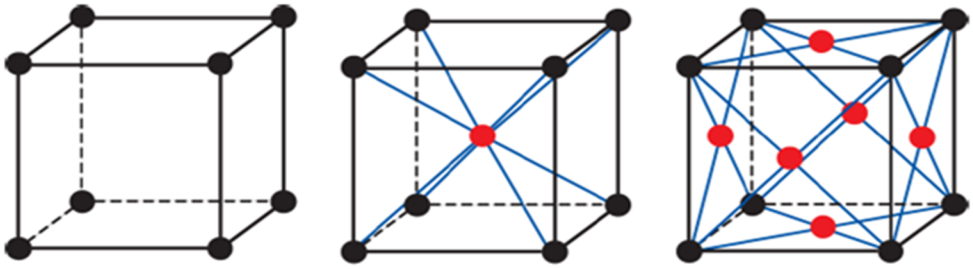

Figure 1.5. Examples of unit cell (atomic) arrangements in matter. Cubic lattice (a), base centred cubic (b), and face centred cubic (c). The unit cell is a minimum volume which contains atoms organised in 3 dimensions. The repetition of unit cells in a three-dimensional space define a crystal lattice. Crystallography studies show these atomic configurations and how they can be modified under specific parameters such as high pressure and temperature. Image from Fang[38].

In 1895, the discovery of x-rays by Wilhelm Röntgen (a German professor of physics) marked the beginning of crystallography as a scientific field. While other scientist had observed x-ray beams before, Röntgen was the first person to study them methodically. He obtained the Nobel Prize in Physics for his findings in 1901[39]. Following these events, Max von Laue investigated interactions of x-rays with crystals, and how a diffraction pattern is produced. He was awarded the Nobel Prize in Physics in 1914[40]. The discipline of crystallography continued its advances with works by William Bragg and his son who formulated the relationship between a crystal atomic structure and its x-ray diffraction pattern. They both were awarded the Nobel Prize in Physics in 1915[41].

Generating images from diffraction patterns involves an iterative process called refinement. Through this method, the mathematically predicted diffraction pattern (a model) is compared to a pattern generated by the crystalline sample. The refining process is made until both predicted model and data acquired match to a great degree. Computers have made this approach less difficult. Additionally, refinement software allows scientists to simulate interactions of beam and sample, creating an estimation of the diffraction patterns.

Certain molecular information can be extracted from diffraction patterns which are produced by powders and fibres, exhibiting a degree of order while not being a perfect solid crystal. This can be enough to obtain the structure of simple molecules, or to determine characteristics of more complex molecules. As an example, the double-helical structure of DNA was obtained from an x-ray diffraction pattern generated by a fibrous sample[42].

Furthermore, crystallography is also an important method in phase identification. When a process is performed on a material, it is ideal to know what compounds and phases are present. Each phase has a specific atomic organisation, and x-ray or neutron diffraction can be used to recognize which patterns (and compounds) exist in the material.

To show how a crystal structure can be identified in a diffraction experiment, Figure 1.6 exposes a model with an incident beam and two lattice planes. When beam and matter interact, the beam is scattered by the crystal lattice. A detector is placed to record the interference patterns of the diffracted beam. Information associated to the crystal lattice (elements contained, interplanar spacing, crystal size, phase identification, defects, among others) can be estimated with Bragg's Law, based on the diffraction angle obtained:

$$n\lambda = 2dsin\theta$$

Where θ is the diffraction angle, λ radiation wavelength, n diffraction order (n=1,2,3…) and d corresponds to distance between atomic layers in the lattice[37].

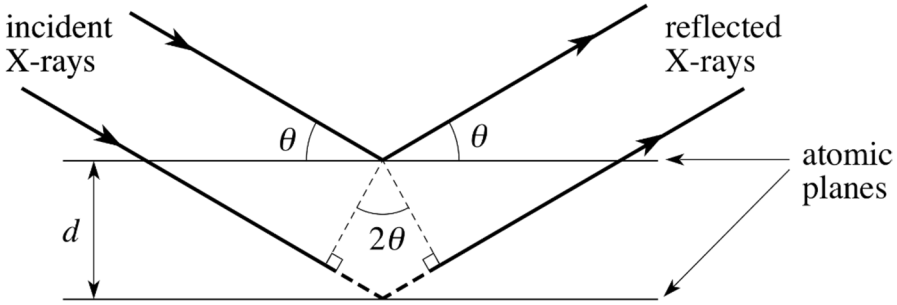

Figure 1.6. Schematic illustration of an x-ray beam scattered by two crystal lattice planes. Bragg's law can be used to obtain information regarding atomic planes distance. Image from PPLATO/FLAP[43].

Crystallography has evolved as a central branch of science and engineering, being essential in the advance of materials such as ceramics, metals, polymers, and alloys. Furthermore, biological sciences have a better understanding of proteins and viruses. Today, innovative techniques are available to experimentally determine the crystal lattice of complex materials. Numerous textbooks discuss the importance of this topic[37,44,45].

1.2.1 Powder and Single Crystal Diffraction

In diffraction experiments, a relevant aspect is the type of sample to analyse (powder or single crystal). In powder diffraction, a neutron, x-ray or other kind of beam is directed to a powder sample, producing a diffraction pattern providing the necessary data to characterise structural properties of a compound.

X-ray diffraction on powder samples is a widespread method on materials characterisation due to its accessibility in many laboratories. At synchrotron facilities, highly intense x-ray beams allow to perform experiments in a rapid and effective manner. They can be performed on small sample volumes with an increased resolution, as synchrotron data has reduced background noise. In particular cases, single crystal diffraction and its intense diffracted beam becomes a valuable tool as it provides extra information regarding the lattice structure. However, it is a difficult step to obtain a suitable crystal of the material to investigate. The crystal must be pure in composition and have a regular structure without any internal damage such as crack[46].

In high pressure experiments, single crystal diffraction has been challenged by certain difficulties. Single crystals can be easily damaged when high pressure is applied. Their fragility makes it difficult to load them into a cell. Today, it is possible to grow single crystals in situ, requiring an extremely delicate conditions control[47]. Powder diffraction data and methods are robust when compared with single crystal samples, especially at high pressure. Figure 1.7 illustrates both type of patterns, showing individual cases of a single crystal and a powder diffraction pattern.

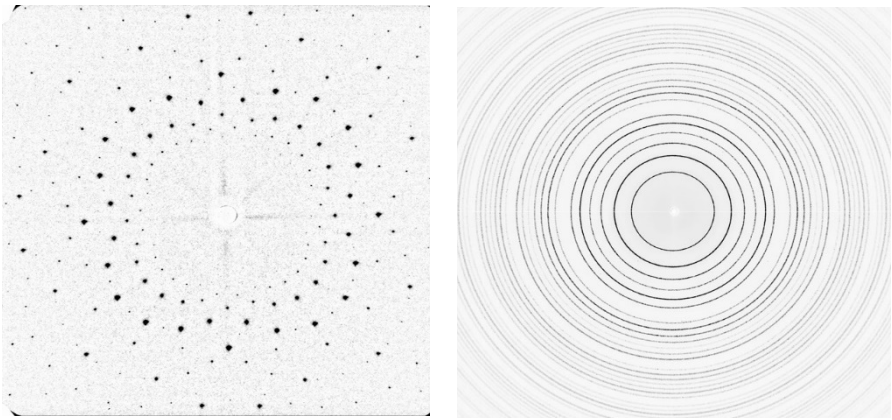

Figure 1.7. Examples of x-ray diffraction patterns. Left: Single crystal x-ray diffraction pattern of Silicon (0010 orientation). Right: LaB_6 powder diffraction pattern. Images from Diamond Light Source[48].

1.2.2 Neutron Diffraction

Modern research in materials and compounds require multiple techniques to confront particular problems. Neutron diffraction is a valuable characterisation technique, determining magnetic and/or atomic structure of a material and providing highly complementary data additional to information generated by other scattering methods. Neutrons are electrically uncharged subatomic particles, forming the atomic nuclei together with protons. Neutrons are estimated to have an average lifetime of 1000 seconds as a free particle[49].

While x-rays are scattered by valence electrons, neutrons are dispersed by the atomic nuclei of a sample. This particularity makes neutron diffraction a suitable method to be employed in a large range of materials, at atomic and molecular levels. Due to this series of features about interaction of neutrons with matter, neutron diffraction has numerous advantages when compared to other methods such as x-rays, for instance:

- Data collected on neutron diffraction can identify neighboring elements in the periodic table. This also applies to isotopes of the same element, as they present different scattering lengths for neutrons.

- Neutrons are ideal for biological samples and materials, as well as medical applications. Neutron beams are non-destructive as they are electrically-neutral, penetrating deep into the matter.
- Neutron scattering makes possible to localise light atoms while heavier are present. At the moment, this method is the most effective determining the structure of hydrogen bonds.
- Neutrons are responsive to magnetic fields as they have a magnetic dipole moment; therefore neutrons interacting with compounds with unpaired electrons, which generate magnetic fields, will indicate the structure of the materials.

Neutron diffraction certainly provides relevant information on materials and structures, but its application is not wide because of its limited access around the world (approximately 15 facilities in total[50]). In Europe, the Instutit Laue-Langevin (ILL, Grenoble, France) and ISIS (Oxfordshire, UK) are two neutron sources with high impact in several research areas. At ISIS, neutron beams have wavelengths from 0.05 to 20 Å. Training material from this institution offers many details of this technique, as well as its history and relevant facts[49]. In 2019, the European Spallation Source (ESS, Sweden) is planning to start operations and will provide beams approximately 30 times brighter than the existing neutron sources[51].

Neutron beam low intensity is perhaps the main challenge regarding this method. Radiation sources have not high brightness, and both spallation sources and continuous beam reactors are considerably much weaker than common x-rays and synchrotrons. Also, most materials and samples have low scattering indexes, as the neutron beam interacts with the nucleus, being smaller than the electron cloud. To make a complete analysis in a practical time, including precise thermal motion data, structural refinement and atomic positions, samples of large volume are necessary (few cm^3 for powder and few mm^3 for single crystal)[52].

In high pressure devices lower pressures are generated when sample volume is higher. This requirement represents a real engineering challenge for high pressure neutron scattering. Today, pressures around 30 GPa can be achieved on instruments with large

volume sample. In contrast, diamond anvil cells can reach pressures up to 300 GPa for x-ray diffraction experiments[53].

Design and manufacture of high pressure experimental accessories and devices for neutron diffraction requires a careful selection of materials. Neutron transparency is a property of high importance in this matter. As materials encapsulate the sample and exert high pressure, it is important for the neutron beam to reach the sample and diffract its pattern, not being attenuated by the surrounding material. Aluminium, Zirconia Toughened Alumina, Sintered Diamond and alloys such as Titanium-Zirconia and Copper-Berilium have transparency properties appropriated for these devices[52].

Neutrons are used to study drug synthesis, food science, chemical and biochemical engineering, healthcare among many others. Neutrons examine deep into solid matter such as gas pipelines, turbine blades and welds. This can provide an excellent understanding into the strains and stresses which are present in active lifetimes of critical engineering components. Neutron scattering is a gentle non-destructive method, ideal in heritage science investigations. Research of low-dimensional systems, nano-particles, and magnetism is also possible with this characterisation technique[50], being important for the advance of computer technology, sensors, data storage, and superconducting materials.

Additionally, neutron diffraction may be employed at large (macroscopic) scales, with tomographic and radiographic imaging being examples of this. As neutrons penetrate large objects, they can deliver a picture which is opposite (and therefore complimentary) to x-rays. Coming applications of this method include neutron diffraction in energy selective imaging. This procedure can identify among different elements or crystallographic textures, being a critical aspect to determine the strength of materials. Together with neutron diffraction, energy selective imaging can make available a three-dimensional diagram of residual stress. The applications of this technique range from Formula 1 motor racing to wind turbines[50].

1.3 High Pressure Neutron Diffraction Experiments

The Paris Edinburgh press (PE press) is currently one of the most used high pressure apparatus for neutron diffraction, being available at many neutron and synchrotron facilities around the world. The press and the cell are the two main parts of this instrument. The press is responsible of providing axial compressive force to the cell by using a hydraulic ram, being compact for its load capabilities. PE presses with load capabilities between 50 and 500 tonnes (t) have been developed[52]. Figure 1.8 shows a typical four-column PE press configuration.

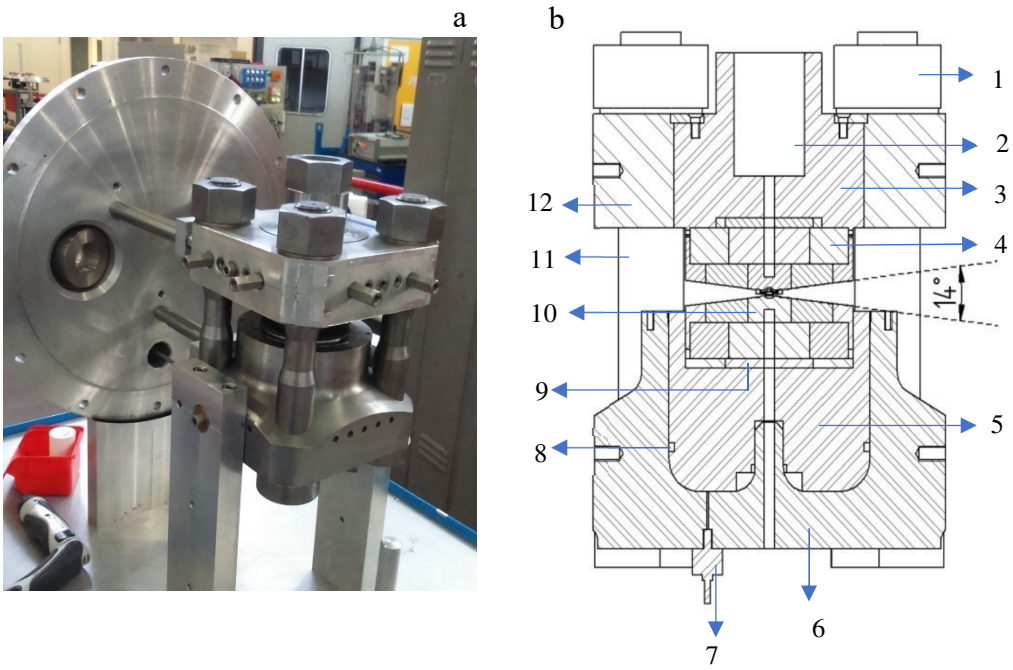

Figure 1.8. PE press (a) and operational scheme (b, Image from Fang[38]). A hydraulic ram generates pressure which is transmitted to the anvils and sample. A metallic gasket encapsulates the compound to analyse. Because its high volume capacity, PE presses are a widely employed device for high pressure neutron diffraction studies. For (b): (1) nut, (2) front collimator, (3) breech, (4) TC backing plates, (5) piston, (6) cylinder, (7) hydraulic fluid inlet, (8) O-ring seal, (9) backing disc, (10) anvils, (11) tie rod, (12) top platen.

Weighing approximately 60 kg, a standard PE press (Figure 1.8) has a loading capacity of 250 tonnes. This load allows compressing a 100 mm^3 sample up to 10 GPa[54], and samples of 35 mm^3 to 25 GPa[55]. In a similar manner to the DAC, the cell corresponds to

an assembly of anvils, metallic gaskets and sample. As their geometry matches the anvil's surface profile, the gaskets function is to encapsulate the sample and bring mechanical support to the anvils when compressive loads are transmitted. Under operational loads, gasket flow is restrained by the toroidal recess, increasing pressure at the sample chamber.

Its configuration allows large sample volumes, maintaining a reasonable space between anvils under working loads to allow neutron scattering to take place. Mechanical resistance and neutron transparency are the most important characteristics for gasket material selection. Toroidal anvils have played a major role in the advancement of this technology, increasing the cell capabilities in volume and high pressure. Figure 1.9 illustrates the constituents of a toroidal anvil cell.

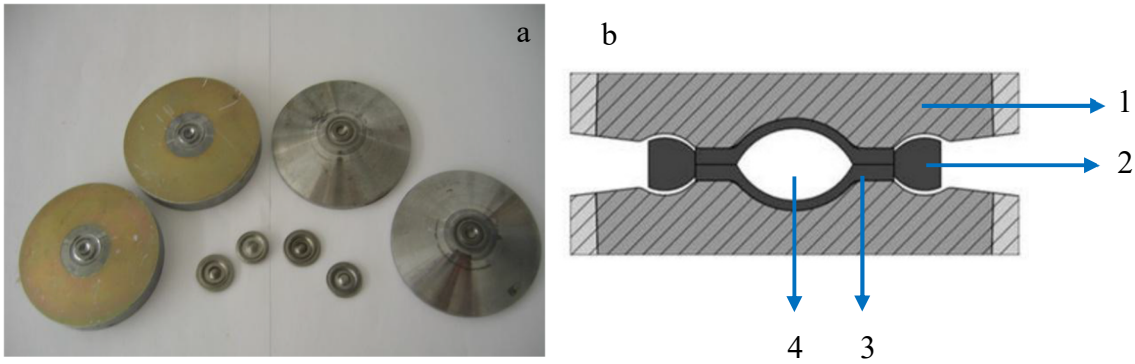

Figure 1.9. Toroidal anvils and gaskets (a) and operation scheme (b). Anvils are manufactured with materials such as Polycrystalline Diamond, Tungsten Carbide and Zirconia Toughened Alumina. Typical gasket materials are Titanium - Zirconia and Copper - Beryllium alloys. A reasonable neutron transparency is a requirement in those elements. For (b): (1) Toroidal anvil, (2) gasket (ring), (3) encapsulating gasket, (4) sample chamber. Image from Fang[38] (a) and Klotz[52] (b).

1.3.1 Toroidal Anvils

Toroidal anvils are central and critical elements on the PE press. The cell is composed by two identical coaxial dies with mutually facing surfaces, having a toroidal recess around the central part. This toroidal groove decreases extrusion of gasket's central part (sample chamber). As a result, the working lifetime of pieces is extended, increasing working pressures[56]. Early models of toroidal anvils were developed in Russia in the 1960s, mostly

for new materials synthesis. This is an effective and simple method to generate high pressure on large volume samples[57].

Among manufacturing materials for toroidal anvils, Tungsten Carbide (TC) and Polycrystalline Diamond (PCD) offer advantages such as mechanical resistance and neutron transparency. Double-toroidal anvils have been also developed, having two concentric toroidal recesses around the sample chamber of the anvil. Pressures around 30 GPa in samples with a volume of 35 mm^3 have been reported using Sintered Diamond as anvil material[55].

As both strength and neutron transparency are aimed to be maximised for high quality experimental results, ceramics such as Zirconia Toughened Alumina (ZTA) are being tested[52]. Recent experiments developed in the ISIS neutron facility (where these devices are used regularly) reported pressures up to 8 GPa in a water sample. A PE press with ZTA toroidal anvils was employed, with sample volumes of approximately ~47 mm^3.

1.3.2 Zirconia Toughened Alumina

Extensively known as a general purpose ceramic, Alumina (Al_2O_3) is mechanically hard and wear resistant. It is an excellent electrical insulator, strength against corrosion, and extreme temperature environments. Its properties enhance when Alumina is combined with Zirconia, typically between 10% – 20% such as in ZTA.

ZTA mechanical toughness when compared to Alumina is credited to the displacive phase transformation of the metastable tetragonal Zirconia grains when ZTA is stressed. Stress concentration at a crack tip produces a transition from a tetragonal crystal structure to monoclinic, which is related with a volume expansion of Zirconia. This volume expansion stops crack propagation, resulting in higher toughness and strength[58].

Having a compression strength of 4.7 GPa, and fracture toughness of 6-7 $MPam^{1/2}$, ZTA shows mechanical properties close to TC[52]. However, Alumina based ceramics display a remarkable transparency to neutron beams, positioning them as a strong candidate for the next generation of toroidal anvils. ZTA is largely implemented in cutting tools, medical devices, ballistic armour, and orthopaedic implants due to its biocompatibility.

1.4 Finite Element Analysis

Computer-based simulations are popular in contemporary engineering design. They represent an effective low cost method for analysis and development of products and processes. A numerical computational process called Finite Element Analysis (FEA) occupies a top position in this subject.

FEA's objective is to approximate solutions in continuous physical systems. This method subdivides an entire problem into a composition of small parts (mathematically generated) named finite elements. These elements can be in one, two or three dimensions with different geometries and orientations, having each the properties of a macro-system (i.e. mechanical strength, friction coefficient, and electric conductivity). By connecting the solutions of each element, FEA approximates complex solutions of the full arrangement. FEA is a powerful tool to solve a considerable range of engineering problems, such as in fluid dynamics, structural mechanics, heat transfer, and magnetic/electric field.

Since the whole system is represented as a sequence of algebraic equations, high and sophisticated calculation capacity is essential. Today, computers allow us to accomplish solutions in a practical amount of time. Considerable numbers of FEA software is commercially available; ANSYS is one of the most used in science and industry. Analysis in stress distribution and failure, thermodynamics, magnetism and many other phenomena can be studied in this convenient manner. Figure 1.10 illustrate cases of FEA for stress analysis in common engineering applications.

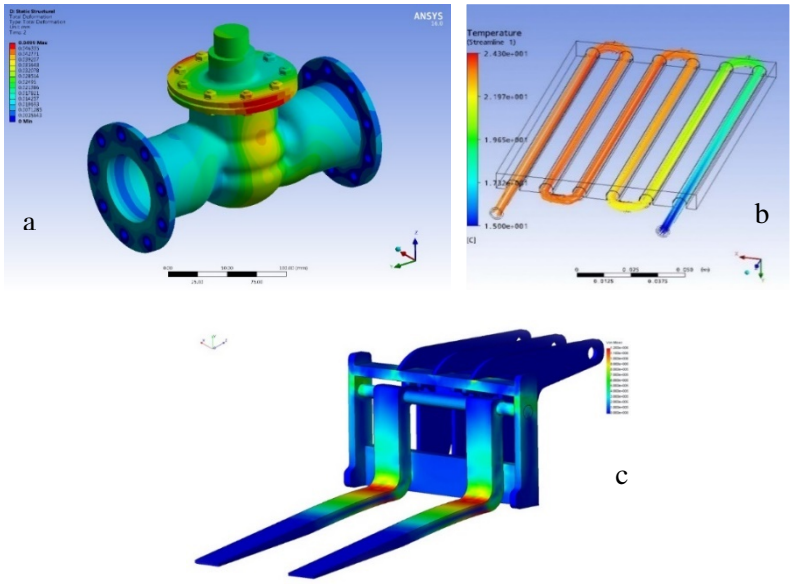

Figure 1.10. Examples of FEA studies in mechanical deformation and stress (a and c) and temperature distribution (b) in various industrial assemblies[59–61].

1.5 Thesis Layout

At this point it is clear how high pressure instrumentation has contributed in a considerable number of scientific and engineering advances. Toroidal anvils currently used in studying compressed samples via neutron diffraction deliver significant results in many facilities around the world. Constant enhancements are necessary to maintain this important field up to date. Therefore, innovative materials require to be analysed and incorporated in the manufacturing of anvils, gaskets and other components. Meanwhile, computational FEA methods are a consolidated tool to evaluate components performance during operative conditions. It is interesting to apply this technique in the assessment of a ZTA toroidal anvil configuration, being this a promising material due to its neutron transparency and mechanical resistance.

From experimental and literature data, technical information of materials and components, and experimental evidence this PhD project establishes an FEA model and methodology for stress and failure analysis of these types of anvils. Among others, aspects such as anvils' stress patterns under working loads, causes of failure, and optimisation of current anvil design are proposed, developed and discussed. This thesis also proves the

usefulness of the FEA method to model the complex behaviour of a compressed water sample in a ZTA anvil cell, obtaining static pressure steps, phase transitions, and molar volume evolution. Results gathered in this thesis are beneficial for future experiments and high pressure instrument design guidelines. The following paragraphs describe the content of this PhD thesis.

Chapter 1: Introduction

An introduction to relevant concepts for this PhD project is offered in this Chapter, describing the areas of science at extreme conditions, high pressure instrumentation, crystallography, and neutron diffraction. The PE press and toroidal anvil cell are explained and illustrated as they have a main role in this thesis, together with ZTA and TiZr specialised materials. As this research project is primarily developed employing the computational FEA method, this numerical technique is presented as well.

- Section 1.1: High pressure. Description of static and dynamic high pressure generation, research examples in chemistry and materials science, astrophysics and geosciences, biology and energetic materials.
- Section 1.2: Crystallography. Topics in powder and single crystal x-ray diffraction, and neutron diffraction.
- Section 1.3: High pressure neutron diffraction experiments. Use of toroidal anvils and introduction to ZTA as anvil material.
- Section 1.4: Finite Element Analysis. Introduction to this computational based method and portrayal of its importance in contemporary engineering.

Chapter 2: Literature review

Chapter 2 reviews topics and literature relevant for this PhD thesis. Important concepts in design, stress, and failure analysis are discussed in detail among others. These areas occupy a central position in the study of the high pressure instrument to develop containing a water sample.

- Section 2.1: Design. An overview of the design process is given in this section, as well as the importance of safety factors, engineering codes, and product integrity.
- Section 2.2 Stress analysis. This section describes central ideas concerning the stress and failure analysis process, relevant for science and engineering. Concepts

such as materials resistance, stress-strain curve, ductile and brittle materials, and principal stresses are explained as they are central in the analysis of ZTA anvils and sample to examine.

- Section 2.3: Materials. A number of important materials for high pressure neutron diffraction instruments are technically described, including mechanical properties and behaviour. Advanced ceramics and alloys such as Polycrystalline Diamond, Cubic Boron-Nitride, Zirconia Toughened Alumina, and Titanium-Zirconium are included.
- Section 2.4: High pressure neutron diffraction instruments. Multiple literature references regarding design and development of instruments for high pressure neutron diffraction are exposed.
- Section 2.5: FEA studies in high pressure devices. Publications on the use of FEA for high pressure instruments design and evaluation are reviewed.
- Section 2.6: Pressure-Temperature water phase diagram. Being a water sample included in the FEA study of ZTA toroidal anvils, its properties at high pressure and temperature are discussed. In particular, this section sets a reference on the phase transitions from liquid to Ice VI and Ice VII at room temperature.

Chapter 3: Finite Element Analysis Methodology

Due to the importance of the FEA technique in this project, Chapter 3 includes a literature review on this topic. This is followed by the FEA model development of the ZTA anvil and surrounding components to be used in this thesis, including relevant parameters to obtain accurate results in stress analysis and modelling of a compressed water sample.

- Section 3.1: Introduction. An introduction to the FEA technique is given in this section.
- Section 3.2: FEA literature review. Due to the importance of the FEA method in this PhD thesis, a separated review on this topic was produced and delivered in this Chapter. Its origin from numerical methods to analyse complex problems involving simultaneous physics phenomena is studied. Concepts such as boundary conditions, mesh, contacts, element types and solvers are explained as they are applied in the generation of a FEA model for the ZTA toroidal anvils and sample.

- Section 3.3: FEA model of a ZTA anvil cell. Information collected on ZTA anvils geometry, components, and materials is employed to produce an FEA model of this device. As mentioned, this will be employed to obtain stress patterns in the anvil and sample for further analysis.

Chapter 4: Finite element analysis of compressed liquid water in a ZTA toroidal anvil.

Having produced the FEA model required for this thesis, a series of static room temperature pressure steps in the liquid water sample (~47 mm^3) are developed, emulating data available in literature and experiments developed in ISIS Neutron Laboratory. As a result, water pressure versus load curves for the sample have been produced, including areas of phase transition to Ice VI. Data in molar volume has been used to validate results.

- Section 4.1: Introduction. In this section an introduction to the FEA modelling process to perform is given, as well as information of liquid water phase transitions at high pressures and room temperature.
- Section 4.2: Modelling of compressed liquid water (0 – 0.588 GPa). In first instance, a series of static pressure steps are simulated to match experimental data available in literature, obtaining accurate results for a pressure range of 0 – 0.588 GPa. Due to the employment of an implicit solver, a methodology is explained along with information about liquid water elastic properties input in the FEA model.
- Section 4.3: FEA modelling of compressed liquid water from ISIS experimental data (0 – 0.979 GPa). Having attained successful results benchmarking the performance of a compressed water sample via FEA with literature data, experimental static pressure steps obtained from experiments developed for this thesis at ISIS Neutron Laboratory are modelled (0 – 0.979 GPa pressure range). Adjustments to match the broad phase transition to Ice VI and data in molar volume mark the importance and versatility of the FEA method simulating complex sample behaviour.
- Section 4.4: Modelling of compressed liquid water at 1 GPa. A liquid water model at its room temperature phase transition limit has been developed. The aim is to observe the behaviour of liquid water at this limit and to understand the

capabilities of the model in terms of hydrostatic conditions and stress distribution to surrounding elements.

Chapter 5: ZTA Toroidal Anvils Stress Analysis

The mechanical stress behaviour of ZTA toroidal anvils under operational conditions is detailed in Chapter 5. Maximum and minimum principal stresses are examined across the body of the anvils to determine stress concentration areas, which command the failure process. The FEA results and failure criteria are benchmarked with experimental evidence to validate results. Specific changes in the anvil's geometry are proposed to increase its pressure and sample volume operational range.

- Section 5.1: Introduction. An introduction to the stress and failure analysis to perform in ZTA toroidal anvils is given in this section.
- Section 5.2: FEA of ZTA anvils with Ice VI and VII. A series of statically compressed Ice VI and VII (1 – 6.7 GPa) is produced with the FEA model available in this thesis. Equations of state obtained from experiments performed in ISIS Neutron Facility helped to find bulk Moduli values. Adjustments in this property and Poisson's ratio were done to reproduce the broad phase transition between these two forms of ice.
- Section 5.3: ZTA toroidal anvils stress analysis. During modelling of Ice VI and VII on the previous section, a large stress data collection was also produced in ZTA anvils, gaskets and other components of the set. Based on these stress patterns, areas where stress concentrates are identified and analysed to obtain regions likely to trigger failure in the anvils.
- Section 5.4: Stress analysis at ZTA anvil-gasket interface. Having identified this area as critical, a stress analysis and a failure criteria are developed and compared with evidence of failure in this region.
- Section 5.5: Stress analysis at ZTA toroidal anvil's beam aperture. Having this area characteristics of a discontinuity in a material, stress patterns were collected and analysed with proof of failure reported in this area to generate a failure criteria.

- Section 5.6: Chamfer area. Stress concentration in this area has been observed in part due to pre-stress induced in the binding ring. This is analysed and quantified as failure has been reported.
- Section 5.7: Summary. A summary of the results gathered in this Chapter is provided, towards having design guidelines in ZTA toroidal anvils.

Chapter 6: ZTA Anvils Optimisation

Based in stress patterns and results obtained in the previous Chapter for standard ZTA anvils, a number of ideas regarding anvils' optimisation are explained and studied via FEA. It was demonstrated how these geometrical modifications present less stress accumulation in critical areas, with high possibilities of increasing anvils' service lifetime.

- Section 6.1: Introduction. An introduction to the optimisation process produced in this Chapter is given.
- Section 6.2: Beam aperture. Being this the area with higher failure rates in standard ZTA anvils studied, a series of modifications are proposed in the beam aperture. A new geometry is analysed via FEA to demonstrate better stress conditions than in the original ZTA anvil design, leading to a higher mechanical resistance.
- Section 6.3: Toroid area. A toroid area with added surrounding material is proposed in this section. The idea is to increase support in this critical area and prevent failure from occurring at 75 tonnes.
- Section 6.4: FEA non-toroidal adapted model. The stress analysis methodology and FEA model developed in this thesis is applied to another ZTA anvil design proposed in literature. This is important to demonstrate how the guidelines established in this thesis are useful when implemented in other anvil geometries and materials.

Chapter 7: Conclusions and future work

Closing remarks for this thesis are provided, together with ideas to develop in this type of FEA high pressure instrumentation analysis projects.

- Section 7.1: Introduction. An introduction to this Chapter is provided.

- Section 7.2: Summary and conclusions. A summary of the work performed in this PhD thesis is given, as well as the most important conclusions attained.
- Section 7.3 Future work. Suggestions to implement in the FEA models and methodology developed in this project are explained, towards improve this method and its employment.

Chapter 2

Literature Review

This Chapter presents a detailed review of methods, materials, and instruments employed and analysed in this thesis. An introduction to engineering design and stress analysis is provided, together with references of the use of various methods for these determinations. Its association with mechanical properties of materials and its relevance to high pressure neutron diffraction instruments is discussed. In addition, information about history, evolution and current use of high pressure devices such as toroidal anvils and PE presses is also supplied, highlighting important research outcomes based on their use.

2.1 Design

This PhD thesis strongly focuses on the design of instruments for high pressure neutron diffraction experiments. According to multiple authors, perspectives, and fields, design can be defined in several terms. R. Budynas and J. Nisbett[62], top contributors in machine design education, claim:

"To design is either to formulate a plan for the satisfaction of a specified need or to solve a problem. If the plan results in the creation of something having a physical reality, then the product must be functional, safe, reliable, competitive, usable, manufacturable, and marketable".

Real-life engineering problems interrelate a broad variety of disciplines such as fluid and solid mechanics, materials selection, heat transfer, and electronics. During the design process, decisions in many aspects must be made. Information can be contradictory or scarce, prompting the designer into a problem-solving position. Tools such as technical catalogues, statistics, mathematics, databases and computer aid engineering (CAD) are of common use in the process.

The decision making process in design must consider safety and reliability before any other procedure. When creating a determined product or process, it is necessary to avoid any possible harm to users and supply detailed instructions. It is also required to perform analyses and testing in order to prevent failure under normal working ranges, including an appropriate service lifetime and maintenance. Engineering standards and codes are available for both safety and reliability. Institutions such as ISO, IMECHE, ASTM, BSI and many others provide standards for product quality, construction, the automobile industry, and materials, among others. Budynas and Niesbett[62] deliver further basic principles in mechanical engineering design.

In products and processes, lifetime and integrity depends largely on how maximum stresses distribute among components or structures. Generally, it is important that stress magnitudes are below the material's strength at specific (critical) locations. A design must consider safe operational stresses, with enough margins to avoid failure even with uncertainties. For example, when designing a passengers lift, numerous aspects must be taken into account. Due to a weight limit (10 – 15 people), the designer must contemplate scenarios during which more people are inside the lift or it is used to transport

construction materials or heavy goods to higher floors. Maintenance problems (corrosion, high temperatures, lack of lubrication on the motor) or electric power cuts must not endanger users.

There are different manners to implement safety factors in a design. Fundamentally, a safety factor (also known as factor of safety in literature) represents how resistant a component or structure is in comparison to the working loads the system is expected to experience. The following expression synthesizes this concept.

$$Safety\ factor = \frac{yield\ stress}{working\ stress}$$

Following the previous definition, a structure or component with a safety factor of 1 withstands exactly the calculated working load without any margin. A safety factor of 2 will tolerate twice as much load as the working load. In an overhead (bridge) crane, wire rope safety factor is 5 – 7 times the load to convey.

Figure 2.1. Overhead crane. Wire rope is selected to withstand a load 5 to 7 times larger than the crane's working limit (40 tonnes in this case). Image from Konecranes Inc.[63]

2.2 Stress Analysis

2.2.1 Solid Mechanics, Stress, and Strain

Continuum mechanics is a branch of physics which assumes that a body or substance entirely fills the space it occupies. It ignores discontinuities (i.e. interatomic distances) as length scales are larger. Many physics laws such as conservation of energy, mass, and momentum are based on this postulation[64]. To assess the reaction of a body under an applied force (internal or external), it is required to know the force intensity and the body's cross section area. In a continuous material, stress (σ) is defined as the average

intensity of the force (or forces) divided by the body's cross section area. On the other hand, strain (ε) corresponds to the amount of elongation or shortening per unit length caused in the body due to the stress[65]. These basic definitions refer to average values, as stress and strain can be irregularly distributed over the cross section of the body. While strain is a dimensionless parameter, common stress units in literature are Pascals (1 Pa=1N/m^2) and psi (1 psi = 1lbf/in^2). Figures 2.2 and 2.3 illustrate both concepts.

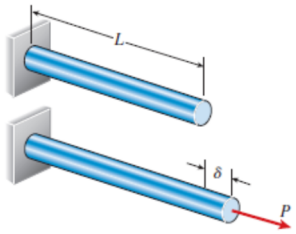

$$Strain(\epsilon) = \frac{Elongation}{Original\ length} = \frac{\delta}{L}$$

Figure 2.2. Elongated solid bar under axial load. Average strain is defined by elongation divided by the bar's original length. Image from Gere[66].

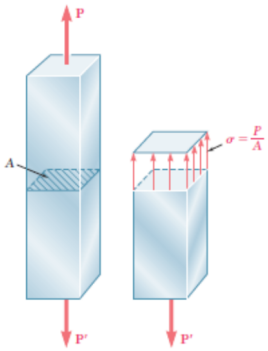

$$Stress(\sigma) = \frac{Force}{Cross - sectional\ area} = \frac{P}{A}$$

Figure 2.3. Prismatic solid under axial load. Average stress can be defined by force divided by the bar's cross-sectional area. Image taken from Beer[67].

Stress can be generally classified in compressive, tensile, and shear stress. Compressive and tensile stresses are normal (perpendicular) to the cross section area of an element, inducing shortening or stretching of a material when applied. Stress acting in an angle can be expressed in normal components. Structural columns or a chair's legs are examples of elements subject to compressive stresses, while a bridge's supporting cable illustrates tensile stress. Sign conventions in literature establish that the magnitudes for normal tensile stresses are positive whereas for compressive stresses are negative. Shear stress is

coplanar with a material's cross section. When a ski slides across the snow, shear stress is induced at the ski surface.

Stress elements are a useful representation of stress acting in a determined point on a body. Figure 2.4 (a) shows the general stress state of an infinitesimal body element. It is possible to notice how for cartesian coordinates, normal stress components are identified by subscripts x, y and z (relating each cartesian axis). In this Figure, it is clear how σ_x acts on a surface perpendicular to the x axis, likewise for σ_y and σ_z cases. Shear stresses require two subscripts. While the first subscript indicates the perpendicular surface where shear stress acts (as explained for normal stress), the second subscript denotes its direction. Figure 2.4 (a) illustrates how τ_{xy} acts in a surface perpendicular to the x axis, with direction to the y axis. Generally for equilibrium, shear stresses with crossed subscripts have the same magnitude. Therefore τ_{xy} equals τ_{yx}, τ_{zx} equals τ_{xz}, and τ_{zy} equals τ_{yz}. This is noticeable in Figure 2.4 (b).

At this point it is interesting to mention plane stress. This situation arises when the normal stress in one surface of a body with uniform material is zero, simplifying the stress analysis to only 2 dimensions. This condition can be found in thin elements such as pressurised thin-walled cylinders or structural plates, where perpendicular loads are zero or insignificant in comparison with loads in parallel[67]. Figure 2.4 (b) illustrates this condition.

In a relatable concept (plane strain), one dimension is significantly larger in comparison with the other two in the body. As in the case of a river dam or tunnel, loads are evenly distributed and perpendicular to the long dimension. Strain in the direction of the lengthiest dimension can be assumed as zero, simplifying the analysis as well[67]. Figure 2.4 (b and c) illustrate both concepts.

The consideration and use of both plain stress and strain in engineering problems is convenient, even in complex structures with intrinsic shapes. By taking two-dimensional slices in an area of interest, rapid first-hand stress results can be obtained. As explained later, computer methods such as FEA utilise this approach in an efficient manner. While full three-dimensional calculations and models give a more accurate panorama of the

stress in a particular area or element, the use of plane stress and plain strain provides valuable insights.

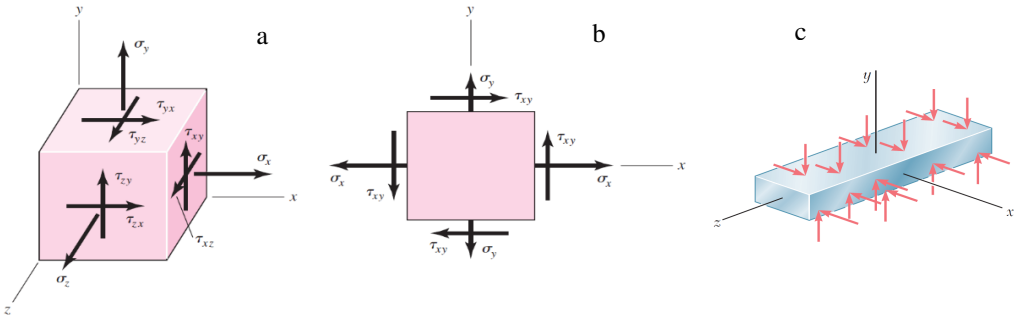

Figure 2.4. General stress state (a) and plane stress representation (b) at a point. Infinite bar plain strain example (c). Images from Beer[67].

Compressive stress can induce bending in a structure. Characterisation of this phenomena depends on the geometry of the elements and load location among other factors. When a component such as a column or beam suffers from bending, tensile stress is introduced in its configuration. A neutral axis divides the region where tensile and compressive stresses meet inside the component.

Buckling is a phenomenon of similar nature, causing a sudden and unpredictable deformation by loads smaller than the material's strength. Both buckling and bending are explained in literature due to their relevance in column and other slender elements design[62,67]. Bending and buckling can also occur locally in a component, causing a redistribution of the loads if there is no catastrophic damage. Buckling and its effects has been broadly studied and documented for slender elements under compressive stresses. While there is not a direct link between buckling and the device or components examined in this thesis, its relevance for certain elements under compressive stresses makes it worth to be referenced.

The field mechanics of materials (also called strength or materials or solid mechanics) analyses the behaviour of solids under stress and strain. This area offers resources and criteria to analyse and design machine elements and structures such as shafts, gears, columns and beams. Stephen Timoshenko is recognised as a pioneer of solid mechanics since the early 1900s. Multiple textbooks detail the magnitude of this subject[65,66].

Stress analysis has a central position in engineering and in a broad variety of disciplines involving design and maintenance of products, machine parts and structures. Design of bridges, aircrafts, automobiles and products such as medical implants exemplify this. Failure - safety investigation and forensic engineering can also be studied by stress analysis. Stress in gases and liquids is studied by fluid mechanics.

A variety of methods has been developed for stress analysis, including mathematical modelling via numerical analysis, experimental tests, simulation software or a combination of techniques. As a result, it is possible to obtain estimations on bending, fatigue, strain, fracture and buckling among other relevant information. In stress analysis, various theories have been developed, depending on the materials behaviour under stress and their safe use. The following sections provide specific insights on materials properties and theories relevant to stress analysis.

2.2.2 Stress- Strain Curve

A stress - strain curve can be produced by measuring the amount of strain a material registers at determined tensile or compressive stress ranges. The curve generated is unique for individual materials, being possible to associate with mechanical properties. Figure 2.5 (a) shows a generic stress – strain curve where two main stages can be identified. The elastic region extends from no load conditions to yield stress (σ_y), allowing the material to recover its original dimensions from deformations induced after load release. When stress increases beyond yield, deformations are permanent (plastic region). Ultimate stress, also called strength (σ_u) corresponds to the maximum stress achievable on the stress-strain plot. While many materials have a descending tendency after σ_u (leading to rupture of the material), others continue a rising trend, matching σ_u with rupture.[67]

Materials where plastic deformation is not registered, are called brittle; such as ceramics, glasses, and certain types of cast irons are examples of them. Materials with plastic deformation regions are called ductile. Metals such as Gold, Copper, and Aluminium are known by their large plastic deformations.

The slope of the stress – strain plot in the elastic region is known as Elastic (or Young) Modulus. This value characterises how resistant a material is to deformation when force

is applied. A rubber band has a low value of Elastic modulus whereas diamonds would be a counterexample[67].

It is important to remark that Figure 2.5 (a) corresponds to what is defined in literature as an engineering stress-strain diagram. Cross section area used to calculate stress values is not varied during the entire range. True stress diagrams simultaneously measures stress and changes in the cross section area. In real conditions, the cross section area varies when load is applied. As an example, ductile materials in tension usually present a "neck" after σ_u, reducing drastically its cross section area. Due to this effect, true stress (σ_t) is higher than engineering stress after "necking". Figure 2.5 (b) displays a generic plot of true stress at tension, showing higher stress values when compared with the engineering stress diagram. Compression tests require different settings, as phenomena such as buckling or bulging is present. Stress definitions explained in this section apply in these cases. The books by Beer[67] and Budynas[62] cover the topics discussed in this section extensively.

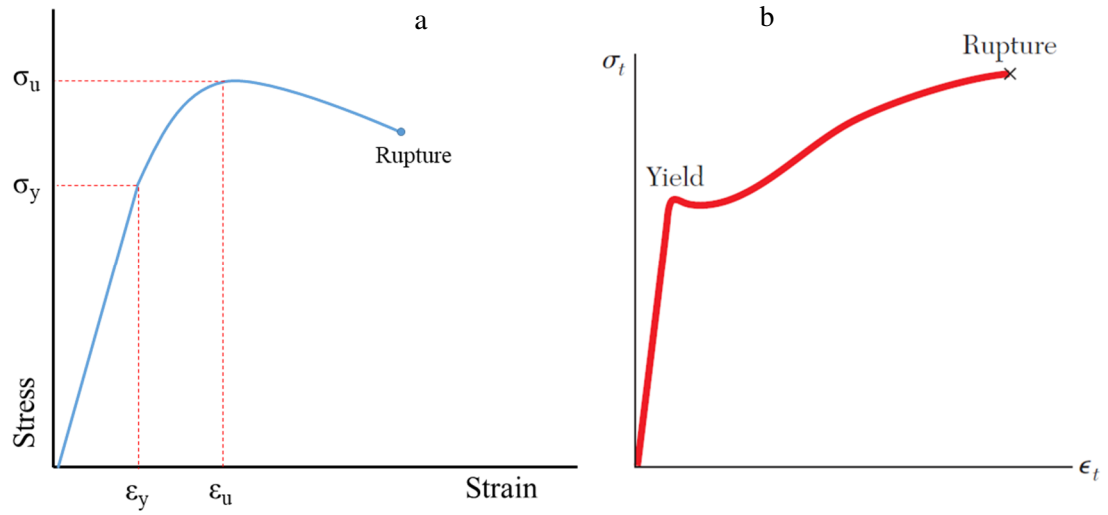

Figure 2.5. Generic engineering (a) and true (b) stress-strain diagrams for ductile materials. This representation provides key information in materials such as elastic and plastic behaviour, yield strength (σ_y), and, ultimate strength (σ_u) among others. Brittle materials do not typically present a large plastic region, as failure occurs close to their yield limit. Image (b) from Beer[67].

A material presenting uniform mechanical properties in all directions is named isotropic. Common fluids (including air and water) and multiple commercial metals such as Copper are isotropic. Anisotropy on the contrary stands for materials presenting directional properties. While wood is a typical example in nature, composites such as carbon fibre can be manufactured to withstand more tension in one direction. Manufacturing processes in metals such as cold rolling can also induce anisotropy.

When an isotropic solid undergoes uniform compression, its behaviour can be quantified by bulk modulus, determining how compressible a material is. Bulk modulus ("B") can be calculated by following Equations 2.1 and 2.2, where "V" represents volume, "P" pressure and "ρ" density.

$$B = -V\frac{dP}{dV} \qquad B = \rho\frac{dP}{d\rho}$$ Equations 2.1 and 2.2

As a result of axial elongation, materials experience transversal compression (being the opposite effect for axial compression). Within the elastic range, the ratio of transverse and longitudinal strains is called Poisson's ratio (ν). Classic literature mentions how Poisson's ratio values are between 0 (perfectly compressible) and 0.5 (perfectly incompressible). Metals have values around 0.3. Figure 2.6 illustrates this effect.

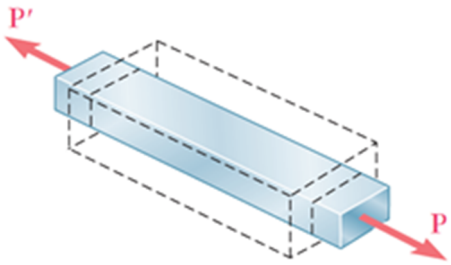

Figure 2.6. Illustration of a material under axial load (tension). An axial elongation is produced when the load is applied, resulting in a transversal compression (Poisson's effect). Compressive loads have opposite results. Poisson's ratio associates both deformations as a characteristic in a material. Image from Beer[67].

The concept of Poisson's ratio and its limits was originally developed more than 200 years ago. Modern methods and materials provide different insights to those initially conceived. Literature mentions reviews of 596 different substances (more than 3000

measurements) including most common materials for engineering, alloys, ceramics and pure elements, showing $\nu \geq 0.2$ (with exception of few hard materials such as diamond). On the other hand, when compression is applied to a material, the work done is converted into internal energy according with First Law of Thermodynamics. This increases temperature and therefore volume in the substance. A Poisson's ratio of 0.5 (incompressible) would imply no increase in volume, therefore, $\nu < 0.5$. Different authors have analysed these limits in deep[318-319].

As research advances, experimental materials push boundaries in many fronts. Auxetic materials have negative Poisson's ratios, becoming thicker when stretched[318], while recent investigations suggest the possibility of materials with ratios beyond 0.5[321].

Elastic ("E") and bulk modulus along with Poisson's ratio are key properties for stress analysis. Equation 2.3 links these three properties at the elastic regime in a particular isotropic material.

$$B = \frac{E}{3(1-2v)} \qquad \text{Equation 2.3}$$

2.2.3 Transformation of Plane Stress

At a given load, the magnitude of normal and shear stresses varies with respect to rotation angles. Figure 2.7 shows a stress element subject to this analysis for plane stress, where stresses have parallel directions to x and y axes. Transformation of stresses allows to obtain these values at specific angles. Equations 2.4 to 2.6 provide the stress values at a determined angle (θ).

$$\sigma_{x'} = \frac{\sigma_x+\sigma_y}{2} + \frac{\sigma_x-\sigma_y}{2}\cos(2\theta) + \tau_{xy}sin(2\theta) \qquad \text{Equation 2.4}$$

$$\sigma_{y'} = \frac{\sigma_x+\sigma_y}{2} - \frac{\sigma_x-\sigma_y}{2}\cos(2\theta) - \tau_{xy}sin(2\theta) \qquad \text{Equation 2.5}$$

$$\tau_{x'y'} = -\frac{\sigma_x-\sigma_y}{2}sin(2\theta) + \tau_{xy}cos(2\theta) \qquad \text{Equation 2.6}$$

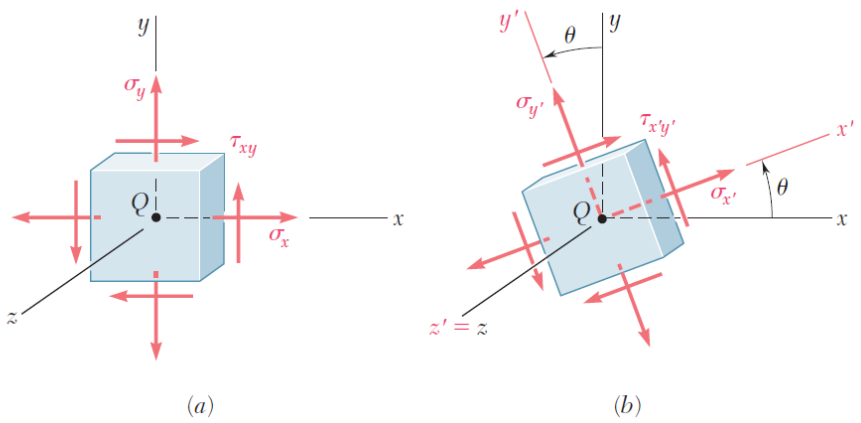

Figure 2.7. Normal stress (a) and principal stress (b) state in a specific point. Images from Beer[67].

2.2.4 Principal Stresses and Maximum Shear Stress

Normal and shear stresses vary uninterruptedly when axes are rotated, reaching minimum and maximum magnitudes at 90° intervals. Maximum (σ_{max} or σ_1) and minimum (σ_{min} or σ_2) normal stresses are called principal stresses and the principal angle (θ_p) define their positioning. From Equation 2.4, obtaining the derivative of σ_x' with respect to θ and making the expression equal to 0, an equation for θ which σ_x' is maximum and minimum is found. Equation 2.7 derives from this reasoning.

$$tan(2\theta_p) = \frac{2\tau_{xy}}{\sigma_x - \sigma_y} \qquad \text{Equation 2.7}$$

From Equation 2.7 and illustrated in Figure 2.8, two θ values can be found in the range from 0° to 180°, differing by 90°. Either of these angles may be employed to find the orientation of both maximum and minimum principal stresses. The planes on which principal stresses act are called principal planes. It is important to remark that no shear stress is registered on the principal planes ($\tau_{x'y'}$=0).

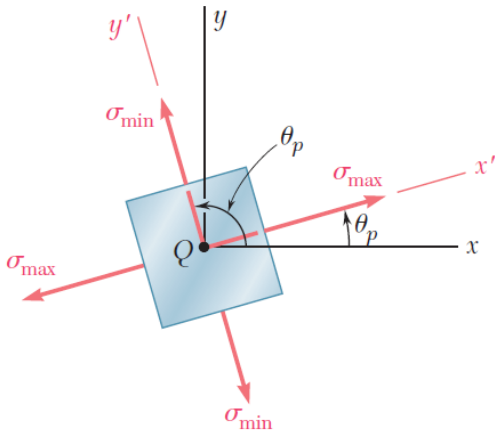

Figure 2.8. Representation of principal stresses acting in a specific point. Their angle and magnitude can be determined from normal stresses by employing Equations 2.8 and 2.9. Image from Beer[67].

For principal stress magnitudes, Equation 2.8 combines both of them. The plus sign gives the maximum principal stress while the minus provides the minimum principal stress. The derivation of Equations 2.8 to 2.11 can be seen in literature[67].

$$\sigma_{max,min} = \frac{\sigma_x+\sigma_y}{2} \pm \sqrt{\left(\frac{\sigma_x-\sigma_y}{2}\right)^2 + \tau_{xy}^2} \qquad \text{Equation 2.8}$$

Similarly to the principal angles, Equation 2.9 provides an algebraic expression to find the orientation of the maximum shear stress. Normal stress corresponding to that condition is the average between σ_x and σ_y (Equation 2.10). The maximum shear stress magnitude can be calculated with Equation 2.11.

$$\tan(2\theta_s) = -\frac{\sigma_x-\sigma_y}{2\tau_{xy}} \qquad \text{Equation 2.9}$$

$$\sigma' = \sigma_{ave} = \frac{\sigma_x+\sigma_y}{2} \qquad \text{Equation 2.10}$$

$$\tau_{max} = \sqrt{\left(\frac{\sigma_x-\sigma_y}{2}\right)^2 + {\tau_{xy}}^2} \qquad \text{Equation 2.11}$$

Figure 2.9 illustrates the situation concerning maximum shear stress, its orientation and normal stress.

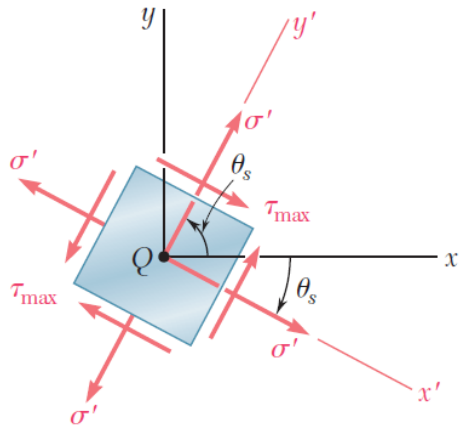

Figure 2.9. Maximum shearing stress representation. Its angle and magnitude can be determined by using Equation 2.11. Image from Beer[67].

As expected, principal stresses and maximum shear stress values are crucial for design purposes.

2.3 Materials

2.3.1 Ceramics

Materials science establishes five categories of materials: ceramics, metals, polymers, semiconductors and composites. Ceramics are non-metallic inorganic solid compounds containing metal, non-metal or metalloid elements with covalent or ionic bonds. Their structural order is often non-crystalline as it is possible to visualise in Figure 2.10. The word ceramic originates from the greek “keramos” (pottery). This word was employed to label clay-containing materials such as fireclay refractories and bricks[68].

These materials are commonly used for dinner plates, coffee mugs, flower vessels, and glasses. Brittleness is a main characteristic of ceramics due to their mixed ionic-covalent bonding[68]. At high temperature, ceramics in general transform into viscous liquids, being able to be modelled into intrinsic shapes. Other properties include good thermal and electrical insulating features, chemical insensitivity, transparency and high compressive strength.

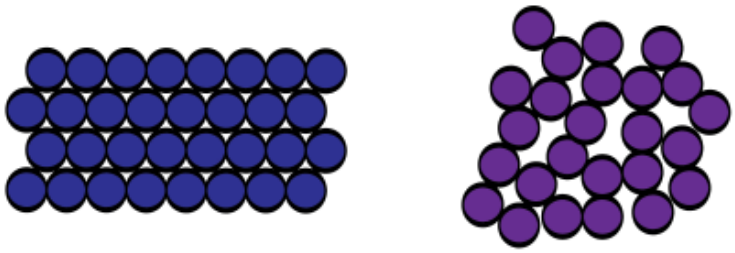

Figure 2.10. Crystalline (left) and non-crystalline atomic arrangements scheme[69].

Known and used for over 25000 years, traditional ceramics are based on clay or silica and low technology production methods are involved. Advanced ceramics on the other hand, are tailored for engineering uses, enhancing superior specific properties. These ceramics have been available for the last 100 years approximately. Engineering textbooks thoroughly explain ceramics, uses, and characteristics[68,70]. Sintering is a method used to produce intrinsic shapes with determined ceramic materials. By applying high temperature (below melting points) or pressure, powder ceramic materials can be mixed forming a solid. This method is also employed in metals and plastics. DeJonghe[70] further explains the sintering of ceramics.

In high pressure science, the use of ceramics in devices and instruments has increased as experiments have gained popularity during recent decades. Although Carbon is not a ceramic, its allotropic form diamond can be catalogued as a type of ceramic material[68]. There are over 35000 literature references to experiments performed with diamond anvil cells since 1950. Instruments for high pressure neutron diffraction have incorporated a new generation of sintered materials. Tungsten Carbide, Sintered Diamond and ZTA are perhaps the most representative at this stage. The following paragraphs describe these relevant materials.

2.3.2 Tungsten Carbide

Since early designs and instruments, Tungsten Carbide (WC or TC in literature) has been used in high pressure science. Its mechanical properties such as compression strength, hardness, stiffness and neutron transparency offer a good combination for its use in compressive experiments.

In the 1950s, Bridgman's pioneering research employed TC instead of hardened steels to reach 10 GPa on his instruments[71]. During the following years, TC was incorporated into piston-cylinder high pressure devices, obtaining values up to 5 GPa[72–74]. In two publications regarding developments of high pressure science and apparatuses, Jayaraman[4] discusses the use of TC in other accessories such as backing plates and rockers for high pressure cells.

Produced mainly by sintering, pure TC contains approximately equal parts of Tungsten and Carbon. Metal binders such as Cobalt and Nickel are added for grain size control or to enhance particular properties. TC is used in a wide range of industrial applications such as cutting tools, abrasives and jewellery. Klotz[52] provides a good review on this material and its production. As an available and reliable material, neutron diffraction high pressure instruments such as the McWhan cell[75] and the PE press have many important elements manufactured with TC. PE press anvils were originally developed with TC anvils and seats[76].

2.3.3 Polycrystalline Diamond

Also known as Sintered Diamond (SD), Polycrystalline diamond (PCD) has remarkable mechanical and neutron transparency properties (superior to TC), as it is composed principally from diamond powder (70-90% in volume). Other additives include Cobalt and Silicon Carbide (SiC). However, a relevant aspect of this material concerns its limited number of manufacturers for high pressure devices geometries, as its market lays mainly in cutting tools.

PCD suitability for high pressure instruments has been noticed since the 1970s. Bundy[77] developed an apparatus for resistance measurements up to 50 GPa using Sintered Diamond tipped pistons. In high pressure neutron diffraction science, this material has gained attention since the early 1990s in neutron scattering high pressure devices for pressures over 15 GPa[52]. TC is practically limited to ~14 GPa[52,78]. Pressures above 30 GPa have been obtained with PCD anvils with a double toroidal configuration[47,54,55,78,79]. Loveday[80] have published details of its importance and uses in high pressure neutron science instrumentation.

2.3.4 Zirconia Toughened Alumina

This PhD thesis has a strong analysis component of ZTA anvils. ZTA has suitable mechanical properties for high pressure instruments. ZTA's neutron transparency (specially at large wavelengths) is perhaps its most remarkable characteristic. As stated in Chapter 1, ZTA composition corresponds to Alumina (Al_2O_3) combined with Zirconia (10-20%).

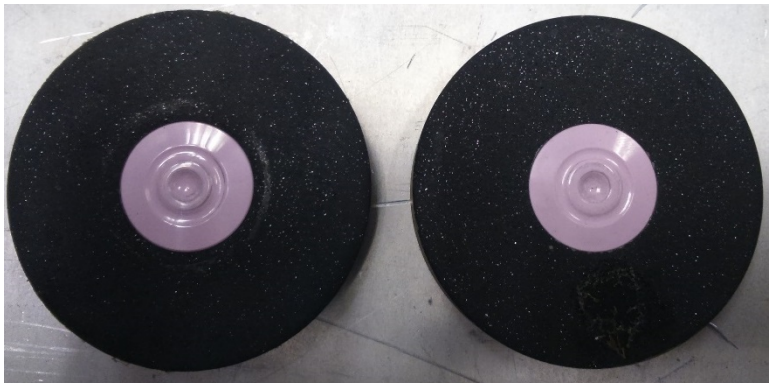

Figure 2.11. ZTA toroidal anvils and maraging steel binding rings. Binding rings are covered with Boron enriched paint to reduce background in the signal.

In 1974, McWhan's neutron diffraction high pressure apparatus contained a Polycrystalline Alumina cylinder to enclose the TC pistons. This publication lists Alumina's neutron transparency benefits[75]. In 1995, Ivanov[81] and collaborators manufactured and tested an Aluminium Oxide anvil cell for neutron diffraction experiments with 64 mm^3 sample volume. Successful results yielded into pressures up to 7 GPa. Since mid-2011, ZTA has been implemented as anvil material in PE press at ISIS laboratory (Oxfordshire, UK)[52]. Its successful routine usage at 0 – 7 GPa range makes it a candidate for further advancements towards an increased working capacity. Recent efforts on ZTA anvils include tests with a 17.6 mm^3 anvil up to ~11 GPa[82]. ZTA is currently under research for many applications such as dental implants[83], surgical implants[84–86] and ballistics[87]. Table 2.1 shows ZTA properties. An excellent review on ZTA is given by Wang and Stevens[88].

Table 2.1. Properties of ZTA (from Klotz[52]).

Grade	Al_2O_3-ZrO_2
Composition (mass% ZrO_2)	25
Density (g/cm^3)	4.37
Compression Strength (GPa)	4.7
Flexure Strength (GPa)	1.35
Toughness K_{IC} (MPam$^{1/2}$)	6.4
Hardness, HV1	1760
Young Modulus (GPa)	357
Poisson Ratio	0.24
Thermal Conductivity (W/mK)	17
Specific Heat (J/gK)	0.7

2.3.5 Cubic Boron-Nitride

Finally, it is important to say how research has been conducted on suitability of Cubic Boron-Nitride (c-BN) as anvil material. Due to its high hardness, this material is a competitor with diamonds for certain engineering applications. Specific properties and technical details can be found in literature[52,89].

Goncharenko[14] explored its uses on gem anvils as a substitute of diamond or Sapphire. Klotz[52,90] used c-BN anvils in a PE press up to 10 GPa. In terms of costs and mechanical properties, c-BN is an exceptional material. However, Boron neutron transparency properties are not ideal, being a heavy absorber. For short wavelengths, certain patterns can be obtained, in contrast with longer wavelengths for standard experiments, where reflections are almost null[52]. There are also reports of c-BN used as gasket material for diamond anvil cell experiments[91,92].

2.3.6 Titanium/Zirconium Alloy

Titanium/Zirconium (TiZr) alloy has outstanding mechanical strength properties and low coherent neutron scattering qualities (high neutron transparency). These combined features make TiZr alloy relevant for design and manufacture of experimental accessories

in neutron diffraction experiments, such as sample holders and gaskets. By mass ratio, TiZr is composed of 52.5% Titanium / 47.5% Zirconium. Its appearance and machining properties are similar to Stainless Steel.

At ambient conditions, TiZr is in α-phase, having hexagonal closed-packed structure. A transition to the body centered cubic β-phase occurs at 650 °C, melting at 1550 °C. Due to its pyrophoric (spontaneous ignition) nature, TiZr alloy is limited in its performance and use. Exhibiting a fire risk, TiZr maximum service temperature in air is 200 °C. Processes as welding must be performed under controlled atmospheres[52].

TiZr alloy is employed as gasket material on the PE press. Therefore it is significant to understand its high pressure behaviour. At room temperature (300 K), Titanium and Zirconium experience a phase transition from the α-phase (hexagonal closed-packed) to the hexagonal ω-phase at 5 and 7 GPa respectively. Volume change of 1-2% is linked in both cases. The alloy itself has a slow α to ω transition from 10 to 25 GPa, with a volume change of 2%. Additional compression leads to the ω phase at 50 GPa with a 0.3%volume change. At higher pressures, the ω-phase changes to the bcc β-phase at 30 GPa in Zirconia, and 40 GPa in Titanium, with a volume change of 1-2% as well. However, this transition in Titanium seems to depend on the particular pressure-temperature path[52].

Phase transitions occurring on TiZr at the pressure range of interest have no great influence on mechanical properties, possibly because the transition is slow and extend over several GPa. This material is used as a gasket up to 30 GPa. TiZr is a specialised alloy, not broadly used, therefore its mechanical properties are difficult to find in literature. As a relevant material in neutron experiments, Klotz[52] discusses how TiZr mechanical properties have been measured and assessed. Mechanical tests have been performed from 13 ingots of three different companies delivered to ISIS Neutron Facility for the past 20 years. Table 2.2 provides TiZr mechanical properties available in this publication. Klotz[52] additionally indicates that TiZr yield and tensile strength properties are highly temperature dependent. Kobayashi[93] provides further information in TiZr heat treatments for biomedical applications (containing Niobium).

Table 2.2. TiZr properties at various temperatures (from Klotz[52]).

Density (g/cm^3)	5.23
Young's Modulus (GPa)	90-95 at 300 K
	110 at 4 K
	102 at 77 K
Yield Strength (MPa)	545-700 at 300 K
	1320 at 4 K
	920 at 77 K
	545 at 473 K
	420 at 773 K
Tensile Strength (GPa)	700-840 at 300 K
	1320 at 4 K
	1090 at 77 K
	690 at 473 K
	540 at 773 K
Elongation	typically 8% at 300 K
Bulk Modulus	148 GPa

2.4 High Pressure Neutron Diffraction Instruments

Historically, initial neutron diffraction experiments date from 1945 by E. Wollan at Oak Ridge Laboratory (USA). Joined by C. Shull soon after, they founded the basics of this technique[94]. From approximately 1966, efforts have been made to carry out neutron scattering experiments at pressures up to 1 GPa, Devices such as piston-cylinder arrangements and pressure vessels were employed[95–98] and reached pressures up to 3 GPa by 1969[99]. In 1974, crucial results were published by McWhan[75] discussing the

development of a piston-cylinder device. This apparatus became popular for the following 25 years, being widely used for high pressure neutron scattering over 1 GPa.

A key component of the McWhan cell is a conical cylinder manufactured of high density sintered Al_2O_3 or ZrO_2 with a sample space and two Tungsten Carbide pistons. The McWhan cell original design was provided of two hydraulic rams to induce high pressure. Maximum pressure reported was 4.2 GPa. This device was later adjusted and miniaturized for multiple applications[100–102]. Due to its pressure limits (~3 GPa), the McWhan cell is less used today.

2.4.1 Massive Support Principle

Literature on design and development of high pressure devices often cites the massive support principle as a fundamental idea on how these devices can withstand operational loads and pressures. Discussed initially by Bridgman[71], he explained how anvils are able to sustain compressive stresses beyond their strength by a factor of 2 – 4 (strengthening factor) depending on their geometry and materials. The original statement of the massive support principle is mentioned by Spain[74]:

"*The yield stress of a flat semi-infinite plate subject to an indenter is several times higher than the compressive yield strength of the plate material*".

When applying this idea on two truncated-cone anvils, a similar effect can be observed. The amount of compressive stress which an anvil can achieve, is larger than the strength of the anvil. This is caused by the extra support delivered by the material located laterally to the pressure generating face[103].

The strengthening factor has been studied as a function of the cone half-angle for specific materials, existing a direct relationship between both. An increase on the half-angle means an increase on the strengthening factor. Additionally, in 1962 Gerard[104] and in 1966 Lees (in Chapter 1 of the book by Bradley[105]) made evident how massive support increases when including a binding ring on the anvil flanks. The use of gaskets on high pressure devices offers further mechanical support to compressive failure in the anvils[103,106]. Yousuf[107] offers a comprehensive study on theoretical insights of the massive support principle.

In their books on high pressure technology Spain[108] and Klotz[52] gathered data showing strengthening factors for anvils manufactured with specific materials. Figure 2.12 shows the behaviour of the strengthening factor with the cone half-angle for TC, Copper, Steel and TC with a binding ring.

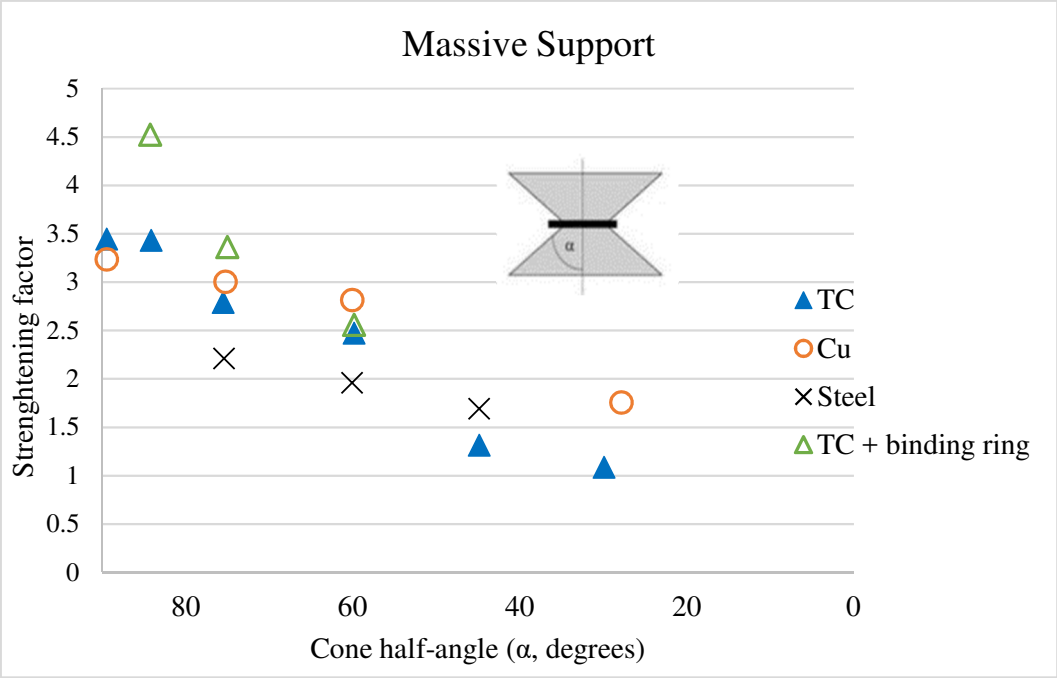

Figure 2.12. Strengthening factor in conic anvils as a function of cone half-angle (α) for various materials. It is possible to observe that the use of a binding ring increases this parameter of great importance in high pressure instruments. Figure adapted from Spain[108].

From Figure 2.12 it is possible to see how TC anvils have 3 times more resistance to compression for semi-angles of approximately of 85° and 4 times more when a binding ring is installed.

Commercial TC is sintered with specific amounts of Cobalt content as a binder. Its compressive strength is a function of this parameter as well as grain size. Standard TC grades have ~10% of Co content. Its compressive strength can fluctuate from ~3.5 GPa to ~6 GPa[52]. Considering an anvil geometry such as the one presented by Bull[56], for a TC supported anvil with a semi-angle of 70°, compressive stresses may register stress values up to ~9 GPa in the anvil (considering a compressive strength of ~3.5 GPa for TC).

Agreeing with these parameters, Klotz[52] mentions how Sintered Diamond anvils with a binding ring have a record of failing at ~24 GPa. Sintered Diamond has a compressive strength value of ~8 GPa, matching a strengthening factor of ~4.

2.4.2 Paris-Edinburgh Press for Neutron Diffraction Experiments at High Pressure

The Paris-Edinburgh press (PE press, also known as Paris Edinburgh cells) was conceived in the early 1990s as a result of a collaboration between the University of Edinburgh (R. Nelmes) and the University of Paris (J. Besson). As described in two publications from 1992, the idea was to build a compact implement for high pressure neutron diffraction (1 – 10 GPa) for the ISIS Facility in Oxfordshire, UK[76,109].

The PE press has been manufactured in many sizes. Its hydraulic press has been designed for maximum loads between 50 and 500 tonnes. A pair of opposing anvils centrally located compresses a sample volume between 1 and 100 mm^3. The idea behind the development of the PE press was to produce a reasonably portable device, currently weighing between 10 - 100 kg.

Soon after its first development, the PE press demonstrated its value for high pressure science. Research groups from both Universities (Paris and Edinburgh) published results in several compounds. Bulk moduli of β-Boron and the structural pressure dependence of Deuterated Ice VIII (both at pressure up to 10 GPa) were measured by neutron diffraction[110,111]. A review from 1994 highlights developments in low temperature measurements using the PE press[112].

By 1995, Klotz[55] published results of experiments reaching pressures up to ~25 GPa by changing PE press anvils from the original concept (TC) to Sintered Diamond. During the same year, Besson[113] confirmed reaching those pressure ranges by employing Sintered Diamond anvils. In 1995, a report from the Los Alamos National Laboratory (USA) mentioned how successful results were obtained with this instrument in neutron powder experiments up to 10 GPa[114].

By 1996, multiple research papers and reviews included the use of the PE press routinely in many types of compounds[115–120]. Today PE presses are available in spallation sources

around the world, being highly compatible for the benefit of researchers. Having positively impacted high pressure science, this device is likely to continue in the field for the foreseeable future.

According to their frames, PE presses can be classified in two types. The four-column V-design (the original version of this apparatus) and the two-column VX-type (available since 2003[121]). A compact version of the VX-type has also been proposed in literature[122]. Figure 2.13 shows these concepts. Selecting a determined geometry depends on the particularities of the neutron facility to use. In his book, Klotz[52] explains how:

"The choice of one or the other geometry is very much dictated by the type of neutron source where the cell is used as well as its applications: pulsed sources collect data usually in an energy-dispersive mode with a constant diffraction angle 2θ where the presence of four columns is not an inconvenience. In contrast, continuous sources need large contiguous windows to record data over a large 2θ-range which can only be provided by the VX-type cells with their two horizontal openings of 160◦ each".

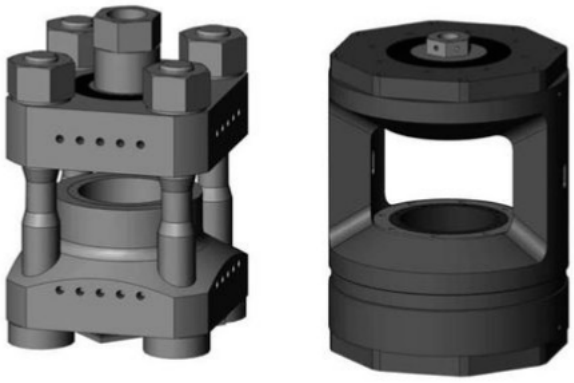

Figure 2.13. Representation of the PE press main models. The original four-column V-type configuration (left) and the VX-type (right). Load frames have a capacity of 130 tonnes. Image from Klotz[52].

Both types of PE press shown in Figure 2.13 exist in different sizes as well as load and sample capacities, depending on their applications. The smallest VX press has a 50 tonnes capacity and a mass of 10 kg approximately, whereas the largest V-type press available (V7) has 450 tonnes capacity weighing approximately 95 kg[52].

Figure 2.14 illustrates both press types' cross section together with anvils and other components. The basic operation of the PE press starts when hydraulic fluid is thrusted through an inlet (1) pushing a piston (2). The resulting force is transmitted to the steel supported TC plates (7) where the anvils are mounted. The PE press top part consists of a breech (8) screwed on the top load frame (5) or top platen (11). The upper anvil-backing disc set (attached to the breech) allows a rapid removal when unscrewing the breech. Additionally, thickness variations of gaskets can be adjusted by changing the position of the breech via the screws.

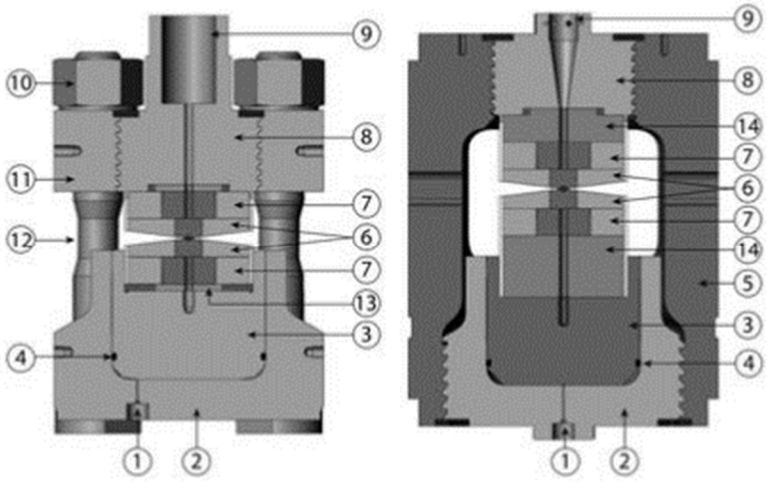

Figure 2.14. Cross section of PE press (V-type left, VX-type right). (1) Hydraulic fluid inlet, (2) cylinder, (3) piston, (4) O-ring seal, (5) load frame, (6) anvils, (7) TC backing plates (seats), (8) breech, (9) front collimator, (10) nut, (11) top platen, (12) tie rod, (13) backing disc, (14) steel spacer. Image from Klotz[52].

PE press frames are manufactured of high tensile steel for aeronautic applications (819AW). The necessity of a compact press corresponds to the working space existing on the neutron experimental stages, often being a small tank designed to provide high vacuum environment and/or cryogenic conditions. Figure 2.15 illustrates a V-type PE press available at ISIS laboratories, along with a tank.

Stephan Klotz (University of Paris) has been part of many efforts related with the PE press, its optimisation and use. This thesis has multiple citations to his work and book "*Techniques in high pressure neutron scattering*"[52] which details history, design,

materials, and many other relevant topics in this field. Among the first experiments performed with the PE press, samples of Iron, Lithium Deuteride and Deuterated Ices VI and VIII were examined[76,109,123]. Although this apparatus was originally conceived for high pressure powder diffraction experiments, single crystals of Fe_3Pt and Ge have been studied[124].

Figure 2.15. V-type PE press (left) and tank (right). Equipment available at ISIS Neutron Facility (UK). The PE press is located inside the tank to provide high vacuum and/or cryogenic conditions for the neutron diffraction high pressure experiments. The tank is provided with a feed-through for data acquisition and with a window for the neutron beam. The PE press is aligned with the tank's window for neutron beam access. The tank's lid is visible on the PE press image.

Improving data acquisition has generated a series of studies concerning accessories designed for the PE press. Among the most relevant, Fang[38] developed a rotating appliance for the PE press. As the tie-rods of the press can interfere with the data collection, rotating the PE press allows to access neutron diffraction data at particular angles for a determined sample. In 2010, Bocian[125] described an accessory for loading gases on the sample chamber of the PE press. The system explained can be employed to load gases as pressure media or to study pure or mixed gases at high pressure. This publication illustrates the use of this accessory with data results of neutron diffraction experiments on compressed Nitrogen.

Despite its original conception for neutron diffraction studies, other characterisation methods have been used with the PE press. There are multiple investigations involving PE presses used for high pressure-temperature x-ray diffraction. In 1999, Mezouar[126] employed a PE press for high pressure-temperature synchrotron x-ray diffraction measurements. A fast imaging-plate detector was paired with the press in order to obtain improved quality data in a reduced amount of time. Morard[127] performed adaptations to employ the press in x-ray diffraction high pressure-temperature studies at pressures up to 16.5 GPa and temperatures up to 1800 K. Sintered Diamonds were employed as anvils due to their x-ray transparency in comparison with TC anvils.

In 2015 Jacobsen and Velisavljevic[128] explain the design and implementation of a containment system for radioactive and hazardous materials when performing high pressure-temperature experiments using the PE press. Experiments were done with Uranium and Cerium Dioxide (CeO_2) to prove this accessory's suitability. Matityahu[129] developed a series of electrical resistance measurements in a PE press for a pressure - temperature range of 0 - 6 GPa and 300 – 1000 K. A recent publication by Playford[130] describes how adaptations on the PE press can be made in order to obtain high quality neutron total scattering data of crystalline materials at high pressure. Recent publications include a large number of studies using the PE press applied in a vast range of materials[80,82,131–133].

Klotz[121] developed a PE press version for both neutron and x-ray scattering. Designed for 200 tonnes capacity and with 60 kg weight, a smaller version was also considered and conceptualised (50 tonnes capacity, 8 kg mass).

Other studies of high pressure-temperature x-ray diffraction with PE presses include publications by Lheureux[134], Yamada[135], Katayama[136] and Morard[137]. Kono[138] developed an inclusive study combining structure, elastic wave velocity and viscosity measurements using the PE press. Katayama[139] in 1998 and Vaccari[140] in 2009 coupled the PE press with extended x-ray absorption fine structure (EXAFS) spectroscopy to study compressed Tellurium and GeO_2 respectively. Perrillat[141] studied the viscosity of compressed FeS in a PE press with x-ray diffraction.

2.4.3 Toroidal Anvils and Gaskets

Since initial high pressure experimental set-ups and prototypes, high pressure has been produced by compressing a sample between two opposing hard anvils. The previous section showed the crucial role anvils have on PE presses. Being at the forefront of high pressure generation, anvils selection and design is a complex process generally relying on trial-and-error approaches.

Large volume high pressure anvils were introduced in Russia in the 1960s by the Institute for High Pressure Physics of the Russian Academy of Sciences. Anvil models such as the cup anvil were used in early tests[6,142]. Along with its predecessor the Chechevitsa (lentil) cell (Figure 2.16), the toroidal anvil was mainly used for synthesis of new materials.

As an active part of its invention, Khvostantsev[57,143] provides a historical review in toroidal anvils. From the late 1970s, studies performed in Russia illustrate how toroidal anvils were used in experiments involving topics other than synthesis, transferring this technology to the study of compressed matter. In 1978, Khovostantsev[144] investigated how pressure influences the thermoelectric properties of antimony up to ~9 GPa. Two years after this author explored phase transitions in Sb_2Te_3 at a similar pressure range[145]. In the same year Bashkin[146] employed a toroidal cell to study structural transitions in alkali hydrides.

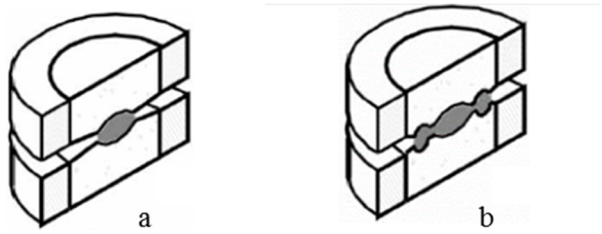

Figure 2.16. Scheme of early concepts in high pressure anvils. Chechevitsa (a) and early toroidal anvil (b). Image from Khvostantsev[57].

In 1982, Tsidil'kovskil[147] studied the metallization of Mercury Chalcogenides at high pressure employing toroidal anvils. Other early investigations include the work by Kechin[148] and Vlasov[149]. In 1988, Besson appreciated their potential on neutron scattering[52]. Their adaptation to the PE press caused a positive impact in the field of high pressure neutron diffraction, being now habitually used for pressures around 10 GPa.

Today, 90% of all high pressure neutron diffraction experiments are produced with toroidal anvils[52].

As explained, the toroidal anvil cell constituents are two coaxial dies with reciprocally facing surfaces which have one (or more) toroidal cavity. A pair of metallic gaskets match the anvil's surface geometry, also encapsulating the sample. Figure 2.17 shows a representative assembly of a toroidal anvil and gasket.

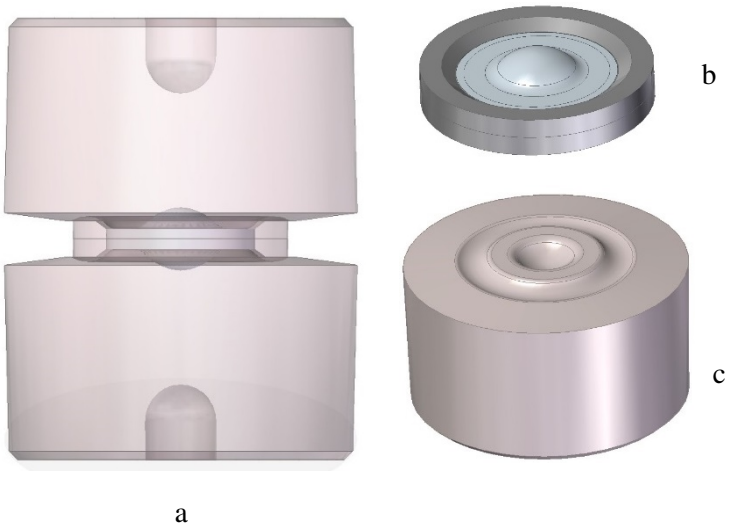

Figure 2.17. CAD representation of an assembled (a) and disassembled toroidal anvil cell. Encapsulating gaskets (b) and a single toroidal anvil (c) are included in the illustration.

Gasket material requires a certain resistance, as soft materials would fail containing the sample and producing high levels of pressure. Sample volume is constrained by the anvils surface and gasket thickness.

The classic toroidal anvil design included one toroidal recess and a taper angle of 7°. New models include greater taper angle (20°) improving access for experiments involving single crystal neutron scattering[56]. Multiple recesses to reach higher pressure conditions have also been teste. A double toroidal anvil (two concentric toroidal cavities around the central sample chamber) has proven successful to rise operative pressure ranges.

There are early mentions to double toroidal anvils reaching pressure values of 25 GPa approximately[55,150], for sample volumes of 35 mm^3. These anvils have been relatively recently implemented, Klotz[90] and Bull[56] mentioned them in 2005 – 2006 publications as a real possibility to reach pressures beyond 10 GPa. In 2008, Wilding[151] performed neutron diffraction studies in non-crystalline silicates up to 25 GPa using double toroidal anvils. Funnell[152] in 2011 employed this device to induce pressures 15 GPa in Alanine, and Fitzgibbons[153] discussed on its use for Benzene-derived Carbon nano-threads in 2014. Fang[38,154] provides good insights on the use of double toroidal anvils.

Encapsulating gaskets have been an important step forward in high pressure generation, allowing the use of high pressure media (such as the typical 4:1 methanol-ethanol mixture or silicon oil). Experience has also shown how this type of gaskets increased lifetime of anvils, reducing their collapse[52] and being of common use today. To be discussed further, this thesis project has employed encapsulating gaskets in the analysis.

Gasket thicknesses selection is a delicate task due to a number of reasons. On the sample chamber, a relatively thick gasket reduces the sample pressure to only few GPa, being 2 mm an upper limit for this. On the other hand, thin gaskets can compromise sample volume reduction and can fail at relatively low pressures. A recommended initial thickness value is 1.6 mm. The outer gasket piece (corresponding to the toroidal groove) should be designed to avoid deformation on the first compression stage (typically below 10 tonnes), with the load compressing only the inner gasket section. As an example, literature mentions how a thickness of 2.5 mm for the outer segment would be recommended for an inner gasket thickness of 1.6 mm[52]. Further sections of this thesis show how thickness will depend on every experiment and gasket material.

Apart from relevant mechanical properties such as resistance, gasket manufacturing and materials selection, it is important step for successful research outcomes. A key property for compressive neutron diffraction experiments is neutron transparency. Titanium and TiZr has remarkable mechanical properties as well as neutron transparency, as mentioned earlier in this Chapter. Copper-Beryllium (CuBe) has an attenuation of 50% for determined neutron wavelengths. Aluminum has good neutron transparency but unsuitable mechanical resistance for compressive experiments[52]. Figure 2.18 illustrates a

set of used TiZr gaskets, as well as a CAD representation of a closed and open gasket (showing the sample chamber).

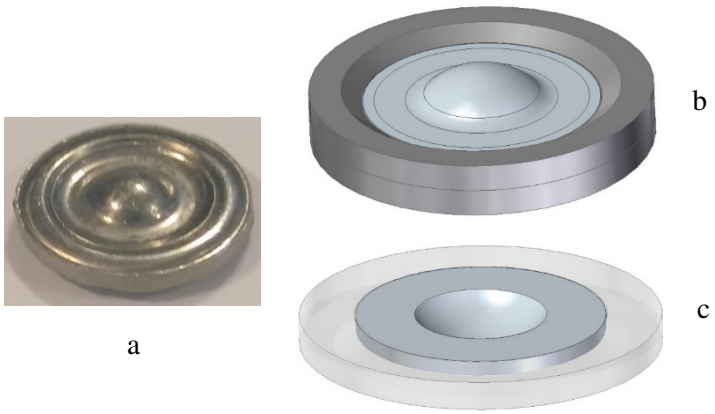

Figure 2.18. Compressed (used) TiZr gasket (a), CAD representation of uncompressed gasket (b) and CAD depiction of half gasket showing sample chamber (c).

2.5 FEA Studies in High Pressure Devices

Since the 1970s, numerical methods including FEA have proven to be useful in the assessment of high pressure scientific instruments' designs and stress distributions. Advancement in computers and software has boosted this type of analysis. The book by Eremets "*High pressure experimental methods*", apart from introducing high pressure devices, their history and components, provides good insights in early stress distribution analyses for instruments and anvils[6].

A common goal in these investigations is to calculate whether operative stresses are larger than the limits in any particular area of a device, and how failure starts. Optimization in geometries and elements provide higher experimental pressures and sample volumes, both crucial aspects for new findings in science at extreme conditions. In ductile materials under tension or compression loads, the maximum and minimum principal stresses, maximum shear stresses and Von Mises strain[67] give a precise signal of the limits the material can withstand.

However, well-defined data for innovative materials is rarely available or it is difficult to determine for brittle materials and gaskets. As large deformations are produced during high pressure experiments, gaskets properties are unknown at certain extends. In gem

anvils, the final quality of polish highly affects its properties, being virtually impossible to calculate its modulus and strength theoretically[155]. The brittle nature of most anvil materials and their reduced tensile strength suggests that zones accumulating this kind of stress are likely to activate failure.

When material properties are unknown or unavailable, a series of values are applied and the best fit data is corroborated by experimental results or vice versa. This routine involves greater computational resources, being necessary to assume a large range of values for each of the properties which are unknown. Numerical models are subject to specific assumptions as well. A variety of numerical studies have been developed on the DAC, toroidal anvils and PE press as well as in other gems used in high pressure devices such as Sapphire. The following paragraphs contain chronological references on relevant studies of this nature.

Initial numerical studies in high pressure scientific instrumentation can be traced back to the late 1970s. A study completed in 1977 by Bundy[156], made a basic generic analysis of loading distribution on the face and flanks of a tapered anvil for a high pressure apparatus. The author's idea was to establish a process toward anvils optimization, to reach high pressures on devices available at that time. This early analysis already assumed that shear strength of the anvil material must not be exceeded at any point, explaining how gasket material possess a chief role in the stress system. The author also mentions the concept of gasket transparency, making him a pioneer of this kind of studies for high pressure devices. Bundy has also been involved in early designs and creation of high pressure apparatuses[77].

Among the findings, curves for different strengths (materials) were developed. In a publication slightly earlier, Dunn[157] (from the same research group) incorporated the Lur'e solution for an elastic cone, providing a more accurate solution to the stress distribution of a Bridgman anvil. Lur'e involves the elastic solution when a punctual load is applied at the cone's vertex with an inward direction along the axis of the cone.

In 1982, Adams[158] executed a theoretical and computer-aided study on diamond anvils under stress and their behaviour. Results showed how potentially destructive shear and compressive stress values are located in the surroundings of the anvils culet. In this area,

yield (plastic flow) starts, constraining anvils performance. In a much later publication, Adams[159] estimated maximum principal tensile stresses on the basal part of a diamond anvil. Elastic modulus and Poisson's ratio were methodically varied. The author stated how the basal tension seems to be responsible of experimental malfunctions, as diamonds are extremely brittle and predisposed to be damaged by cleavage in tension. Stress concentration can be reduced to minimum values by using a conical angle between 25° and 30°.

In 1984, Bruno[160] delivered an FEA study on a brilliant-cut diamond and a metallic gasket up to 21 GPa. The models considered a perfectly cohesive interface between the metallic gasket and the diamond anvil. It also assumed that there is no brittle failure of the diamond anvil before its elastic limit is reached. The stress analysis included compressive vertical, radial and hoop stresses, as well as octahedral shear stress. Their work describes how a minuscule chipping at the edge of the diamond anvil results in a shear stress concentrator, being the most probable cause of failure. The implement of a bevel generates favourable stress distributions in the edge surrounds, with an optimum stress distribution with a bevel angle of 15°.

In 1986 and 1987, Moss[161,162] published relevant works in diamond anvil design and analysis via FEA. The models developed demonstrated how double bevelling offers better shear stress distributions in the anvil, bringing better gasket fluency and more stability to the sample (being frequently compromised when diamonds with large angle single bevels are employed). These factors certainly reduced the probability of failure. By optimising gasket material and diamond anvil tip, the study concludes that it is possible to assure that the diamonds fracture occurs due to tensile stresses or plastic flow rather than the two diamonds in contact with each other due to a "cupping" detected (and later confirmed by synchrotron x-ray[163]) of the DAC face. Moss also developed a theoretical study on the stability of a sample in a DAC[164], closely related to this matter.

In 1986, Novikov[165] studied the stress distributions and resistance of high pressure instruments for synthesis of materials via numerical methods. In 1990 and 1992, Novikov[166,167] also produced a numerical model of stress-strain states on a DAC and its components, as well as a study on numerical optimisation. In these publications,

outcomes such as a theoretically predicted resistance of 465 GPa was found and a series of parameters for anvil's geometry optimisation were exposed.

As cited, gasket materials are a crucial for anvil cells performance. In 1996, Levitas[168] studied extensively gasket deformation in diamond anvil cells. This study takes into account the influence of high pressure and high elastoplastic strains, establishing and implementing via FEA a method to investigate gasket properties with an iterative algorithm. Pressed lithographic limestone and hardened stainless steel T301 were assessed as gasket materials. The work models the lithographic limestone at a pressure of ~24 GPa, and T301 at ~50 GPa. Outcomes of this publication helped to improve high pressure generation by providing relevant information regarding material properties deformed by megabar-range pressure.

In 1999, a FEA model of a DAC at multimegabar pressures was developed by Merkel[169]. This study uses a set of curves to explain the strong relation between pressure achieved and the assumed yield stress of the gaskets. The model suggested in this publication provides a good understanding of the diamond anvils' stress behaviour. Stress tensor elements were obtained nearby the tip, where large variations in the optical properties of diamond have been detected.

Since the decade of the 2000s, progression in computers and FEA software packages has increased the use of numerical methods in design and evaluation of DAC devices. A large number of publications can be found on this topic from 2010[170–177]. Recent studies include a paper by Li[178] where two diamond anvils at 300 GPa were modelled to obtain the stress-strain field evolution for both sample and diamond.

Hydrostatic conditions on the DAC sample chamber have been studied via numerical methods. In 2006, Conil[179] authored a study detailing the pressure relationship between a sample and a calibrant under hydrostatic conditions, and how the second might have stress gradients which affect experimental measurements. In a similar study, Tempere[180] in 2011 analysed also how pressures distributes in a DAC's sample chamber with pressure media present, identifying sources of systematic errors when estimating pressures in a DAC. The authors describe for instance how ruby chips (commonly used as pressure gauge) can be at higher pressures than the pressure media and how the sources of error

(10%) in pressure measurements must be taken into account for precise pressure measurements.

In 2012, Giriat[181] published an FEA work on the body of a DAC and piston cylinder cell for a SQUID Magnetometer. Kepa[182] in 2013 mentioned how FEA method helped in the design of a high pressure cell for ultrasonic measurements. Targeting single crystals at cryogenic temperatures (2K) and pressures up to 5 GPa, the cell was tested with UGe_2. In 2016, Binns[183] used FEA to optimise a miniature DAC with a cell body and backing plate made of a Beryllium-Copper alloy, selected for low thermal contraction and high thermal conductivity.

Temperature distributions have also been the focus of attention in numerical analysis for DAC devices. Rainey[184] employed a numerical approach to determine temperature distributions in a laser heated DAC, demonstrating how heating devices do not provide heat in a uniform fashion, having extreme temperature gradients which may affect certain experiments.

Due to high costs associated with diamonds, materials with hard and transparent characteristics such as Sapphire and Cubic Zirconia have been tested and used as gem anvils. Advantages like larger sample volumes and relatively low cost are a motivation for studies successfully reaching 16.7 GPa and 25.8 GPa for Sapphire and Cubic Zirconia cases respectively[13]. Moissanite (6h-SiC) has also been used as an alternative gem[185,186] with a positive implementation in many laboratories. Available studies report its routine usage in ranges from 1 – 12 GPa[187–190], reporting pressures up to 52.1 GPa confirming its functionality and convenience[185]. Additionally, experiments involving large sample volume (10 mm^3) at high pressure demonstrates its suitability for neutron diffraction studies[191]. Experiments in Moissanite strength, thermal stability and fracture toughness have been successfully accomplished[192–196].

Via FEA, Ridley[197] studied Sapphire anvils as an alternative for diamonds. This study links the good performance on Sapphire anvils with soft gasket materials such as Copper, Aluminium or Stainless Steel (the hardest gasket allowable). The author concludes that Sapphire anvils fail as a result of shear stresses caused by the compressibility of the gasket

and sample, producing tensile stresses in the culet surface due to the flow of gasket material and by cupping of the culet at high pressure samples.

With reference to FEA studies in large volume cubic high-pressure apparatus, literature shows a variety of interesting studies. Han's studies[198–203] from 2007 has employed numerical methods for stress analysis and optimisation of these apparatuses. Aspects such as lateral support, geometries and double bevel anvils and alternative materials have been included towards optimising the cubic high pressure apparatus. In 2016, Li[204] and Polotnyak[205] published studies on stress distribution of this device. Both works aim to understand stress distributions in the anvils, operational limits and how pressure media affects its performance.

Due to its advantages and adaptability, numerical methods are gaining popularity in other high pressure areas. Today, it is possible to simulate the behaviour of compounds under DAC or toroidal anvils compression, obtaining phase transitions as in laboratory setups. A publication by Feng[206] in 2013 discusses stress induced phase transformations of a sample in a DAC. FEA was employed to solve equations for large plastic deformations and strain induced phase transformations. Stepping forward in 2017, Feng[207] performed a study on the α - ω phase transformation in Zirconium on a DAC using FEA. Results were used to understand and correct published studies on that particular transition, as well as in the α – β and ω – β transitions in compressed Zirconia.

In a recent study from 2014, Jacobsen[208] employed FEA in the cell body design of a new high pressure low temperature neutron diffraction apparatus. Being theoretically expected to reach 11 GPa, this apparatus was able to produce up to 6 GPa. Good diffraction patterns of NaCl and $BiNiO_3$ were obtained. Escobedo[209] in 2010 showed a new concept of a trianvil cell for experiments up to 10 GPa. Finite element calculations were used to analyse geometries and configurations for the anvils.

Directly related with the objectives of this thesis, FEA studies have been conducted on single and double toroidal anvil cells, involving more intricate geometries, soft gaskets and anvils made of TC or Sintered Diamond. Relevant studies are considered in the following paragraphs.

Due to its original conceptualization during the 1990 decade, the PE press has now evolved by incorporating innovative techniques and studies to its design, manufacture and optimisation. Early publications briefly mention the use of FEA as a contributing factor for the progress of this instrument[55,76] and on the optimization of anvil seats[54]. Unfortunately, these studies do not provide details on how the FEA process was applied.

In 2002, Solozhenko[210] employed finite element calculations for a complex experimental set up. In a PE press, a 7 mm^3 sample of amorphous Boron and Anhydrous Hydrazine was sealed with dry Nitrogen in a Copper capsule. A graphite furnace was designed and optimized via FEA to be heater and pressure transmitter to the sample. Pressures up to 5.2 GPa and temperatures up to 1600 K were reached and a synchrotron x-ray study completed.

In 2003, Debord[211] performed an assessment and optimization of high pressure - high temperature set up for the PE press via FEA (MODULEF software). Pressures up to 10 GPa and temperatures up to 1000 K were analysed, mapping temperature distributions otherwise difficult to obtain in experiments.

In 2004, the VX - PE press was developed with the use of FEA. The authors of this work used the CAST3M software, being able to define areas of high deformation and stress accumulation. As a result, a PE press with large openings for neutron data collection with 200 tonnes capacity and 60 kg weight was created. A compact version of 50 tonnes capacity and 8 kg mass was also considered[121]. A further study[212] on VX - PE presses remark how a gas loader was adapted and finite element calculations established that clamps can tolerate loads of 20 – 30 tonnes approximately. Experiments were performed under these conditions to preserve components.

Other FEA studies in PE press components and accessories include a publication by Bull[56] in 2005 confirming how a binding ring in a toroidal anvil with larger aperture angle is able to withstand working loads. In 2008, a study on the α-γ-ε triple point of Iron it is mentioned how FEA was used to calculate temperature gradients in the sample on a VX-PE press[213]. Two years later Bocian[125] employed FEA in the design of an apparatus to load gasses on the PE press sample volume. Deformation and stress distribution results made possible to select an appropriated material (819 AW steel) for the clamp and latches.

In 2011, Wang[214,215] incorporated FEA calculations to the design of a large volume neutron scattering high pressure cell. Although this concept was independent from the PE press, the cell was configured with a volume capacity of 425 mm^3 (almost 10 times larger than the available PE press toroidal anvil models). This pressure cell has an operational limit of 1.8 GPa and illustrates the objective of having larger samples for high pressure neutron experiments. A similar concept is explained by Chen[216], designing a large volume device (980 mm^3) for high pressure/temperature neutron scattering. This study also used FEA for design and optimization purposes.

In 2012, Fang[38,154] produced an FEA model of a double toroidal polycrystalline diamond anvil for failure assessment. Examining a large number of real anvils which failed at 240 tonnes and linking this with stress results from his FEA mode, it was possible to associate failure with tensile and shear stresses at the anvil's working surface. Certain material properties were estimated for the FEA model as they were not available in literature and specific ideas were shared in order to optimize this device.

From this literature review, it is possible to notice how both institutions originally involved in the development of the PE press are still committed to its optimization and improvements.

2.6 Pressure-Temperature Water Phase Diagram

The study of water under high pressure conditions is as long-standing as the field itself. References made by Bridgman on his pioneering high pressure work mention compressed water as a subject of study since 1912[217]. As water in liquid and solid phases is studied in this PhD thesis, it is important to provide key points to understand its behaviour when compressed.

Water (H_2O) is one of the most abundant and significant substances in the Earth, covering approximately 71% of its surface. It is critical to life forms and it is perhaps the most investigated compound, with scientist studying it daily around the world. Numerous authors offer rich detailed studies on water, its structure and properties[218]. Computer simulations have played an important role in water research. Guillot[219] provides a good review on the history of the evolution of theoretical methods applied on water.

Water exhibits at least 13 ice forms. Petrenko[220] provides a detailed textbook on ice, its forms and properties, from ordinary Ice Ih (obtained by freezing water) to other crystalline phases of water stable in under certain pressure – temperature conditions. Icy satellites as Europa, Titan, Ganymede and water-rich exoplanets enlarge the list of celestial bodies where water prevails[221–223]. A large number of publications on compressed water are available in literature. Multiple shock-wave experiments (dynamic pressure) have been performed in water[224–227] as well as employing diamond anvil cells[228–231].

Showing uniform physical states (phases) of matter at certain ranges of pressure, temperature, and composition, phase diagrams are a common method to visualise a compound's behaviour in a chart. Water has an interesting phase diagram, displaying large polymorphism at high pressure[232]. Figure 2.19 displays water's pressure-temperature phase diagram. It is possible to observe a variety of solid phases (ices) according to the variable conditions.

There are several studies on thermodynamic properties of liquid water under high pressure and temperature[233] for industrial purposes (pressures relatively low when compared with the scope of this thesis). In 1935, Bridgman[234] developed a table on molecular volume of liquid water and heavy water at variable pressures (1 – 12000 kgf/cm^2) and temperatures (-20 – 100 °C). This publication maintains its relevance as a valid reference point for obtaining water's equation of state and properties at high pressure of the liquid phase (such as density and bulk moduli). In a similar study, Grindley[235] provides specific volumes of water at a pressure and temperature range of 0 – 0.8 GPa and 25 – 150 °C.

At room temperature (300 K), the water phase diagram shows a transition from liquid to Ice VI at ~1 GPa and to Ice VII at ~2.1 GPa. The evolution of high pressure apparatuses in the 1960s and 1970s made these kind of experiments possible in common laboratory environments. The structure of Ice VI was initially determined by Kamb[236,237] and Block[238]. (tetragonal unit cell, $P4_2/nmc$). Ice VII has a body-centered-cubic unit cell ($Pn\text{-}3m$)[239,240].

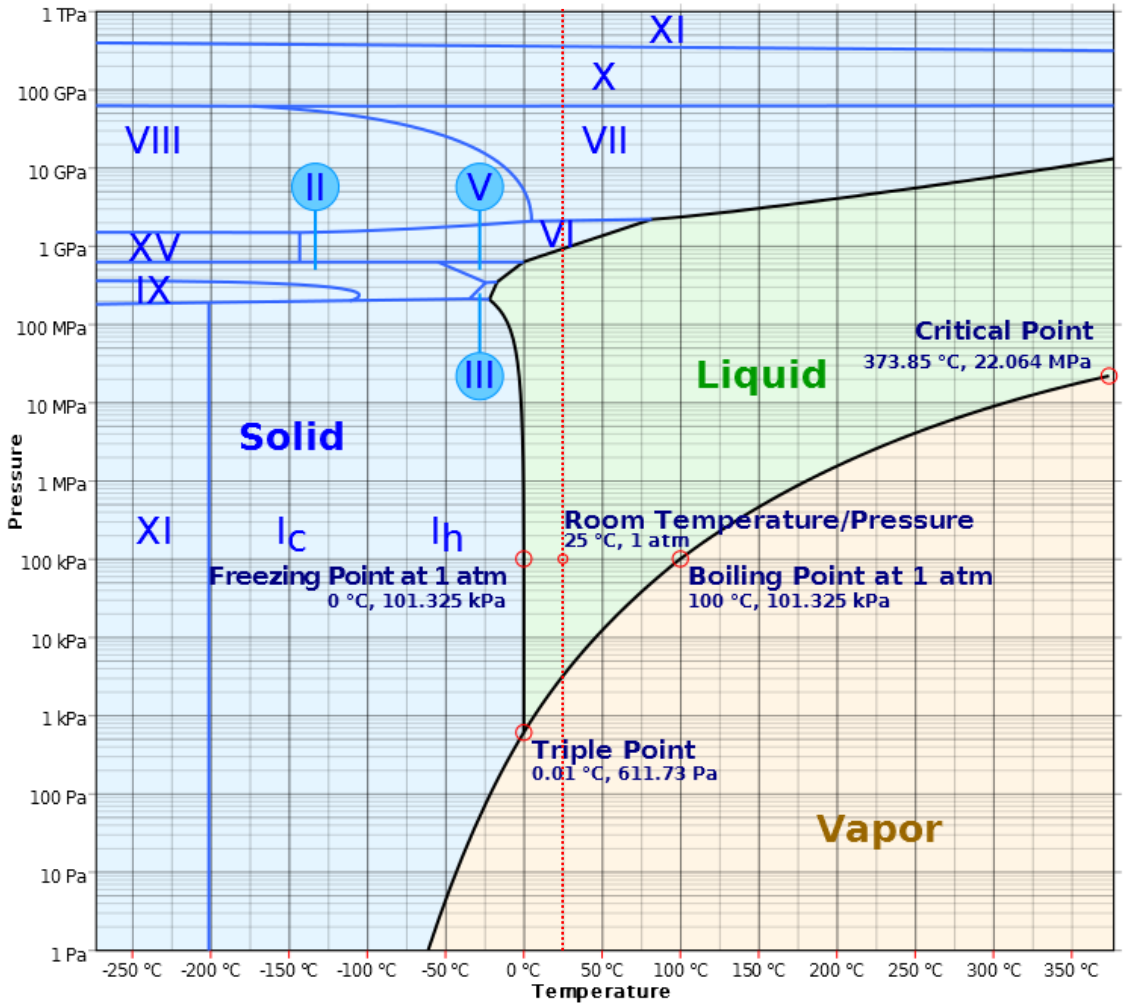

Figure 2.19. Pressure - Temperature water phase diagram[232]*. Two relevant phase transitions for this thesis can be observed at room temperature (25 °C) and ~1 GPa (water to Ice VI) and ~2.1 GPa (Ice VI to Ice VII). Dotted (red) line illustrates how pressurisation occurs at 25 °C.*

Due to its importance in many scientific fields, there is a large literature collection in both experimental and theoretical studies on Ice VI and VII. In 1937, Bridgman[241] provided results on properties of both forms of ice. Among relevant studies performed with DACs, it is possible to cite publications by Baer[242], Somayazulu[243] and Polian[244]. Meanwhile Chiu[245], Sanz[246] and Choukroun[247] provide theoretical studies for these ice forms. Combined methods were employed by Sugimura[248].

Using a DAC and synchrotron x-ray diffraction, Bezacier[240] provides a comprehensive volume data collection on Ice VI and VII at variable pressure. Ice VI to VII phase transition occurs in a broad manner. Bezacier experiments found stable Ice VI up to 2.56 GPa and Ice VII starting from 2.1 GPa. Through similar methods, Fei[249] studied the pressure, volume and temperature (*PVT*) relationships on Ice VII from 3.16 to 15.95 GPa. Using Brillouin scattering Shimizu[250] delivered a study on elastic moduli of Ice VI and VII. Chen[251] also discusses this behaviour.

Chapter 3

Finite Element Analysis Methodology and Model Development

The FEA method and its correct implementation is crucial to properly accomplish the objectives established in this thesis. The following Chapter provides a comprehensive description of this computational numerical method and its fundamental theory. Details regarding its employment to model a ZTA anvil cell with a water sample under realistic operational conditions are explained.

An effective model execution requires the consideration of multiple variables. Device geometry, material properties, sample phase transitions, and frictional coefficients are among relevant aspects extracted from literature, determined by experiments, or approximated based on experience and relevant references. This Chapter provides the necessary information to understand how the FEA model used on this thesis was produced.

3.1 Introduction

Engineering and scientific designs, processes and investigations have gained complexity in recent decades. Areas such as aerospace, energy and new materials illustrate how the use of classical mathematical analysis can be extremely complicated and may not be capable of incorporating the entire set of parameters involved. The use of numerical methods via software, particularly the consolidation of the finite element method, allows computational simulation of various coupled physical phenomena, which enables accurate solutions for sophisticated problems to be obtained.

This thesis employs FEA to examine the stress behaviour of high pressure ZTA toroidal anvils together with surrounding accessories and a compressed water sample. This Chapter describes how FEA has been implemented to these effects. Due to its importance in this PhD thesis, a literature review in FEA is included in this Chapter together with the methodology followed to produce the FEA model. Technical aspects such as solvers, mesh, number of steps, and contacts are covered, as they play a major role in the simulation results.

ANSYS Workbench 15 software has been used in both geometry generation and analysis. This computer program is extensively employed for engineering and multiphysics analysis around the world. Numerous textbooks and manuals offer many perspectives on its correct use. As this software constantly renovates and adds tools and functions, different websites provide a strong platform to improve simulations and models [252–257].

3.2 FEA Literature Review

3.2.1 Numerical Methods and Analysis

The field of numerical methods considers the utilisation of algorithms for the approximation of solutions, to those problems which may not have an exact or easily obtainable one. An algorithm can be understood as a set of stepwise operations which lead to the estimation of one or multiple solutions. Factors to consider when applying numerical analysis include accuracy and validity of the solution, rate of convergence and the existence of other solutions. Numerical analysis consists in the implementation of the method, finding a determined solution of a particular physical problem[258].

Numerical analysis is well established, having been developed and applied by Newton, Lagrange, Euler and Gauss among many others historical mathematicians. However, the introduction of computer technology has improved its use for more complex problems. This marks the modern era of numerical analysis and is believed to have begun with a publication by John von Neumann and Herman Goldstine in 1947, discussing aspects such as scientific computing and rounding error[259].

Numerical methods have become widely implemented due to rapid advances in software and their acceptance as a powerful tool in many disciplines such as engineering, finances, insurance, sciences and even art. The following examples of numerical analysis highlight their contemporary application:

- Numerical weather prediction.
- Actuarial analysis (for insurance).
- Private investment funds (hedge funds).
- Computer structural simulations (finite element analysis).
- Spacecraft trajectory calculations.

Numerical methods can be divided into direct and iterative. Direct methods calculate answers in a finite number of steps. Gaussian elimination, simplex method of linear programming or the QR factorization method for solving systems of linear equations represent direct methods.

Iterative methods on the other hand, start from an initial presumption and are not projected to end in a finite number of steps, converging in a solution. In other words, in this infinite series of steps, it is expected to have answers which behave towards a limit (not much variation between results after several iterations). The analyst defines a level (usually a percentage) of variation between solutions and decides if more calculations and time are required.

Iterative methods are more commonly employed than direct methods in numerical analysis. Likewise, discretization allows a continuous problem to be substituted by a discrete problem in order to approximate its solution. As furtherly detailed in this Chapter, the size and refinement of these discrete elements will determine how accurate a solution

is. As in the solution convergence case, size of the elements can be varied (typically refined) until a limiting behaviour in the solution is defined and identified.

For both solution and elements (also called mesh) convergence, there is certain amount of error to be taken into account and reduced[260]. Further information on this topic can be found in textbooks[261–263] which have been adopted in contemporary study programs.

3.2.2 Multiphysics

Innovations in numerical methods via software have proven useful in generating models to recreate and study physical phenomena. Due to their limited capacity, initial computer models treated only isolated physical events. It is understood that real physical phenomena occur simultaneously, combining non-linear multiple physics phenomena at once. The field of multiphysics proceeds to simulate via numerical analysis coupled systems for further study[264–266]. The following examples illustrate this branch[267]:

- Thermo-mechanical problems: how temperature distribution may alter structural integrity and shape in a determined material and vice versa.

- Thermal-fluid structural problems: fluid mechanics, heat transfer, mechanical resistance and other interactions. The fluid flow modifies the system temperature, producing a certain degree of mechanical deformation in a pipe, affecting the flow as it changes its boundary conditions.
- Piezoelectric materials: mechanical deformation can be induced by applying an electric field to a determined material, being fundamental for many actuators and sensors.

Software used for this analysis contains necessary elements to combine in a model e.g. materials resistance, dynamics, heat transfer, electromagnetism, transport phenomena and many others. Figure 3.1 provides a case of an automobile's exhaust manifold and the various studies which can be performed.

3.2.3 Finite Element Method

As explained, unsophisticated systems or components such as simple bars, adiabatic systems or beams can be understood by straightforward analytical equations. Real

mechanisms, processes and equipment are complex, forcing an approximation-based study by experimentation or numerical methods.

The Finite Element Method (FEM) is a numerical technique centred on the partition (or discretisation) of a large problem into minor and simpler adjacent parts named finite elements. The equations describing these finite elements are incorporated into a larger arrangement of equations modelling the whole problem, accurately approximating its solution. FEM has been implemented in many scenarios due to the extensive use of partial differential equations (PDEs) to describe physics laws and phenomena. As the majority of PDEs cannot be resolved by analytical methods, solutions can be accessed by using discretisation followed by numerical methods.

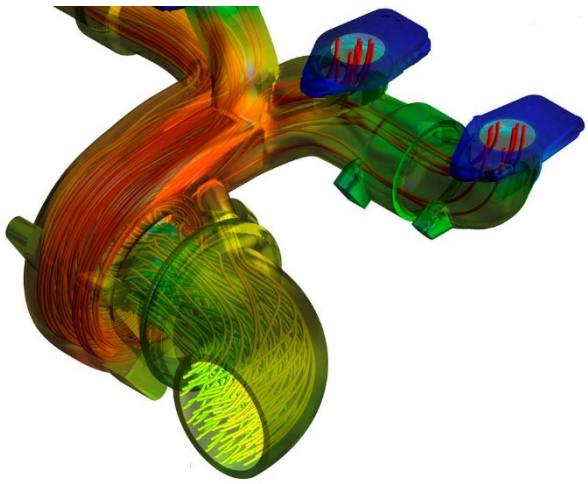

Figure 3.1. FEA model of an automobile exhaust manifold. By computational fluid dynamics and structural analyses it is possible to study aspects such as the turbulent fluid flow through the manifold, temperatures in both structure and fluid and mechanical stress in the structure. Image from ANSYS[265].

The practical application of FEM is known as Finite Element Analysis (FEA). The importance of this technique has grown in recent decades, benefitting as mentioned previously from the progress made in software and computer processing capacity. Computer Aided Design (CAD) and its evolution for graphic representation has been an integral component of this method, being able to reproduce geometries and dimensions to be processed via FEA.

FEA allows accurate study of a determined system and estimations to be made about it in various scenarios. Implementation of this tool has led to reduction in the number of experiments and prototypes required during the design or optimization of devices, products and processes.

Although the origins of FEM are difficult to determine accurately, it is possible to link it with the work by Hrennikoff[268] and Courant[269] in the 1940s for civil and aeronautical engineering respectively. Despite their differing disciplines, both studies share the employment of discrete elements to divide a continuous domain. The text by Strang and Fix[270] "*An Analysis of the Finite Element Method*", published in 1973 contributed to the popularization of FEA for the modelling of diverse physics and engineering cases. The term "finite element" is accredited to Clough[271]. Budynas[62] provides insights on the evolution and history of this method.

FEA is currently utilised in a broad range of scientific and engineering applications, being widely accepted as a valuable tool in the design and evaluation of products and processes as well as in the analysis of physical phenomena. Contemporary textbooks provide a detailed perspective of FEA and its implementation[256,272–274]. Additionally, multiple commercial and open source software such as ADYNA, ANSYS, COMSOL and ABAQUS is available for analysis of problems in fluid dynamics, heat transfer, materials resistance and electromagnetism. Figure 3.2 illustrates an engineering case (stress analysis of a landing gear torque link) using NASTRAN FEA software.

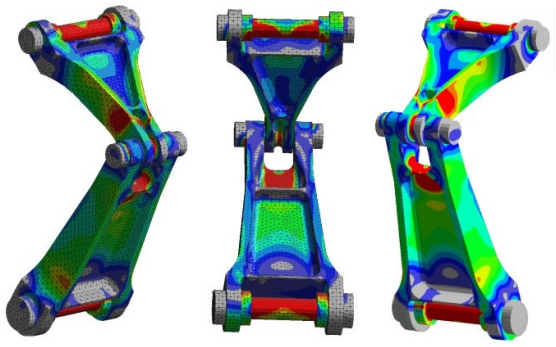

Figure 3.2. Example of a FEA structural analysis of a commercial aircraft landing gear torque link. Simulations executed with FEMAP-NASTRAN software. Image from Predictive Engineering[275].

Considering that FEM is a numerical technique based on the discretisation of a continuous structure or domain, it must be recognised that errors in this approach exist. Discretisation errors are associated with matching the geometry and displacement spreading, via finite elements, on the domain to analyse. Figure 3.3 illustrates an example of shape approximation errors. Additionally, computational errors are produced by the formulation of the numerical algorithms used. Being both type of errors associated with the concept of convergence explained in Section 3.2.1, most commercial software focus on the reduction of computational errors, with discretisation considered a factor of user concern which can be modified and adjusted accordingly.

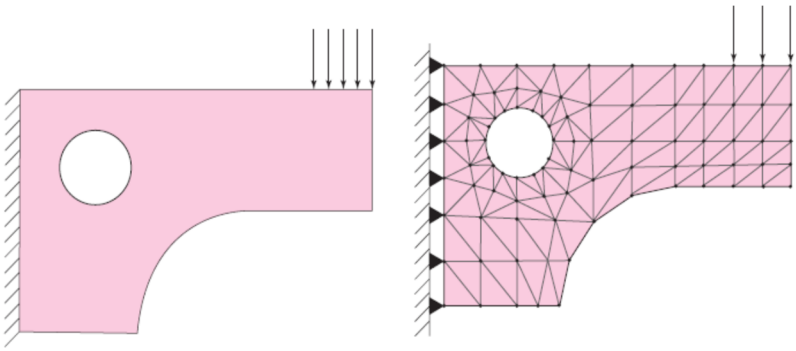

Figure 3.3. Example of a shape approximation with a finite element mesh. Although errors will exist in FEA, software tools and user's experience can minimizes them toward obtaining accurate results. Image from Budynas[62].

3.2.4 Element Types

Several geometric arrangements are employed as FEA elements for determined cases. In commercial FEA software these options conform the element library. A number of nodes is associated with the elements, depending on their configuration. Figure 3.4 illustrate some relevant element types for structural cases via FEA. Each node corresponds to a coordinate in the model where degrees of freedom are defined. In a system, degrees of freedom can be described as the number of parameters that vary freely. For structural stress analysis cases, degrees of freedom describe the displacement of a node as a result of the loads present in the body. Translational degrees of freedom can be associated with forces and rotational ones with moments transmitted through the nodes. Strains can be determined from that relative motion, while stresses calculated from the strains and material properties[62].

Integration points are discrete locations within each element where stress and strain values are calculated and monitored, based in nodal displacements. Its quantity and location inside the elements depends on the integration method selected. As stress and strain values want to be visualised at the nodes, results from integration points are copied or extrapolated to the nearest node[314].

Generally speaking, elements can be classified into line, surface and solid elements (also illustrated in Figure 3.4). Line elements can be subdivided in trusses, beams and frames. These elements assume a constant cross section area. Truss elements represent a pinned-bar resisting only tensile or compressive axial forces. A beam element corresponds to a rigidly joint bar transmitting bending moments (only loaded in the Y axis). Frame elements combine both properties. These elements can be considered for the study of long and slender analogous construction systems such as structural beams, planar or space frames, and planar trusses among others. Trusses, beams and frames can be employed in planar and spatial analyses. Trusses will have displacements and beams rotations on each axis[315].

On the other hand, surface elements are popular due to their adaptability in plane and spatial uses. Generally composed by 3 or 4 nodes, they are divided in the following cases:

- Two-dimensional planar elements: these elements only support translations and are typically employed for two-dimensional plane stress or plane strain analysis. Uses include axisymmetric bodies and long sections with constant cross sectional areas.

- Membrane elements: these elements can be oriented in three-dimensional space and are regularly used to represent thin metallic layers or fabric membranes, handling only in-plane loads and translational degrees of freedom. Its thickness is required to be smaller in comparison with its length or width.

- Shell elements: these elements can also be positioned anywhere in the 3D space, supporting all translational and rotational degrees of freedom that are not out of plane. Shell elements are commonly employed to model structures such as pressure vessels, airplane fuselages and car bodies (thicker walls than in membrane elements).

Having up to 15 or 20 nodes, solid elements are used to model solid objects for which shell elements are not suitable. Forged, machined or cast manufactured components can be representative of solid elements applications. At each node, solid elements handle only translational degrees of freedom as they can translate or rotate by only translating the nodes. Its use requires larger processing times when compared with other elements[316].

Special purpose elements are in charge of modelling different scenarios such as layered shell elements (for composites), hydrostatic elements (enclosed pressurised fluids), or other cases where common elements are not practical.

Type	Name	Shape	Number of nodes	Applications
Line	Truss		2	Pin-ended bar in tension or compression
	Beam		2	Bending
	Frame		2	Axial, torsional, and bending. With or without load stiffening.
Surface	4-node quadri-lateral	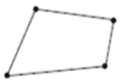	4	Plane stress or strain, axisymmetry, shear panel, thin flat plate in bending
	8-node quadri-lateral		8	Plane stress or strain, thin plate or shell in bending
	3-node triangular		3	Plane stress or strain, axisymmetry, shear panel, thin flat plate in bending. Prefer quad where possible. Used for transitions of quads.
	6-node Triangular		6	Plane stress or strain, axisymmetry, thin plate or shell in bending. Prefer quad where possible. Used for transitions of quads.
Solid†	8-node hexagonal (brick)	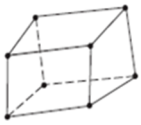	8	Solid, thick plate
	6-node pentagonal (wedge)	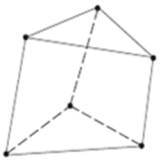	6	Solid, thick plate. Used for transitions.
	4-node tetrahedron (tet)		4	Solid, thick plate. Used for transitions.
Special purpose	Gap		2	Free displacement for prescribed compressive gap
	Hook		2	Free displacement for prescribed extension gap
	Rigid		Vari-able	Rigid constraints between nodes

Figure 3.4. Finite element types and number of nodes. FEA divides a continuum into an arrangement of finite elements mathematically, in order to approximate solutions in complex problems. The use of a determined set of finite elements will depend on factors as geometry, areas of interest and computer-time to obtain a solution. Image from Budynas[62].

In FEA, three-dimensional elements deliver the most solution accuracy but at the expense of greater computational processing time. Due to costs and delays associated, it is advantageous to simplify the geometry to two-dimensional surface elements by using plane stress, plain strain, exploiting its symmetry along one or two axes, or using an axisymmetric approach (symmetric with respect an axis of rotation). Figure 3.5 shows an example of symmetry in solids simulation.

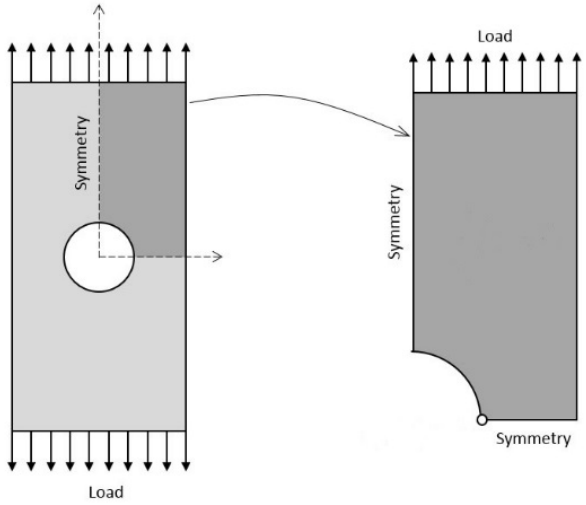

Figure 3.5. Example of a symmetric geometry simplification. In a solid it is possible to apply load in only one quarter of an object to examine, as the FEA software will reproduce it along its symmetry axes[254].

As seen in Figure 3.4, linear elements have straight boundaries while elements with a larger amount of nodes (6 - 8) may have curved boundaries. Elements can also be of first-order (linear interpolation between nodes) or second-order (quadratic interpolation between nodes)[317]. Curved and second-order elements can also adjust better to intrinsic geometries, handling steeper gradients of stress, temperature, and other parameters under scrutiny but increasing computational processing time. In a model, a combination of elements can be included, with curved and higher order elements placed in critical areas.

Figure 3.6 shows a scheme of how elements of higher order adjusts better to critical regions. Numerous references discuss perspectives regarding elements order, detailing the use of elements including up to 20 nodes and mathematics involved[276,277].

3.2.5 Mesh

Mesh (or grid) generation corresponds to the method of approximating a geometry by subdividing it in a polygonal or polyhedral mesh. In other words, mesh is the already mentioned discretisation of a domain in one, two or three dimensions (1D, 2D or 3D). Contemporary FEA software incorporates automatic mesh functions, facilitating this task. In addition, complex 2D or 3D geometries generated in a CAD package can be imported or drafted in the FEA software and then meshed.

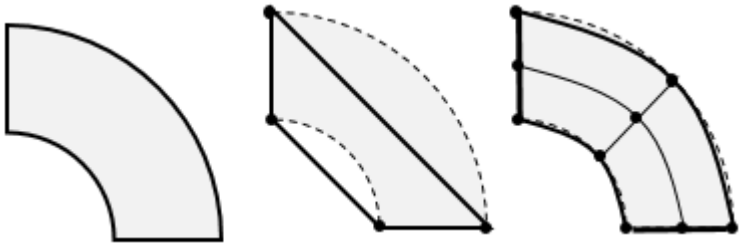

Figure 3.6. Domain approximation by an element with straight boundaries (centre), and by a curved element with a larger number of nodes (right). As seen on Section 3.2.3, errors can be induced when approximating an object's geometry. Image from Comsol Inc[276].

To optimise the models in terms of computer processing time, fine mesh can be assigned to areas of high stress concentration while coarse mesh can be positioned in less critical areas, delivering appropriated results. Mesh refinement (to adequately identify these areas) require previous experience and results in FEA models and it is crucial for specific solutions. Previously discussed, a common method to assess mesh quality is the refinement of a mesh until results become significantly consistent. This procedure is possible in models which are relatively non-complex as multiple operations can be carried out in a reasonable time frame. Figure 3.7 shows the process of mesh refinement in a domain. It is possible to observe how there is a better shape approximation with finer mesh[62].

In stress concentration areas, singularities (also known as artifacts) can occur, being parts of the problem's solution tending to an infinite value, therefore delivering inaccurate results. It has been observed that these anomalies reduce when mesh density increases.

Another method to validate mesh is to obtain the average stress value in the critical nodes and compare it in adjacent elements[62,252,253]. Large differences may indicate a certain degree of error in the results as shown in Figure 3.8.

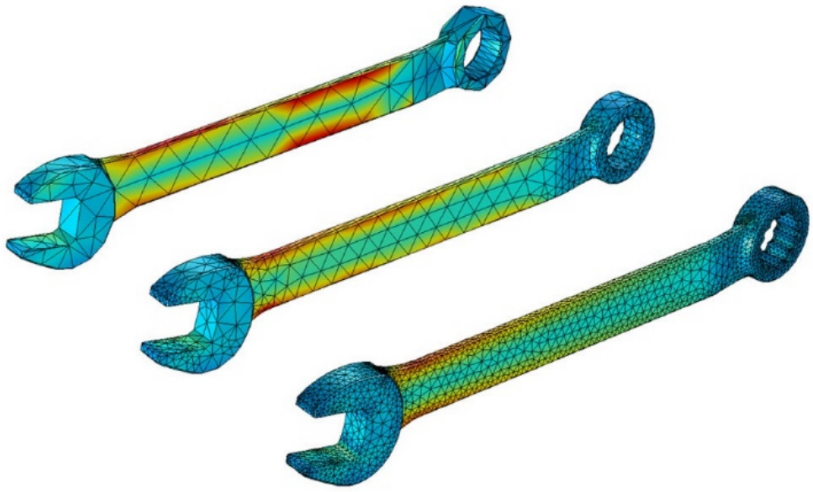

Figure 3.7. Coarse, intermediate and fine mesh approximations of a wrench geometry in an FEA simulation (in usual order). It is noticeable how the domain geometry for the coarse mesh example is not approximated as good as on the intermediate and fine mesh cases. Accuracy can be compromised by the selection of an unappropriated mesh size, particularly in critical areas. Image from COMSOL Inc[278].

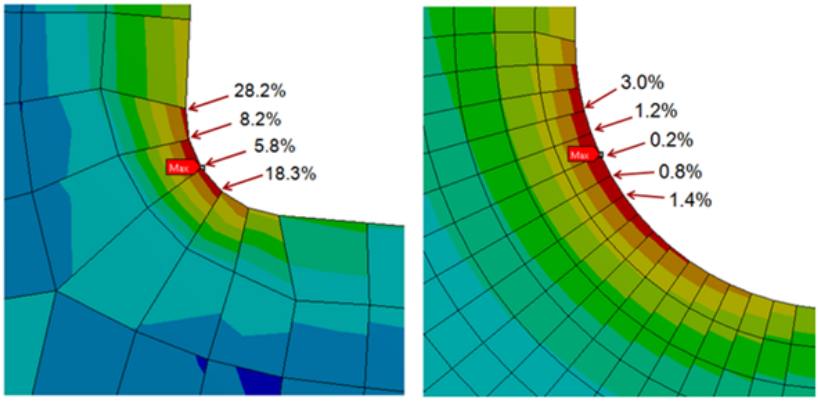

Figure 3.8: Relative stress differences in shared nodes. For coarse mesh (left) this percentage has larger values when compared with fine mesh (right), indicating more accuracy on the latter case. Percentages obtained dividing the adjacent elements' difference in unaveraged stresses by the shared nodal averaged stress. Image from CAE Associates[279].

It is important to note that these considerations vary among cases and it could be satisfactory to have relatively high stress difference in non-critical regions, where stress values are lower. Software also has a limit on the size of mesh can be generated, making stress peaks unavoidable in some circumstances. It is the FEA user who decides the level of accuracy in specific regions and evaluates mesh densities for optimum results.

3.2.6 Boundary Conditions

Boundary conditions can be defined as loads and constraints representing surrounding settings on a FEA model. They are crucial for obtaining realistic results, being one of the most difficult things to implement in FEA simulations. To define the adequate boundary conditions in a model it may be required to try various approaches and test for model convergence[62]. A basic example is provided by Adams[280], who refers to FEA modelling of a chair. Considerations such as load placement on the seat, rigid leg attachment to the floor and bending capabilities of the legs define boundary conditions of the problem.

Numerous types of boundary conditions are available in FEA software, the following being among the most important:

- Loads: accelerations, temperatures, pressures, forces, moments.
- Constrains: frictional or frictionless supports, and bonded, frictional or frictionless contacts.
- Element degrees of freedom: each element is allowed or restricted to have all possible degrees of freedom.

Including appropriated boundary conditions will help the model to converge. Redundant supports or unnecessary constrains would produce a model stiffer than in reality. Boundary conditions must neither allow deformations nor arise in reality. Both cases would present errors in the model and compromise convergence.

3.2.7 Implicit and Explicit FEA Solvers

Implicit and explicit solutions can be implemented to solve a determined problem (main differential equations in the time domain) via FEA. The implicit approach can be employed in situations where time dependency is not a relevant matter. Large time steps are implemented for solving the problem providing that a limited non-linear behaviour is

present. Static and quasi-static problems are an example. On the other hand, an explicit approach involves short time steps, coping well with large non-linear behaviour. Impact (ballistics) and vehicle crash illustrate the use of this approach[281].

In FEA models, implicit and explicit approaches take various considerations of velocity and acceleration into account. To visualize this it is worth considering the equation which relates force (F) with mass (m), damping coefficient (c) and stiffness (k) (Equation 3.1). Here, "x" means displacement while $\dot{x}$ and $\ddot{x}$ are the first and second time derivatives (velocity and acceleration)[281,282].

$$m\ddot{x} + c\dot{x} + kx = F \qquad \text{Equation 3.1}$$

For implicit arrangements displacement is not a function of time (x = constant). Consequently the velocities and accelerations become zero, discarding mass and damping. The implicit method can be based on Newark's method, or Newton Raphson Method among others. To solve a problem by employing this method, inversion of the stiffness matrix (k) is necessary. Engineering cases with large deformation would increase the size of the k matrix and the amount of computer time required to converge in a solution.

Explicit methods are a function of time and take into account velocity, acceleration, damping and mass from Equation 3.1. Requiring incremental time steps, the explicit method estimates displacements as time proceeds. An example of this is the simulation of an impact, modifying the deformation of the crash as time progresses. At time step 1 (0 ms) the impact hasn't caused any deformation. For time step 2 (5 ms) the algorithms proceed to calculate the deformation produced by the impact and will subsequently do for the remaining time steps programmed[281,282]. LS-Dyna[283] is a popular explicit solver included also in ANSYS[284]. Explicit solvers can be adapted to static or quasi-static problems[283]. APDL and MAPDL are solvers used for implicit analysis in ANSYS[285,286] (not likely to be employed or adaptable in dynamic cases).

3.3 FEA Model of a ZTA Anvil Cell

Preceding sections hallmarked the importance and technicalities of numerical methods and FEA. In view of its proven suitability for stress analysis, an FEA model has been

developed towards understanding stress distributions and failure in a ZTA toroidal anvil cell. In addition, the model includes a compressed water sample, numerically studying its behaviour under high pressure conditions. Following sections explains the detail of FEA model design and the technical aspects in producing accurate results.

3.3.1 ZTA Anvil Cell Geometries

In preparation for FEA model design, a precise reproduction of components via software is essential. ZTA single toroidal anvils are routinely used at research centres such as ISIS Neutron Laboratory (Oxfordshire, UK). This institution employs ZTA anvils manufactured in Germany by CeramTech, installed in a PE press and utilised for high pressure experiments since 2011. Technical information and drawings were kindly provided by ISIS Neutron Laboratory for this project, allowing an accurate reproduction via CAD (SolidEdge) and FEA (ANSYS) software. Figure 3.9 shows component detail of both exploded and assembled front views of the ZTA toroidal anvil cell.

ZTA anvils employed in ISIS Neutron Laboratory and subject of study in this project have a specific geometry. These are called standard anvils in this thesis to differentiate from other cases. TiZr gaskets provide a sample chamber with capacity for ~47 mm^3. Figures 3.10 shows the configuration of these key components, as well as basic geometrical information of standard ZTA anvils. Appendix 3 provides the entire set of detailed technical drawings used in SolidEdge and ANSYS to model the ZTA toroidal anvil cell.

3.3.2 ZTA Anvil Cell Material Properties

FEA model planning requires understanding of how the different materials interact and behave under working loads, as well as how their mechanical properties are altered by high pressure. ANSYS engineering data offers a broad options menu depending on properties to input and analyses to develop. As a static structural stress analysis is required, isotropic elastic data was included in the models. This comprise the mechanical properties necessary to describe TC, maraging steel and ZTA behaviour under operational conditions. By using this alternative, ANSYS automatically derives other properties from Young / bulk moduli and Poisson's ratio input values.

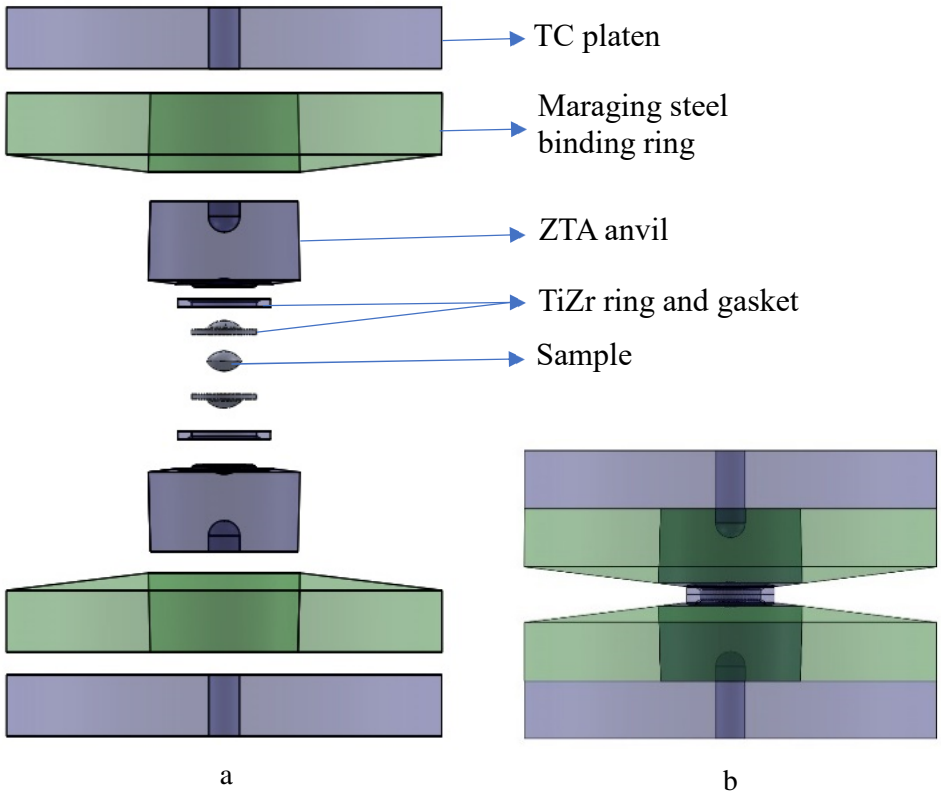

Figure 3.9. Exploded (a) and assembled (b) front view of ZTA anvil cell and components. Precise component dimensions were reproduced via SolidWorks® and SolidEdge® CAD software.

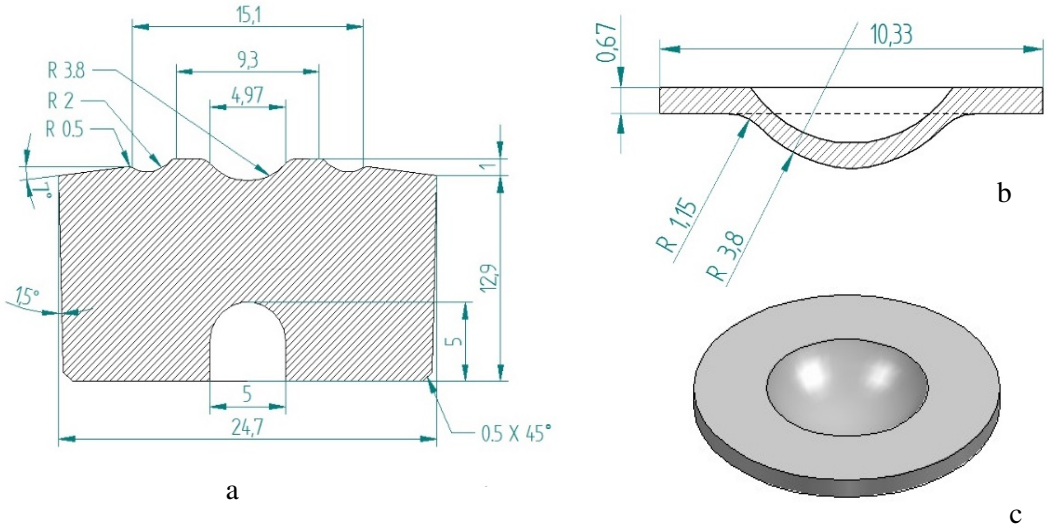

Figure 3.10. CAD section and dimensions of ZTA toroidal anvils and gaskets (a, b) and 3D model (c) of the gasket sample chamber studied in this thesis. A complete set of drawings for these components is present in Appendix 3.

While ZTA, TC and maraging steel have a predictable mechanical performance at the PE press, lack of information on TiZr gaskets and its plastic modulus prevails. Additionally, water solidification above ~1 GPa has dramatic effects in bulk moduli and Poisson's ratio values. Sections 3.3.3 and 3.3.4 explain how information was extracted from TiZr and water cases, for its input on the FEA model. Table 3.1 shows a compilation of mechanical properties involved on this arrangement..

Table 3.1. Mechanical properties of ZTA anvil cell materials. While ZTA, TC and maraging steel have a more predictable behaviour at high pressure, TiZr and water require further data due to their pressure dependence.

Material	Compressive Strength (GPa)	Tensile Strength (GPa)	Poisson Ratio	Young's Modulus (GPa)	Bulk Modulus (GPa)	Plastic Modulus (GPa)
ZTA[52]	4.7	0.29	0.24	350	224.3	
Maraging steel[287]	1.4 - 2.4 (Yield)	1.4 - 2.4 (Yield)	0.3	190	158.3	
TiZr[52]	0.7 (Yield)	0.7 (yield)	0.3	95	79.1	5 / 10 (see Section 3.3.3)
TC[38]	4.7	0.35	0.24	680	435.9	
Water	Pressure dependent (see Appendix 1)					

3.3.3 TiZr Plasticity

Mechanical properties of gaskets and its plastic deformation process have a considerable impact in obtaining reliable FEA results. This thesis considers an approach developed by Fang[38], treating TiZr with a bilinear isotropic hardening behaviour, including both elastic (Young's) modulus (E1) and plastic modulus (E2).

TiZr's E1 has been previously reported, corresponding to its elastic behaviour (linear stress-strain relationship). On this aspect, it is possible to notice how manufacturing and testing conditions produce different E1 outcomes. While Klotz[52] records for TiZr show how the room temperature E1 value is between 90 and 95 GPa (Table 2.2), and Fang used a value of 85 GPa, TiZr employed in the experiments developed for this thesis reported E1 values between 95.1 and 97.2 GPa (as communicated by ISIS Neutron Laboratory[288]).

The value of 95 GPa adjusted target pressures and volumes correctly in this thesis, being selected.

Representing its plastic performance, E2 was varied from 3.5 to 85 GPa. Fang[38] established that for small E2 values, the sample pressure increases considerably while higher E2 values cause the opposite effect. Below 3.5 GPa, there were convergence problems. A value of 5 GPa for E2 provided the best match to his target pressure. In a similar style for this project, a sequence of simulations were generated with different plastic moduli. For lower pressures (0 – 0.9 GPa approximately), the E2 value of 5 GPa also matches pressures experimentally recorded. Higher pressures require an E2 value of 10 GPa due to gasket's work hardening. This E2 dissimilarity between Fang's results and this thesis can be attributed to differences in the TiZr batch used. Anvils, binding ring, and platen are much more rigid. Plastic modulus is not as critical in these components.

3.3.4 Compressed Water Sample

Initially included as a validation method for loads input in the ZTA anvil model, numerically studying a compressed water sample became an interesting and motivating challenge. The static structural FEA model generated here is able to reproduce water pressure behaviour at multiple loads, including phase transitions and molar volumes. For these tasks covered in Chapters 4 and 5, experimental and literature data were analysed to obtain isotropic elastic properties of water. Values of bulk moduli and Poisson's ratio at variable pressure are crucial for modelling.

At ISIS Neutron Laboratory, a sequence of neutron diffraction experiments using a PE press equipped with a standard ZTA anvil cell were performed in a room temperature sample. It is important to remark how a sample of Deuterium (D_2O) was employed in these experiments for neutron diffraction purposes. Mechanical properties of D_2O when compared with water (H_2O) are extremely similar. Deuterium results are correlated and used along with literature data in water (H_2O) to study its compressed behaviour. To avoid further confusions the term "water" is adopted when discussing the experiments developed at ISIS Laboratory.

Figure 3.11 shows the resulting loading curve of water (using Lead as a pressure gauge). To be explained in Chapter 5, this curve is also significant for stress analysis. As anvils'

failure was reported from 75 tonnes, gathering of experimental data finishes at 60 tonnes to preserve these parts. A final pressure of 5.38 GPa was measured.

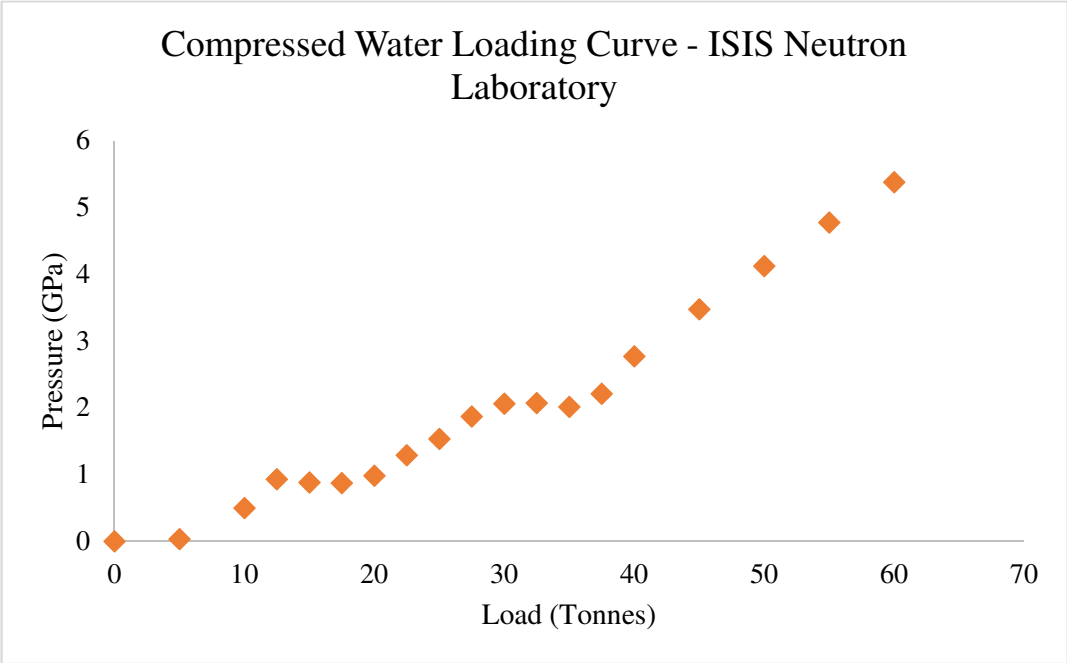

Figure 3.11. Compressed water loading curve. Experiments were performed using a standard ZTA anvil cell, subject of analysis in this thesis. This plot is relevant towards finding mechanical properties of the water at high pressure, particularly bulk moduli and molar volume at various phases, as well as for validation of the FEA model results. Data points are available in Tables 4.4 and 5.1.

Reviewed in Chapter 2, room temperature liquid water solidifies at ~1 GPa into Ice VI. A second transition into Ice VII occurs above ~2 GPa. Both phase transition do not arise in a sharp manner but occur across a broad range of pressures. Figure 3.11 shows two areas, where load was incremented and pressure remained relatively constant, being attributed to a density increase associated with water's phase transitions. Additional to the water loading curve, ISIS Laboratory experiments include neutron scattering data gathered for the solid phases Ice VI and VII, providing lattice volume data for each pressure step. This allows extraction of key information such as molar volumes (and densities) and bulk moduli to input and validate FEA results. For the liquid water segment of the experimental loading curve (0 – 1 GPa approximately), literature data was incorporated in the models to obtain the necessary properties.

Being this information specific for different pressure ranges and phases, Chapter 4, 5 and Appendix 1 show in detail the water properties input for the studies performed in this thesis.

At this point it is important to mention that due to the broad nature of the phase transitions, investigations on Ice VI and VII give rise to different loading curve outcomes and equations of state, depending on characterisation methods employed and laboratory procedures. Brillouin spectroscopy for instance leads to adiabatic results while synchrotron x-ray diffraction and neutron diffraction include isothermal effects. Shimizu[250] and Tulk[289] performed adiabatic studies whereas authors such as Johari[290], Chen[251], Bezacier[240], Hemley[291], Munro[292], Klotz[293] and Yoshimura[294] generated isothermal results. Antsyshkin[295] developed an interesting study combining experimental and mathematical approaches. It is worth noting that the outcomes reported by Bezacier[240] provide an excellent data collection, delivering a comprehensive amount of pressure – volume data for both phases.

3.3.5 ANSYS Finite Element Model

The information gathered on the standard ZTA anvil cell (components' geometries and material properties) was incorporated into ANSYS Workbench R15.0. As a result, a fully functional numerical model of a ZTA anvil cell with a static-structural configuration and a mechanical meshing was completed. As stated in various sections of this thesis, FEA methods have challenges which need to be addressed due to a number of unknown parameters. It is necessary to introduce certain technical considerations centred on previous studies or experience. The next paragraphs clarify specific assumptions on boundary conditions (contacts, loads and supports), mesh and number of steps.

3.3.6 ZTA Anvils Cell FEA Methodology

With the information regarding components geometries (Figure 3.10 and Appendix 3), a static structural model was drafted using the ANSYS geometry editor. The entire high pressure set has axial symmetry along their central axis and symmetry relative to the central plane. By using 2D axisymmetric settings, simulations require only a quarter of the cross section. This option was applied as it reduces computer time when running calculations. Figure 3.12 shows the configuration of the FEA model.

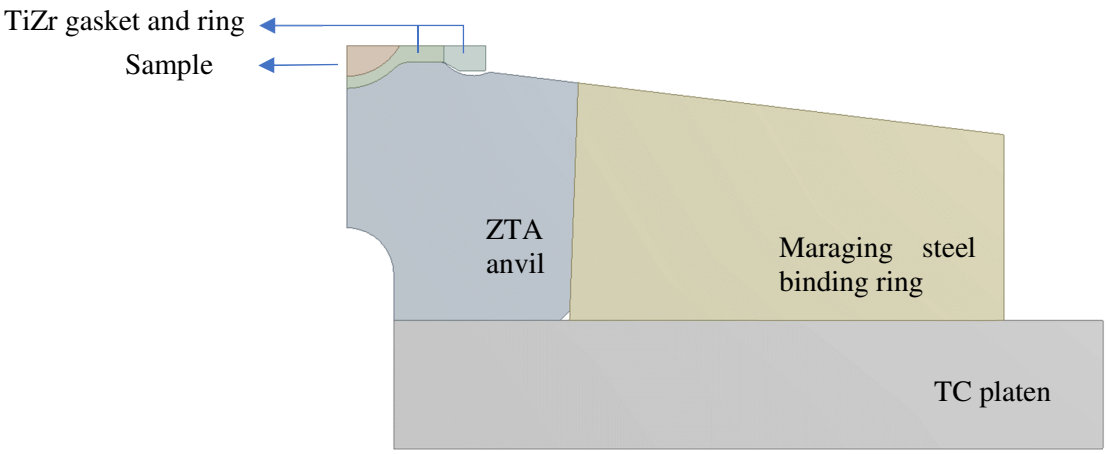

Figure 3.12. Two-dimensional axisymmetric depiction of ZTA anvil cell. By exploiting the high pressure set rotational and central plane symmetries, it is possible to increase computer-time efficiency on the FEA simulations, obtaining reliable results.

Axial thrust load is applied from the bottom anvils. Frictionless supports were incorporated, acting as a "symmetry" boundary condition and avoiding singularities on the FEA process[257]. Figure 3.13 displays the location of the load and frictionless supports. Following Sections 3.3.2 to 3.3.4, material engineering data was fed into ANSYS. As mentioned, TC, maraging steel and ZTA materials have straightforward values in terms of isotropic elasticity, while TiZr and water values are pressure dependent. They will vary according to each study as specified in Chapters 4 and 5 where this FEA model is employed. Figure 3.14 shows how these values are incorporated into ANSYS Workbench.

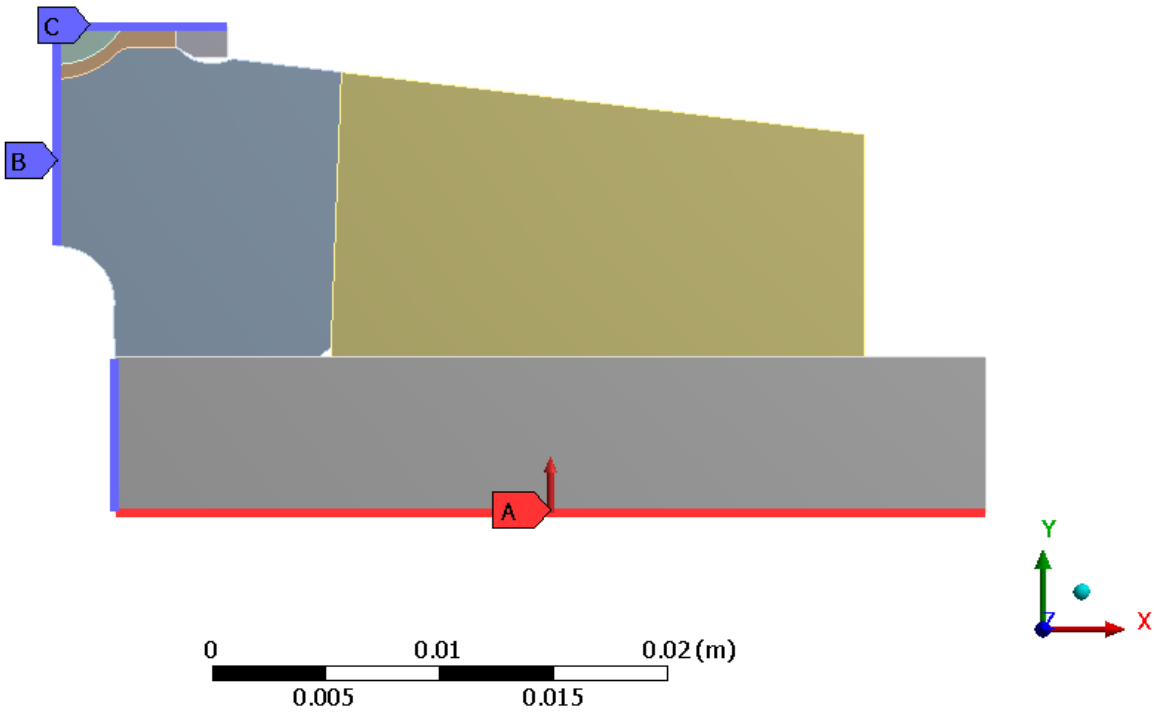

Figure 3.13. Boundary conditions of load and frictionless supports on the ZTA anvil cell FEA model produced in this thesis. Load (A) has an even application at the TC platen surface of the model. Frictionless supports (B and C) are important to help the two-dimensional model to converge.

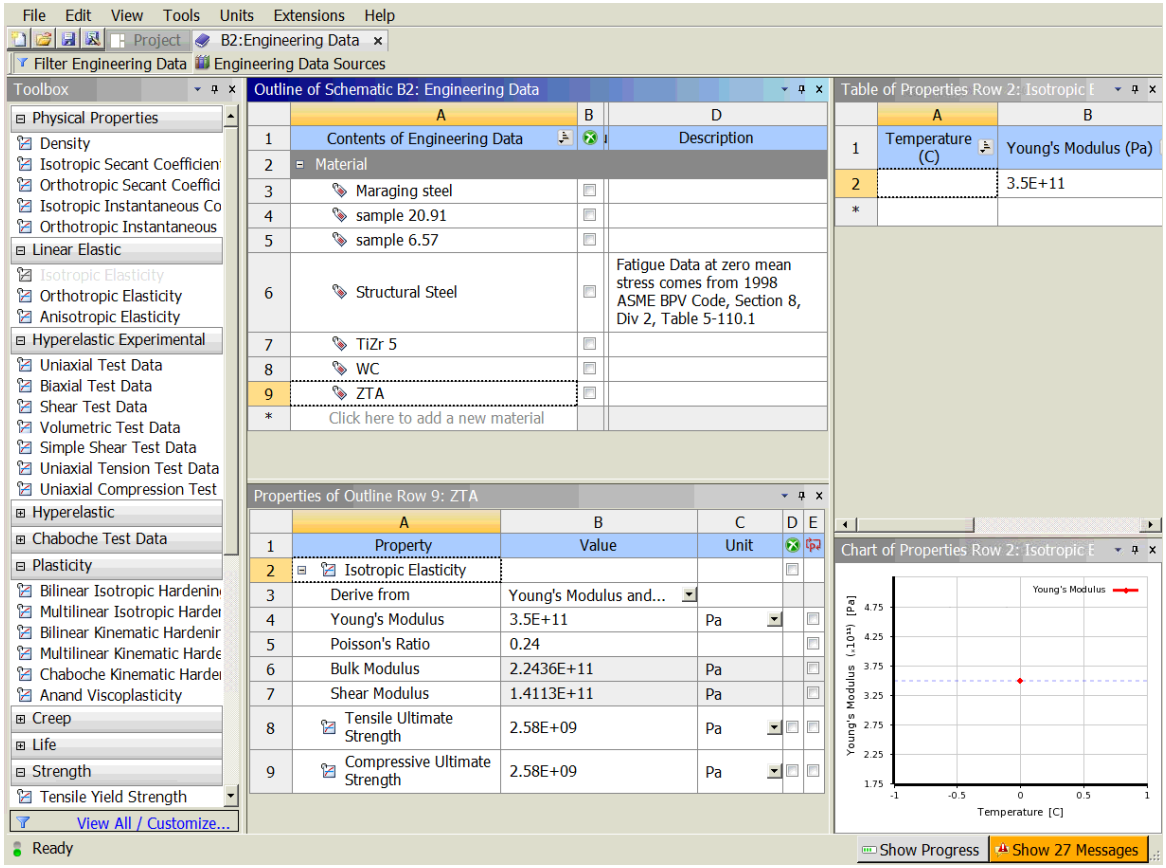

Figure 3.14. ANSYS engineering data input. As static structural stress analyses will be performed, it is possible to observe that the isotropic elasticity option was selected to add the corresponding materials properties.

To obtain precise stress patterns results and to identify stress concentration areas, the mesh selected for the anvil and gasket was refined in particular regions such as beam aperture and anvils sample and toroid surfaces. As explained further, coarse mesh was employed as well as it proved useful in the sample region. In this project mesh was modified depending on the specific area to study. Chapters 4 and 5 detail those variations for each case. It is important to recall how fine mesh increases model's computer time. Figure 3.15 shows a generic example of mesh on the elements.

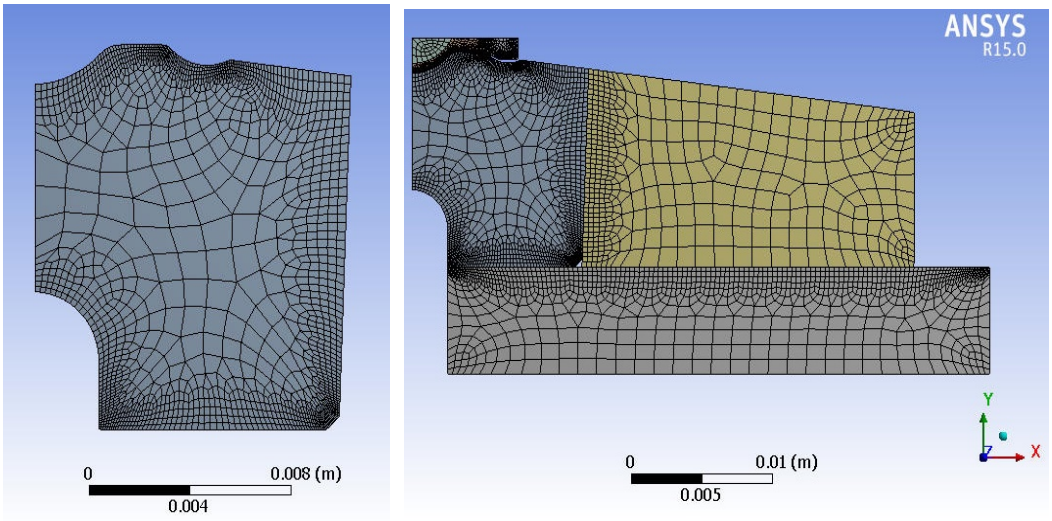

Figure 3.15. Implementation of mechanical mesh at the ZTA anvil (left) and at the entire set of components (right) of the ZTA anvil cell. It is possible to see on the ZTA anvil a finer mesh selection in critical sections and coarse in less sensitive areas to improve computer-time efficiency. A similar situation occurs in the rest of the components (right).

FEA methods frequently require significant amounts of computer processing time. As software packages become progressively more important to mechanical design and analysis, improvements and releases are continually improving their performance. In ANSYS static structural models, steps are variations in the load history which can be managed by the user. Time (usually in seconds) is connected with the steps in order to gradually apply load. Larger numbers of steps and longer time help to reach or improve convergence and accuracy in the models, while computer processing time increases.

3.3.7 Contacts

The FEA model requires specific considerations about contact behaviour among components of the ZTA anvil cell. The type of contacts to be designated depend on each component location and function. The following list describe the contact options and how they were implemented in the model:

- Bonded contacts denote non-sliding conditions on surfaces. This type of contact was used only between the binding ring and TC platen, allowing convergence in the model and reducing unrealistic binding ring displacements.
- Frictional contacts were activated for the remaining components. Merkel[169] mentions how this factor does not interfere with final results in numerical studies of diamond anvil cells. Fang[38] mentions how a range of friction coefficients (0.2 – 0.5) matched target pressure on an FEA model of a double toroidal anvil (made of PCD). This study evaluated a series of values, noticing how friction coefficients from 0.2 to 0.6 produce close results to pressures detected in the experiments. Certain models may experience converge issues when friction coefficient is below 0.2. Therefore, models generated for this study used a friction coefficient of 0.3.
- Interference contacts are embedded into frictional contacts and are used to reproduce the press-fitting of the anvil and binding ring. The binding ring contact has an offset of 0.0642 mm towards the anvil to produce lateral pre-stress. Appendix 2 shows calculations for this offset.

Furthermore, other contact settings were required to be tuned or program controlled. Training material[254,255,296–298] gives advice on configuration of variables depending on the problem to solve. The following settings were considered:

- Behaviour: symmetric as surfaces (contact and target) are constrained from penetrating each other.
- Formulation: depending on the formulation, contacts are detected differently. Augmented Lagrange uses integration point detection, resulting in more detection points than Normal Lagrange, which uses nodal detection points (based on mesh nodes in contact). As mesh was refined in areas of interest, results are practically equal

using both approaches. Penetration is also controlled with these two approaches, being computer time longer than other contact formulations.

- Trim contact: this parameter can accelerate computer processing time by decreasing the amount of contact elements referred to the solver for consideration. This feature is recommended “off” for large deflections as the one produced in gaskets.
- Shell thickness effect: Recommended on for large deflections as it allows to update thickness in contact calculations.

Chapter 4

Finite Element Analysis Modelling of Compressed Liquid Water in a ZTA Toroidal Anvil

This Chapter describes how the FEA model generated in this thesis was implemented to study a room temperature compressed liquid water sample (~47 mm^3) in a standard ZTA toroidal anvil cell. For the 0 – 1 GPa pressure range (water liquid phase), substantial results have been gathered and assessed by combining relevant literature and experimental data with this computational technique.

The numerical model is also capable of reaching quasi-hydrostatic conditions when liquid water is compressed until its phase limit for room temperature (1 GPa). Currently this is the first FEA study performed in compressed liquid water.

4.1 Introduction

Water is possibly the most studied substance on the planet, several publications explain its behaviour and structure under many scenarios. Engineering and scientific applications require knowledge of water properties at variable pressure - temperature conditions, being thermodynamic tables and their use an example[233]. Science and technology progress involve data updates, expanding ranges and examining extremer parameters. Chapter 2 cited how high pressure instruments and computational methods have contributed to this matter.

Implementation of FEA in high pressure instrument design has had great impact on their effectivity and functioning range. As detailed in Chapter 3, an FEA model of a ZTA toroidal anvil cell has been created based on a standard version in use at ISIS Neutron Laboratory for working loads up to 75 tonnes. Including a water sample to evaluate its operation, it was rapidly noticed how this computational technique can be used to simulate compressed water experiments.

The water pressure – temperature phase diagram (Figure 2.19) establishes how room temperature liquid water solidifies into Ice VI at ~1 GPa. This phase transition has a distinctively broad nature. Modelling the rich phase behaviour of compressed water is an interesting task, which has not been done through FEA to date. Based on *PVT* water properties from literature and input in the model, a sequence of numerical results was successfully evaluated and validated. This work additionally contributes with the estimation of sample properties such as bulk moduli and Poisson's ratio at conditions not yet reported.

The analysis will be delivered in three parts. First, water properties will be extracted from literature to feed the FEA model. Simulations will be performed and verified for an initial pressure range of 0 – 0.588 GPa. Then, adjustments in water properties will be made in order to model the ISIS experimental loading curve (0 - 0.979 GPa) including its wide phase transition. Finally, a hydrostatic model of liquid water at 1 GPa will provide insights of this point in particular.

4.2 Modelling of Compressed Liquid Water (0 – 0.588 GPa)

The static structural nature of the FEA model developed in this thesis is crucial to calculate and add liquid water properties for target pressure steps (bulk moduli in particular). ISIS' neutron experimental water data developed for this thesis is available from 1 GPa, corresponding to solid phases. Therefore, it is necessary to access data from literature to numerically study lower pressure scenarios. Bridgman[234] presented in 1935 a pioneering collection of results in compressed liquid water at variable temperature. Outcomes in pressure (kgf/cm^2) and molecular volume (cm^3/mol) at 20 °C are of high interest in this section.

Pressure units were converted in Pascals considering 1 kgf/cm^2 is ~98.066 kPa. Combining Bridgman's[234] molecular volume data with water's molecular weight (18.01 g/mol), densities for the variable pressure steps were approximated. Bulk moduli can be defined by density multiplied by the derivative of pressure vs density (Equation 2.2). Appendix 1 details bulk moduli calculations based on this principle while Table 4.1 compiles relevant information.

Table 4.1. Bridgman's[234] compressed water properties at 20 °C. Density and bulk moduli were calculated from the original publication (Appendix 1).

Pressure (kgf/cm^2)	Pressure (GPa)	Water Molecular volume (20 °C) cm^3/mol	Density (g/cm^3)	Bulk Moduli (GPa)
1	9.8E-5	18.048	1.00	1.95
500	0.049	17.690	1.02	2.35
1000	0.098	17.352	1.04	2.75
1500	0.147	17.072	1.05	3.11
2000	0.196	16.805	1.07	3.48
2500	0.245	16.573	1.09	3.81
3000	0.294	16.366	1.10	4.12
3500	0.343	16.185	1.11	4.41
4000	0.392	16.012	1.12	4.69
5000	0.490	15.698	1.15	5.24
6000	0.588	15.430	1.17	5.74

In Table 4.1, highlighted data sets were selected to be numerically modelled. To simulate compressed liquid water behaviour at this pressure range, the following procedure was applied:

- The standard ZTA toroidal anvil model developed in Chapter 3 was employed, including geometries, boundary conditions and components discussed. Certain mesh variations (further explained) were incorporated to improve the sample's hydrostatic conditions.
- Having a set of target sample pressures (selected from Table 4.1), bulk moduli and Poisson's ratio were input in the FEA model and load increased. Water pressure and load were recorded when reaching a desired value. A loading curve was generated for compressed liquid water in the standard ZTA toroidal anvil cell via FEA.
- For results validation, water molar volumes obtained via FEA were compared with Bridgman's values in Table 4.1. As numerical models are in 2D axisymmetric format, resulting compressed water samples (half) were analysed in 3D via SolidEdge CAD software to obtain its volume. In accordance with the model's geometry, half sample contains ~0.0013 moles of water.

This thesis static structural models are performed by employing and implicit solver (ANSYS Workbench MAPDL). During the simulation process it was noticed that, by adding only isotropic elastic data corresponding to a specific final pressure step, sample pressure and volume collected does not match Table 4.1 values. Modelling this series of hydrostatic water pressure steps involves implementation of an alternative strategy. Pressure and molar volume progression is correlated with bulk moduli evolution produced during preceding load steps.

This stimulating challenge was solved by including a variety of small temperature increments in the isotropic elastic data of water. ANSYS' static structural solver has capacity for adding a matrix of isotropic elastic properties in accordance with temperatures programmed in materials data. Therefore, temperature and load steps evolution were synchronised with simulation time (s). At a specific simulation time, a load value will correspond to a temperature value and the calculations are performed with

a corresponding bulk moduli and Poisson's ratio. As mentioned, loads were registered when reaching a desired sample pressure.

The following load – time step allows calculations with adjusted isotropic elastic properties (in the same run). As the temperature increments are minimal, material properties of ZTA anvils, adjacent components, and sample are not affected. Table 4.2 summarises the isotropic elastic values and their corresponding time – temperature.

Table 4.2. Isotropic elasticity - temperature - time - load matrix for compressed liquid water FEA models.

Time (s)	Water Temperature (°C)	Poisson's Ratio	Bulk Modulus Bridgman (GPa)	Load (tonnes)
0	22	0.49	1.95	0
15	23	0.47	2.35	6.75
25	24	0.47	3.11	11
40	25	0.47	3.81	12
50	26	0.47	4.41	13.5
55	27	0.45	5.24	15
63	28	0.45	5.74	16

Table 4.2 displays how Poisson's ratio was adjusted according to the load. While classic literature mentions how liquid water has a Poisson's ratio value of 0.5 (theoretically incompressible[299]), Chapter 2 mentioned that recent publications are finding this inconsistent for real materials[300,301]. To add a Poisson's ratio value of 0.5 in ANSYS static structural models generates a singularity according with the relationship among elastic constants in Equation 2.3. As performed in this thesis, multiple FEA studies have approached this problem by using a value of 0.49[302–304], producing quasi-hydrostatic models. At present, there are no studies on the evolution of Poisson's ratio of compressed liquid water.

Due to liquid water's increase in pressure and density, Poisson's ratio is believed to decrease, evolving toward 0.3 in solid phases. This trend has been noticed in other compounds[305]. In this thesis, Poisson's ratio was slightly adjusted to help convergence

and for a better approximation of volume results. Modifications in Poisson's ratio do not have a high impact in sample pressure results. Figure 4.1 illustrates the sequence of temperatures, bulk moduli and Poisson's ration as programmed in ANSYS engineering data, while Figure 4.2 and 4.3 show time and thermal conditions in the models.

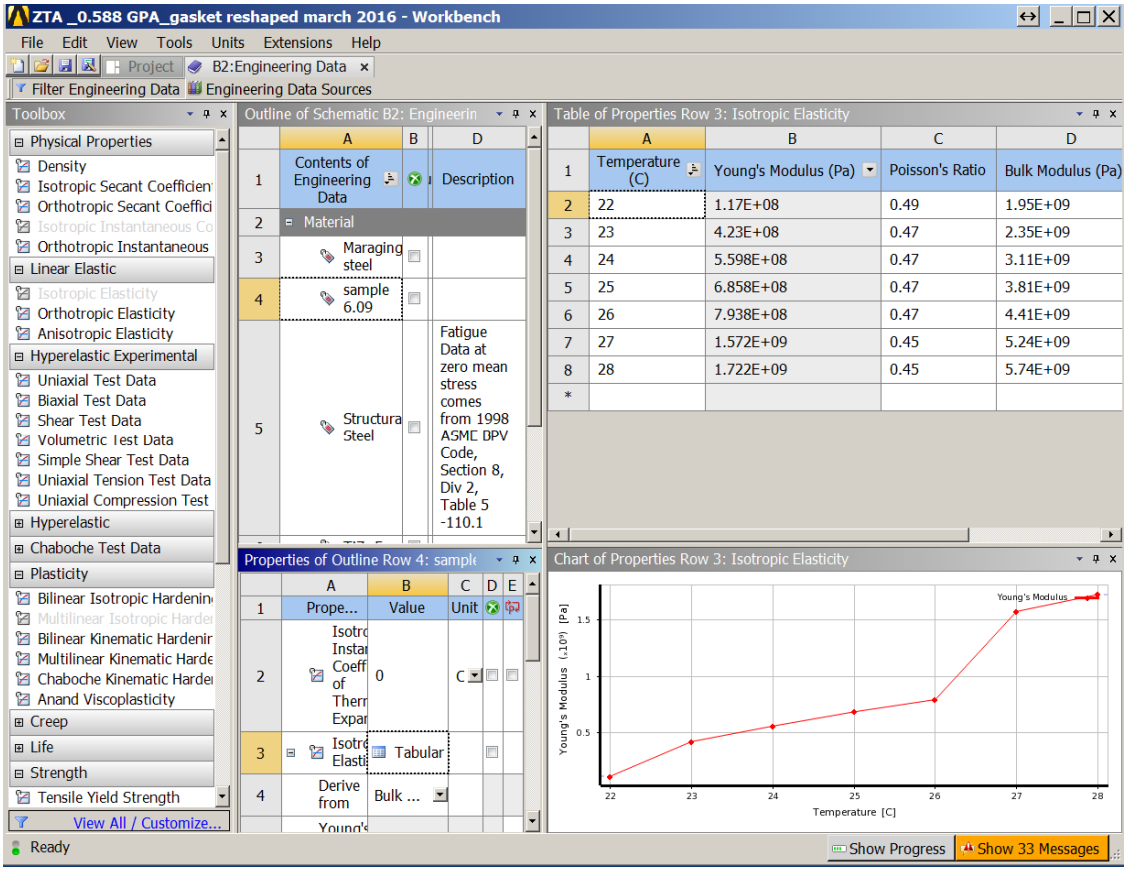

Figure 4.1. ANSYS engineering data for compressed liquid water models (0 - 0.588 GPa). A series of time and load steps (Table 4.2 and next Figure) were synchronised with temperature and isotropic elastic data in order to model sample's pressure and molar volume at this pressure range.

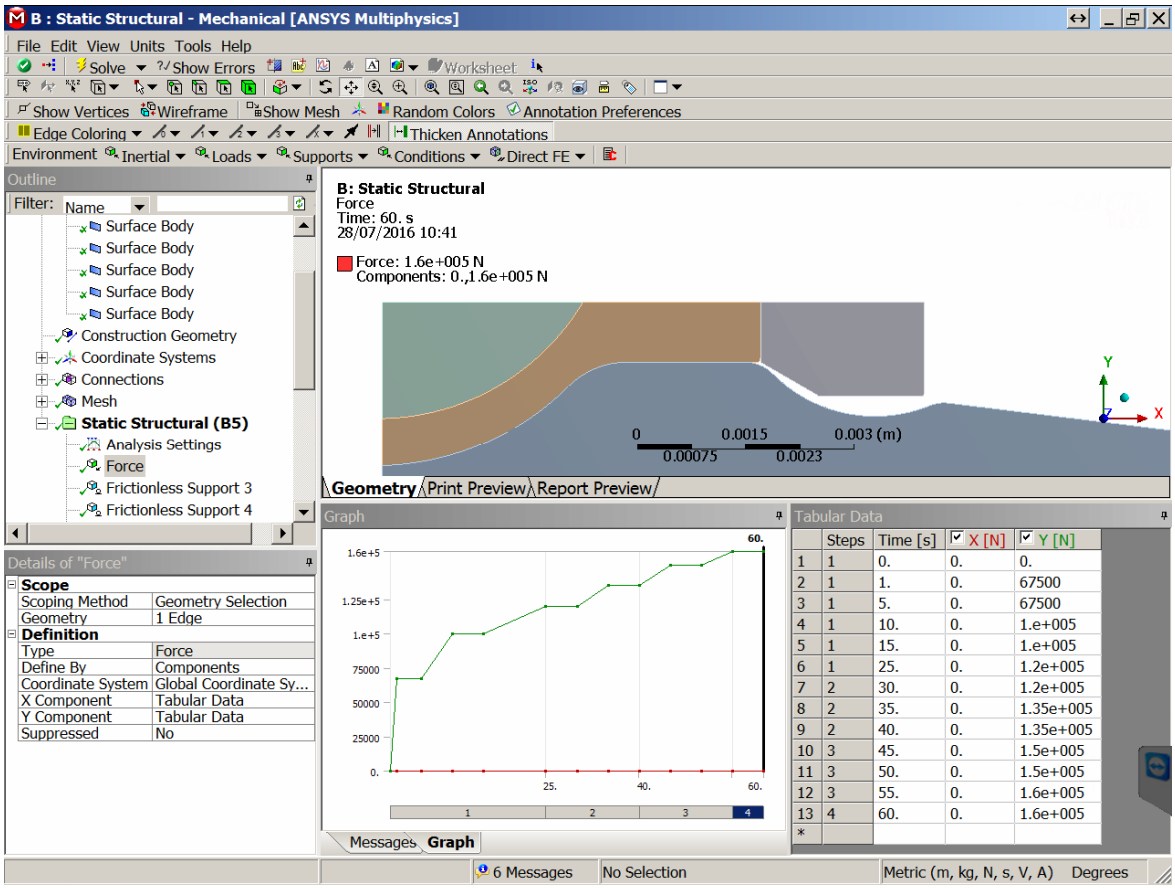

Figure 4.2. ANSYS time and load steps for liquid water models from 0 to 0.588 GPa. It is possible to correctly model the sample pressure and molar volume decrease for liquid water at this pressure range in a static structural FEA model by correlating isotropic elastic properties with temperature, time and force steps.

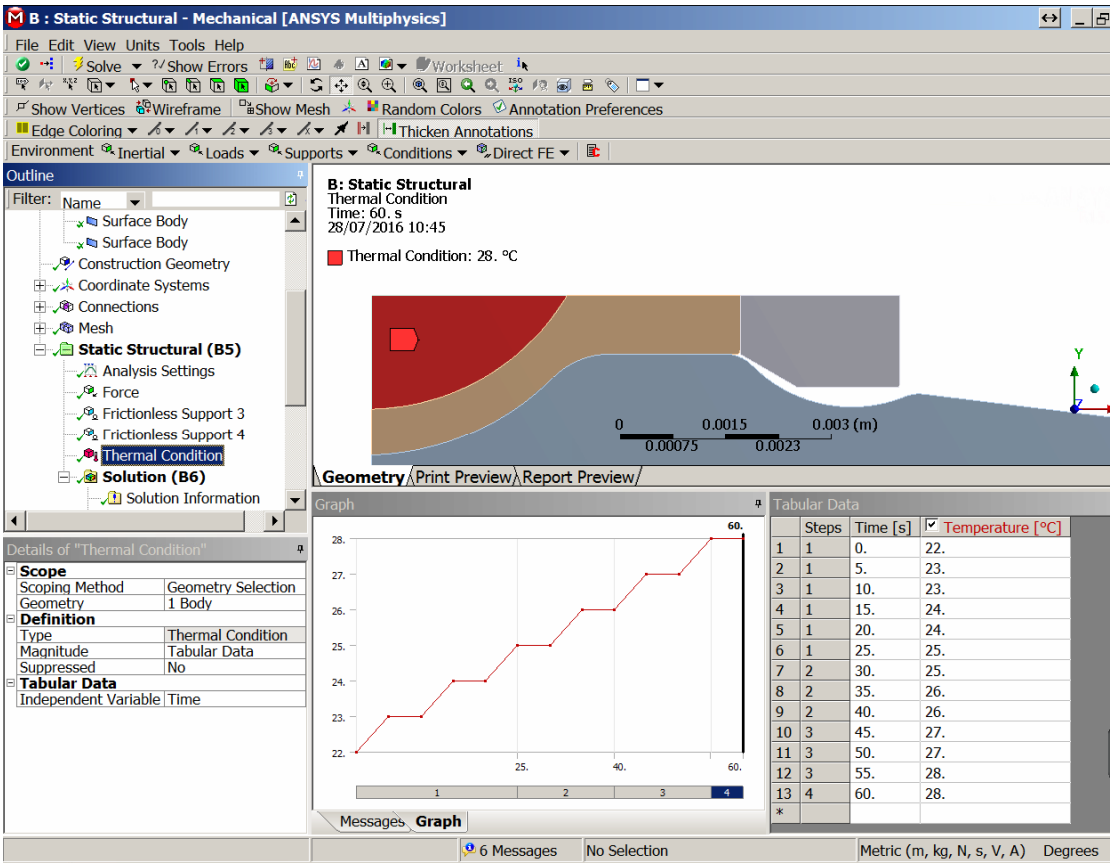

Figure 4.3. ANSYS time and temperature steps for liquid water models from 0 to 0.588 GPa. As seen in previous Figures and Table 4.2, these parameters are in synchrony with isotropic elastic data and temperature to simulate compressed liquid water pressure and molar volume at a given pressure range.

Explained in Section 3.2.5, mesh is a significant factor in FEA models. Size and refinement in key areas determine various levels of accuracy in a solution. This research noticed how coarse mesh helps improving hydrostatic conditions when implemented at the sample and gasket. It was noticed how numerical hydrostatic conditions vary when load is augmented, being ±1 MPa on the 6.75 tonnes case (49 MPa) and ±28 MPa in the 16 tonnes case (0.588 GPa). Figure 4.4 displays mesh size on the sample, gasket and surrounding areas of the liquid water models (0 – 0.588 GPa).

Having set the relevant parameters essential to this process, a numerical loading curve was generated. Figure 4.5 shows the resulting curve of compressed water on a standard ZTA anvil cell via FEA and its comparison with Bridgman's[234] data. In synthesis, for

each loading curve data point, the FEA sample was exported to SolidEdge to obtain its volume (half). Combining sample volumes with the amount of moles of liquid water in the sample (~0.0013 in half sample), results were compared with Bridgman's data and validated. Figure 4.6 illustrates this procedure.

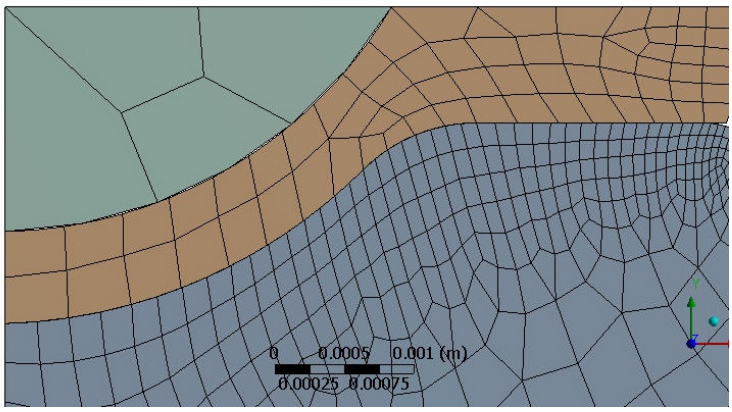

Figure 4.4. Mesh configuration on liquid water sample and gasket for compressed liquid water FEA model (0 – 0.588 GPa). Coarse mesh at the sample and gasket showed successful towards improving hydrostatic conditions in compressed water numerical results.

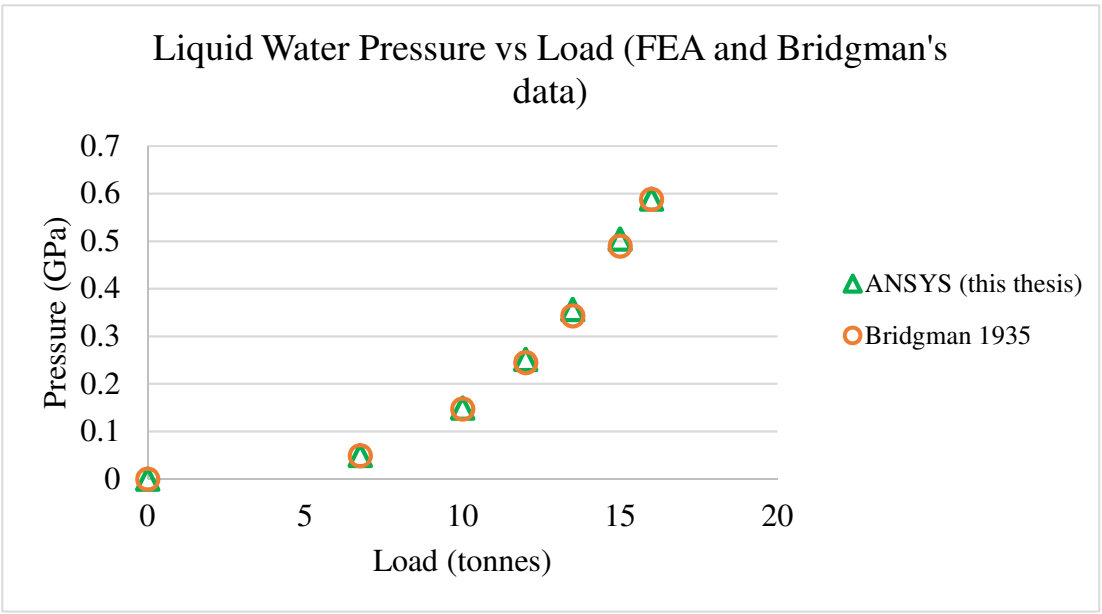

Figure 4.5. Liquid water loading curve for 0 - 0.588 GPa pressure range, based on Bridgman's[234] data implemented in the ANSYS FEA model of a standard ZTA toroidal anvil. When FEA pressure values at the sample matched Bridgman's[234], loads were registered to generate this curve.

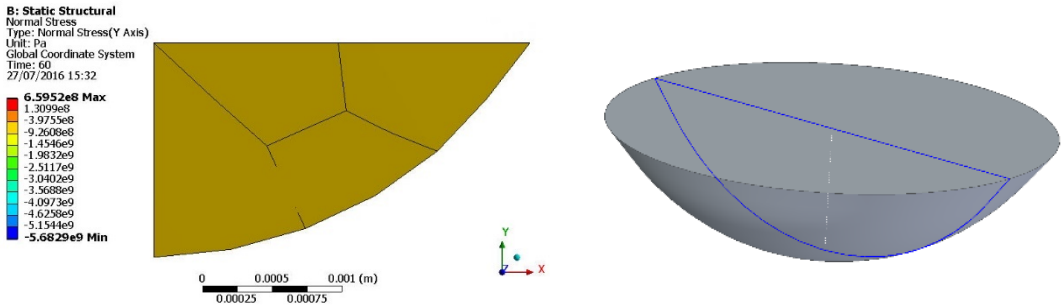

Figure 4.6. Compressed ANSYS sample (left) and its three-dimensional representation via SolidEdge CAD software (right, half sample). Once FEA results were available, this procedure was employed to obtain sample volume values for the pressure range of interest (0 to 0.588 GPa). Volume results were combined with the sample's amount of substance in half sample (~0.0013 moles) to obtain molar volumes and validate results with Bridgman's[234] *data.*

Figure 4.5 shows a clear match between Bridgman's experimental results and sample pressures obtained with this thesis' FEA model. When assessing molar volume vs pressure data, a remarkable match between Bridgman's (experimental) and numerical values can be noticed, validating the FEA work completed in compressed liquid water. Figure 4.7 graphically shows these results while Table 4.3 summarises them. ANSYS volume results only have a 2.85% maximum difference with respect to the one experimentally observed by Bridgman.

This innovative approach allows scientists to examine a sample under high pressure in a practical manner. By adjusting this method to other situations (such as phase transition areas), knowledge about sample properties can be estimated. The following paragraphs provide interesting numerical insights to sample's properties in areas of difficult experimental access.

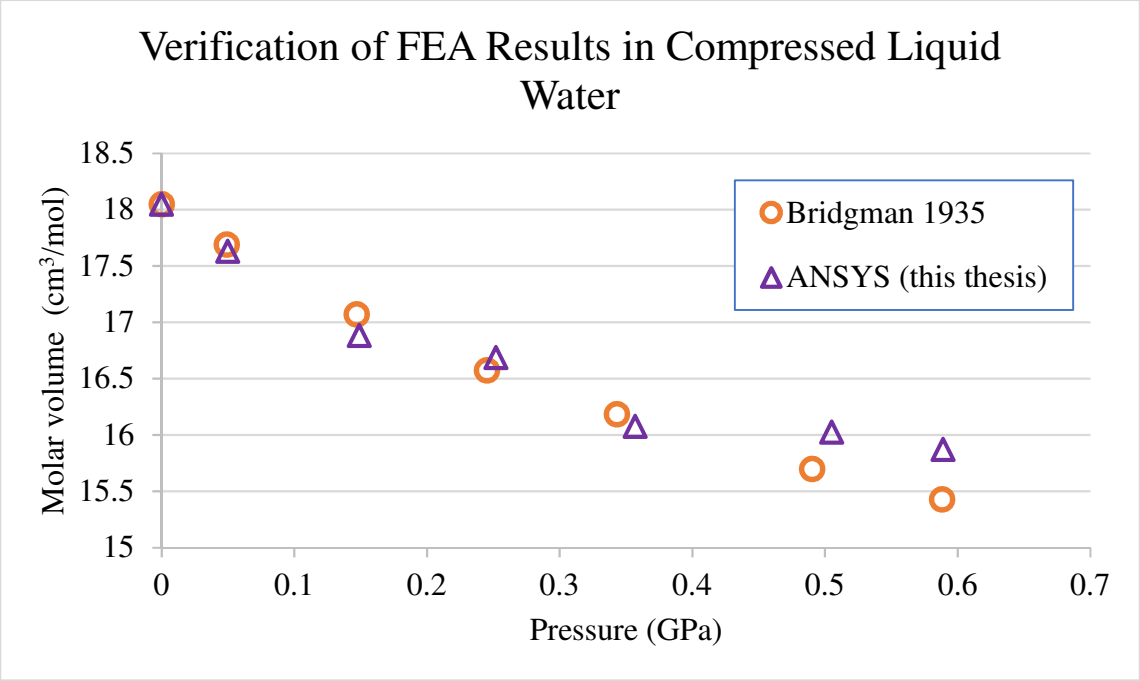

Figure 4.7. Compressed liquid water molar volume vs pressure data. By comparing compressed liquid water results from Bridgman's experiments and modelled via FEA, it is visible how the numerical model was effectively implemented. Molar volume values are extremely similar from 0 to 0.357 GPa and only ~2.85% different for the last two cases.

Table 4.3. Pressure and volume benchmark between FEA liquid water models and Bridgman's[234] experimental data.

Pressure (Bridgman/ANSYS) GPa	Molar volume Bridgman (cm^3/mol)	Volume ANSYS (gasket) (cm^3/mol)	Difference (%)
0	18.048	18.05	0
0.0490 / 0.0498	17.69	17.63	0.33
0.147 / 0.149	17.072	16.88	1.11
0.245 / 0.252	16.573	16.68	0.69
0.343 / 0.357	16.185	16.07	0.66
0.490 / 0.505	15.698	16.02	2.08
0.588 / 0.589	15.43	15.87	2.85

4.3 FEA Modelling of Compressed Liquid Water from ISIS Experimental Data (0 – 0.979 GPa)

The previous section successfully modelled compressed liquid water for a 0 – 0.588 GPa pressure range. It is interesting to complete a similar action with experimental data obtained in ISIS Neutron Facility, with pressure values up to 0.979 GPa and including a broad phase transition liquid water – Ice VI.

Regarding ISIS experimental data acquired for this thesis, Figure 3.11 displays an area where pressure remains quasi-stable despite a load increase from 12.5 to 20 tonnes. This effect can be associated with a raise in water density at the phase transformation region, also visible in Ice VI – VII phase change. Additionally, experimental data shows a rapid pressure increase at initial loads when compared with Bridgman's[234] series analysed in the previous section.

On the opposite of a sharp case (occurring at a specific point), having an ample phase transition means that, experimentally, it is conceivable to have multiple sample pressure scenarios for a particular load range. In other words, ISIS experimental data shows a region subject to factors such as thermodynamic fluctuations, sample impurities, surface irregularities, and others which contribute with alternative experimental outcomes for similar load conditions[306,307].

ISIS experimental loading curve was modelled via FEA, following the exact methodology developed for the previous section. A matrix linking temperature, time, load, bulk moduli, and Poisson's ratio, was incorporated into ANSYS and preliminary data was obtained. To initially estimate an equation of state and bulk moduli for this new pressure range and steps, Bridgman's[234] results were complemented with information extracted from Grindley[235] (up to 0.8 GPa) and extrapolated when necessary.

As expected and due to the previously explained variation in density between 12.5 and 20 tonnes, a difference between FEA and ISIS experimental pressure results was noticed when incorporating calculated bulk moduli from both Bridgman[234] and Grindley[235]. Considering that density proportional to bulk moduli ($B=\rho\, dP/d\rho$), adjustments must be made to reflect the co-occurrence of both liquid water – Ice VI phases. Bulk moduli was tuned in ANSYS and ISIS experimental loading curve simulated. While Appendix 1

shows calculations involved, Table 4.4 summarises experimental data, ANSYS results and bulk moduli used in each load. Figure 4.8 shows ANSYS data arrangement and Figure 4.9 illustrates pressure vs load results.

Table 4.4. Experimental data and numerical results for compressed water from 0 to 0.979 GPa, estimations made using data from literature and adjusted bulk moduli values.

	Liquid water				
Load (tonnes)	Pressure ISIS Experiments (GPa)	Pressure ANSYS	Bulk Mod. (GPa) Bridgman[234]	Bulk Mod. (GPa) Grindley[235]	Bulk Mod. (adjusted, GPa)
0	0	---	1.64		---
5	0.029	0.026	2.2		---
10	0.498	0.452	5.28		15.7
12.5	0.93	0.944		7.08	26
15	0.879	0.878		6.92	15
17.5	0.871	0.865		6.89	8.8
20	0.979	1.09		7.22	9

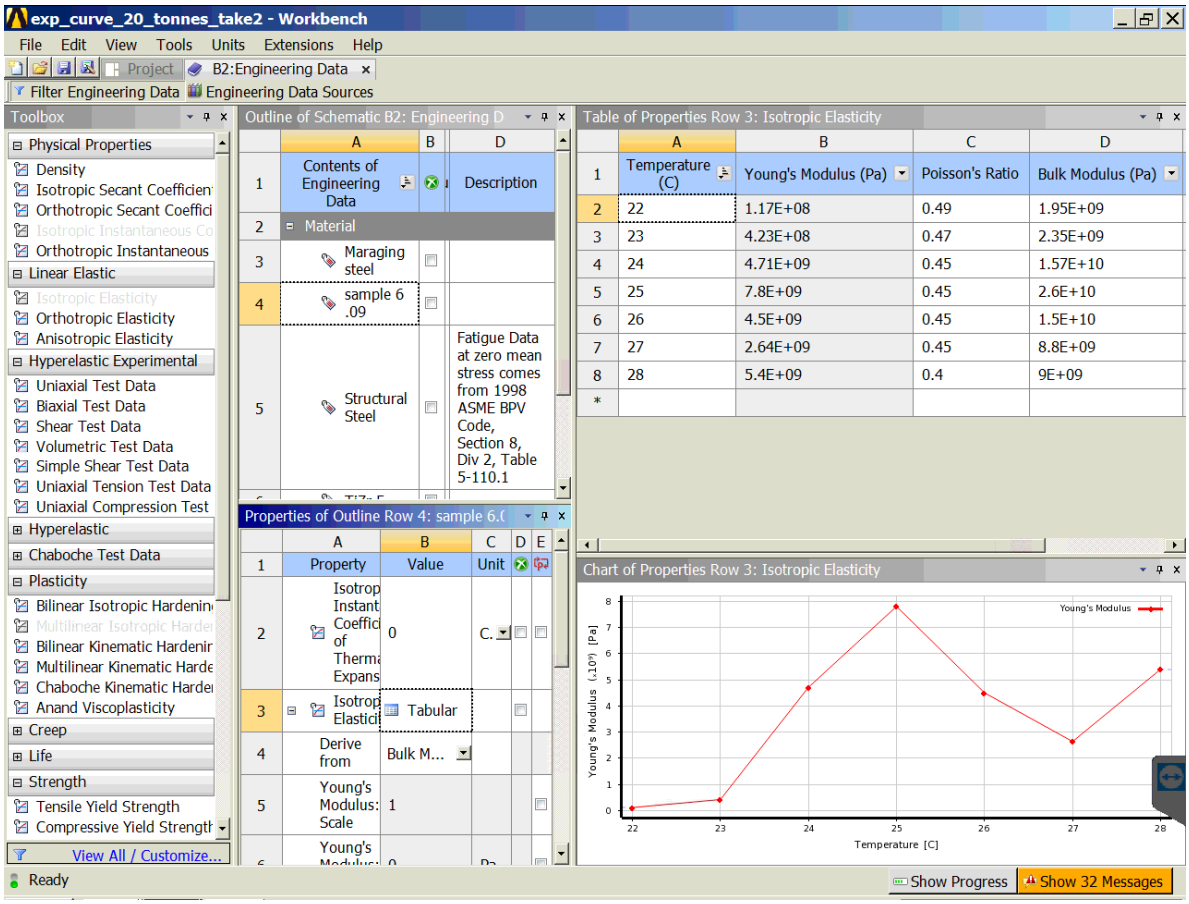

Figure 4.8. ANSYS engineering data for compressed liquid water models (0 - 0.979 GPa). A series of time and force steps (Table 4.4 and next Figure) were synchronised with temperature and isotropic elastic data in order to model sample's pressure and molar volume at this pressure range.

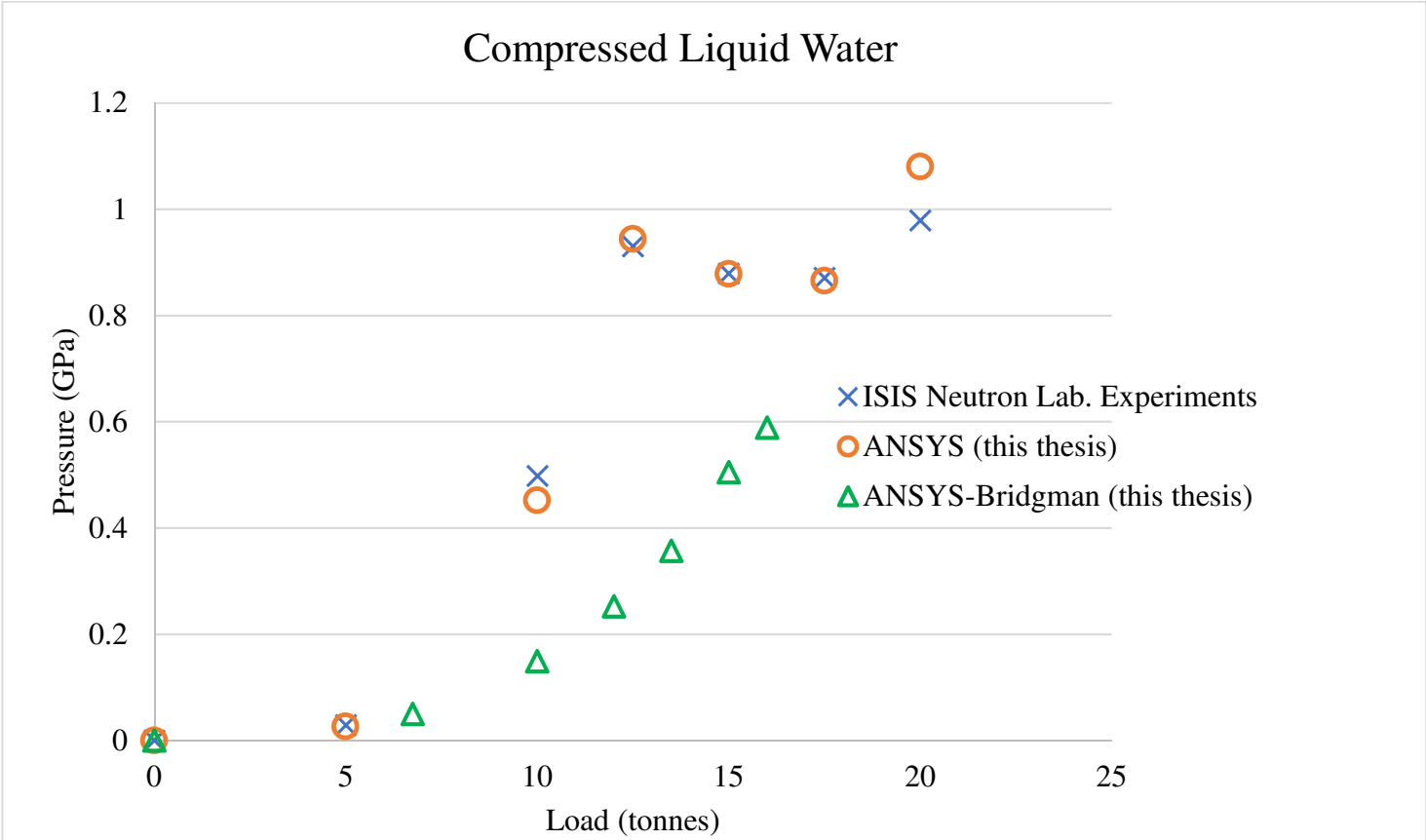

Figure 4.9. Loading curves for water from 0 to 1.08 GPa. Experimental data from ISIS Neutron Laboratory was accurately modelled via FEA. The broad phase transition from liquid water to Ice VI in the region of 12.5 to 20 tonnes is visible, as load increases and pressure remains quasi-stable. To numerically approach this phenomenon, bulk moduli was adjusted via FEA. The numerical loading curve from 0 to 0.588 from the previous section was also included for comparison purposes (named ANSYS-Bridgman in the graph).

At this stage important results can be discussed. Water pressure values for 10 - 20 tonnes range are close to solidification in ISIS experiments, when compared with Bridgman[234] and Grindley[235] data. At 10 tonnes, bulk moduli adjustment of 15.07 GPa matches with its peer for a load of 22.5 tonnes (Ice VI, to be analysed in Chapter 5). By connecting the literature reviewed with the numerical results obtained in this work, it is suggested that after 10 tonnes load the experimental sample in ISIS Neutron Laboratory experienced a sequence were both liquid water and Ice VI co-existed, with larger characteristics of Ice VI in the system. Bezacier[240] identified a similar behaviour in Ice VI – VII transition, of a broad nature as well.

Summarised in Table 4.5, molar volume FEA results were obtained and benchmarked with data from the selected references. The sudden pressure increase detected at a load of 10 tonnes in ISIS liquid water data is directly relatable with a large drop in molar volume. Its molar volume vs pressure pattern does not decrease as progressively as in Bridgman[234] and Grindley[235] cases. Figure 4.10 graphically illustrates these results.

A molar volume drop of ~11% can be established between liquid water extrapolated from Grindley[235] (0.979 GPa) and Ice VI (ISIS experiments, 1.29 GPa). This behaviour is similar when compared with a 9.44% molar volume decay detected in ANSYS for the ISIS liquid water sample between 10 and 15 tonnes load. In other words, this is further proof of how the fluctuation included in ISIS liquid water data can be linked with a rapid tendency to transform into Ice VI at lower loads.

Table 4.5. Molar volume FEA results and comparison with literature calculated data.

Load (tonnes)	Experimental Pressure ISIS (GPa)	Pressure ANSYS (GPa)	Molar Volume (ANSYS) cm^3/mol	Molar Volume Bridgman[234] cm^3/mol	Molar Volume Grindley[235] cm^3/mol	Molar volume FEA – Literature Difference (%)
0	0	---	---	18.05	18.06	---
5	0.029	0.026	17.58	17.84	17.83	1.42
10	0.498	0.452	17.38	15.68	15.66	11.01
12.5	0.93	0.944	17.25	---	14.76	16.85
15	0.879	0.878	16.63	---	14.82	12.22
17.5	0.871	0.865	15.62	---	14.84	5.27
20	0.979	1.09	15.56	---	14.71	5.79

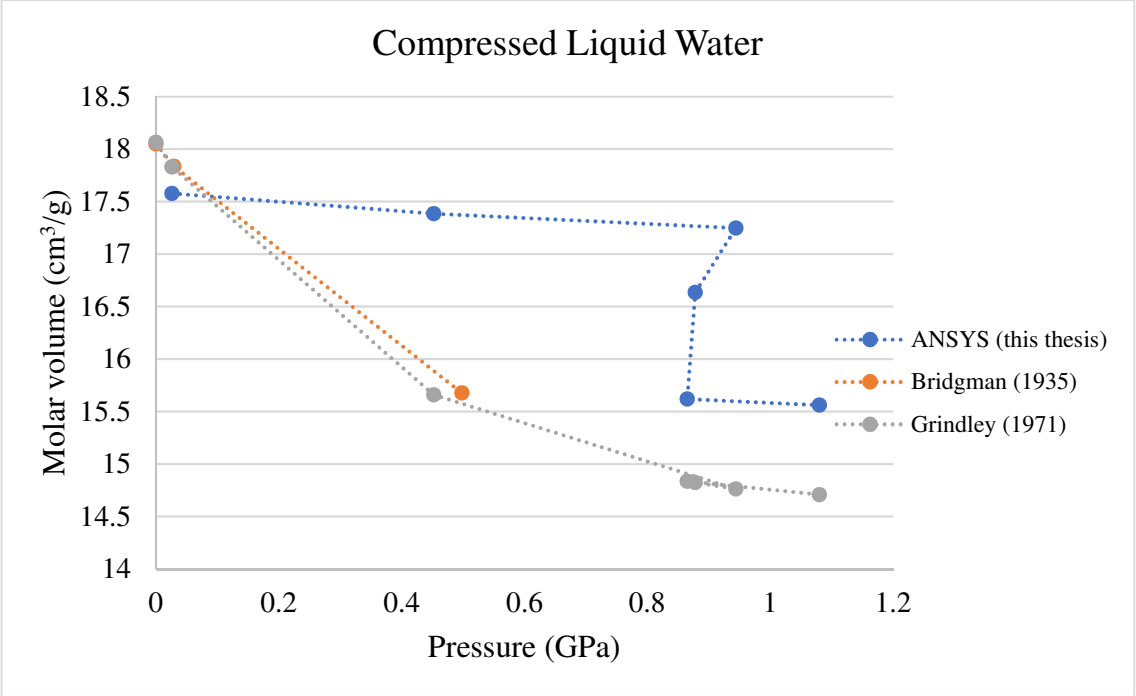

Figure 4.10. Molar volume vs. pressure curves for selected literature references (experimental) and the FEA model established in this thesis. As the ANSYS model follows the ISIS experimental data, it is possible to observe a large molar volume drop after 0.944 GPa, with pressure values also oscillating. This molar volume decrease estimated via FEA in ISIS experiments can be associated with a rapid transformation of liquid water into Ice VI due to the broad phase transition.

Results in this section are interesting from many perspectives. The FEA model was able to include a phase transition in the analysis, delivering an accurate behaviour in sample pressure. The gathered molar volumes show a natural distortion from the broad phase transition experimentally obtained, which allows a connection of these results with the facts observed in literature. Bulk moduli and Poisson's ratio values were estimated for the phase transition case. This shows the versatility of the FEA method to examine a compressed sample, obtaining in a convenient manner data which can prove difficult to gather or estimate experimentally.

4.4 Modelling of Compressed Liquid Water at 1 GPa

According to the water's pressure – temperature phase diagram (Figure 2.19), the highest pressure point for room temperature liquid phase is ~1 GPa. As demonstrated, a broad phase transition can cause difficulties obtaining liquid water at this point in certain experimental arrangements such as the one studied in this thesis. The FEA model designed here can be adjusted for results at this specific pressure point, delivering interesting outcomes. Section 4.3 showed how a load of 20 tonnes corresponds to a sample pressure of 1.09 GPa in the model. A multilinear bulk moduli approach was established, effectively reproducing the sample's behaviour at variable pressure. These types of models will be named *Type I* in this section.

Moreover, there are engineering cases focusing on how a sample behaves in terms of pressure, transmitting stress to adjacent instrument components. Due to the static structural nature of the FEA model, *Type II* category (in this section and the following Chapter) is ideal when a final stress state is required. ANSYS' engineering data requires bulk moduli and Poisson's ratio only at a target pressure, not including the entire set of bulk moduli of previous pressure steps. Chapter 5 details their use in stress and failure studies in ZTA anvils, gaskets and other PE press elements. Although FEA sample pressure modelling is accurate, volume analysis is secondary. The following paragraphs assess both models for this specific case (~1 GPa), establishing advantages and disadvantages in their use.

4.4.1 Type I Models

These types of models have been widely considered in this Chapter, having successful results with their use at this point. Section 4.2 and 4.3 described how *Type I* models incorporate a matrix with isotropic elastic sample properties at variable load, synchronised with temperatures and time to simulate compressed liquid water behaviour in a static structural ANSYS model. At 20 tonnes load, FEA closely approaches the highest pressure that room temperature liquid water can experience (~1 GPa as mentioned). Its pressure (1.09 GPa) and molar volume (15.56 cm^3/mol) approximate extrapolated literature values as seen in Table 4.5. Developing a punctual analysis about hydrostatic conditions in this model, it is possible to observe in Table 4.6 how stress values oscillate on the FEA sample (±0.26 GPa).

Table 4.6. Maximum and minimum principal stress values at each node of the liquid water sample at 1 GPa (Type I model).

Node Number	Minimum Principal Stress (GPa)	Maximum Principal Stress (GPa)
912	-1.08	-1.00
913	-1.35	-1.16
914	-1.10	-0.99
915	-1.19	-1.05
916	-1.08	-1.06
917	-1.11	-1.09
918	-1.08	-1.04
919	-1.12	-1.07
920	-1.09	-0.99
921	-1.07	-1.04
922	-1.27	-1.10
923	-1.22	-1.13
924	-1.14	-1.02
925	-1.09	-1.02
926	-1.15	-1.06
927	-1.10	-1.08
928	-1.07	-1.06
929	-1.12	-1.08
930	-1.10	-1.05
Average	-1.13	-1.06
Global average	-1.090	
Standard deviation	0.0738	0.0452

4.4.2 Type II Models

Figure 3.11 illustrates how in ISIS experiments ~1 GPa occurs approximately between 20 and 22.5 tonnes load. Employing the static structural (implicit) solver in the FEA model, the target pressure requires to input bulk modulus and Poisson's ratio for liquid water properties at 1 GPa. Initial bulk modulus was extracted from literature as seen in Table 4.4 (7.22 GPa). With this information, numerical results between 20 and 22.5 tonnes were generated.

By tuning bulk modulus to a value of 6.64 GPa, the model produces a quasi-hydrostatic sample pressure of 1 GPa at 21.5 tonnes load. Bulk modulus is slightly smaller when compared with data obtained from literature, this difference being attributable also to the explained instabilities from liquid water to Ice VI.

As discussed earlier, coarse mesh improves hydrostatic conditions across the modelled sample. Figure 4.11 provides a comparison between both coarse and fine mesh at the sample area, where scales in the images show how compressive stress oscillates. Average compressive stress value across the sample is practically equal for both models (-1.00 fine and -1.01 GPa coarse model). Figures 4.12 and 4.13 show the minimum and maximum principal stress distribution at the sample, showing its quasi-hydrostatic conditions. Table 4.7 shows each node stress value, showing a remarkable 99% of hydrostaticity.

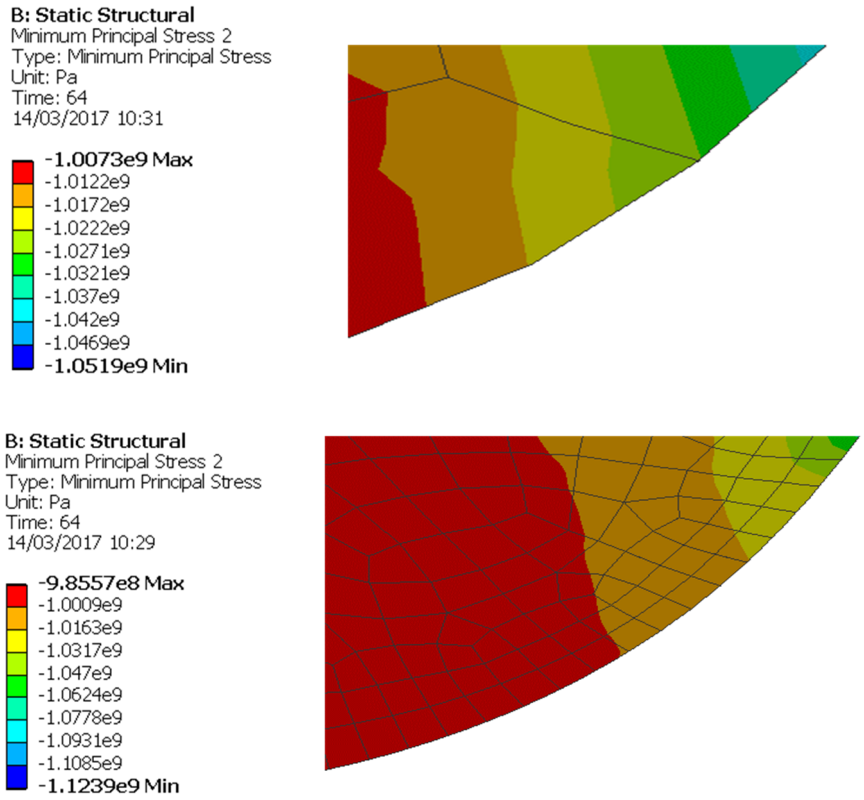

Figure 4.11. Liquid water FEA results at 1 GPa. Comparing mesh configurations (coarse and fine), it is noticeable how coarse mesh helps to obtain results with higher hydrostatic conditions.

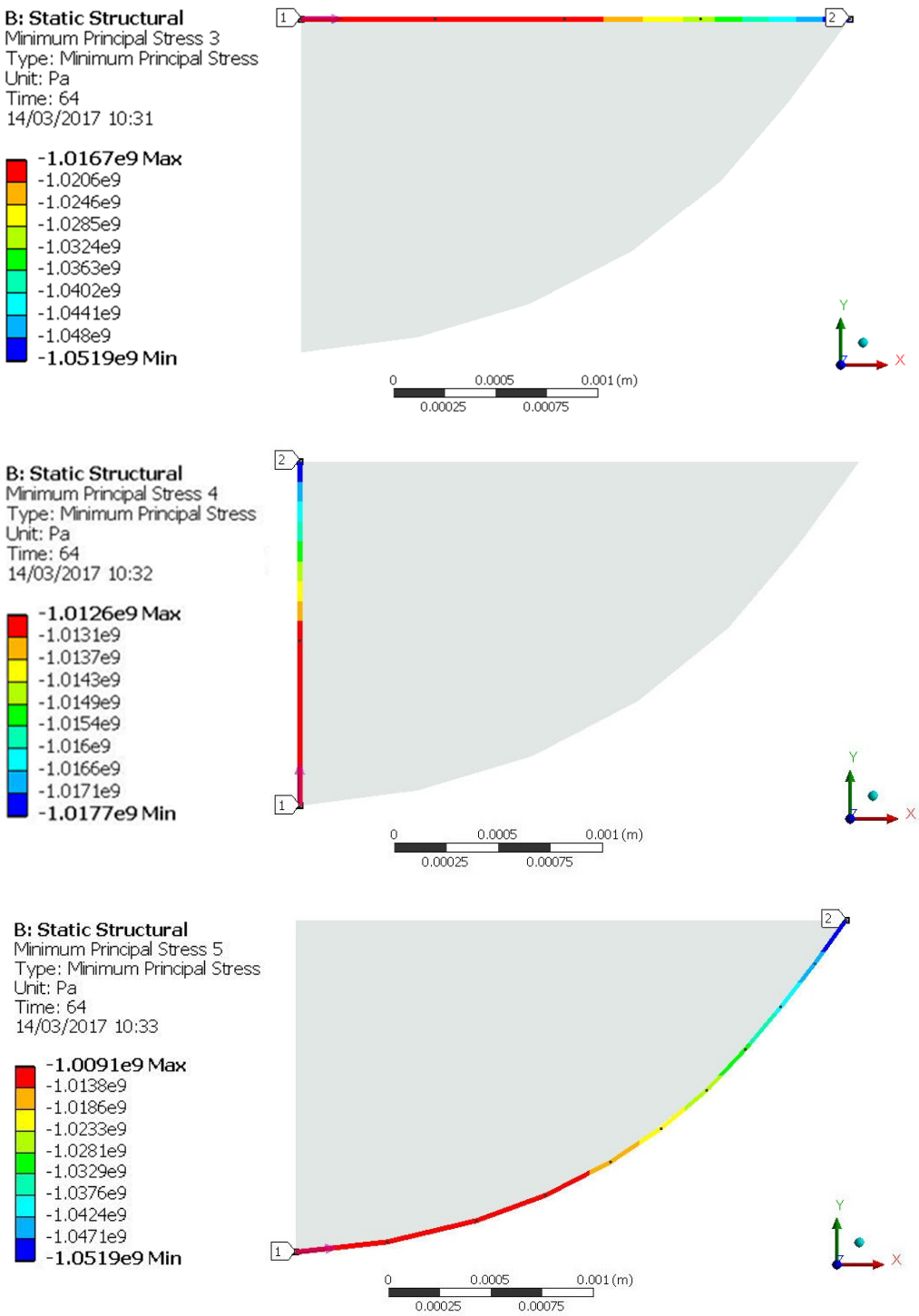

Figure 4.12. Minimum principal stress FEA results of liquid water at 1 GPa. In order to assess hydrostatic conditions, contour paths were studied at the compressed liquid water sample on a ZTA toroidal anvil. The scale on the left shows how the variance between pressure values is minimal.

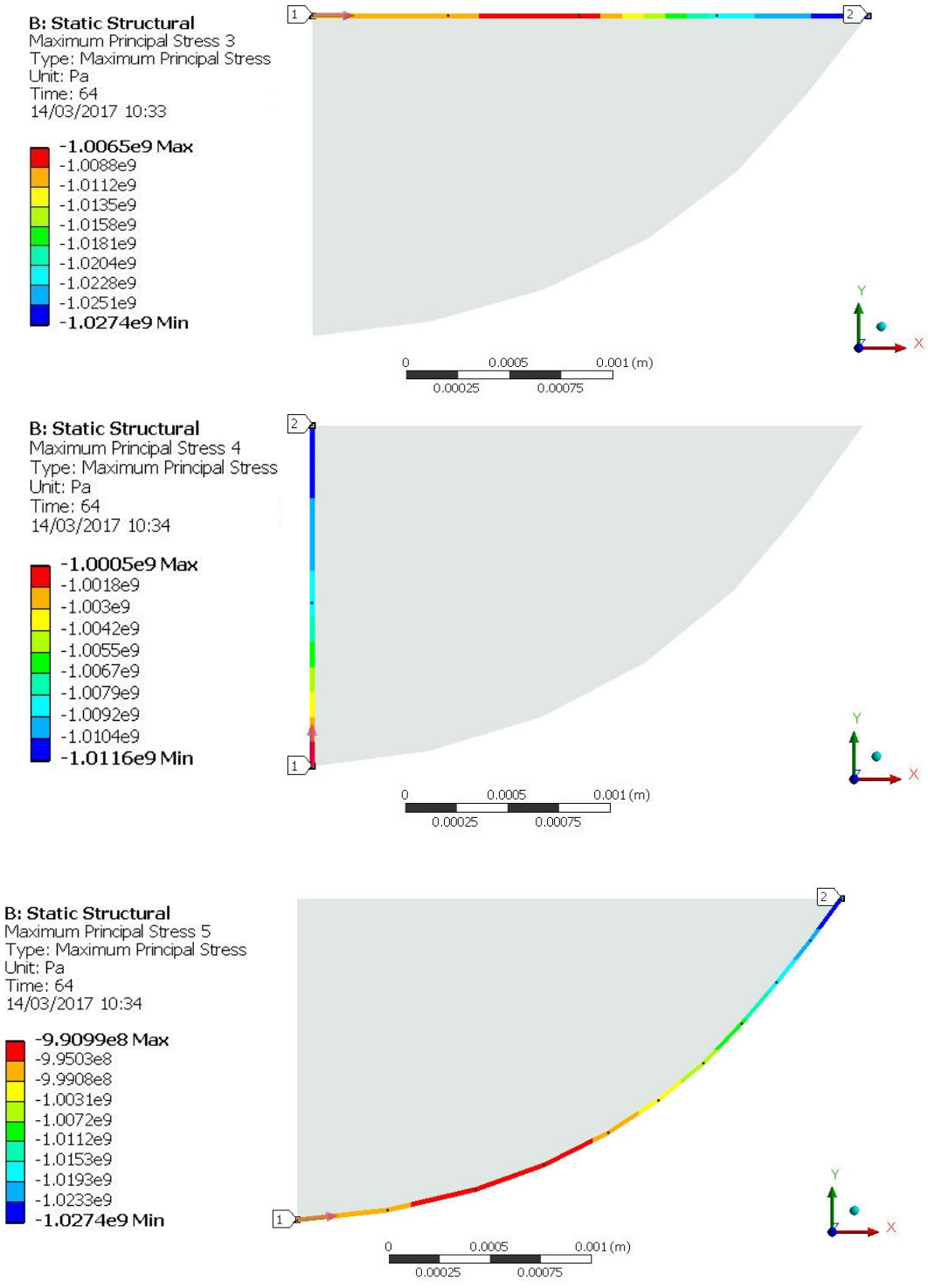

Figure 4.13. Maximum principal stress FEA results of liquid water at 1 GPa. Multiple paths at the sample area were studied at the compressed liquid water sample on a ZTA toroidal anvil. The scales demonstrate how the oscillation between pressure values is minimal.

Table 4.7. Maximum and minimum principal stress values at each node of the liquid water Type II model at 1 GPa.

Node Number	Maximum Principal Stress (GPa)	Minimum Principal Stress (GPa)
1	-1.000	-1.013
2	-1.030	-1.052
3	-0.989	-1.008
4	-1.010	-1.027
5	-1.010	-1.018
6	-1.010	-1.017
7	-1.000	-1.010
8	-1.010	-1.014
9	-0.995	-1.010
10	-1.010	-1.013
11	-1.020	-1.039
12	-1.020	-1.030
13	-0.998	-1.017
14	-0.998	-1.007
15	-1.010	-1.020
16	-1.010	-1.017
17	-1.010	-1.012
18	-1.010	-1.014
19	-1.000	-1.011
Average	-1.007	-1.018
Standard Deviation	0.010	0.011

The use of Poisson's ratio values of 0.49 and 0.45 did not affect pressure and hydrostaticity results of the sample in the *Type II* model. A change in molar volume was detected upon changing value, as presented in Table 4.8. In comparison to earlier cases, mesh in the gasket had to be decreased even more in order to reach such a high hydrostatic level in the sample. Other mesh configurations directly influenced results. As explained, TiZr gaskets have a thickness of 0.66 mm. Figure 4.14 illustrates mesh selected at this area.

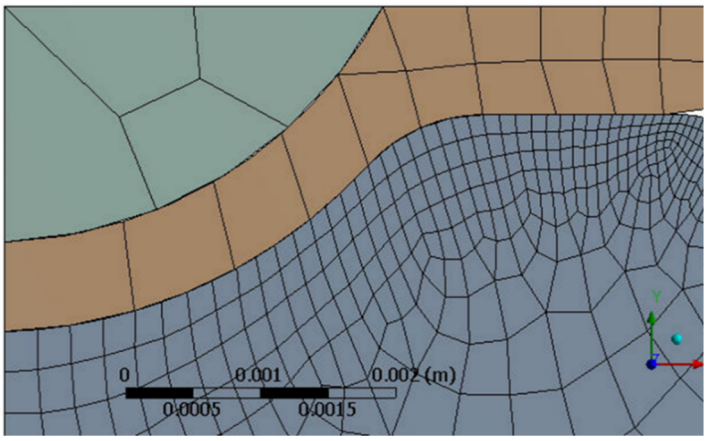

Figure 4.14. Mesh configuration at gasket, sample and surrounding areas for the FEA model of compressed liquid water at 1 GPa. Coarse mesh has proven effective on maintaining hydrostatic conditions at the sample.

Having proved successful and versatile on many fronts, the FEA model and methodology delivered by this thesis can pursue an extreme pressure value in liquid water. FEA has demonstrated to be a convenient tool examining conditions difficult to obtain in-situ.

4.4.3 Remarks

In synthesis, it is possible to observe how *Type I and II* models have particular styles and uses, depending on the scrutiny required. In *Type I* models, molar volume can be numerically calculated with high levels of accuracy when compared with literature values (Tables 4.3 and 4.5 provide details). Oscillations in hydrostatic conditions attained can be attributed to the presence of both liquid and solid phases in the sample. It was noticed how these variations increase with pressure.

Type II models have advantages modelling a sample with higher hydrostatic conditions and pressure extremely close to a target. However, these models are not suitable for precise molar volume calculations. The use of hydrostatic elements and dynamic solvers as explained in Chapter 7 is the next step towards improving accuracy in the models. Table 4.8 summarises and compares hydrostatic conditions and molar volumes for both types of FEA models.

Table 4.8. Comparison between FEA model versions (Type I and II). Liquid water pressure of 1 GPa.

Model Type	Molar volume (ANSYS) cm^3/mol	Molar volume (cm^3/mol, see Table 4.5)	Maximum Standard Deviation (GPa, hydrostatic conditions)
Type I	15.56	14.70	0.0738
Type II (Poisson's ratio 0.49 / 0.4)	16.75 / 16.50		0.011 / 0.018

While assessing mechanical stability of ZTA toroidal anvils (to be discussed in Chapter 5), it has been discovered that modelling water's behaviour at high pressure is as equally as interesting. This Chapter established how, by adjusting specific parameters on an FEA model and using data from relatable experiments and literature, it is possible to study a sample under extreme conditions, achieving accurate numerical results and generating significant knowledge on a compound.

Employment of FEA methods for these endeavours opens new alternatives in materials science. Numerical outcomes were validated by literature and experimental data, proving that this technique has a high degree of adaptability during challenges such as simulating hydrostatic conditions and volumetric changes by including a temperature matrix.

As the presence of an extended phase transition was distinguished, it was noticed how experimental results have certain variance under different conditions. FEA allows to set those conditions and study liquid water at a specific point of the phase diagram, studying its behaviour and obtaining water's properties in regions which otherwise would be difficult to reproduce due to thermodynamic instabilities among other factors, which influence certain phase transition patterns. At the moment, there are no similar publications on the effects of high pressure in water via FEA, making this thesis an innovative work on a promising method.

Chapter 5

ZTA Toroidal Anvils Stress Analysis

Employing the FEA model established in this thesis, a rigorous examination on the stress conditions and failure of standard ZTA toroidal anvils under normal operative conditions are achieved in this Chapter. Relevant aspects such as Weibull modulus and massive support principle are included, towards finding precise results in this comprehensive study. Furthermore, due to the relevance of the water sample included in the model, a finite element pressure vs load assessment in Ice VI – Ice VII is produced. This is the first time, these water phases are studied via static structural FEA.

Numerical results collected are benchmarked with reports from ISIS Neutron Facility on standard ZTA anvils experimental damages, validating the analysis performed and understanding failure mechanisms. Results are important in order to establish guidelines in design and implementation of high pressure anvils for neutron diffraction with greater operative capacities.

5.1 Introduction

The FEA model developed in this thesis has been carefully examined in order to produce accurate results. Specific aspects of meshing, material properties, and contacts, among others have been investigated to produce effective results in compressed liquid water (Chapter 4). In this Chapter, the model is applied to analyse and provide new and fascinating insights into mechanical stress conditions of standard ZTA toroidal anvils under working loads.

To model ZTA toroidal anvils at high compressive loads with this method has interesting challenges, such as absence of plastic deformation, influence of massive support principle, Weibull modulus, and the effect of water phase transitions on the stress conditions of the anvils. This thesis defines and validates a failure criteria based on FEA results and evidence provided by ISIS Neutron Laboratory, where standard ZTA anvils are of routine use.

In this Chapter, maximum and minimum principal stresses as well as maximum shear stress have been carefully chosen as the main focus of analysis. Principal stresses characterise the extreme values of normal stress (tensile and compressive) registered in the anvils and adjacent elements. In other words, this project was able to obtain via FEA peak stresses registered above ZTA strength as well as their location, linking them with proofs of damage to establish failure criteria.

Toroidal anvils are designed to undergo heavy compressive loads, leading to phenomena such as localised buckling, bending and lateral expansion inducing tensile and shear stress in various parts of the anvil[65]. Shear stress is also present at the anvil-gasket interface as a consequence of gaskets deformation, laterally pulling neighbouring ZTA material.

Ceramic nature of ZTA involves a large disparity between tensile (290 MPa) and compressive (4.7 GPa) strengths. Due to the massive support principle, ZTA strength values are not possible to directly connect with stress peaks generated in operational conditions. ISIS Neutron Laboratory reports failure in standard ZTA anvils starting from 75 tonnes loads. This value will be considered as reference breaking point for the FEA stress and failure analysis, following a conservative approach.

5.2 FEA of ZTA Anvils with Ice VI and VII

Chapter 4 elucidated how the static-structural FEA model produced in this thesis successfully modelled a series of compressed liquid water pressure steps for a range of 0 – 1 GPa approximately. *Type I* models accurately simulated water static pressure and molar volume steps while a *Type II* model was in charge of studying sample pressure behaviour, centring its analysis in stress transmission to adjacent elements such as gaskets and ZTA anvils. This being a relevant aspect in stress and failure analysis of standard ZTA anvils, sample properties were adjusted to reproduce the rest of the experimental water loading curve obtained in ISIS for this thesis via *Type II models*. This includes pressures up to 5.38 GPa with water phase transformations into solid Ice VI and VII.

Studying water's rich phase behaviour via computational FEA is stimulating for numerous reasons. This is the first FEA work in high pressure instruments which also has a focus on a compressed sample, opening a new and powerful alternative to high pressure research. Including the stress analysis realistic liquid-to-solid phase transitions is extremely beneficial, to validate and understand its influence on the stress behaviour of ZTA anvils and other high pressure components at each load step.

ISIS experimental data for solid water phases include lattice parameters and its evolution according to pressure. From this data, it is possible to generate equations of state for Ice VI and Ice VII, obtaining relevant information for the models such as bulk moduli and multilinear isotropic hardening data. Appendix 1 details calculations developed to obtain these relevant numbers while Table 5.1 summarises bulk moduli data for each experimental pressure step for 1 – 6.3 GPa pressure range. Poisson ratio value for Ice VI and VII has been reported in literature[289,290] with values of 0.3. Chapter 3 showed how this data is input in ANSYS (Figure 3.14).

Chapter 2 and 4 made reference to the broad nature of the phase transitions analysed in this thesis. ISIS experimental loading curve (Figure 5.1) shows areas where water pressure remains quasi-stable regardless of a load rise (30 - 37.5 tonnes). This outcome can be linked with a rapid increase in density at the Ice VI – Ice VII phase transition regions, similar to liquid water – Ice VI case explained in Chapter 4. This co-existence of phases (with unknown proportions) can be influenced by factors such as thermodynamic

fluctuations, sample impurities, surface irregularities, and others allowing different experimental results for similar load conditions. Illustrating this phenomena, experimental data displays a rapid pressure increase at lower loads (0 – 0.979 GPa, 0 to 20 tonnes) when compared with data of similar nature and pressure range by Bridgman[234] (also included in Figure 5.1).

As anticipated, the density oscillation described introduces a difference between ISIS experiments and FEA sample pressure results in phase transition areas. The set of equations employed to obtain water's bulk moduli in Appendix 1 do not contemplate the co-occurrence of phases present in the experimental curve.

Having a target sample pressure for the FEA models at the phase transition area, bulk moduli was adjusted to estimate its value in particular cases via FEA. Table 5.1 shows bulk moduli values as calculated and its associated adjustment to match experimental sample pressure. Bulk moduli does not need further amendments in areas where a specific water phase is stable (45 tonnes load and beyond). FEA sample pressure results match experimental data avoiding adjustments in these segments.

Figure 5.1 displays the FEA reproduction of the experimental loading curve, showing the versatility of this numerical methods. Liquid water values were included to show the entire sequence of simulations and experimental – literature data. As mentioned earlier, ISIS experiments had a 60 tonnes limit to preserve components. Data at 75 and 80 tonnes was extrapolated to further study ZTA anvils stress conditions.

Estimations of bulk moduli in Ice VI-VII transition areas demonstrate the high flexibility FEA methods offer. Experimentally finding bulk moduli in this particular loading curve segment can prove difficult and expensive. A global numerical – experimental pressure difference of 1.44% in Ice VI and 3.08% in Ice VII was obtained.

Similar to the case of liquid water, there are no current studies in static compressed Ice VI – VII via FEA. At this point, the FEA model has reproduced the sample properties correctly under high pressure at specific loads, allowing the accurately examination of the stress conditions of ZTA anvils and components at each experimental load. Numerical results in the following sections are of great significance, quantifying the stress

accumulation in critical area, precisely locating peak values along the ZTA anvil – gasket interface.

Table 5.1. Load, pressure and isotropic elastic data for room temperature water at variable pressure input in ANSYS for the FEA model reproduction of the experimental and literature loading curve.

Ice VI (ISIS Neutron Laboratory)					
Load (tonnes)	Pressure (GPa)	Pressure ANSYS	Isotropic Linear Elastic Bulk Moduli (GPa)	Bulk (adjusted in ANSYS, GPa)	Poisson's Ratio
22.5	1.290	1.28	15.071		0.3
25	1.533	1.58	21.342	17	
27.5	1.871	1.89	26.476	20	
30	2.062	2.04	30.257	20	
32.5	2.068	2.04	30.028	20	
Ice VII (ISIS Neutron Laboratory)					
35	2.068	2.13	22.934	17	0.3
37.5	2.210	2.12	25.576	15	
40	2.772	2.95	28.336	25	
45	3.475	3.69	33.088		
50	4.124	4.22	37.181		
55	4.775	4.72	40.881		
60	5.380	5.18	44.326		
75	6.439	6.35	50.898	Extrapolated data	
80	6.704	6.70	52.119		

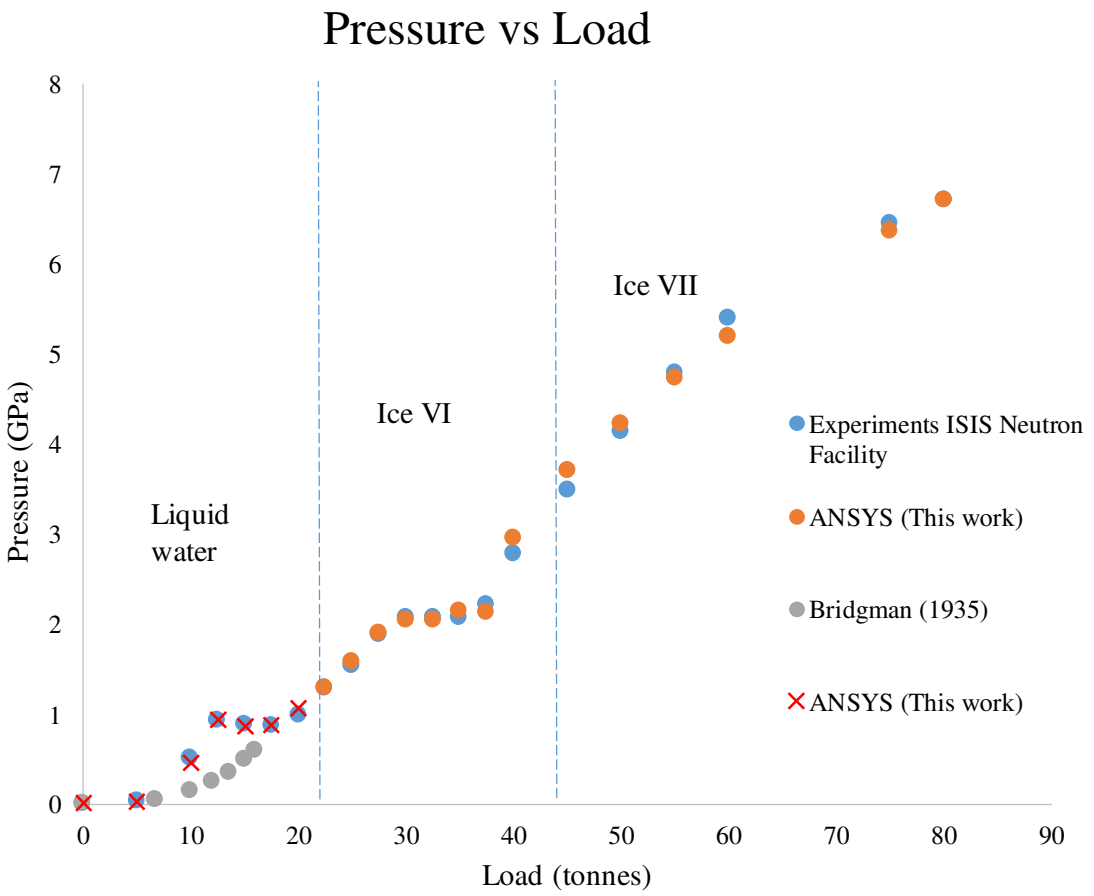

Figure 5.1. Numerical, experimental (ISIS Neutron Laboratory) and literature loading curves for water (0 – 80 tonnes). It is possible to observe how the FEA model of a standard ZTA anvil developed in this thesis correctly adjusts pressure data from various sources. For Ice VI and VII cases, each pressure step delivers information on stress conditions of the high pressure anvils, gaskets and components. This is of interest for stress and failure analysis of ZTA anvils and further optimisation. Data at 75 and 80 tonnes is extrapolated.

5.3 ZTA Toroidal Anvils Stress Analysis

Numerical results gathered at this point provide a comprehensive stress data collection in ZTA anvils and adjacent components at multiple static load steps. As the anvils are subject to both massive support principle and Weibull theory, an interesting challenge in stress analysis and design its formulated in this project. Section 2.4.1 explained that the massive support principle allows strength limits to be surpassed in high pressure anvil configurations (strengthening factor), while the Weibull theory[308,309] refers to an

oscillation in the rupture stress of ceramics due to the distribution of inner flaws (not having precise limits as in the case of ductile materials).

ZTA ceramic nature introduces a disproportion between tensile (290 MPa) and compressive (4.7 GPa) strengths. As these points can be exceeded in the system, a failure criteria methodology must be tailored for standard ZTA anvils. Failure theories in brittle materials such as the Maximum Normal Stress Theory concentrate on how a component resists compressive or tensile stress up to its specific strength value[62]. This thesis combines FEA stress data with experimental evidence to understand and establish realistic strength limits, accounting important phenomena in ZTA which allows surpassing of strength parameters.

Remarks about the massive support principle and Weibull theory in this Chapter also want to create awareness on significant aspects of design and stress analysis via FEA. At extreme conditions, these processes must be done in parallel with clear evidence and good interpretation of literature sources. As mentioned, in a brittle material conventional criteria would predict failure in a region with stresses beyond strength limits. Cutting edge ceramics and special applications need to assess other interactions and experiences.

In standard ZTA anvils, failure has been documented at loads from 75 tonnes. This section delivers a comprehensive stress and failure analysis at this load for a conservative approach. At the moment, there are no strengthening factors reported for ZTA in literature. While there is a strong presence of compressive stress across the anvil's body due to working loads, these forces lead to phenomena such as bending and lateral expansion inducing tensile and shear stress in different zones[62,67]. Tensile and shear stresses also occur at the anvil-gasket interface as a result of gaskets deformation, pulling laterally ZTA material.

As mentioned, this PhD thesis selected maximum - minimum principal stress and maximum shear stress as the main examination parameter. It is possible to correlate peak stress values obtained via FEA with laboratory evidence of failure. As reviewed in Chapter 2, principal stresses represent the highest values of normal stress recorded in the anvils[67].

To preliminary determine areas of high stress concentration, principal stresses have been reviewed across the anvil for the 75 tonnes case. Figure 5.2 shows the maximum principal stress state of the anvil. As tensile stress values here represent the highest in the anvil, areas of tensile stress concentration are annotated. On the higher right side of the anvil, it is possible to see how tensile stress gathers, with approximated maximum values of 300 MPa. This accumulation can be linked with local bending on the anvil's body, produced by the binding ring press fitting. Similarly, it is possible to identify important tensile stress accumulations in the toroid region (anvil-gasket interface). Values from ~500 MPa to ~1 GPa are registered due to gasket's deformation, as it pulls the anvil laterally causing shear stress.

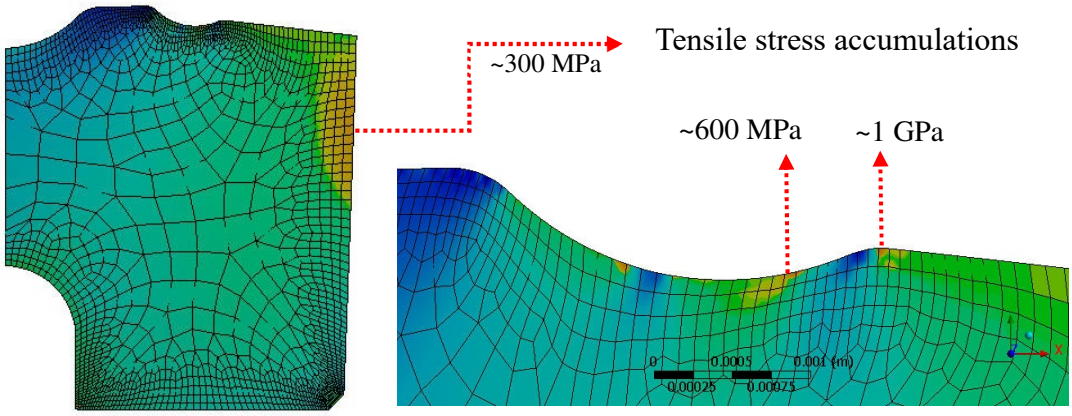

Figure 5.2. FEA maximum principal stress results for a ZTA anvil at 75 tonnes axial load (6.35 GPa sample pressure). Factors as bending and lateral expansion, produced by axial loads, trigger the appearance of tensile stresses. At the anvil-gasket interface, tensile stress values are linked with yield of gasket material. The numerical values annotated in this Figure correspond to the areas with the highest tensile stress concentration in the anvil.

Meanwhile, minimum principal stress FEA results, also at 75 tonnes load, are shown in Figure 5.3. Across the anvil's body, certain regions experience large compressive stresses due to the nature of the ZTA anvils operation, such as the sample chamber vicinity (-14 GPa), beam aperture (-3.5 GPa) and chamfer area (-4.5 GPa). As explained, the relationship between peak compressive and tensile stress values and ZTA strength is not

immediate because of the massive support principle, allowing larger stress values than the material's strength.

Apart from visualising the mesh selected for the ZTA anvil (refined at the edges and coarse at the core) in Figures 5.2 and 5.3, it is possible to identify three regions where tensile and compressive stresses register the highest magnitudes. Anvil's beam aperture, chamfer and toroid area which are now considered critical areas (where failure is highly likely to initiate). As seen in Chapter 2, these areas can also be associated with top shear values across the anvil. Figure 5.4 describes its distribution along the anvil's body.

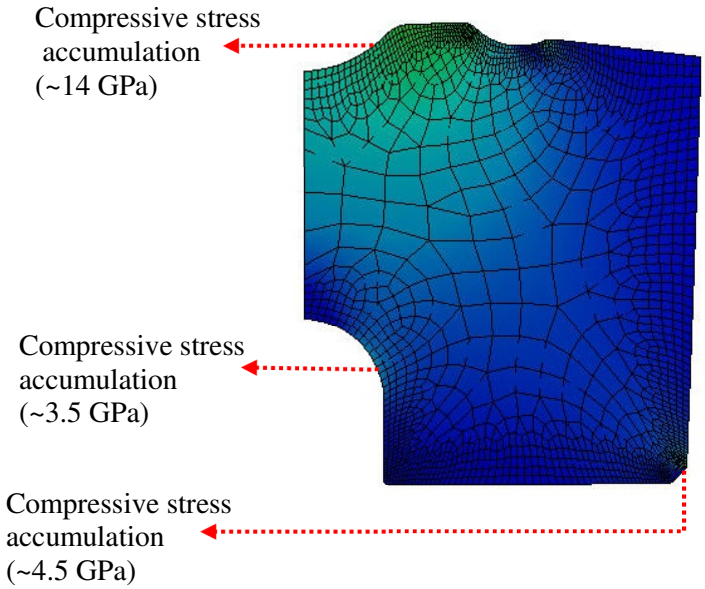

Figure 5.3. FEA minimum principal stress results for a ZTA anvil at 75 tonnes axial load (6.35 GPa sample pressure). Due to the nature of its operation, it is possible to observe high compressive stress values across the entire anvil. Regions near the sample chamber and the toroid register values beyond ZTA compressive strength (4.7 GPa). Numerical values annotated in the diagram show high compressive stress concentration regions.

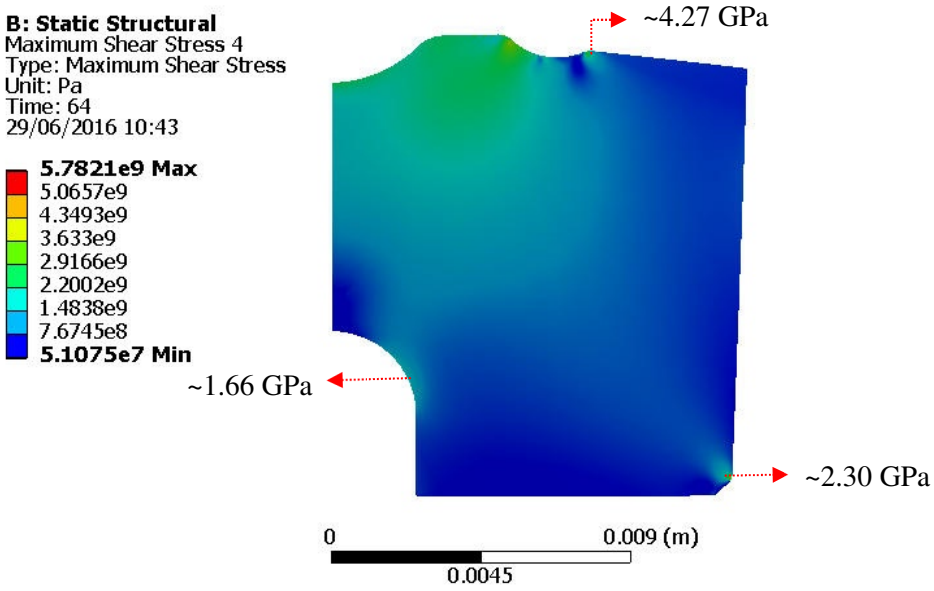

Figure 5.4. FEA maximum shear stress results for a ZTA anvil at 75 tonnes axial load (6.35 GPa sample pressure). Axial loads produce bending and lateral expansion, causing the appearance of internal shear stresses. The numerical results annotated correspond to the areas with the highest shear stress concentration.

Having identified critical areas in the standard ZTA anvil (toroid area, beam aperture and chamfer), a detailed study to precisely know magnitudes and locations of potentially damaging stresses is required. By connecting FEA results with physical evidence, the following sections establish criteria in standard ZTA anvils operational performance and mechanical failure.

5.4 Stress Analysis at ZTA Toroidal Anvil-Gasket Interface

Complex phenomena occurring at the anvil-gasket interface causes high stress accumulation at this region. As explained, large deformation rates induced in the gasket produce lateral forces, introducing tensile and shear stress in the toroid area. Adding this to the compressive stress values registered in the anvil due to its working nature, high shear stresses can be expected[62,67]. Figure 5.5 illustrates maximum shear values on this area, revealing how top stress values are registered at the toroid's area of the anvil-gasket interface.

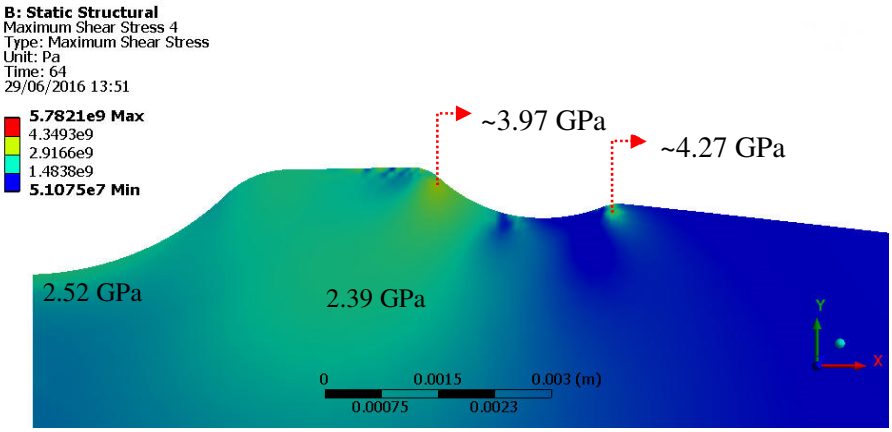

Figure 5.5. FEA maximum shear stress results of ZTA anvil-gasket interface, at 75 tonnes axial load (6.35 GPa sample pressure). This region has the highest shear stress values registered across the anvil (numerical results annotated), induced by gasket yield. A combination of high tensile and compressive stress will lead to areas of high shear stress.

For the analysis, an FEA path has been incorporated following the anvil-gasket interface. Implementing this feature in the model allows to find precise data on stress peaks and their position, being of great advantage towards linking this with failure evidence. Figure 5.6 illustrates the FEA path as well as reference names for segments (sample chamber area, toroid initial segment, and toroid final segment).

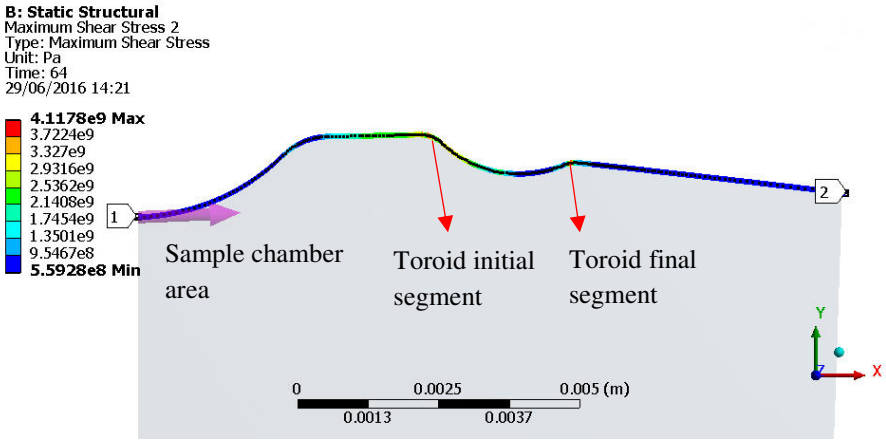

Figure 5.6. Illustration of FEA path at the ZTA anvil-gasket interface. By recording principals and shear stress results at the anvil-gasket interface, it is possible to obtain relevant information to associate with failure reported in this area. The arrow at the beginning of the path indicates the direction of the FEA data sequence (from 1 to 2).

Stress data collected at this FEA path deliver interesting results. Figure 5.7 portrays the minimum principal stress sequence for the anvil-gasket interface. It is noticeable how the highest compressive stress values (-14 GPa, located at 5.55 mm from the anvil's centre) is registered at the initial segment of the toroid, whereas the final segment (8.29 mm) reports another high compressive stress peak of -10.72 GPa. As explained before, massive support principle allows to reach compressive stress values higher than ZTA strength.

Additionally, it is possible to observe how a compressive stress peak suddenly evolves at 6.90 mm (toroid's bottom) for a 75 tonnes load (-7.40 GPa). While lower loads deform the TiZr ring and push it towards the toroidal cavity, large loads fill it which results in an increase of compressive stresses.

Figure 5.8 displays the graphs corresponding to maximum principal stresses. Tensile stress peak values of 1.10 GPa and 0.71 GPa on the toroid final segment are revealed on this evaluation. A 0.53 GPa tensile stress peak at 6.71 mm from the origin (middle part of the toroid) is also noticed, having similar origins than its compressive counterpart. Most of the anvil-gasket interface remains under compressive stress.

Figures 5.7 and 5.8 clarify how the toroid's initial and final segments are subject to high tensile and compressive stress, triggering high shear stress. Figure 5.9 shows in a clear manner the location (8.29 mm from the origin) and magnitude (4.27 GPa) of the highest shear stress value registered at the FEA path under scrutiny, located at the toroid final segment. This peak has a sudden evolution after 60 tonnes, caused by TiZr material filling the toroidal cavity and extending to the toroid final segment. Its magnitude is close to the shear stress peak located at the toroid initial segment (3.97 GPa, 5.55 mm), suggesting a high probability of failure in this point as well.

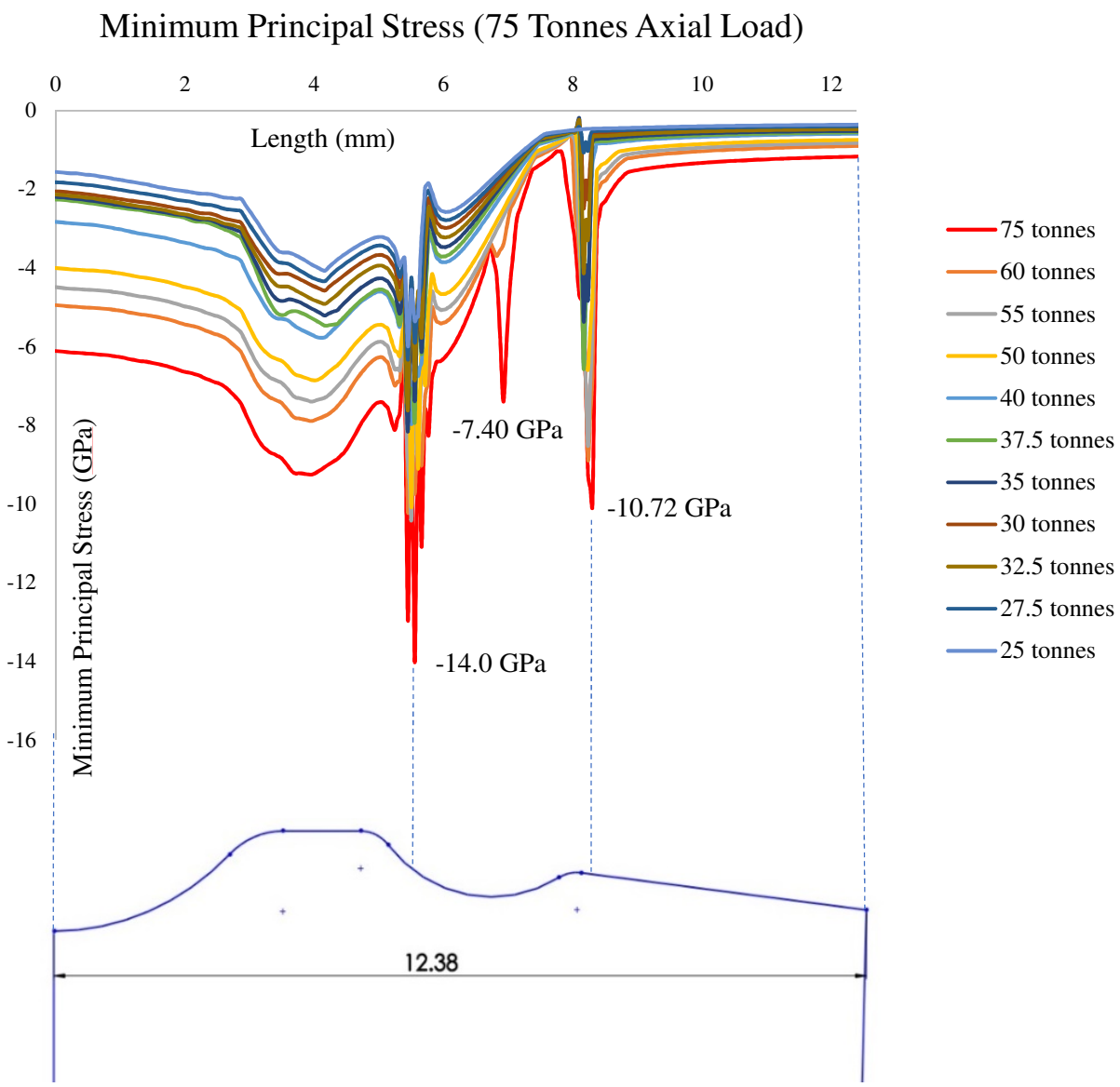

Figure 5.7. Evolution of minimum principal stresses at the ZTA anvil-gasket interface with experimental loads. It is noticeable how multiple values are up to three times beyond ZTA strength in compression (4.7 GPa). This is possible because the interface is supported by the gaskets, sample and the upper anvil (massive support principle). Areas at the toroid vicinity registered the highest compressive stress values as indicated in the graph.

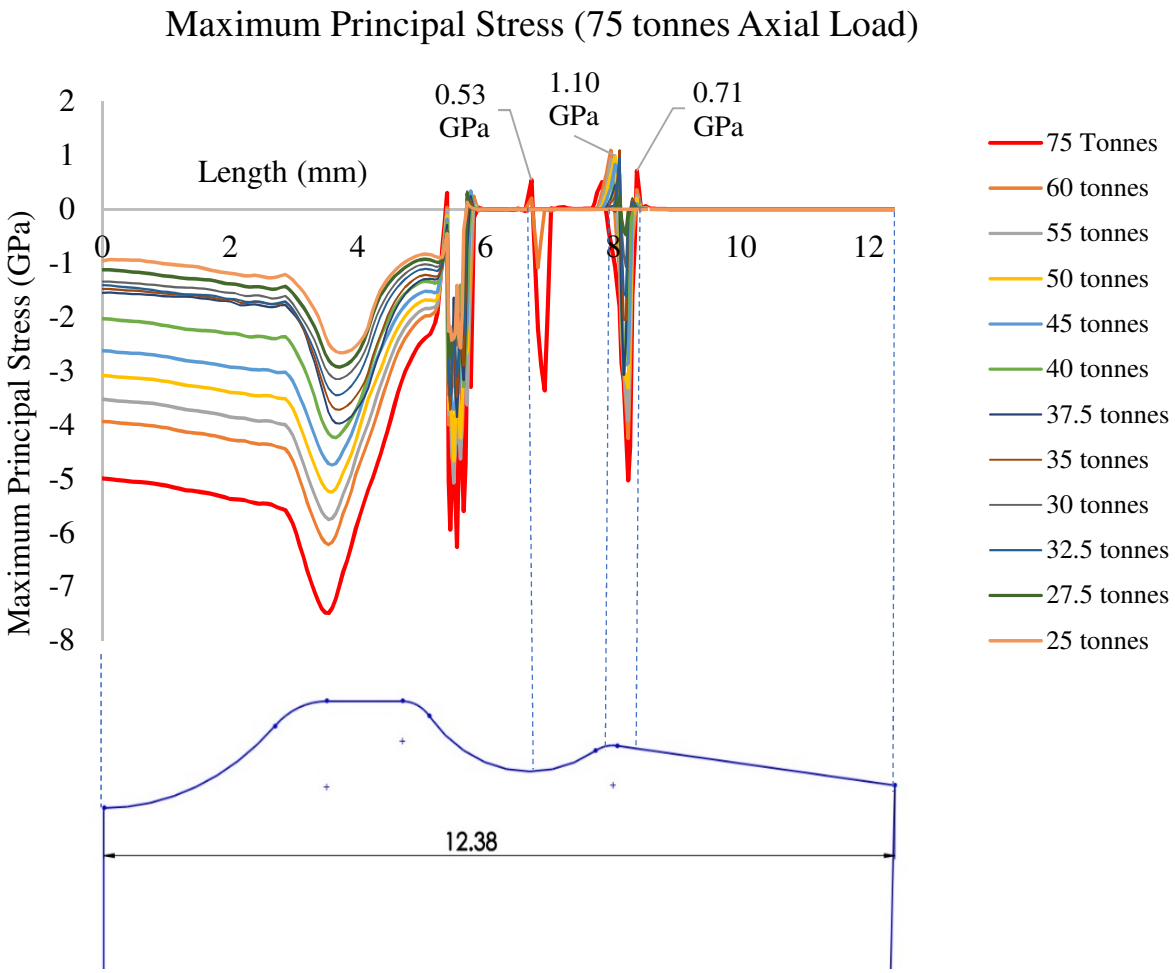

Figure 5.8. Evolution of maximum principal stresses at ZTA anvil-gasket interface with experimental loads. These values are key in the analysis process as ceramics are likely to fail due to tensile stresses. Most of the tensile stresses in this region are caused by the gasket's plastic deformation, laterally dragging ZTA. Values of 1 GPa are registered at 7.96 mm and 8.09 mm, surpassing ZTA strength in tension (0.290 GPa).

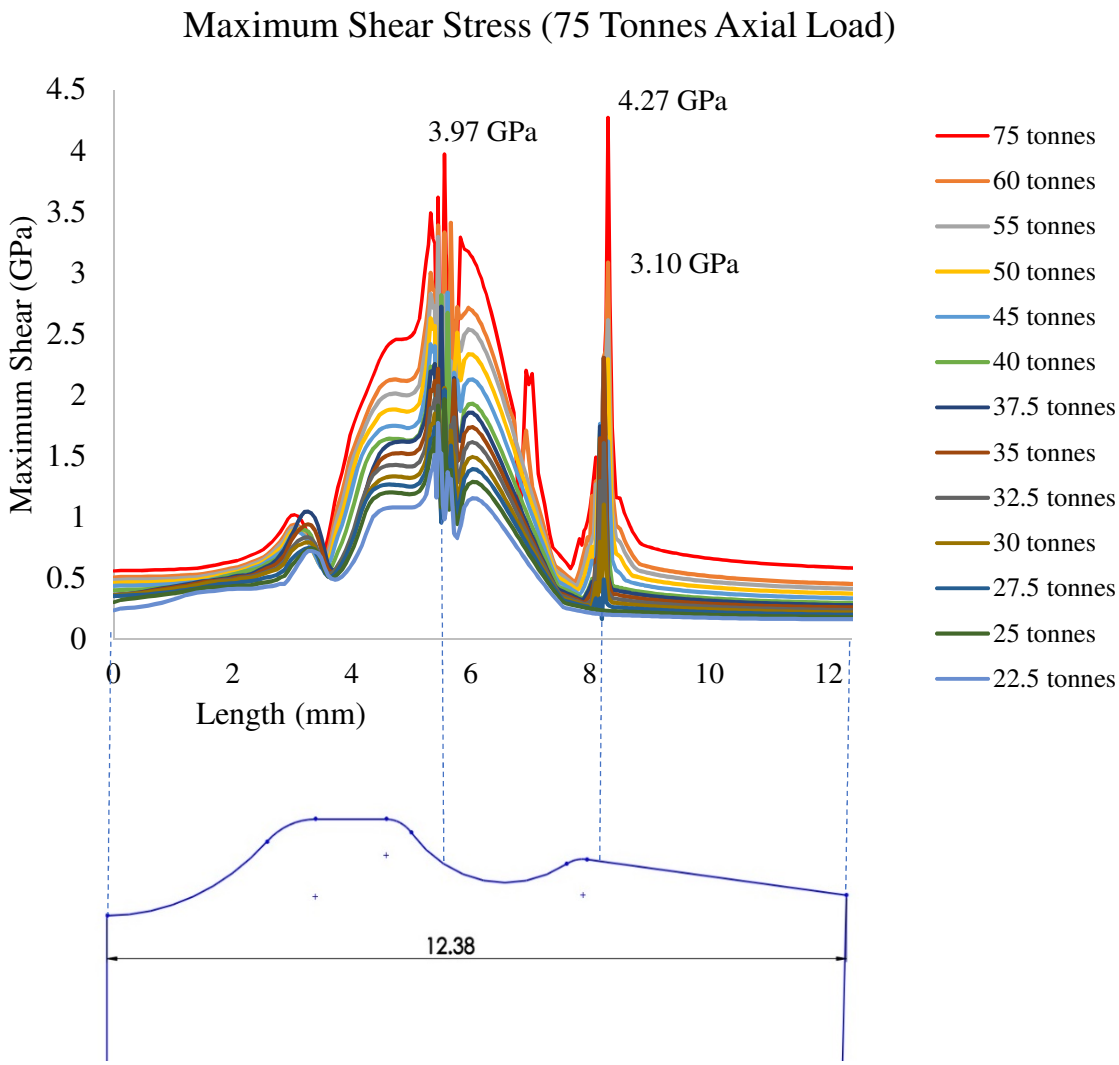

Figure 5.9. Evolution of maximum shear stresses at anvil-gasket interface with experimental loads. As areas near the toroid combine the highest values of maximum and minimum principal stresses across the entire anvil, they also experience the highest shear stress values recorded at this interface (4.27 GPa). It is noticeable how the peak at 8.29 mm has a disproportionate growth after a 60 tonnes load, representative of a high stress concentration area due to geometry and location. This is the exact point where failure has been reported. At 5.55 mm, another high shear stress point exists (3.97 GPa).

Summarising results from Figures 5.7 to 5.9, it is possible to state that failure has high probability to occur on the toroid's final segment, due to high shear stress concentration. Connecting this with laboratory evidence, Figure 5.10 shows the fragmentation (chipping) arising at the toroid final segment, caused by the shear stress peak of 4.27 GPa identified. The fracture location calculated by FEA at a distance of 8.29 mm from the sample chamber centre matches the documented failure events.

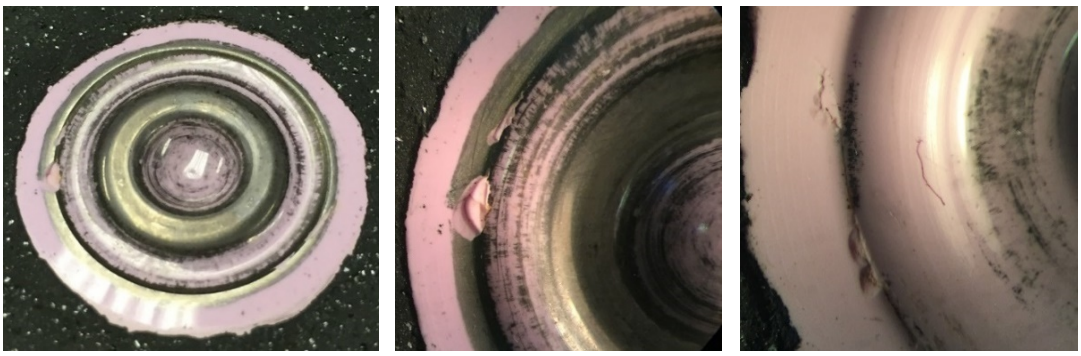

Figure 5.10. Failure evidence at the toroid area. It is possible to see a considerable detachment of material at the external segment of the toroid, as well as other marks of damage. Shear stress produced by the gasket's plastic deformation is responsible for this. The incidence of this event is lower when compared with failures at the beam aperture. Source: ISIS Neutron Laboratory.

Due to the high complexity of the anvil-gasket interface in this thesis, to develop a failure criteria in this area is not as direct as in other engineering cases. The use of Maximum Normal Stress Theory[62] with strengthening factors helps in the design of anvils following a conservative approach. It was visualised how, inside the toroid, tensile stress values of 1.1 GPa are acceptable at 60 tonnes while values of 0.71 GPa at 75 tonnes in the outer part of the toroid can be linked with failure. Relating peak tensile and compressive stresses registered via FEA in this interface with ZTA strength, it is possible to obtain a minimum strengthening factor of 2.6 and a maximum of 2.9. Employing the minimum value for a conservative approach, it is possible to say that tensile stress values surpassing 0.71 GPa at the toroid area risk the anvil's integrity. Chapter 6 offers further information on this critical area.

Shear limits in certain hard brittle materials are estimated slightly higher than their tensile strength. In example, cast iron shear strength is 1.3 times its tensile strength[154]. This FEA

study obtained a shear stress peak of 4.27 GPa, suggesting that ZTA's exceptional mechanical properties offer a shear limit of ~15 times its tensile strength (or ~5 including the strengthening factor of 2.6 previously explained). The shear stress peak found can also be related with ZTA's compressive strength (4.90 GPa), being slightly smaller (90%).

Laboratory reports mention how this fracture is not of regular incidence (but not of less importance), being secondary in occurrence when compared with fissures and cracks at beam aperture, analysed in the following section. It is important to remark that the plots involving a number of pressure steps in a waterfall style, start from 25 tonnes load for clarity and organisation purposes. Data from 5 tonnes is available from the analysis performed in liquid water (Chapter 4).

An interesting observation is worth to discuss in this section. The FEA results revealed specific portions of the TiZr gasket ring not subject to deformation at 75 tonnes load. In other words, the TiZr ring do not completely fill the toroid groove at the operative load limit, this being achieved at higher loads. The TiZr ring deformation pattern is shown in Figure 5.11 for 75 tonnes, having the same non-deformed portions pattern as in the case of 60 tonnes (experimental limit). Together with a middle gap, a non-deformed initial section is present.

To confirm the accuracy of numerical results concerning TiZr ring deformation, the gasket employed in ISIS Laboratory experiments was analysed under microscope. In the component, it is possible to observe a similar deformation tendency at the ring section. Figure 5.11 shows how both physical and FEA gasket initial section do not completely adapt to the toroid groove of the ZTA anvil. While the middle gap is minimal the initial, non-deformed section is clearly visible. It becomes crucial to take this into account in order to validate, once more, the FEA model developed during this project.

5.5 Stress Analysis at ZTA Toroidal Anvil Beam Aperture

The beam aperture region has also been catalogued as critical through the initial FEA analysis performed. Peak stress values have been detected at the edge of this area. The FEA path methodology employed for the anvil-gasket interface can be used in this region

as well. Figure 5.12 shows the FEA path at the beam aperture, where principal and maximum shear stress data was collected for the load range of interest.

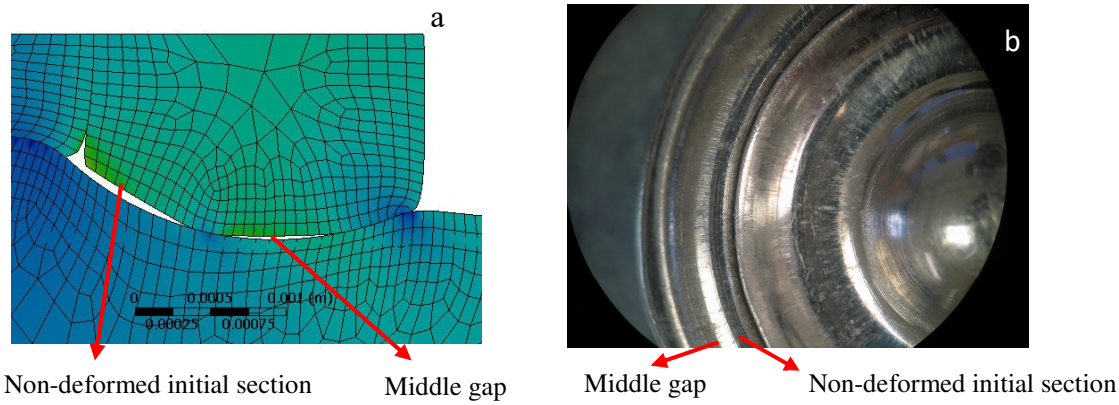

Figure 5.11. TiZr gasket ring deformation at 75 tonnes load. FEA model (a) and microscope image from a real gasket ring deformed (b). A gap where the gasket is not deformed was detected via FEA, and confirmed on the gasket used in the loading curve experiments. The middle gap detected on the FEA models is minimal, not easily noticeable in the used gasket via microscope. Employing FEA, it was noticed that at higher working pressures, both gaps were closed.

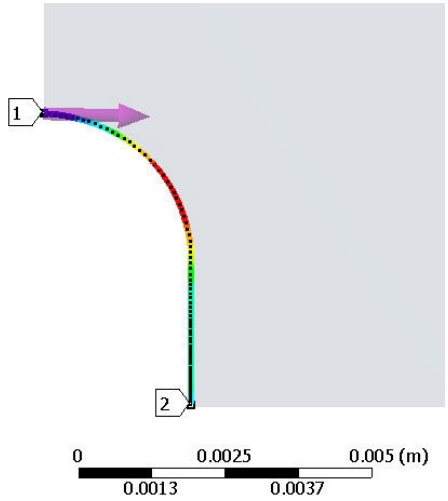

Figure 5.12. Illustration of FEA path at ZTA anvil's beam aperture. As performed with the anvil-gasket interface, maximum shear and principal stresses have been recorded along the path to visualise and understand stress evolution with experimental loads. The arrow at the beginning of the path indicates the direction of the data sequence (from 1 to 2).

Figure 5.13 shows the minimum principal stress evolution at the beam aperture for the selected load steps. A top compressive stress value of 3.56 GPa is registered at 2.63 mm from the FEA path origin. It is clear that the axial loads introduced in the system produce high compressive stress values at the beam aperture. Regarding maximum principal stress, Figure 5.14 demonstrates how tensile stress accumulation is minimal in this region.

Concurrently, it is possible to observe how maximum shear is commanded by compressive stresses at the beam aperture. At its operational load limit (75 tonnes), 1.77 GPa of shear stress is located at the same position as the top compressive stress value reported (2.63 mm). Figure 5.15 shows the maximum shear stress evolution.

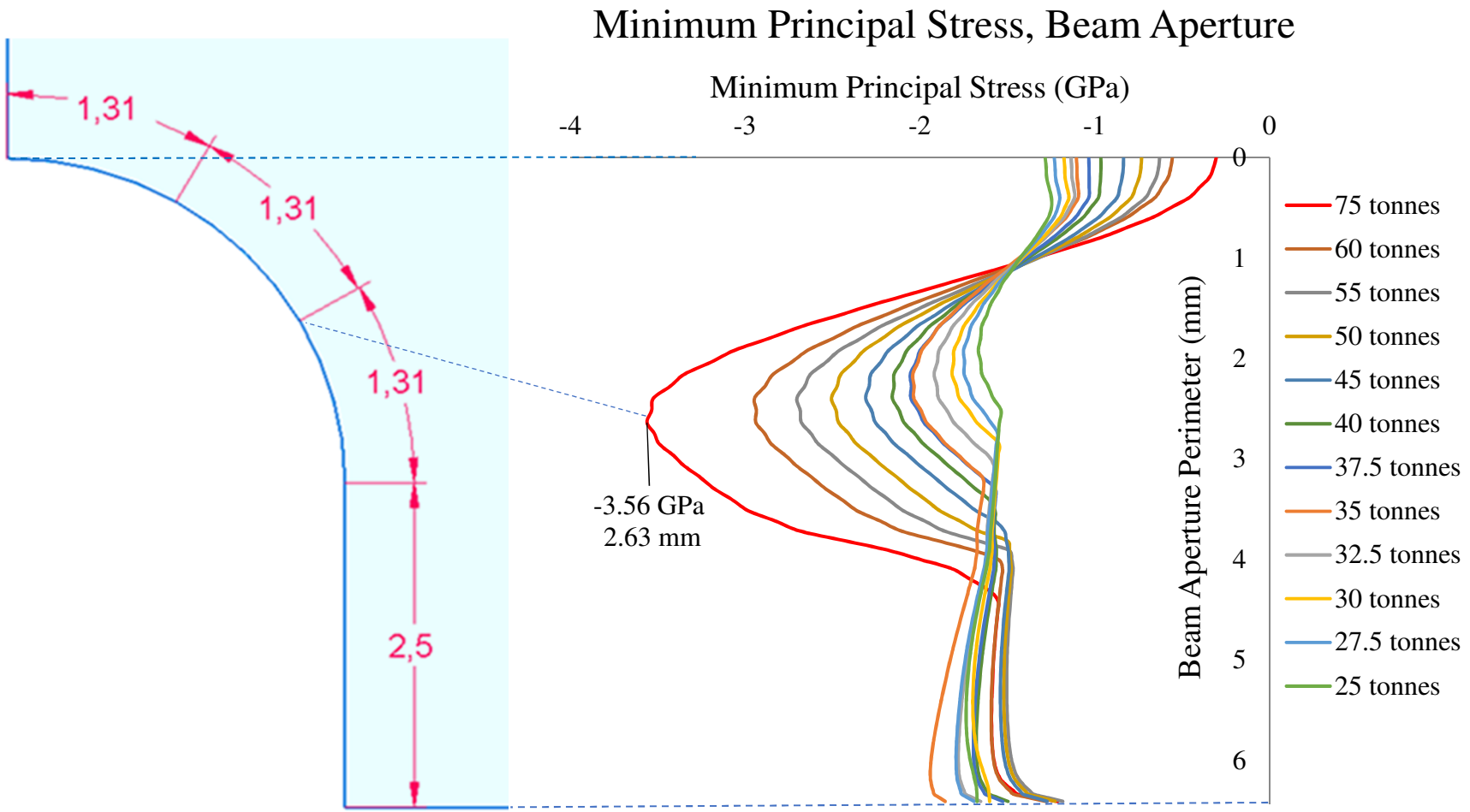

Figure 5.13. FEA minimum principal stress results of ZTA anvil's beam aperture with experimental loads. Fracture can be linked with the distribution of inner flaws in the material (Weibull theory) and with repetitive loads (fatigue). Laboratory evidence of cracks and flaking at this location suggest that damages occurring at loads lower than ZTA strength lead to states of high stress concentration where crack propagation triggers. The beam aperture is a discontinuity in the material, lacking of support to prevent these issues. The maximum compressive stress value obtained via FEA in this location can be used in a conservative approach towards optimisation and design.

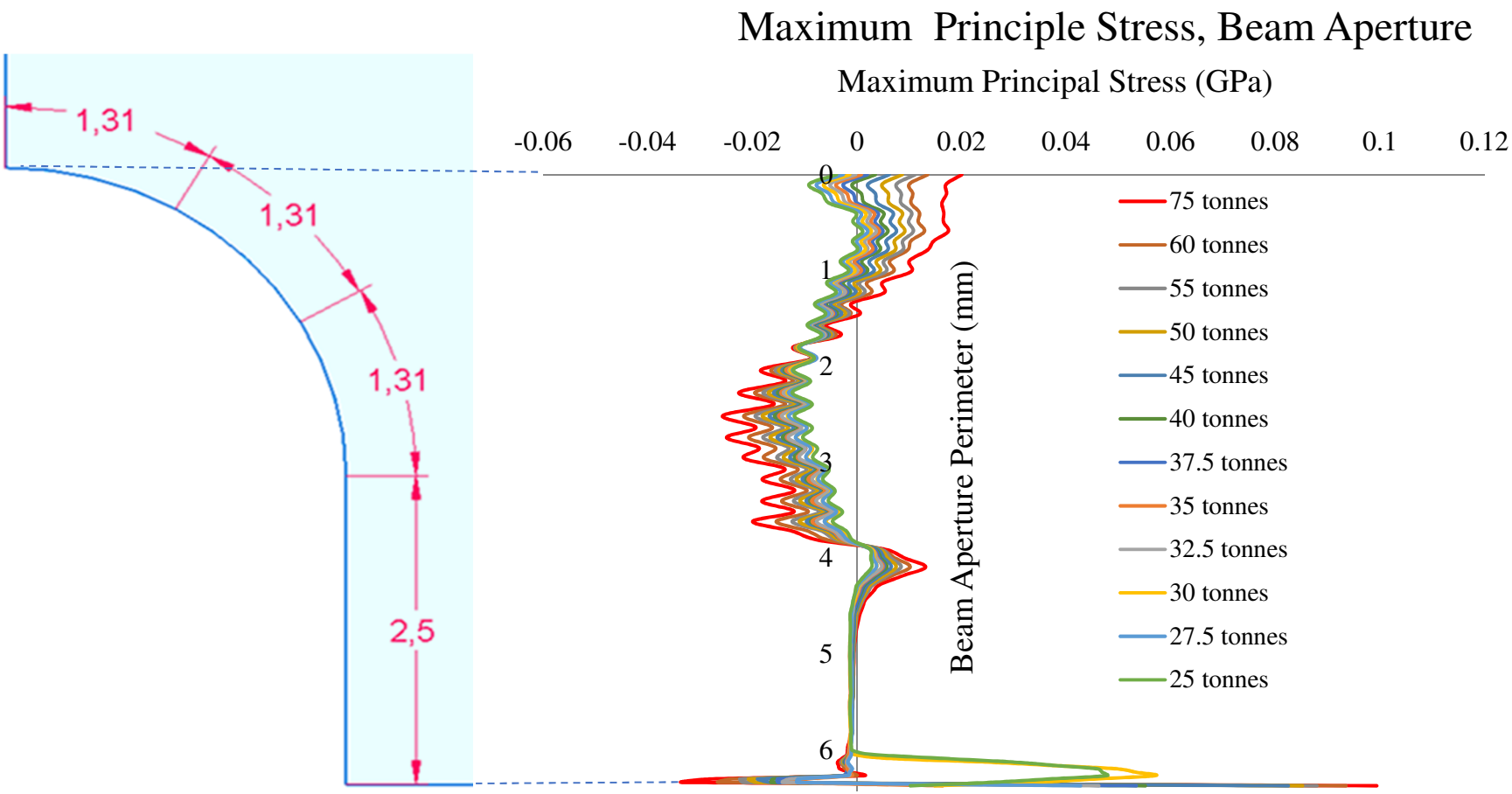

Figure 5.14. Maximum principal stress FEA results at anvil's beam aperture for experimental loads. Due to its location, tensile stresses recorded in this zone has low magnitudes, not connected with failure.

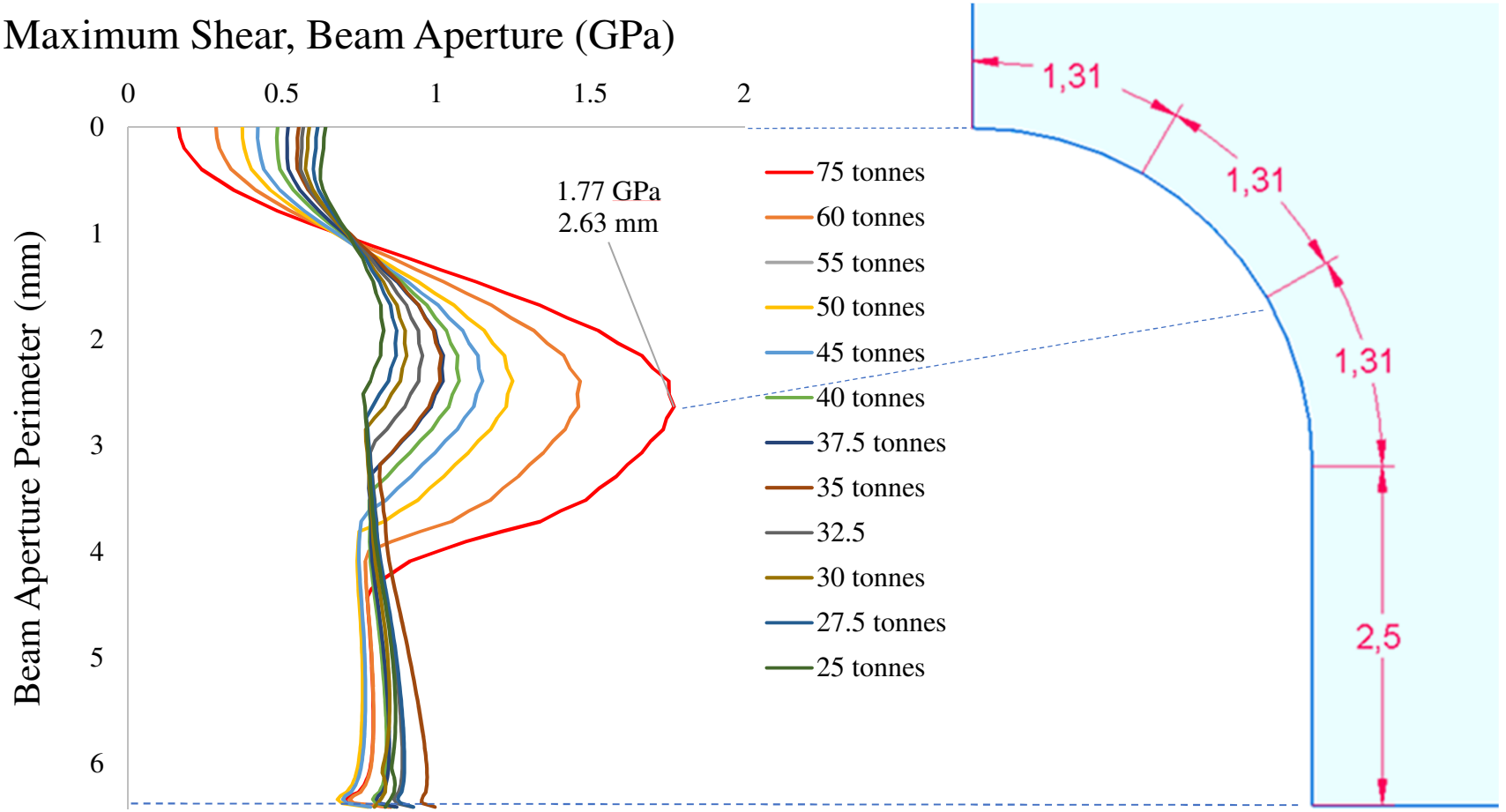

Figure 5.15. FEA maximum shear stress results of ZTA anvil's beam aperture with experimental loads. In this area, shear stress is produced by bending and expansion (Poisson's effect) of the anvil due to axial load. Associating these results with laboratory evidence as cracks, flaking, and large fissures, can be concluded (for design purposes) that 1.77 GPa is the highest shear stress which the beam aperture can withstand with this geometry.

By relating numerical results with failure evidence, it is interesting to see how damages at the beam aperture may occur by compressive stresses lower than ZTA strength (-3.56 GPa vs -4.7 GPa). Figure 5.16 shows how micro-cracks and flaking trigger at 75 tonnes load. Appearance of cracks alter the stress distribution in an object, concentrating more stress and propagating[62].

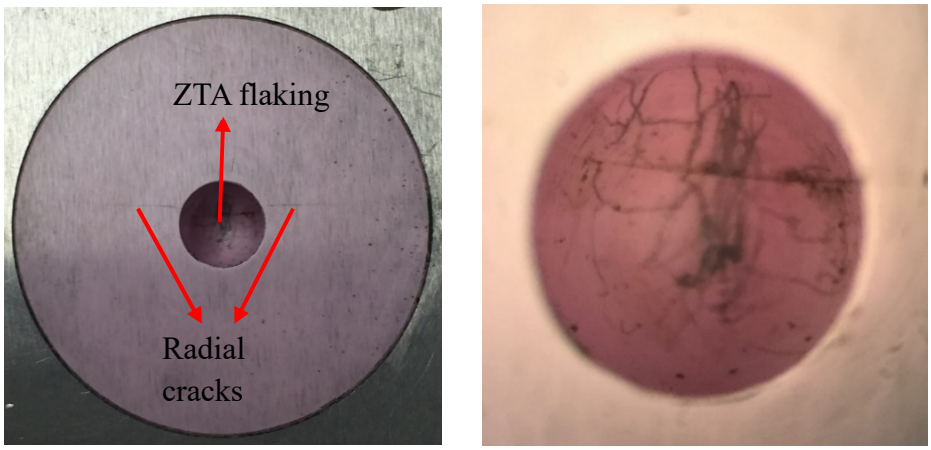

Figure 5.16. Documented failure at beam aperture area. It is possible to observe a series of micro-cracks at the interior of the beam aperture, as well as flaking. Crack propagation is visible with a predominant radial fissure at the back of the ZTA anvil. This damage is the most common which has been detected in ZTA anvils installed in a PE press at ISIS Neutron Laboratory.

FEA stress analysis and evidence provided in this section categorize the beam aperture as a weak area, where cracks can generate at 75 tonnes and damages can easily be triggered. As mentioned, ISIS Laboratory reports higher rates of failure occurance in comparison with the toroid area. Literature comments on the issue of stress concentration produced by discontinuities in an object[67]. The beam aperture has similar characteristics to those in the anvil. Lack of massive support caused by its presence produces stress concentrations in this area, generating and propagating fissures in a more effective manner than in other extents with larger support.

Furthermore, the Weibull theory[308,309] states how, in a ceramic material it is possible to lack an exact ultimate stress such as in ductile materials, failure being possible at a certain range of loads due to inner flaws distribution. According to this thesis, fractures at the beam aperture can occur at compressive stress values under ZTA's limit (-4.7 GPa) or

may resist compressive loads, enough to allow failure to trigger at the toroid area. This explains why failure alternates between both locations (beam aperture and toroid area).

Finally, a relevant factor for the beam aperture's area integrity is the role of the binding ring, laterally compressing the entire body of the anvil. Mentioned earlier in this thesis, press fitting proves beneficial in the reduction of lateral expansion caused by compressive loads (Poisson's effect). However, a certain degree of bending is introduced at the beam aperture area during this initial process. At 0 tonnes load, compressive stress values of ~1.5 GPa are detected at the position where failure has been identified. Fractional interference selected may induce micro-damages at beam aperture. This issue can weaken this region and promote failure. Appendix 2 provides more details and quantifies the impact of the binding ring in the ZTA anvil.

Nevertheless via FEA, it is clear how the binding ring contributes to the minimisation of tensile stresses in this cavity. Not having a binding ring would increase tensile stress values to ~3 GPa as explained in Figure 5.17, with a subsequent increase in maximum shear (Figure 5.18). Chapter 6 considers these details towards optimisation of the standard ZTA anvil geometry.

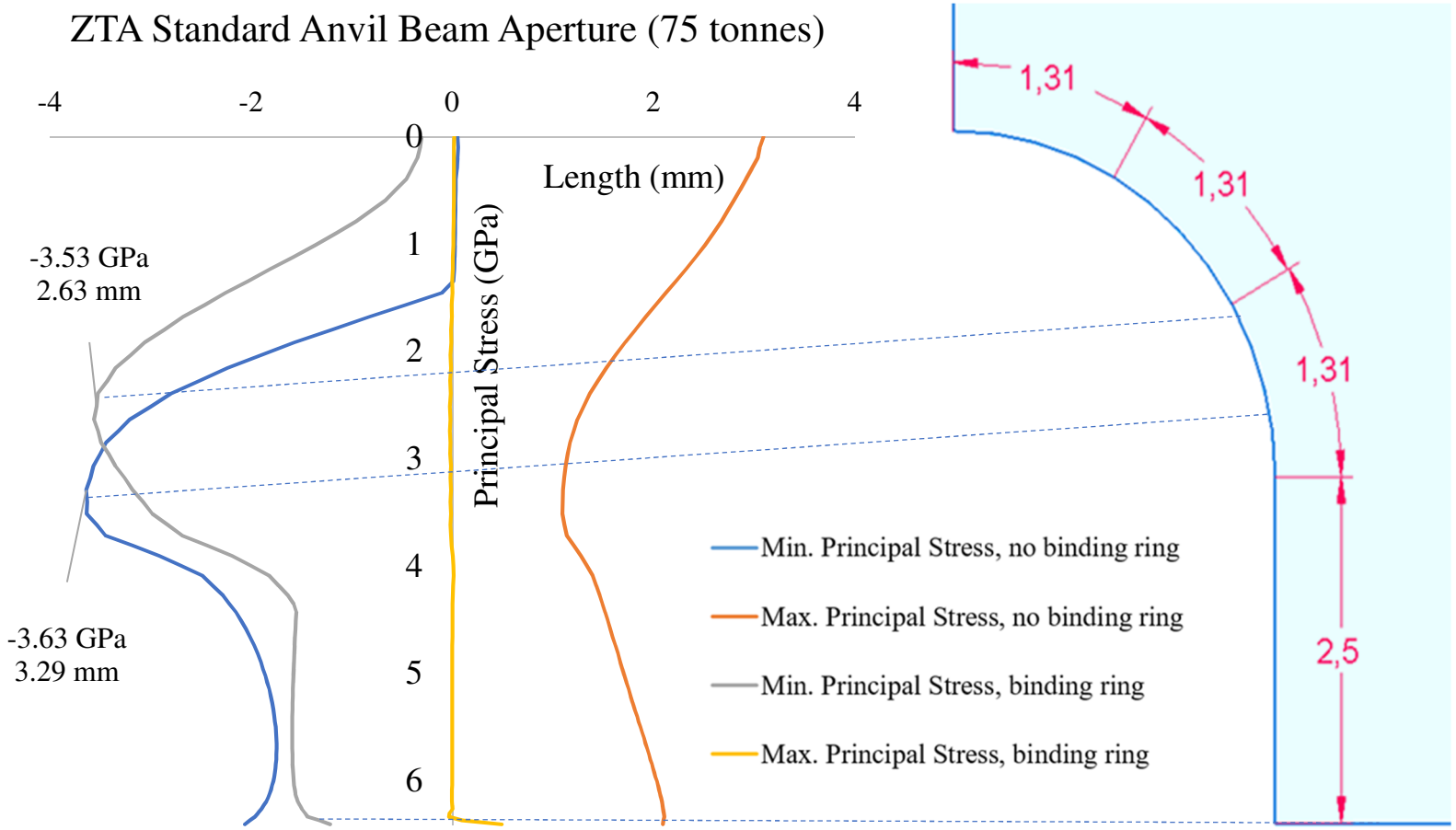

Figure 5.17. FEA maximum and minimum principal stress comparison in a standard ZTA anvil with and without binding ring. While compressive stresses have similar magnitudes and a slightly different location, tensile stress registers values up to ~3 GPa without binding ring. The binding ring provides advantages regarding mechanical stability in the beam aperture area.

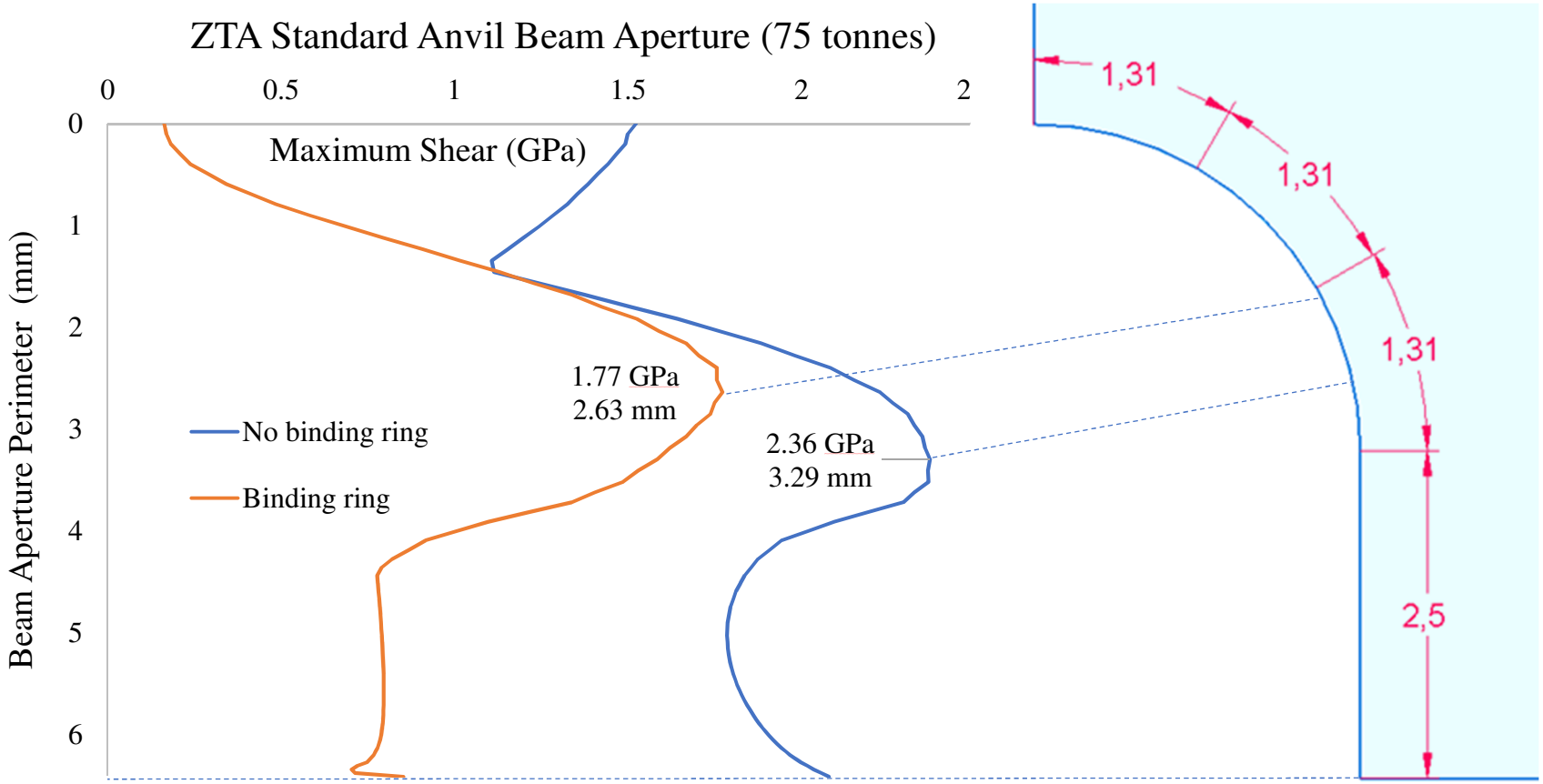

Figure 5.18. Maximum shear stress comparison at the beam aperture area for a standard ZTA anvil with and without binding ring. As the anvil without binding ring has much higher tensile stress values, it also presents an increased shear stress.

5.6 Chamfer Area

The standard ZTA anvil design includes a lateral semi-conic angle (1.5º), generating a wedge effect when press-fitting this device into the binding ring. This arrangement causes larger lateral compressive stress values at the bottom of the anvil (with maximum values at the chamfer area) when compared to the top part. Information provided by ISIS Neutron Laboratory explains the existence of an interference value of 0.124 mm between the anvil and the binding ring. Further analysis concerning lateral pre-stress effects is available in Appendix 2.

To illustrate and quantify the stress behaviour at the chamfer area, an FEA linear path was included at the binding ring – ZTA anvil interface, without considering any operational axial load at this point (Figure 5.19 and 5.20). It was confirmed how lateral pre-stress values vary along the contact area, being minimal at the upper surface of the ZTA anvil (0.106 GPa) and maximum at its bottom (3.29 GPa). Relatively few FEA nodes have stress values larger than 1 GPa, most of the anvil having an average pre-stress values of 0.55 GPa (matching lateral pre-stress hand calculations).

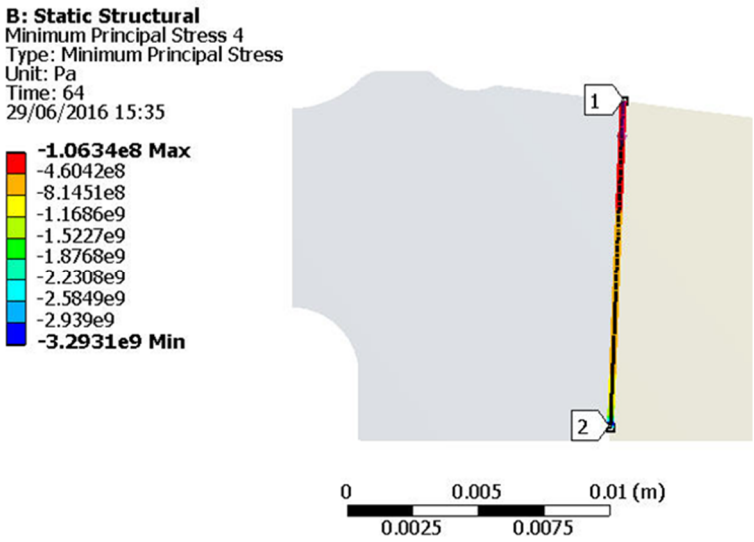

Figure 5.19. FEA path at ZTA anvil and binding ring interface. A model was executed without axial load to record compressive lateral pre-stress data. It is noticeable how lateral compressive stress increases from the anvil's working surface (-0.106 GPa) to the back of the anvil (-3.29 GPa). An average lateral compressive pre-stress value of -0.55 GPa has been gathered via FEA, counteracting lateral expansion of the anvils.

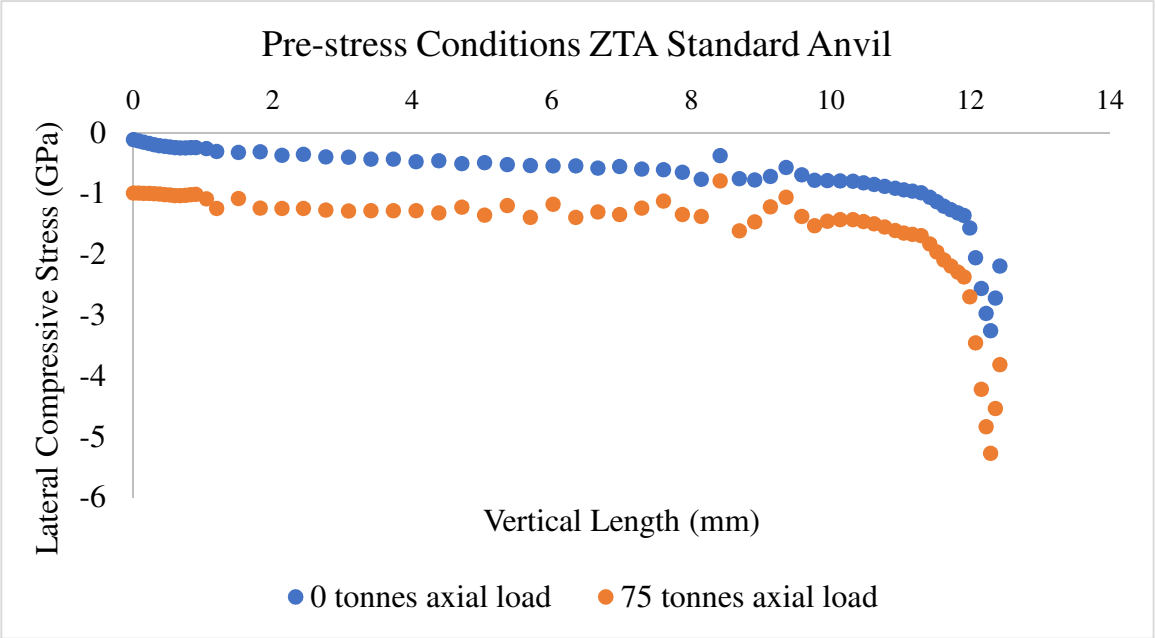

Figure 5.20. Numerical data for lateral pre-stress analysis at the anvil – binding ring interface. Discarding axial load, most of the anvil has pre-stress values below 1 GPa, that section having an average lateral pre-stress of 0.55 GPa. When operational load is applied (75 tonnes), a total average value of 1.66 GPa is detected. Nodes with higher stress values are at the back due to the 1.5° semi-conic shape of the anvil for press-fitting.

Figure 5.20 also shows the lateral stress compressive behaviour at 75 tonnes load. An average pre-stress load of 1.65 GPa is detected, preserving the pattern of higher lateral pre-stress values at the chamfer area. In a closer examination of the chamfer area and slightly outside the FEA path established in this section, principal stresses have peak values of -11.12 GPa and 1.08 GPa in compression and tension. Due to its location and geometry, there is no doubt that the chamfer acts as a stress concentrator. However, it was noticed how these particular stresses are located in an extremely reduced zone. Additionally, stress peaks detected have a high variability according to mesh size, this being characteristic of a numerical particularity.

Combination of both circumstances (stress concentrator and numerical particularity) implies a complex and stimulating situation for the analysis towards finding a reliable result. Figure 5.21 shows both minimum and maximum principal stress situation at the ZTA anvil's chamfer with the current (fine) mesh and no axial load.

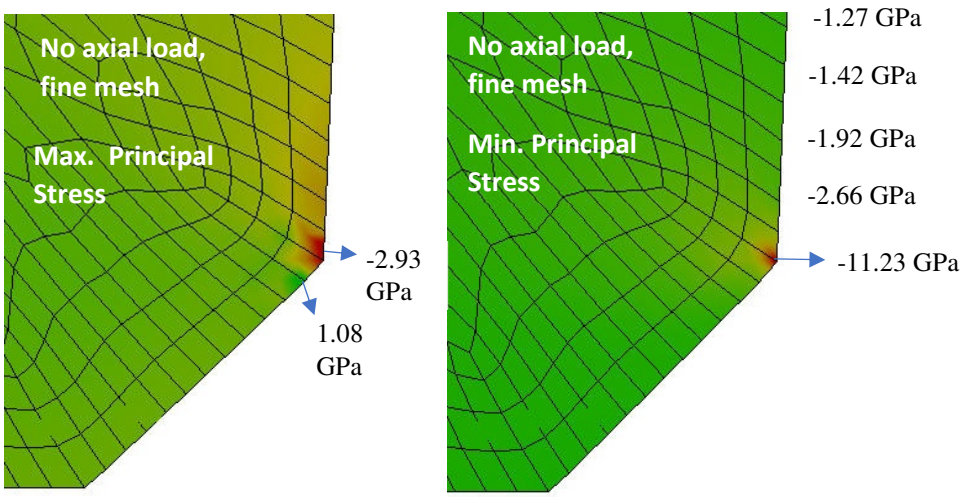

Figure 5.21. FEA maximum (left) minimum (right) principal stress results for lateral pre-stress at ZTA anvil's chamfer vicinity with fine mesh and no axial load. As mentioned, an increase in lateral compressive stresses towards the back of the anvil due to the binding ring effect exists, matching with a stress concentrator (chamfer's corner) and having an impact on the stress values registered in this particular location. Due to location and mesh size difference among adjacent components, stress values at chamfer's corner are subject of analysis.

Chapter 3 described how, in general, fine mesh is associated with accuracy at a large computer time expense. Therefore, it was explained that the mesh configuration used in this project for the standard ZTA anvil considers a maximum refined mesh in critical areas (edges) and a coarse mesh at the core. Mesh was also refined at the edge of components in contact with the anvil (gasket, TC platen and binding ring).

Although maximum mesh refinement was incorporated at the ZTA anvil's chamfer, edge of TC platen and binding ring, ANSYS mesh results are finer at the chamfer area. This cannot be further refined at the TC platen and binding ring edges.

As stated in Chapter 3, a large difference in mesh size between neighbouring elements can cause artificial stress concentrations in the nodes. Figure 5.22 shows the current mesh state, with an approximate proportion of 4 to 1 elements. Therefore, to have a better element proportion in this particular area, mesh size was increased at the chamfer. Figure

5.22 additionally illustrates both configurations, having now a case with a more favourable element proportion (2 to 1 approximately).

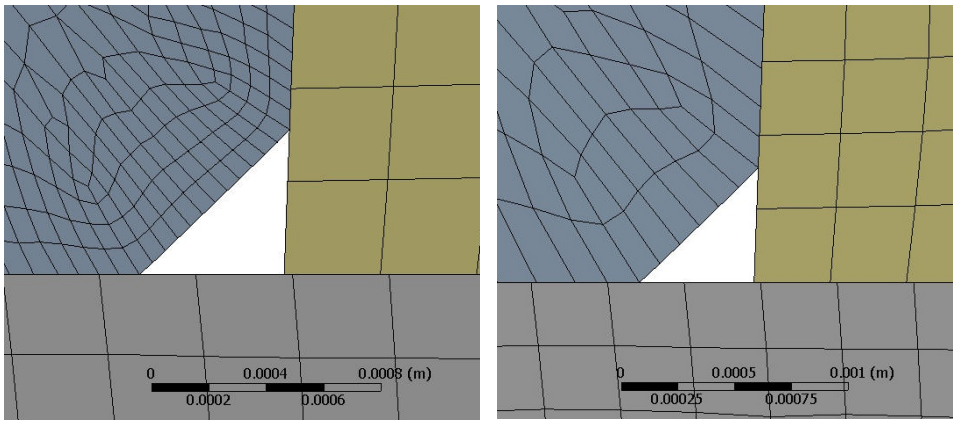

Figure 5.22. Mesh size difference among ZTA anvil's chamfer, binding ring and TC platen. Although the three edges have maximum mesh refinement in ANSYS, due to geometry and location the ZTA chamfer has smaller elements than the binding ring and TC platen (in a 4 to 1 proportion approximately). This difference contributes to the increase of stress concentration on the chamfer's particularity. By reducing the mesh size difference among parts, the stress concentration at the anvil's singularity decreased.

By adjusting the mesh configuration at the chamfer it is possible to observe how stress peak values decrease by 38% in compression and 60% in tension for an anvil with no axial load. Figure 5.23 shows the FEA results for the chamfer area with coarse mesh. Having acquired these insights regarding stress concentration and mesh sizes, the FEA model was employed to obtain results at 75 tonnes. Table 5.2 summarises the numerical results obtained.

FEA models with coarse mesh at the chamfer area provide more realistic results in terms of stress. At 75 tonnes load, compressive stress remains under reasonable parameters of massive support (strengthening factor of ~2.4 in compression). It is possible to notice how tensile stress increases from 730 MPa to 1.79 GPa when axial load varies from 0 to 75 tonnes. This peak tensile stress concentration is slightly higher than cases studied at the toroid.

Apart from arbitrary failure when press-fitting into the binding ring, the chamfer area is able to withstand operative conditions at 75 tonnes. Regarding the detected tensile and compressive stress, it is safe to assume that values below these limits (Table 5.2 with coarse mesh) are manageable by the ZTA anvil massive support.

In ISIS Neutron Laboratory, there are no statistics available regarding anvils failure rates at this point. It is possible to sustain that the Weibull theory plays a role in this region. Factors such as distribution of inner flaws can trigger early failure. Similarly and during the manufacturing of the anvils, sintering moulds, machining processes and even shipping and handling can introduce surface irregularities where stress accumulates, affecting the integrity of the anvils. Figure 5.24 shows a case where a ZTA anvil broke due to press fitting on the binding ring.

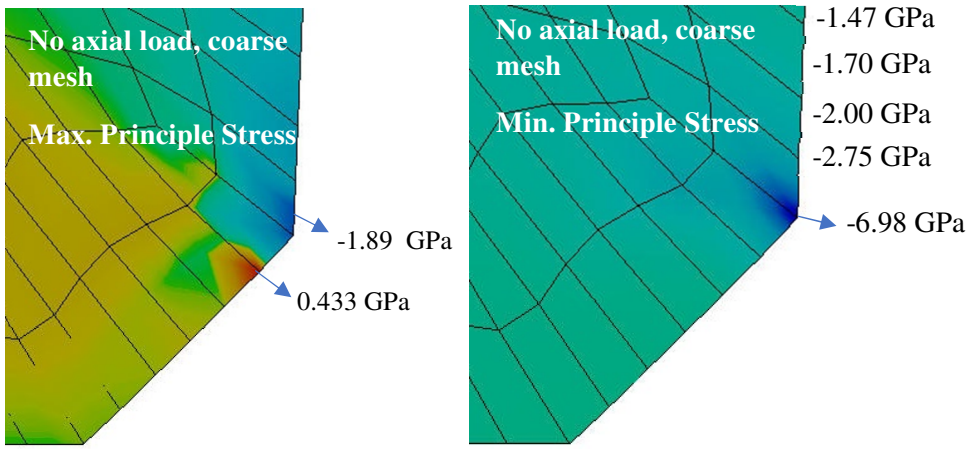

Figure 5.23. FEA minimum principal stress results for lateral pre-stress at ZTA anvil's chamfer vicinity with coarse mesh. When comparing to its counterpart with fine mesh, it is possible to observe a reduction on compressive stress at equal conditions and only attributed to a difference in mesh size, this being characteristic of a FEA singularity.

Based on the FEA mode available in this thesis, specific geometry changes were attempted at the chamfer area in order to reduce stress concentration. A fillet with same proportions (0.5 mm diameter) was introduced instead, having equal stress accumulation results. To reduce compressive and tensile stress peaks here, it would be necessary to decrease fractional interference values or the lateral angle between the anvil and binding

ring. By performing this action, other areas of the anvil would report an increase in tensile stress, leading to damages.

Table 5.2. Summary of stress peaks at ZTA anvil's chamfer for fine and coarse mesh.

Stress analysis at ZTA anvil's chamfer				
Axial load	0 tonnes		75 tonnes	
Stress	Maximum Principal Stress (GPa)	Minimum Principal Stress (GPa)	Maximum Principal Stress (GPa)	Minimum Principal Stress (GPa)
Fine mesh	1.08	-11.23	2.92	-17.39
Coarse mesh	0.73	-6.98	1.79	-11.28
Difference between mesh cases	60%	38%	39%	35%

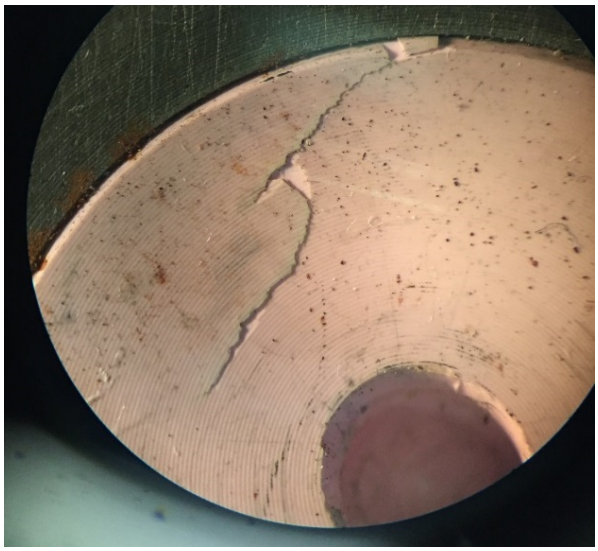

Figure 5.24. Standard ZTA anvil damaged during press-fitting into the binding ring. This process is performed applying ~5 tonnes force to the anvil, which sits proud 2.45 mm in the binding ring. FEA results showed how the wedge effect produced by the 1.5º anvil's lateral angle causes larger lateral pre-stress values at the bottom of the anvil when compared to its top part.

It is clear how a balance between lateral support and anvils integrity must be maintained in the system. As explained, lateral pre-stress is required in order to increase support in the anvils, as well as massive support. This section is useful as it quantifies the stress

condition in the chamfer area of the anvil. The current scenario is the actual maximum lateral pre-stress attainable.

5.7 Summary

As seen in this Chapter, FEA has made it possible to quantify and understand magnitudes, causes, and locations of stress accumulations in ZTA anvils. This is a complex task to achieve experimentally. In general, stress and failure analysis in ductile materials is a well-established process, with yield and strength limits clearly defined for design determinations. On the other hand, it was studied how aspects such as Weibull modulus and massive support principle produce high variability on the mechanical behaviour of brittle materials.

In synthesis, failure criteria developed in this PhD thesis has established the following parameters at 75 tonnes load:

- Section 5.4 showed that peak shear and tensile stress values of 4.7 GPa and 0.71 GPa at the final segment of the toroid activate failure in this area. Another important peak shear stress is reported at the initial toroid segment, caused by the joint of the two gasket pieces.
- Section 5.5 described that a compressive stress peak of 3.5 GPa associated with a shear stress top value of 1.77 GPa triggers failure at the anvil's beam aperture. Being a discontinuity in the ZTA anvil, the beam aperture accumulates stress from normal working conditions as well as from lateral pre-stress. This is a more frequent occurrence in comparison with damages at the toroid area.
- In Section 5.6, principal stress values of -11.28 GPa and 1.79 GPa were detected at the chamfer area. There is no proof of failure at this point caused by the action of both lateral pre-stress and axial loads. These values are important for future references in order not to exceed them as this point has characteristics of a stress concentrator.

Geometrical optimisations and re-design of ZTA anvils must consider these key locations and values, with target stress values to be reduced.

Regular experimental use of standard ZTA anvils installed in a PE press at ISIS Laboratory provided a relevant source of information concerning failure. Evidence

documented and kindly facilitated for this thesis was benchmarked with the numerical results obtained in this thesis. Critical areas matched with cases of failure reported in ISIS Laboratory. Because of the challenges this project has, stress analysis results gathered in this thesis are a remarkable achievement in high pressure instrumentation.

Mapping and identification of the anvil's stress areas (independently of their incidence in anvils' collapse) is important for design and optimisation purposes, as well as for establishing a record of stress conditions of the anvils with a particular geometry.

Chapter 6

ZTA Toroidal Anvils Optimisation

This Chapter describes specific strategies towards obtaining improved stress distributions on standard ZTA toroidal anvils. By studying geometrical modifications in critical areas identified in this thesis (beam aperture and toroid), the FEA model can be adjusted, quantifying the impact these changes have for a better performance of areas linked with failure.

Among the main aspects to evaluate are the removal of the beam aperture and its link with anvil's absorption when the neutron beam flight path is increased. Furthermore, the addition of surrounding material at the toroid's final segment and the possibility of a single piece TiZr gasket are assessed.

The FEA model and stress analysis methodology developed in this PhD thesis also evaluate a ZTA anvil geometry recently proposed in literature. Denoting a high degree of adaptability, this framework demonstrates to be a convenient tool in anvils stress and failure analysis and optimisation.

6.1 Introduction

This PhD work details how an FEA model of a ZTA toroidal anvil cell was planned, designed, and successfully implemented. In Chapter 5, a series of stress patterns were collected and critical areas identified, developing failure criteria. Having established these grounds and relevant data, it is possible to employ it improving ZTA anvil mechanical stability under working loads.

Chapter 5 numerically substantiated how the areas of beam aperture and toroid possess high risk of failure. This observation is also supported by experimental evidence and literature. Having quantified stress values and failure processes at both locations, the FEA model can be adjusted to introduce geometrical changes preventing a premature anvil failure.

The following sections refer to improvements in both critical areas. Developments are explained and supported with numerical results to understand their role in high pressure experiments. Additionally, an evaluation of an already improved ZTA geometry from literature is performed, showing how the FEA model developed can be employed as a reliable tool for stress analysis in these high pressure devices.

6.2 Beam Aperture

At this point, it is clear how the beam aperture area accounts for the majority of failure cases observed in standard ZTA anvils. A concentration of compressive stress with values from 3.56 GPa (Figure 5.13) triggers the emergence of visible cracks. Hence, it is interesting to investigate how specific geometrical adjustments include an increase of mechanical resistance in this area without compromising experimental data to be acquired.

Chapter 2 mentioned how the incoming neutron beam is gradually attenuated when passing through the anvil's body. As a strong neutron - sample interaction is desired, the anvil's geometry and its material must contemplate absorption for an effective data acquisition. Materials such as TC with Nickel binder (widely employed in high pressure neutron scattering experiments) attenuate beyond 80% of incoming neutrons (neutron wavelength of 5 Å) for a 6 mm path into the anvils[82]. To mitigate this radiation loss, a beam aperture was initially conceived in high pressure anvils for neutron diffraction.

The use of ZTA for high pressure anvils is relatively recent (starting from mid-2011[52]). The standard geometry is based in previous devices for neutron diffraction (which include a beam aperture). For a similar path and neutron wavelength (6 mm, 5 Å), ZTA's extraordinary neutron transparency permits the pass of over 90% of the incoming beam. This positive indicator suggests how it is possible to consider a shallow beam aperture. An increment in surrounding material at the beam aperture area can be linked to an increase on massive support, with a subsequent redistribution of stresses and without issues on data acquisition. Klotz[52] provides further details on neutron beam attenuation for relevant materials, including Sintered Diamond with different binders.

Neutron beam flight path on the standard ZTA anvil is 6 mm. Its geometry can be increased up to 12 mm by removing the beam aperture. During this scenario, a neutron transparency over 80% can be expected (Figure 6.1).

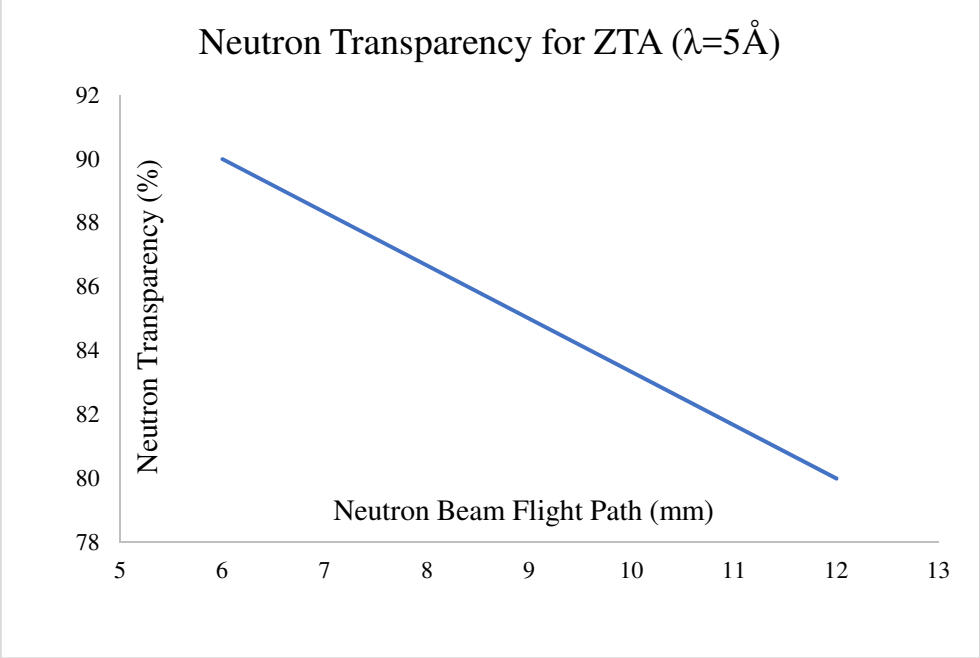

Figure 6.1. Neutron transparency vs beam flight path for ZTA[52]. ZTA transparency allows over 90% of the incoming neutron beam for a flight path of 6 mm. A linear trend can be established, being useful for the analysis of a ZTA anvil with a minor beam aperture.

To assess the stress impact the proposed modifications have in standard ZTA anvils, the FEA model was adjusted initially including a lower beam aperture configuration. For this purpose, the beam aperture curvature was positioned close to the anvil's base, resulting

on a flight path of 7.57 mm. Numerical parameters such as working load limit (75 tonnes), contacts, FEA paths and others were maintained. Figure 6.2 shows the new geometry as well as an FEA path for principal stresses and maximum shear stress at the beam aperture.

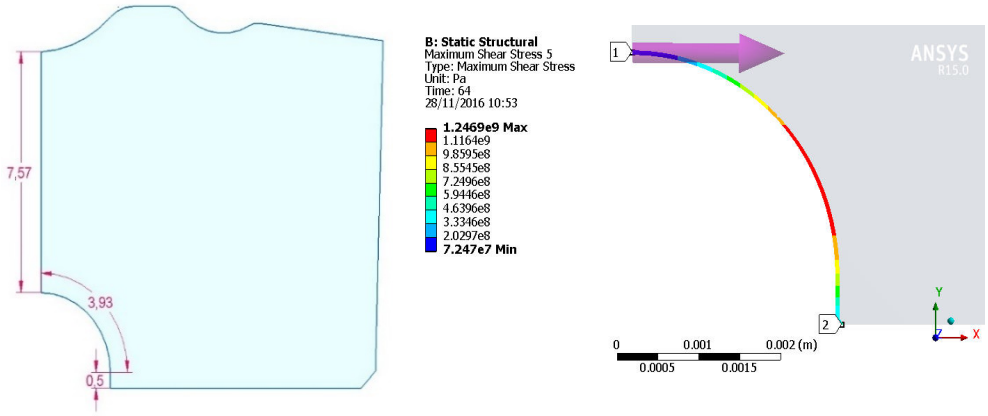

Figure 6.2. ZTA anvil with a low beam aperture (left) and maximum shear stress FEA path (right). A 7.57 mm flight path presents an approximate transparency of 87%, being favourable for data acquisition at the sample. The maximum shear stress registered is 1.24 GPa, 30% lower than in the standard anvil case.

Numerical results show high similitude on stress outcomes for both standard and low beam aperture ZTA anvil models. Explained in Section 5.5, tensile stresses are negligible and maximum shear stress will be commanded by minimum principal stress. Figure 6.3 shows minimum principal stress magnitude and location on the modified beam aperture.

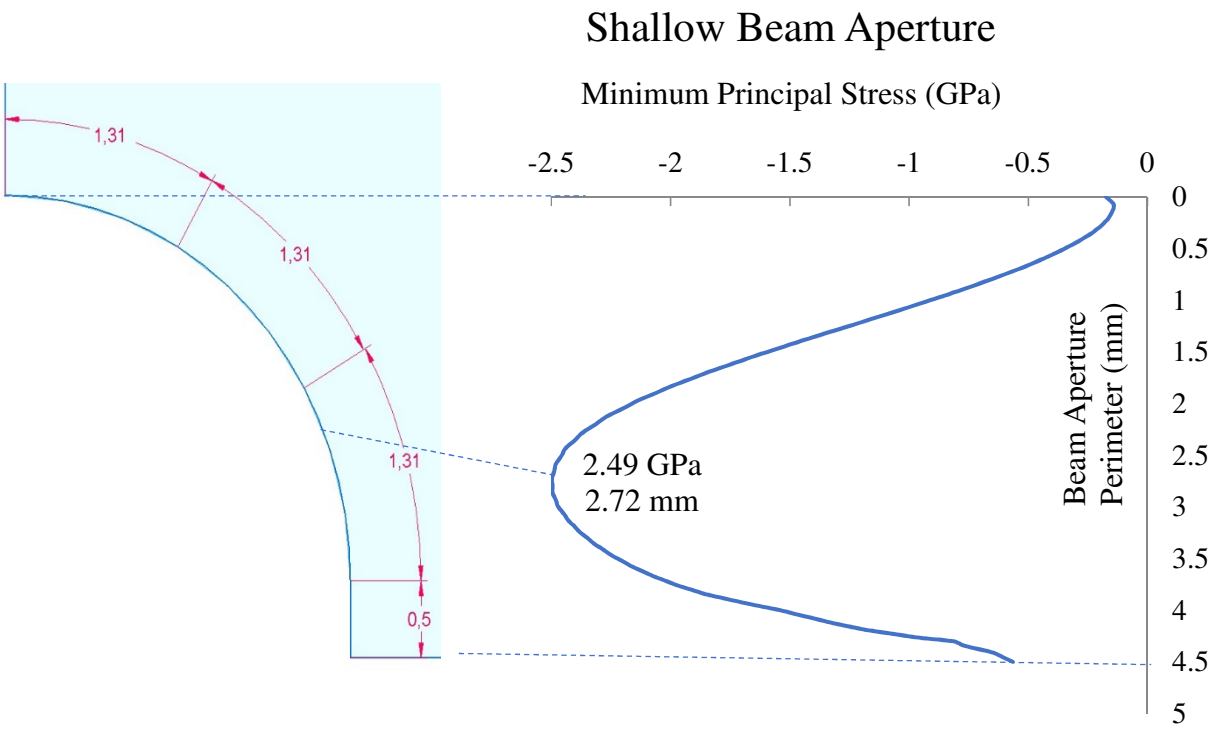

Figure 6.3. Minimum principal stress analysis for a ZTA anvil with low beam aperture. Stress patterns on this region have similar trends when compared to the standard anvil. As maximum principal stress has a small magnitude, minimum principal stress is a major influence on maximum shear stress, leading to eventual failure at this point. A relevant decrease in minimum principal stress has been noted, from 3.56 GPa to 2.49 GPa for this new beam aperture geometry.

From Figure 6.3 it is possible to observe a reduction in minimum principal stress from 3.56 GPa (limit) to 2.49 GPa at the beam aperture when compared with the standard model. There is a minimal displacement of the highest compressive stress location (0.09 mm) as well. This decrease is a good indicator that fracture may be avoided at 75 tonnes. Figure 6.4 shows a decrease in maximum shear stress (1.24 GPa) at the new beam aperture when compared with the standard case (1.77 GPa).

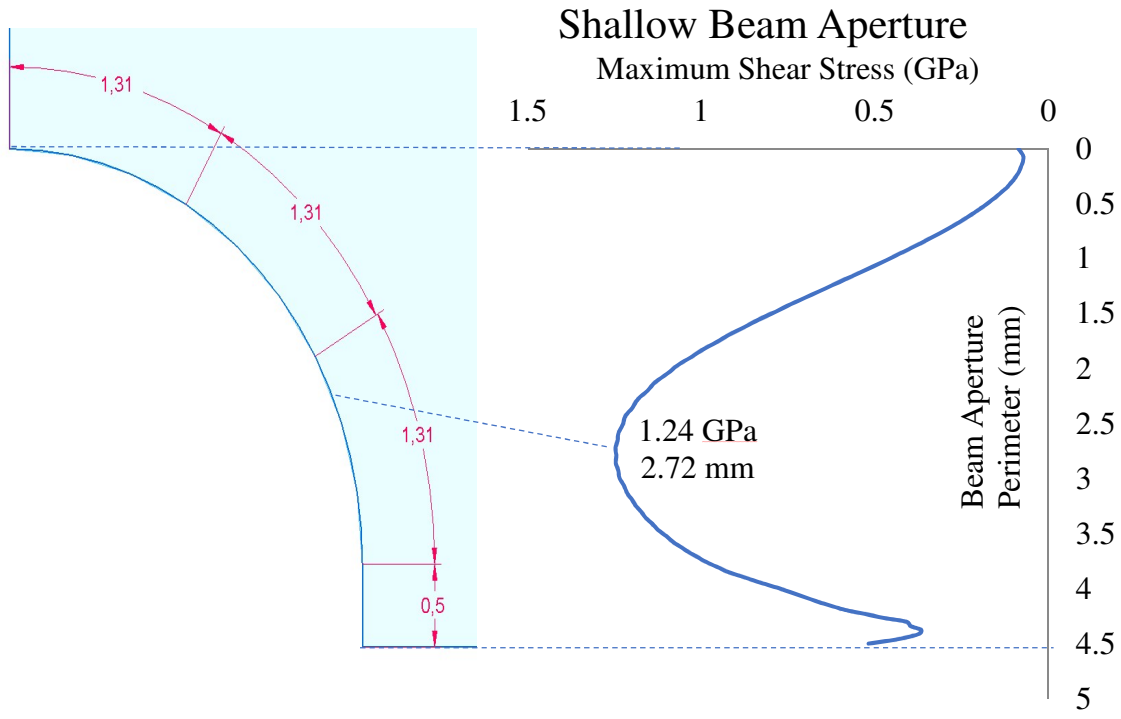

Figure 6.4. Maximum shear stress analysis for a ZTA anvil with a low beam aperture. Having maximum principle stress a small magnitude in this area, maximum shear stress will be commanded by the minimum principal stress according with Mohr's theory. There is a relevant decrease when compared with a standard anvil.

As seen in this section, a low beam aperture configuration benefits stress distributions at this critical area. Failure at working loads (0 – 75 tonnes) could be prevented, extending ZTA anvils' lifetime at this range. This adjustments do not significantly alter stress distribution in other critical areas.

In light of these results, it is interesting to study an anvil configuration completely discarding the beam aperture. The FEA model available in this thesis was adapted for this approach, illustrated in Figure 6.5. An increase on the neutron beam flight path from 7.57 mm to 12.60 mm must be considered for a neutron transparency over 80% according with Figure 6.1.

Performing a principal stresses analysis in the entire anvil, it is noticeable how this configuration has similar patterns at the body and anvil-gasket interface when compared with the standard anvil. Nevertheless, at the area of interest it is possible to identify a

concentration of tensile stress with maximum values of approximate 429 MPa. Figure 6.6 shows this region in detail.

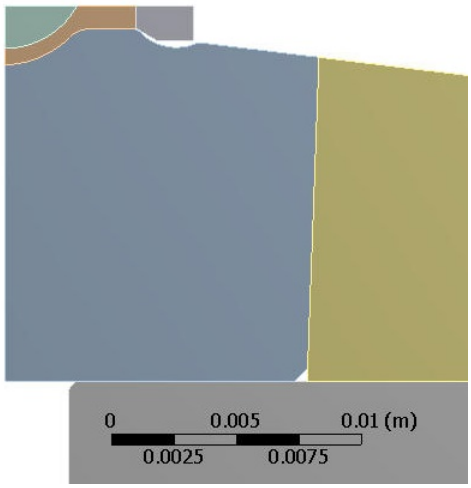

Figure 6.5. Numerical model of a ZTA anvil with supressed beam aperture. Stress analysis can be performed by adapting the FEA model available in this thesis with this geometry. Due to a reduction in damaging stresses by introducing a low beam aperture, it is interesting to analyse the anvil's behaviour with a supressed beam aperture.

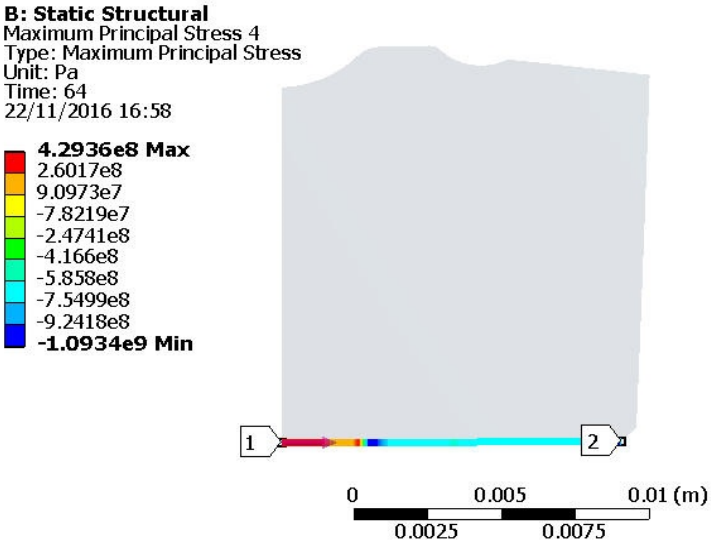

Figure 6.6. Illustration of a numerical path used to study stress distribution at the bottom of the anvil. A tensile stress accumulation was detected with values up to 429 MPa. As the beam aperture was removed, bending produced by the working load affects the area of the ZTA anvil where the TC platen aperture is located.

The addition of material creates an area where tensile stresses are produced by a minimal bending at the base of the anvil. This effect can be created by the beam aperture at the TC platen.

Cases, considering a beam aperture, had negligible tensile stress values (~20 MPa). By performing a principal / maximum shear stress analysis in Figure 6.6 path, it is possible to observe a maximum shear value of 0.93 GPa, being close to its peer at the low beam aperture value (1.2 GPa) but still smaller than the standard anvil, whose values are around 2.49 GPa. Compressive stress reaches a top value of 2.81 GPa. Figure 6.7 summarises these values.

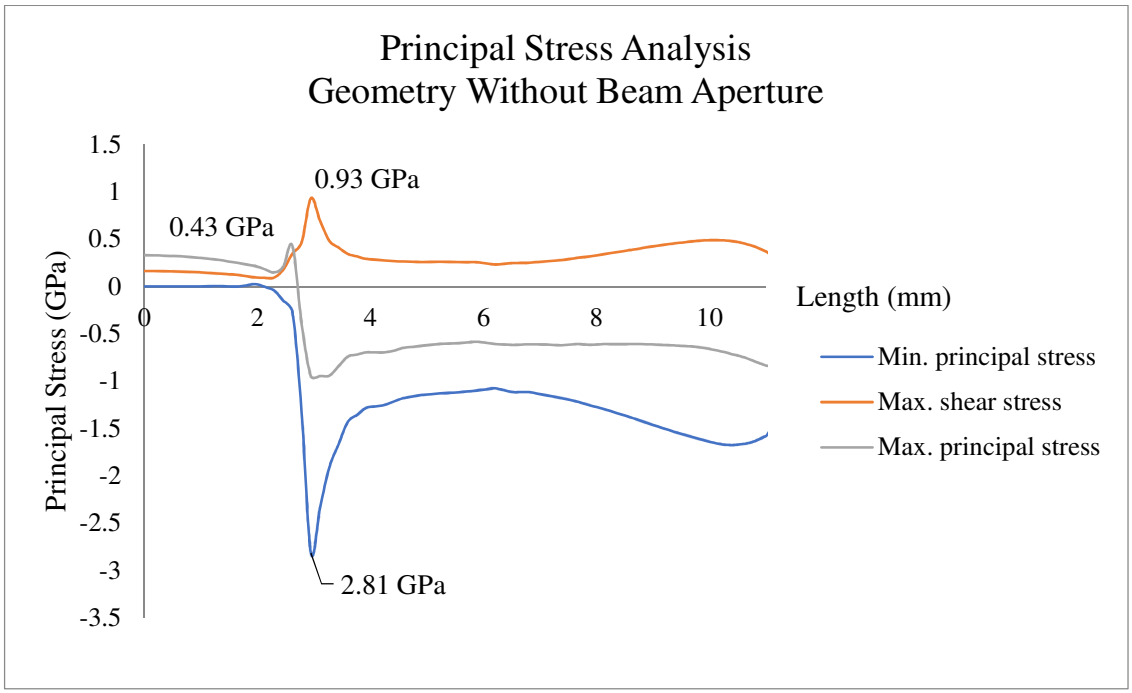

Figure 6.7. Numerical results of the principal stresses at the bottom of ZTA anvil. Peak values are located at the contact point between ZTA anvil and TC platen (3.1 mm). Tensile stress is present along the TC platen beam aperture, caused by bending of the anvil.

Analysing the stress results gathered for a geometry without beam aperture, it is possible to observe how principal stress values are within confines of failure criteria established for the standard anvil. Tensile stress values in this modification are still under ZTA strength, and the massive support principle provides a promising scenario for this new geometry. By removing the beam aperture, press-fitting the anvils will not focus stress in

this particular area, inducing possible micro-damages as described in Chapter 5. To consider this new geometry, experimental data would be necessary.

6.3 Toroid Area

Fracture has been documented in the toroid area, being second in importance after the beam aperture and requiring attention to mitigate damaging stresses. As mentioned, geometry, gasket material, and deformation rates combine to generate a complex scenario. Via FEA, modifications to the standard design have been tested with positive results. This section provides an account of numerical approaches to mechanically enhance the toroid area of ZTA anvils. It is significant to mention how stress distribution at the anvil-gasket interface is strongly linked with gasket material and thickness.

For the standard ZTA anvils, Figure 5.8 showed the tensile stress peaks location and magnitude at the anvil-gasket interface. A more exhaustive stress distribution analysis shows an interesting trend. Peak tensile stress values are located within the toroid chamber (bottom right in the FEA model), this being the area of first contact when the ring is compressed to fill the toroidal cavity as well. Compression forces and the gasket's displacement outside the toroid chamber combine, making this point have the highest shear stress at the interface and top values of tensile stress.

To clarify this phenomenon, Figure 6.8 describes how a tensile peak value of 1.1 GPa is registered at 60 tonnes load (largest experimental load). Due to the large deformation gasket experiences, it is possible to see how the location of this peak value changes at further load steps extrapolated in this thesis, ending at the outer part of the final segment (where failure has been registered).

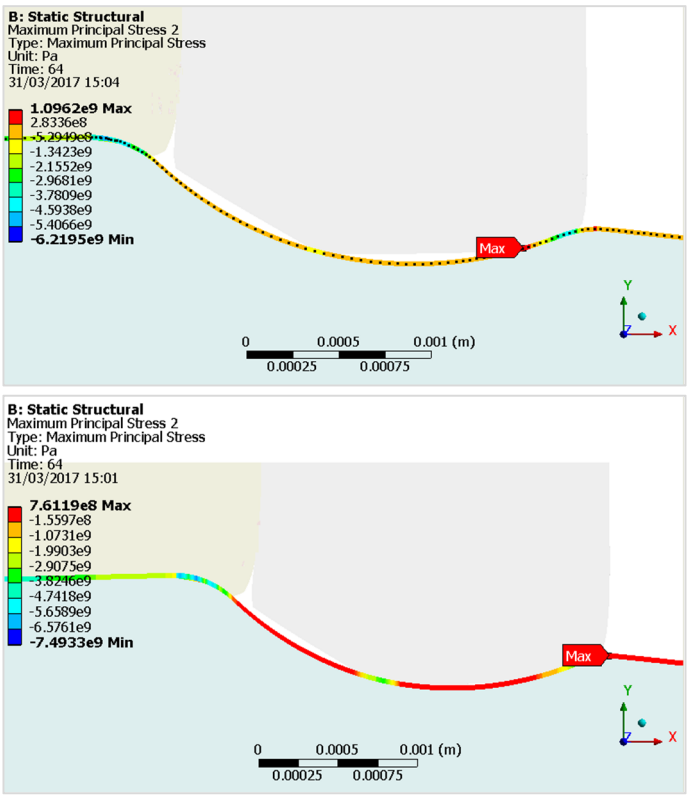

60 tonnes
1.1 GPa tensile stress peak (not linked with failure)

75 tonnes
0.761 GPa tensile stress peak (linked with failure)

Figure 6.8. Peak tensile stress at the anvil-gasket interface for the standard ZTA anvil model at 60 and 75 tonnes. It is possible to see how the peak stress relocates at higher loads due to TiZr gasket deformation. In addition, it is noticeable how its magnitude decreases from 1.1 GPa to 0.761 GPa, being this last value linked to failure.

It is interesting to observe that the anvil-gasket interface is able to resist 1.1 GPa of tensile stress inside the toroid chamber, not being the case for 0.761 GPa in the outer region of the toroid final segment. There is a possibility that the stress inside the toroid area causes micro-fractures weakening the external part where failure occurs.

Having no reports of experimental damages at 60 tonnes, this thesis evaluates a design modification to completely encapsulate the gasket ring into the toroid. Without further amendments to the FEA model settings and parameters, results with this modification show how tensile and shear stress clearly descended at these points of interest. Figure 6.9 demonstrates this alternative in the FEA model and tensile stress results.

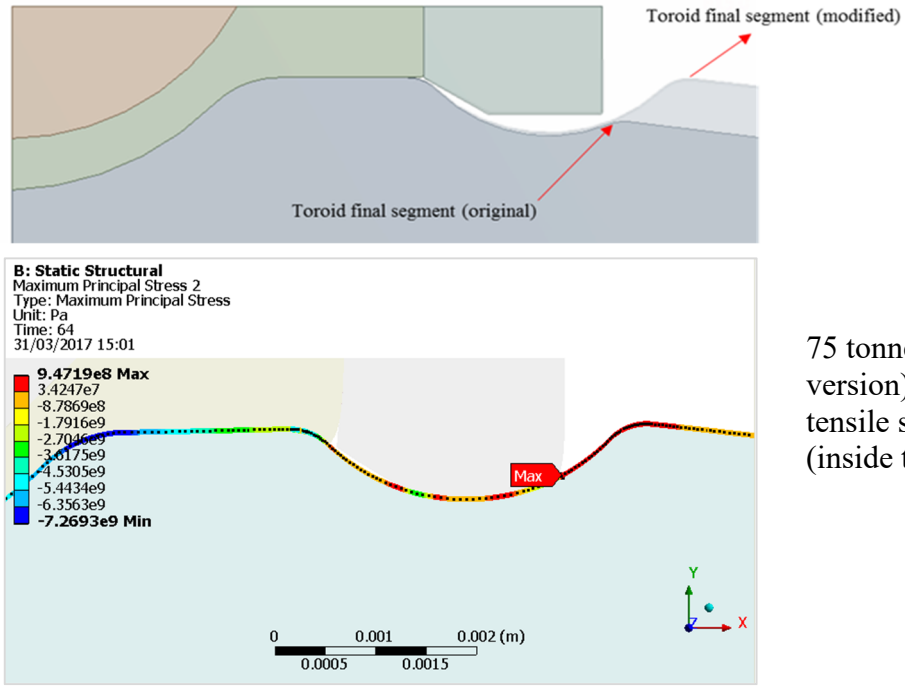

75 tonnes (improved version). 0.947 GPa tensile stress peak (inside toroid area)

Figure 6.9. Geometry modification of toroid's final segment at ZTA anvil numerical model. As failure has been identified in this specific area, this change was introduced to mechanically reinforce it towards a more favourable stress distribution.

Figure 6.9 shows a top tensile stress value of 0.947 GPa for the reformed model, smaller than the 1.1 registered inside the toroid area for the standard anvil. Gasket material is not able to reach the outside the toroid chamber and massive support conditions are improved in the system. The new configuration offers a reduction in shear stress when compared with the standard version (34%, Figure 6.10).

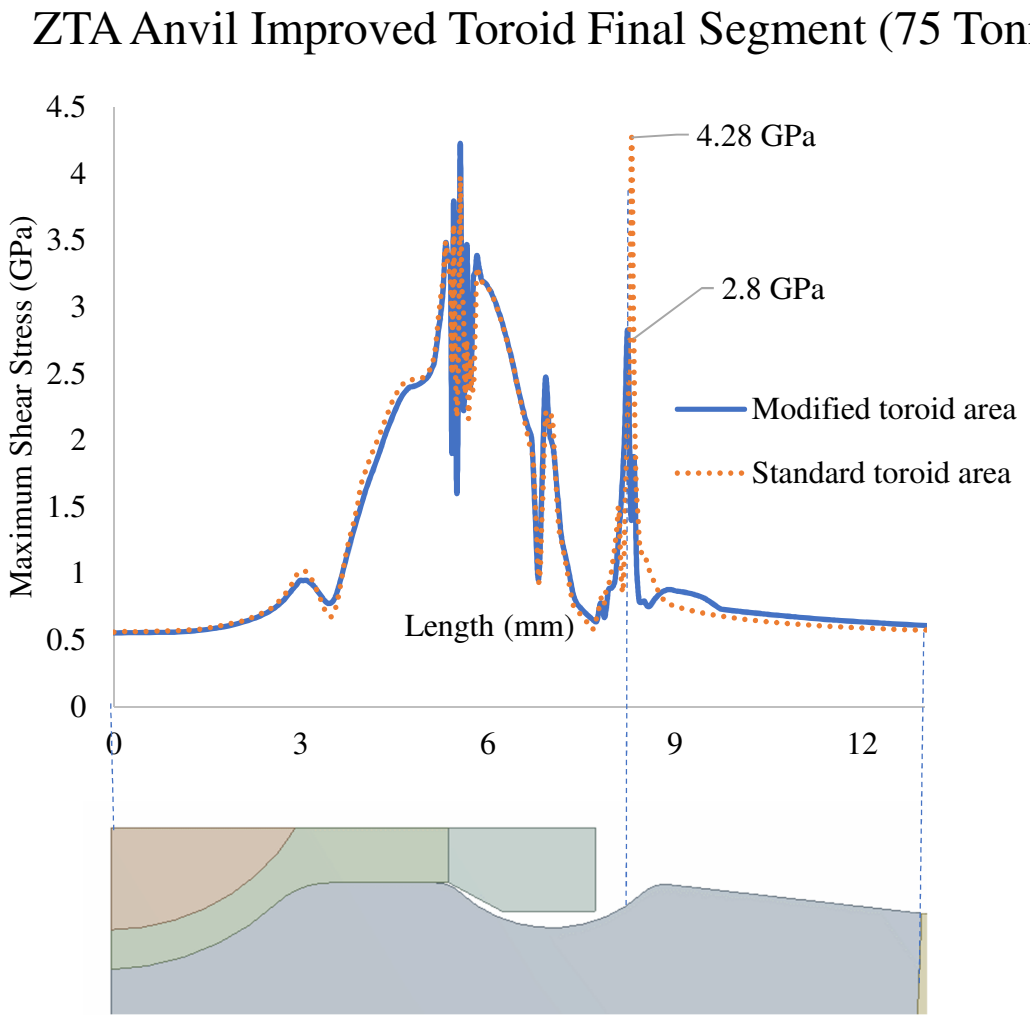

Figure 6.10. Maximum shear stress numerical results at anvil-gasket interface. It is noticeable how the peak at 8.29 mm decreases for the geometrically modified case, which incorporates surrounding material at the toroid's final segment. This peak has been linked with failure on the standard ZTA anvil in Chapter 5. The use of a larger gasket ring reduces sample pressure in ~600 MPa.

An increase in ZTA material at the toroid final segment can generate data acquisition issues. Although ZTA neutron transparency is extraordinarily high, a variation of the angular aperture (15º) was modelled via FEA for this optimised case. Figure 6.11 shows this geometry.

For the 15º angular aperture model, it was noticed how stress patterns are even more favourable when compared with its optimised toroid counterpart (7º angular aperture). A

decrease in top tensile stress from 0.947 (Figure 6.9) to 0.590 was detected at the toroid area. Additionally, a reduction from 2.8 GPa to 2.02 GPa in maximum shear stress (Figure 6.10) provides good insights into this geometry.

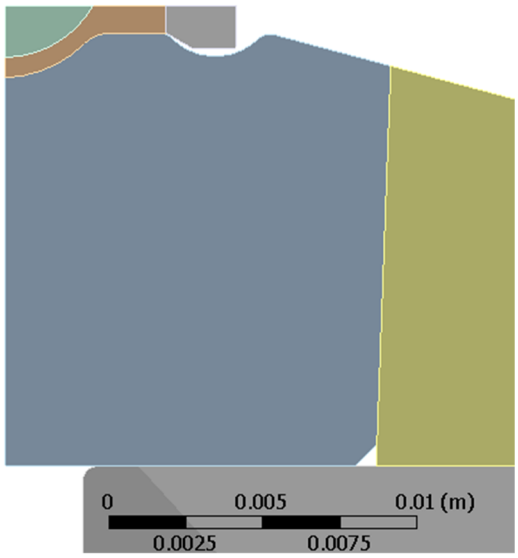

Figure 6.11. Optimised toroid area of a ZTA anvil model with 15º angular aperture. Peak tensile and shear stresses are favourable when compared with an optimised toroid version with 7º angular aperture.

Figure 6.10 displays how the shear stress peak at toroid's initial segment remains after the suggested optimisations. The numerical model clearly shows a direct link of this outcome with the joint of both gasket parts. At approximately 5.5 mm from the gasket's centre, the anvil-gasket interface has high shear stress conditions as both gasket pieces tend to deform in opposite directions. The joint of both gasket parts was located in many places, showing shear stress values of similar magnitude independently of the union's location. Based on this finding, a unified gasket was designed and adjusted to be simulated. Figure 6.12 shows this alternative, additionally including the modification completed on the toroid's final segment.

Figure 6.13 shows an FEA path at the anvil-gasket interface including a single piece TiZr gasket. Shear stress peak at 5.55 mm (location of the gaskets joint) reduces from 4 GPa to 3.5 GPa by employing this idea. Using a unified gasket, a slight decrease on sample pressure, from 6.43 GPa to 5.9 GPa was observed.

Figure 6.12. Introduction of a single piece gasket for the ZTA anvil numerical model. At the standard anvil model, a shear stress peak has been traced at the union of both gasket segments independently of its location. This modification avoids the high shear stress caused by both gasket segments deforming at opposite directions.

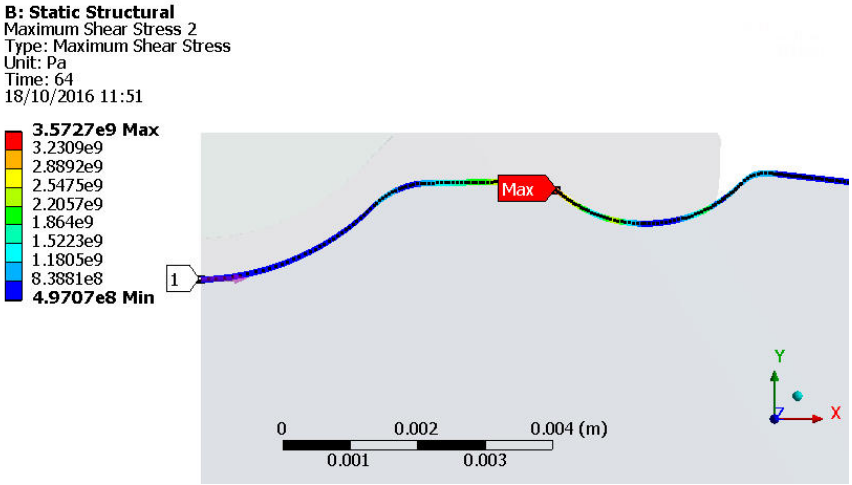

Figure 6.13. FEA path at ZTA toroidal anvil working surface with a single piece TiZr gasket. As maximum shear stress peaks have been found at the gasket joint for standard cases (sample chamber – external ring), this single piece gasket has been evaluated showing a positive impact concerning this behaviour.

While this thesis proposes a single piece gasket as a method to improve the high pressure set, it is important to mention that there is no laboratory evidence of failure at the toroid's initial segment at shear stress values of 4 GPa as in the standard ZTA anvil. More experimental data would be necessary as this geometry can be favourable for massive support, making a single piece gasket for working conditions of 0 – 75 tonnes unnecessary.

By integrating improvements proposed in this Chapter into the FEA model, a reduction on fracture risk at critical areas for the established working conditions studied (0 – 75 tonnes) can be accomplished. This represents an advantage towards reusing ZTA anvils, reducing experiment costs as well as expanding the working range. Figure 6.14 illustrates the improvements on the ZTA anvil geometry (detailed in Appendix 3).

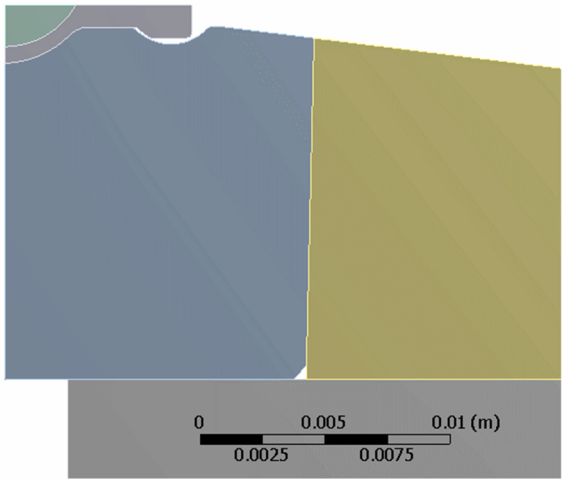

Figure 6.14. FEA model of improved ZTA toroidal anvil, simultaneously including the proposed and studied modifications at beam aperture, toroid groove and gasket (single piece). This figure illustrates the main geometrical changes which can be introduced in the current design to extend the anvils lifetime at the specified working range (0 – 75 tonnes). As illustrated in Figure 6.11, a 15º angular aperture would balance mechanical improvements with neutron access.

6.4 FEA Non-Toroidal Adapted Model

Currently there is a limited number of publications about ZTA anvils stress behaviour. Results gathered in this project are in agreement with a study by Iizuka[310] in 2012, mentioning similar evidence of failure at the toroid area. At this point, it is possible to conclude that the toroidal anvil configuration for ZTA has a limit in working loads caused by shear stress of gasket deformation. Materials with higher mechanical resistance might have absorption problems, being unsuitable for this use.

Aiming to increase sample pressure on ZTA anvils, Iizuka[310] developed a non-toroidal version of the anvil cell for neutron diffraction. This concept was generated to reduce

stress concentration areas at the anvil-gasket interface as identified and explained in this thesis. As a toroidal groove alternative, the author incorporated an Aluminium ring to restrict the gasket and sample chamber deformation and increase pressure. Figure 6.15 illustrate this idea, later applied by Komatzu[82] when comparing anvils performances of a series of ceramics with both toroidal and non-toroidal geometries (Figure 6.16). ZTA non toroidal anvils reached ~11.2 GPa for a volume of 17.6 mm^3. An Aluminium sphere was located on the sample chamber to increase pressure.

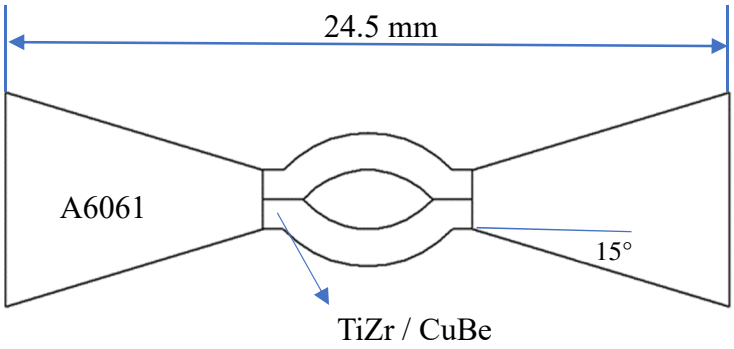

Figure 6.15. Illustration of Iizuka's[310] gasket design. The toroidal groove has been substituted with an Aluminium (A6061) ring to avoid fracture at the ZTA anvil's toroid area. The Aluminium ring restricts the sample chamber plastic deformation under pressure, incrementing its pressure.

Publications mentioned in this section focused on experiments and do not provide enough details for a stress analysis similar to Chapter 5. However, the FEA model developed in this thesis can be adapted to the main concept described in these papers. Figure 6.17 shows how an Aluminium ring was placed on a modified anvil's working surface. Sample volume (~47 mm^3) and FEA parameters such as contacts and frictional coefficients remained unaltered.

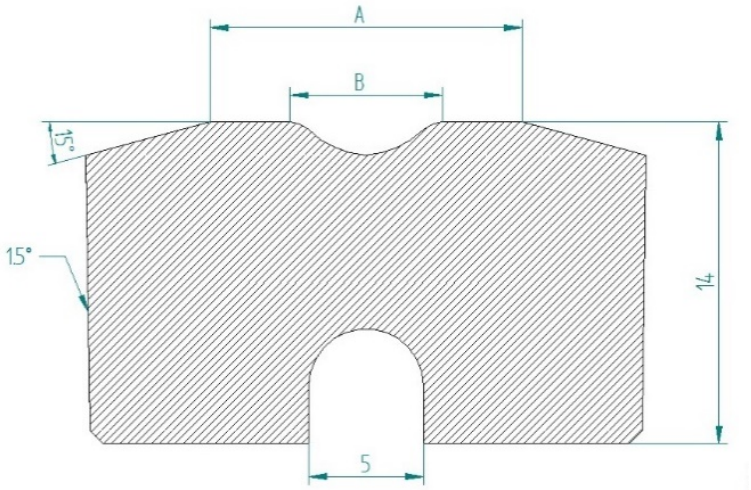

Figure 6.16. Opposed-anvil-type high pressure apparatus with wide-angle aperture for neutron diffraction by Iizuka[310]. This device was conceived as an alternative to the toroidal anvil, due to its tendency of fracture at the toroid area. A ZTA version of this device was manufactured by Komatsu[82] for an A/B relationship of 8/4 mm. Its experiments reached ~11 GPa for a 17 mm^3 volume. Dimensions in mm.

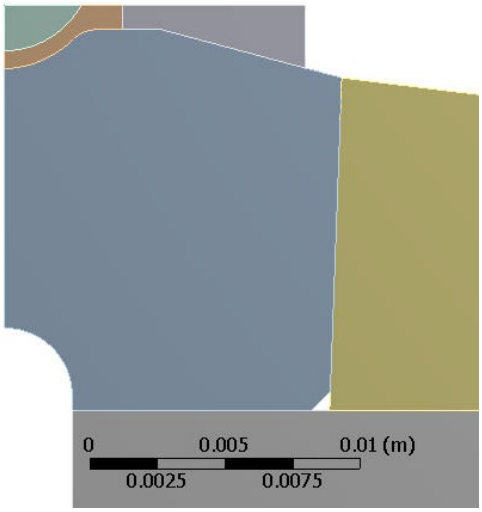

Figure 6.17. FEA model of ZTA anvil cell with adapted geometry from Iizuka[310]. The toroidal groove is substituted by an Aluminium ring in order to avoid failure reported on this critical area. FEA parameters and sample volume (~47 mm^3) remains unaltered from the standard anvil model.

A series of interesting outcomes are available when implementing this geometry in the ZTA anvil numerical model. At 75 tonnes, sample pressure reduces to 4.18 GPa when compared with the standard toroidal anvil (6.3 GPa). Iizuka's Aluminium ring configuration requires up to 125 tonnes to obtain 6.3 GPa. However, for both 75 and 125 tonnes cases the new anvil-gasket interface has a better maximum shear stress distribution when benchmarked with the standard toroidal model. Figure 6.18 displays a FEA path used to study the anvil-gasket interface of this geometry. Figure 6.19 establishes a comparison between a standard ZTA anvil and an Iizuka's adapted anvil at 75 and 125 tonnes.

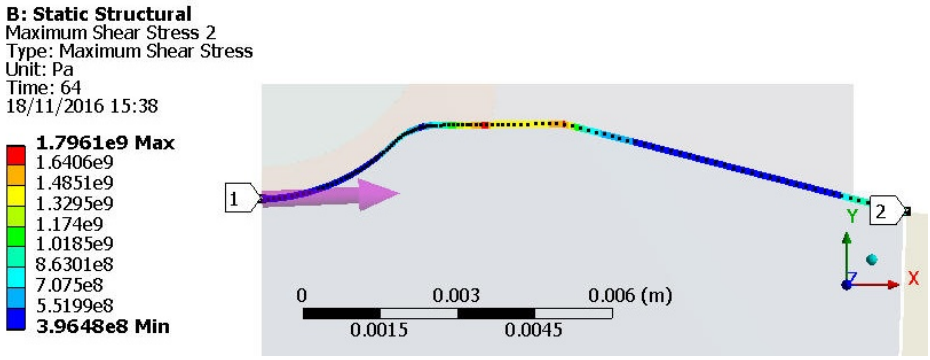

Figure 6.18. FEA path at ZTA anvil's working surface with Iizuka[310] adapted geometry. This type of path has been extensively used in this thesis to evaluate stress behaviour at critical regions of the anvil. As shear stress due to gasket deformation is a well-known fracture agent for high pressure anvils, this path provides a quantification of maximum shear to be evaluated.

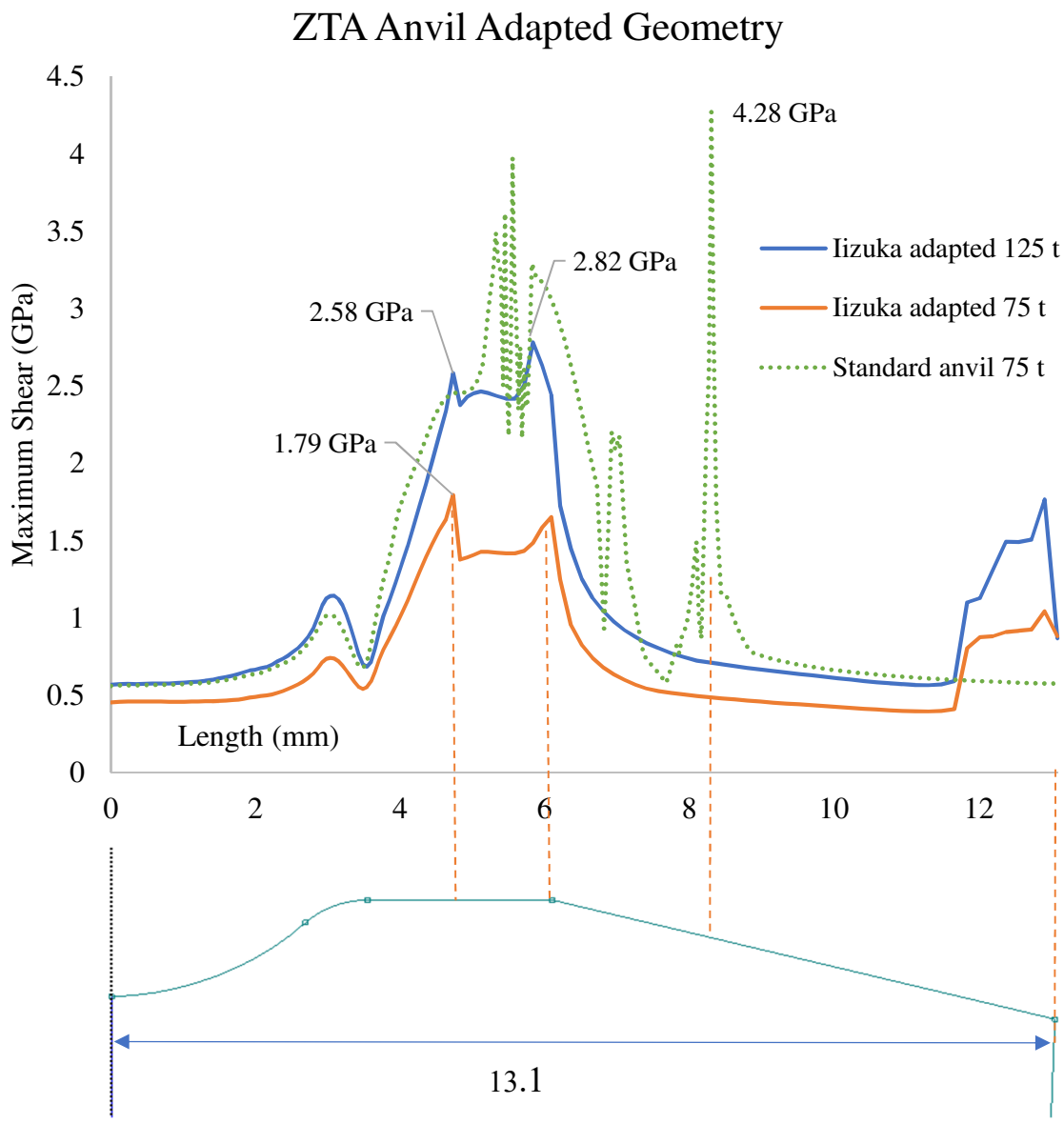

Figure 6.19. Maximum shear stress numerical results of a ZTA anvil working surface with geometrical adaptations and Aluminium ring from Iizuka[310]. Comparing with a standard ZTA anvil geometry, it is possible to visualize how concentration of maximum shear stress is lower at this critical area for the adapted configuration.

For the standard anvil, it was determined how maximum shear (4.28 GPa) was linked with tensile and compressive stress conditions at the failure point at 75 tonnes. The adapted geometry shows a dramatic reduction on this stress at the point where failure has been registered in standard anvils. Maximum shear values of 1.79 GPa for 75 tonnes and 2.82 GPa for 125 tonnes were registered in numerous locations of the anvil-gasket

interface for the adapted geometry. Regarding tensile stress, the adapted geometry shows a prominent peak of 1.41 GPa at the point where the angular aperture initiates. Its magnitude is comparable with tensile stress top values at the standard anvil as it is possible to visualise in Figure 6.20.

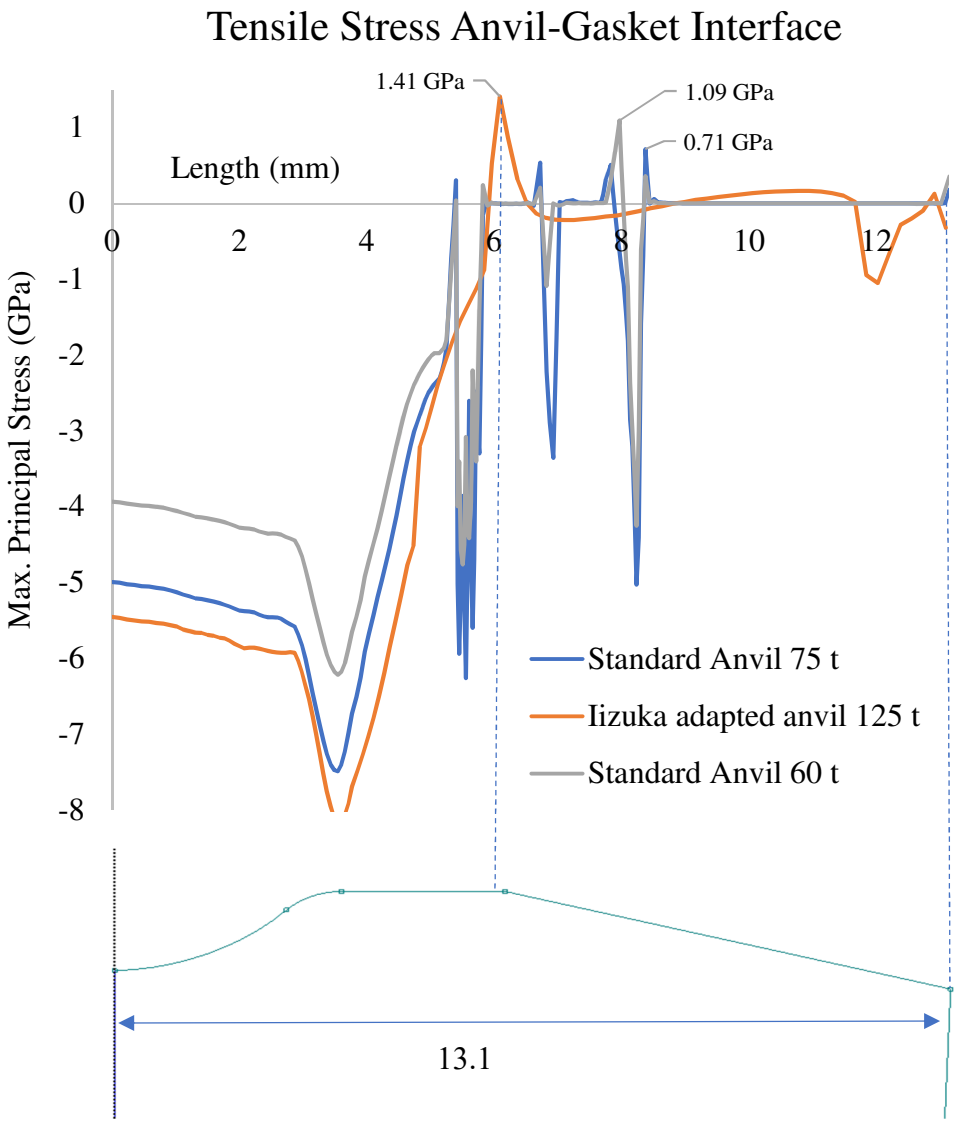

Figure 6.20. Maximum principal stress comparison at the anvil-gasket interface between standard anvil (60 and 75 tonnes) and Iizuka's non-toroidal adapted anvil version (125 tonnes). It is possible to see how the non-toroidal anvil has a prominent tensile stress peak of 1.41 GPa. The FEA model and methodology developed in this thesis can be applied successfully in other geometries and cases.

In synthesis, a non-toroidal gasket adaptation shows reduced shear stress values at the anvil-gasket interface when compared with a standard anvil. The FEA model and methodology developed in this thesis have proven successful when modelling and understanding stress distributions with different geometries and materials. This is promising for the development of new high-pressure instruments and FEA models to support relevant investigations in several fields.

Chapter 7

Conclusions and Future Work

This PhD thesis has effectively implemented the FEA method to model experiments in compressed water, stress and failure modes of standard ZTA toroidal anvils, and geometry optimisation in these components. Additionally, this technique has been applied to assess an alternative ZTA anvil design proposed in literature, showing a great degree of adaptability.

Specific ideas to continue this type of studies are important as computer based numerical methods have an enormous potential in the field of extreme conditions. The following pages synthesise the achievements of this PhD project and provide advice towards future related investigations.

7.1 Introduction

Instrumentation for high pressure neutron diffraction has brought substantial results on various scientific grounds. Chapter 2 is clear about the importance of PE presses equipped with toroidal anvils in contemporary research. This work incorporates a methodology based on the computational numerical method FEA to provide knowledge of the effects of stress accumulation in ZTA toroidal anvils. An experimentally verified failure analysis has been achieved, obtaining results to propose a series of geometrical modifications to optimise mechanical resistance of the anvils and service lifetime.

In addition, it was possible to simulate the rich phase behaviour of statically compressed water for a pressure range of 0 - 6.7 GPa via FEA. Employing the standard ZTA anvil configuration, multiple numerical simulations were performed in water and benchmarked with experimental and literature data. Positive results demonstrate that complex high pressure experiments can be carried out virtually by applying computational numerical methods.

The following sections summarise relevant results collected in this PhD thesis. Advice is given to orientate future research based on FEA methods for high pressure instrumentation and modelling of compressed samples.

7.2 Summary and Conclusions

After a detailed review of high pressure generation, FEA method, ZTA toroidal anvils' standard configuration and its use in PE presses, an FEA model of this high pressure instrument has been produced (Chapters 1- 3). It was a priority to establish a model including realistic conditions in order to obtain accurate results. Aspects such as lateral pre-stress induced by the binding ring, properties of materials, refined mesh in critical areas, gasket's plastic moduli, and frictional coefficients were investigated and explained in detail to be incorporated in the simulations.

By including a water sample in the model, experimental data obtained from ISIS Neutron Laboratory (sample pressure and molar volume versus loads) was used for validation of the loads introduced in the FEA model and to obtain equations of state of water for the simulations. This data series, available in Figure 3.11, has ranges of 0 – 5.38 GPa and 0 – 60 tonnes. Data at 75 tonnes (6.38 GPa) was extrapolated as reports mention how

standard ZTA anvils failure starts from this point. Room temperature liquid water presents a phase transition to Ice VI at ~1 GPa and Ice VII above ~2 GPa.

During the FEA model formulation, it was observed that this procedure is able to simulate the compressed water performance. In light of these results, this project has documented how complex behaviour of a compressed sample can be modelled via computational FEA. Chapters 4 and 5 offer an innovative numerical approach to study statically compressed water steps, including phase transitions for a pressure range of 0 – 6.7 GPa. Low cost and ease of access are among advantages of this technique when compared with experimental set-ups such as gem anvils or PE presses. However, it is important to remark that in natural sciences (specially in Physics), any kind of computer simulations cannot be a substitution for real experiments.

In Chapter 4, static pressure steps for room temperature liquid water were modelled (0 – 1 GPa approximately). Due to the use of a static structural model with an implicit solver in ANSYS, a matrix with slight changes in temperature (22 – 27 ºC) was synchronised with load steps, isotropic elastic properties, and simulation time to obtain accurate results in sample pressure and molar volume. Introduction of a coarse mesh in the compressed sample helped to attain hydrostatic conditions. The loads initially applied in the model were selected to be verifiable with literature results (Bridgman[234] - Grindley[235]).

This methodology was also applied reproducing the experimental liquid water load steps obtained in ISIS Neutron Laboratory. The broad nature of the phase transition liquid water - Ice VI delivered different pressure versus load pattern when compared with literature values previously analysed. Data (bulk moduli and Poisson's ratio in particular) was estimated and adjusted for these experimental cases (Section 4.3), showing FEA flexibility and how mechanical properties of high pressure liquid water can be assessed and obtained from FEA results. There is no precedent in literature regarding FEA studies in compressed liquid water, estimating mechanical properties, pressures and molar volumes.

Including a case of room temperature liquid water at 1 GPa included in Chapter 4, static pressure simulations in solid phases of water (1 – 6.7 GPa) focused on the examination of its impact in adjacent components. The model reproduced the broad phase transition

Ice VI – VII and how stress is transmitted into the TiZr gaskets, ZTA anvils and other surrounding components. In Chapter 5, this series of pressure stages (also following ISIS Laboratory experimental loads) delivered a large data collection of stress distributions used for stress and failure analysis of the standard ZTA anvil.

The main focus of analysis in Chapter 5 lies in maximum and minimum principal stresses and maximum shear stress. These parameters represent the highest stress values in compression, tension, and shear stress in ZTA anvils and surrounding components. Examining stress patterns obtained via FEA, it is clear how shear stress caused by the TiZr gasket deformation impacts the anvil-gasket interface. Meanwhile, the beam aperture area presents stress concentrations typical of a material discontinuity. The region corresponding to the ZTA anvil's chamfer has been also examined due to high stress concentrations caused in part by the binding ring lateral pre-stress.

Having identified areas with high tensile, compressive and shear stress accumulation in the anvil (highly predisposed to suffer damages), FEA results were compared with experimental proof of ZTA anvils collapse starting at 75 tonnes load. ISIS Neutron Laboratory reported how the standard ZTA anvils present high failure rates at the beam aperture, followed by cases during which the damage occurred at the toroid region and at the anvil's chamfer when press-fitting. The model designed in this thesis accurately predicted how these three regions are prone to fail due to stress accumulation.

Further analysis linked failure at the toroid area with a tensile stress accumulation of 710 MPa (shear stress of 4.3 GPa). At the beam aperture, a compressive stress concentration of 3.5 GPa is responsible for the collapse cases. It is clear how massive support principle allows the registration of stress values larger than ZTA strength (4.7 GPa in compression, 290 MPa in tension). Tensile stress at the chamfer area oscillates between 730 MPa and 1.79 GPa. Damages at this region during press-fitting are arbitrary and probably due to inner flaws distribution (Weibull theory). This theory for ceramics can also be associated with the fact that failure alternates between the beam aperture (most of the cases) and the anvil's toroid.

Having completed a variety of stress and failure analyses in the standard ZTA anvil design, a number of geometrical alternatives were proposed in Chapter 6 to prevent stress

accumulation in key areas. The numerical model was adapted without beam aperture (taking into account neutron transparency) and a modified toroid area. These changes allow a better stress distribution in these portions of the anvil, reducing risk of failure at 75 tonnes load and generating valuable knowledge to be considered when designing anvils for neutron diffraction.

Being vital to the increase of mechanical resistance in the anvils, a comprehensive study about the lateral pre-stress effects in the ZTA anvil is included in Appendix 2. Lateral pre-stress reaches maximum values at the standard ZTA configuration, as it has been noticed how anvils suffer damages during the press-fitting process into the binding ring. Correspondingly, stress concentration at the beam aperture produced by the initial lateral pre-stress can produce damages and fissures in this region, weakening the anvil. Before considering a decrease in fractional interference between the anvil and binding ring, the removal of the beam aperture, as suggested in Chapter 6, allows for better massive support conditions. This can maximise the effect of the binding ring without compromising its integrity.

Finally, the stress and failure procedures developed in this thesis were employed also in Chapter 6 to assess an adapted non-toroidal ZTA anvil geometry. This configuration also has different gasket materials than in the standard case and it was recently proposed in literature. The research team in charge of these studies observed and reported how the toroid area is subject to failure, a tendency also identified in this thesis. Therefore, the toroid groove was discarded, including an Aluminium ring as an alternative.

The FEA model and methodology delivered in this PhD thesis has thrived in multiple areas concerning high pressure instruments and experiments, fulfilling the objectives proposed at the start of this project. From estimating material properties at high pressure, to correctly approximate molar volume change and pressure in a water sample and to explain stress behaviour on an anvil, computational methods have a great degree of versatility. Computer-based FEA is a valuable tool for the future of high pressure instrumentation and research.

7.3 Future Work

This PhD project has established FEA as an advantageous and versatile method in high pressure research and instrumentation development. The field of science at extreme conditions requires the analysis of complex models, adapting new trends and information. Computational numerical methods are competitive and adaptable for this matter. Following the results obtained in this thesis, there are various ideas to continue the expansion of this methodology.

- Three-Dimensional Models and Hydrostatic Elements:

In this project, the use of two-dimensional axisymmetric geometries generated accurate results for static structural models. Integration of three-dimensional models would be effective towards adapting dynamic (explicit) solvers. Being a requirement in ANSYS Workbench for dynamic simulations, three-dimensional models could provide powerful insights into the sample volume behaviour and gasket deformation.

Chapter 4 showed that studying molar volume via static structural models (with implicit solvers) requires the involvement of a load, time, temperature, and elastic properties matrix. This was employed to coordinate the evolution of bulk moduli and Poisson's ratio of water with each pressure step. Similarly, Chapter 3 explained how TiZr plastic moduli (E2) were approximated with a technique established by Fang[38]. Dynamic solvers could offer an alternative to these methods as large deformations are induced in both sample and gasket at large loads.

Currently, computer-time is an obstacle when implementing three-dimensional dynamic models. Nevertheless, constant hardware and software progress, besides access to grid-computing and super-computers, can dramatically reduce simulation times in the near future.

Sections 4.2 to 4.4 showed how the water sample was modelled including a coarse mesh, as a strategy to increase hydrostatic conditions. In these sections, compressed liquid water presented hydrostatic results in the range of 95% to 99%. ANSYS has a plug-in to model enclosed fluids for two (HSFLD241) and three (HSFLD242) dimensional models. With this set-up, the fluid to be considered has no temperature, density of pressure gradients,

and is in contact with a solid shell or container (no free surface). Enclosed fluid elements have an extra (pressure) node, where the pressure value for the analysis is evenly applied. Elements are also connected to make a volume and are required to share the same material properties[322].

In this project, to simulate the gasket-sample interaction with HSFLD241 and HSFLD242 ANSYS plug-ins would offer advantages to increase precision in compressed water pressures and volumes results. This incorporation would also contribute on the estimation of mechanical properties and knowledge about a particular sample behaviour.

- Experimental verification of estimated properties:

A number of material properties presently not available in literature were obtained through the FEA methodology produced in this PhD thesis. This is a step forward in high pressure research based on computational numerical methods. Poisson's ratio and bulk moduli values were estimated for water at variable pressure (phase transition areas). ZTA's strengthening factor and TiZr's plastic modulus were also estimated. To expand this useful technique, it is interesting to benchmark numerical results collected in this project with experiments for validation purposes.

- Bending analysis:

Produced by axial loads and lateral pre-stress, bending has been repeatedly mentioned in this project as a source of tensile stress in the anvil. This thesis has focused on the impact the resulting tensile stress has in specific areas of the anvils. However, it would be an interesting design task to quantify the degree of bending induced in the anvils.

In addition, to examine strain in the anvils would be another interesting point to account for design purposes. Having estimated strain values would help to understand how much deformation the (brittle) anvil material suffers under operational conditions, location of critical areas and its limits. Anvil materials such as ZTA are relatively new in this field. Having an extreme conditions strain data collection would help further computational efforts to describe ZTA behaviour for different applications.

To measure strain and bending directly in the ZTA anvils can prove difficult due to the experimental configurations. The current FEA model is capable of calculating both parameters in the entire system.

- Experimental confirmation of optimised geometries:

Chapter 6 proposed a series of modifications in the standard ZTA anvil design, achieving more favourable stress distributions in susceptible areas for a load limit of 75 tonnes. By discarding the beam aperture and adding more surrounding material into the toroid final segment, it has been demonstrated how stress conditions improved via FEA. To validate these new anvil geometries, it is of great interest to manufacture and perform a series of experiments with the optimised anvil geometries.

Given that most of failure cases in standard ZTA anvils happened at the beam aperture, an initial set of experiments can consider a design without this discontinuity. Aspects such as data acquisition and neutron transparency can be initially evaluated, followed by anvil's mechanical resistance and stability at 75 tonnes. A mechanical resistance test could be performed to visualise areas such as the TC platen beam aperture (expected to accumulate stress) and toroid area. The modified toroid area could be included in a second set of experiments in order to assess its impact in the mechanical resistance of this area.

Results can supply data for an FEA model similar to the one developed in this thesis, generating a ZTA anvil design with large sample capacity and higher pressure targets. ZTA has shown a suitable performance as anvil material due to its neutron transparency and mechanical properties. This ceramic material is a strong candidate for a new generation of toroidal anvil to be installed in PE presses available around the world.

Appendix 1

Sample Properties Calculations

Chapters 3 and 4 delivered interesting results in compressed water and ZTA anvil stress distributions via FEA. Simulations developed in this thesis required a series of data regarding mechanical properties of water at room temperature and variable pressure. Bulk moduli being crucial to obtain accurate results, a series of calculations were performed on experimental and literature data to feed the numerical model. This Appendix describes the procedure executed to obtain this information.

As seen in Chapter 2, bulk modulus (B) can be related to the derivative of pressure with respect to density and calculated with Equations 2.1 and 2.2, where ρ is density and P pressure:

$$B = \rho \frac{dP}{d\rho} \qquad \text{Equation A1-1}$$

Also mentioned earlier, values of pressure and density are available from literature (liquid water) and neutron diffraction data (Ice VI and VII). Obtaining and deriving equations of state for each data series provides insights on bulk moduli of water at variable pressure. Before proceeding with the explanation, Table A1-1 shows the sample's initial properties, fundamental to define the rest of the calculations. Densities can be obtained by relating molar volume with molar weight.

Table A1-1. Sample's initial properties.

Sample (water) Properties at Room Temperature and Pressure		
Initial volume (Standard ZTA anvil and gasket)	46.97	mm^3
Molar weight	18.01	g/mol
Initial density	1	g/cm^3
Amount of moles in sample	0.0026	mols

A1-1 Liquid Water (0 – 0.588 GPa Pressure Range)

Chapter 4 provides a sequence of FEA static pressure steps simulations in water up to 1 GPa. Section 4.2 refers to the pressure range of 0 – 0.588 GPa, reproducing via FEA pioneering experimental data from literature. Using the concept described in Equation A1-1, bulk moduli information input in the FEA model was calculated from

Bridgman[234] for this pressure range. Table A1-2 shows the compressed water data at 20 ºC. By plotting pressure vs density from this Table (Figure A1-1), it is possible to find its equation of state from a polynomial approximation.

Table A1-2. Bridgman's compressed water experimental data, 0 – 0.588 GPa pressure range[234].

Pressure (kgf/cm^2)	Pressure (approx., GPa)	Molar Volume (20 °C, cm^3/mol)	Density (g/cm^3)
1	0	18.048	0.997
500	0.049	17.690	1.018
1000	0.098	17.352	1.037
1500	0.147	17.072	1.054
2000	0.196	16.805	1.071
2500	0.245	16.573	1.086
3000	0.294	16.366	1.100
3500	0.343	16.185	1.112
4000	0.392	16.012	1.124
5000	0.490	15.698	1.147
6000	0.588	15.430	1.167

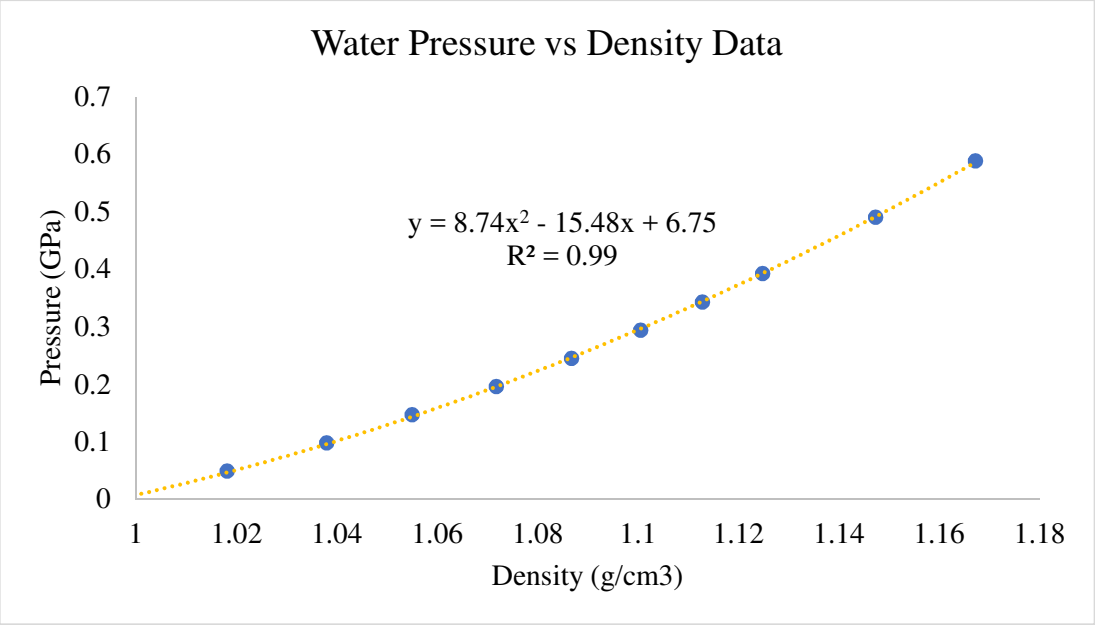

Figure A1-1. Bridgman's[234] water pressure vs density data (0 – 0.588 GPa). From this plot, a polynomial approximation can be delivered towards its derivation into an equation of state for bulk moduli as a function of density using Equation A1-1.

From the equation of state obtained in Figure A1-1 and using Equation A1-1:

$$P = 8.74\rho^2 - 15.48\rho + 6.75 \qquad \text{Equation A1-2}$$

$$B = \rho\frac{dP}{d\rho} = \rho(17.48\rho - 15.48) \qquad \text{Equation A1-3}$$

Evaluating Equation A1-3 with density data from Table A1-2, it is possible to obtain bulk moduli values for 0 – 0.588 GPa pressure range (available in Table A1-3 and used in Table 4.1). From Figure A1-2 a function can be obtained in order to interpolate bulk moduli data in this pressure range.

Table A1-3. Bulk moduli data for water at variable pressure (0 – 0.588 GPa), based on experiments by Bridgman[234].

Pressure (kgf/cm^2)	Pressure (approx., GPa)	Bulk Moduli (GPa)
1	0	1.95
500	0.049	2.35
1000	0.098	2.75
1500	0.147	3.11
2000	0.196	3.48
2500	0.245	3.81
3000	0.294	4.12
3500	0.343	4.41
4000	0.392	4.69
5000	0.490	5.24
6000	0.588	5.74

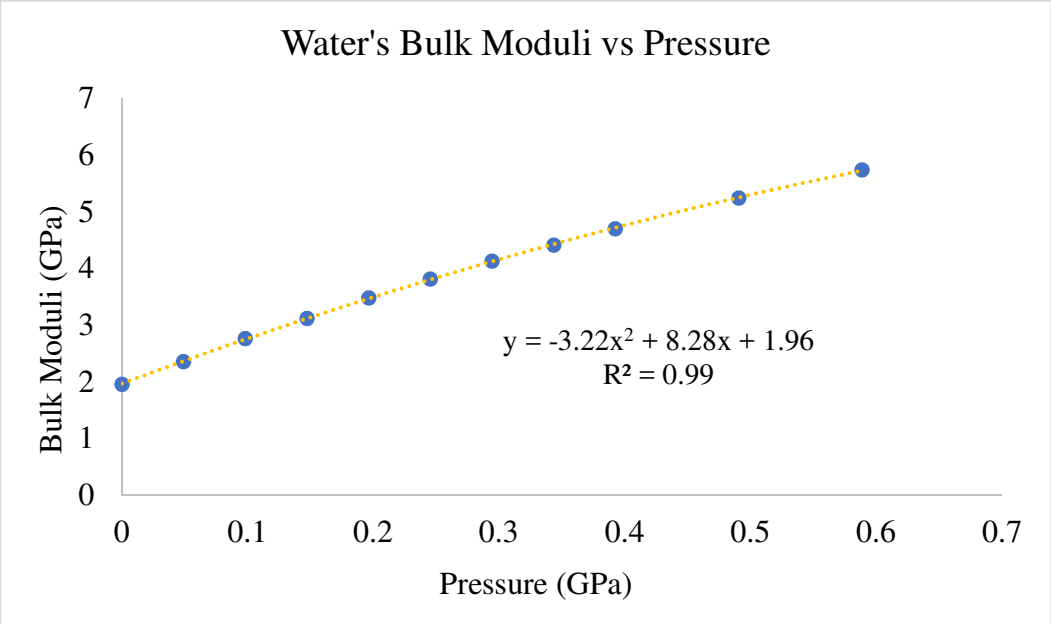

Figure A1-2. Bulk moduli vs. pressure, calculated from the obtained Bridgman's[234] equation of state.

A1-2 Liquid Water (0.588 – 1 GPa Pressure Range)

For water pressures higher than 0.588 GPa corresponding to Section 4.3 of this thesis, experimental data from Grindley[235] was used in the models and extrapolated to obtain

bulk moduli with a similar procedure. Data in compressed water for this publication reaches 0.8 GPa, making extrapolation more accurate up to 1 GPa. Table A1-4 shows the data considered for this endeavour. Grindley's whole data set is visible in Figure A1-3 (from 0 to 8000 bars in steps of 200 bars).

Table A1-4. Compressed water data from Grindley[235] (extrapolated from 8200 bars).

Pressure (bars)	Pressure (GPa)	Specific Volume cm^3/g	Density (g/cm^3)	Bulk Moduli (GPa, Equation A1-5)	Molar Volume (cm^3/mol)
5800	0.58	0.857	1.167	5.67	15.43
6000	0.60	0.854	1.171	5.77	15.38
6200	0.62	0.851	1.175	5.87	15.33
6400	0.64	0.848	1.179	5.97	15.28
6600	0.66	0.846	1.183	6.07	15.23
6800	0.68	0.843	1.186	6.17	15.18
7000	0.70	0.840	1.190	6.27	15.13
7200	0.72	0.838	1.194	6.36	15.09
7400	0.74	0.835	1.197	6.45	15.04
7600	0.76	0.833	1.201	6.55	15.00
7800	0.78	0.830	1.205	6.64	14.95
8000	0.80	0.828	1.208	6.73	14.91
8200	0.82	0.828	1.208	6.73	14.91
8400	0.84	0.826	1.210	6.80	14.88
8600	0.86	0.825	1.213	6.86	14.85
8800	0.88	0.823	1.215	6.92	14.82
9000	0.90	0.822	1.217	6.98	14.80
9200	0.92	0.820	1.219	7.03	14.77
9400	0.94	0.819	1.221	7.09	14.75
9600	0.96	0.818	1.223	7.13	14.73
9800	0.98	0.817	1.224	7.18	14.71
10000	1.00	0.816	1.226	7.22	14.69

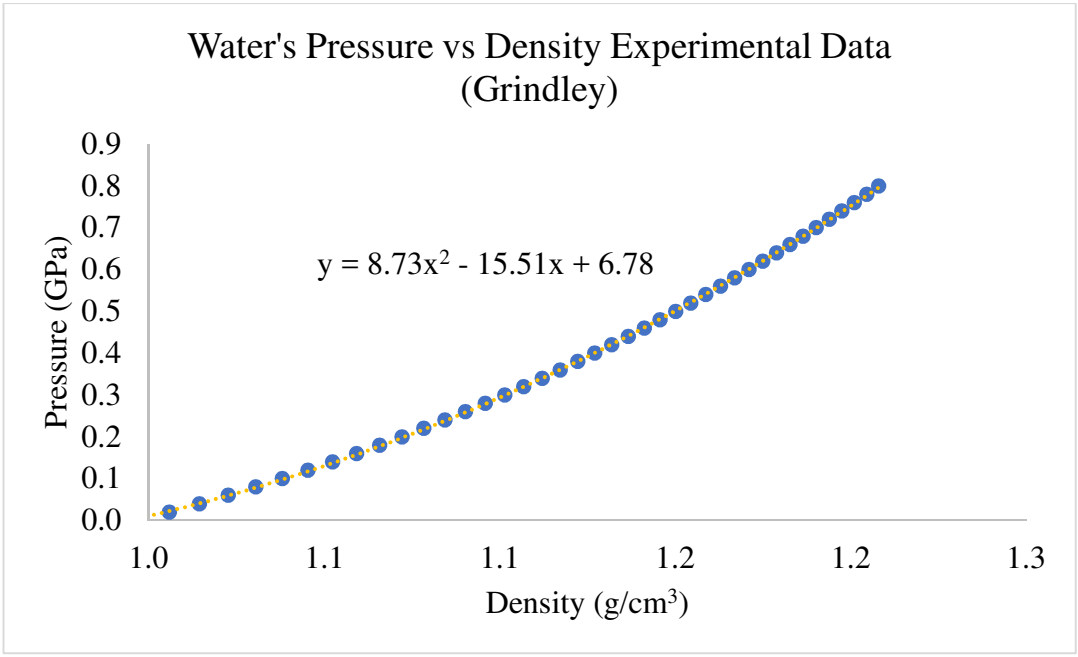

Figure A1-3. Pressure vs density experimental data from Grindley[235].The polynomial approximation obtained from this data set can be derived to find bulk moduli values for water at this pressure range.

Following Equation A1-1, bulk moduli can be calculated from Gridley's experimental data series.

$$P = 8.73\rho^2 - 15.51\rho + 6.78 \qquad \text{Equation A1-4}$$

$$B = \rho\frac{dP}{d\rho} = \rho(17.46\rho - 15.51) \qquad \text{Equation A1-5}$$

Bulk moduli obtained and extrapolated from 0.8 GPa to 1 GPa is present in Table A1-4. Figure A1-4 graphically displays bulk moduli acquired (and extrapolated) versus water pressure.

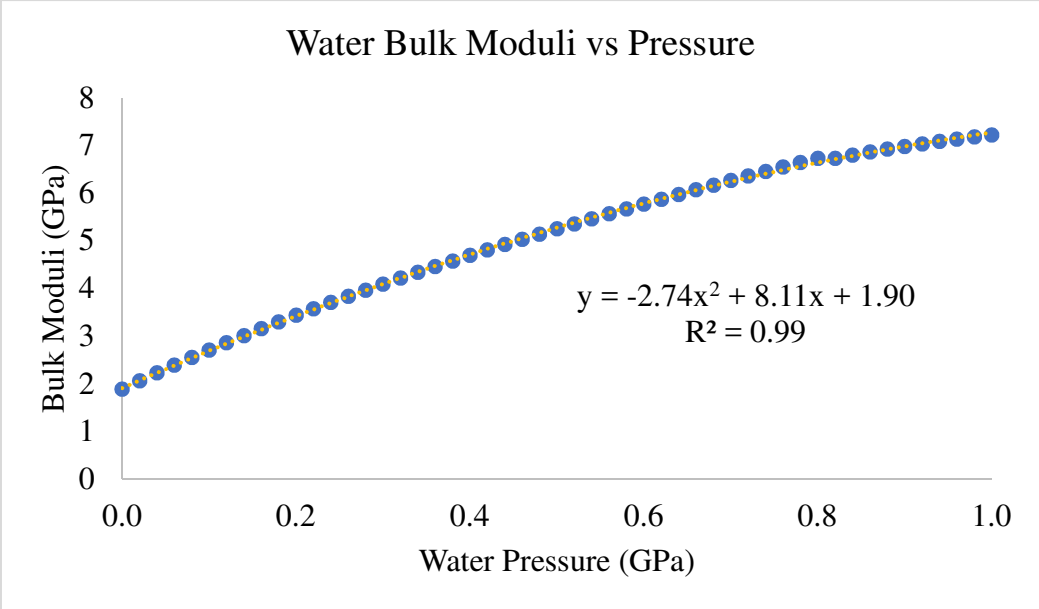

Figure A1-4. Water bulk moduli vs pressure (0 – 0.8 GPa). Data from Grindley[235]

Table 4.4 (repeated in this Appendix) has a selection of data from Bridgman and Grindley, based in calculations showed here.

*Table 4.4 (repeated). Experimental data and numerical results for compressed water from 0 to 0.979 GPa, estimations made using data from literature and adjusted bulk moduli values.*Refers to Type II model in Section 4.4.2.*

Liquid water				
Load (tonnes)	Pressure ISIS Experiments (GPa)	Pressure ANSYS	Bulk Mod. (GPa) Bridgman[234]	Bulk Mod. (GPa) Grindley[235]
0	0	---	1.64	
5	0.029	0.026	2.20	
10	0.498	0.452	5.28	
12.5	0.930	0.944		7.08
15	0.879	8.780		6.92
17.5	0.871	0.865		6.89
20	0.979	1.080		7.22
*21.5	---	1.000		7.27

A1-3 Ice VI and VII

Ice VI and VII neutron data collected in ISIS Neutron Laboratory can be analysed towards obtaining relevant information for the FEA model. Table A1-5 shows the initial data obtained while Table A1-6 shows the lattice parameters, molar volumes and densities at high pressure for both forms of water. Ice VI has a tetragonal structure (a=b≠c, Z=10) and Ice VII cubic (a=b=c, Z=2).

Table A1-5. Ice VI and VII lattice parameters.

Ice VI and VII Structural Data - ISIS Neutron Laboratory				
Ice VI Lattice Parameters Å (Tetragonal)		Ice VII Lattice Parameters Å (Cubic)	Ice VI Pressure (GPa)	Ice VII Pressure (GPa)
a = b	c	a = b = c		
6.18	5.69	3.364	1.290	2.068
6.15	5.66	3.348	1.533	2.210
6.13	5.63	3.332	1.871	2.772
6.115	5.61	3.306	2.062	3.475
6.116	5.611	3.285	2.068	4.124
		3.267		4.775
		3.251		5.380

Table A1-6. Ice VI and VII lattice parameters, molar volumes and densities at various loads and pressures. Experiments performed in ISIS Neutron Laboratory.

Ice VI					
Load (tonnes)	Pressure (GPa)	$V=a^2*c$ ($Å^3$)	Molar Volume ($Å^3$/mol)	Molar Volume (cm^3/mol)	Density (g/cm^3)
22.5	1.290	217.314	1.31E+25	13.09	1.38
25	1.533	214.075	1.29E+25	12.89	1.40
27.5	1.871	211.557	1.27E+25	12.74	1.41
30	2.062	209.775	1.26E+25	12.63	1.43
32.5	2.068	209.882	1.26E+25	12.64	1.42
Ice VII					
35	2.068	38.068	1.15E+25	11.46	1.57
37.5	2.210	37.528	1.13E+25	11.30	1.59
40	2.772	36.992	1.11E+25	11.14	1.62
45	3.475	36.133	1.09E+25	10.88	1.66
50	4.124	35.449	1.07E+25	10.67	1.69
55	4.775	34.869	1.05E+25	10.50	1.72
60	5.380	34.359	1.03E+25	10.35	1.74

Plotting pressure vs density data from Table A1-6, and using Equation A1-1 (as implemented in liquid water cases), an equation of state can be obtained towards its derivation to find bulk moduli values. Figure A1-5 illustrates for both Ice VI and VII cases. After this calculation, the functions can be evaluated and bulk moduli obtained for each pressure value. Figure A1-5 shows pressure versus density behaviour.

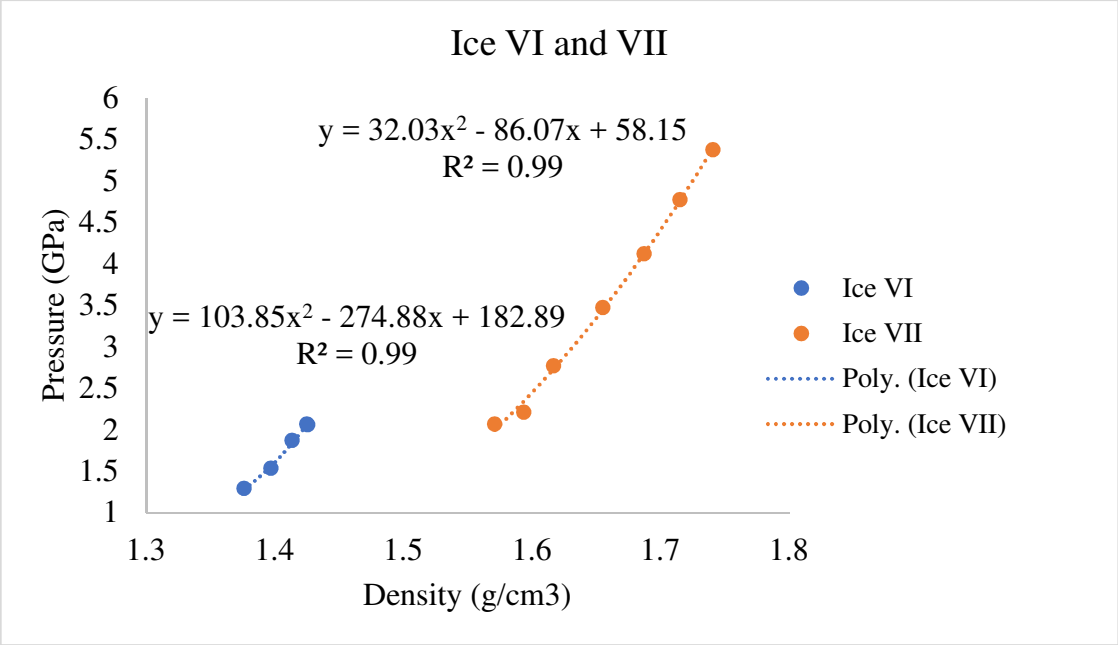

Figure A1-5. Ice VI and VII pressure vs density experimental data, obtained from ISIS Neutron Laboratory. Their polynomial approximations can be derived towards obtaining bulk moduli as performed in the cases of liquid water at variable pressure.

Ice VI:

$$P = 103.85\rho^2 - 274.88\rho + 182.89 \qquad \text{Equation A1-6}$$

$$B = \rho\frac{dP}{d\rho} = \rho[(2 * 103.85\rho) - 274.88] \qquad \text{Equation A1-7}$$

Ice VII:

$$P = 32.038\rho^2 - 86.07\rho + 58.15 \qquad \text{Equation A1-8}$$

$$B = \frac{dP}{d\rho} = \rho[(2 * 32.03\rho) - 86.07] \qquad \text{Equation A1-9}$$

Evaluating Equations A1-7 and A1-9 with density values experimentally acquired in ISIS Neutron Laboratory, bulk moduli for Ice VI and VII was obtained. This is available in Table A1-7 and it was used in Table 5.1. Figure A1-6 plots bulk moduli values vs pressure, delivering a polynomial function for interpolation and extrapolation of bulk moduli values.

Table A1-7. Ice VI and VII bulk moduli data (calculated from Equations A1-7, A1-9 and density data from Table A1-6). Data at 75 and 80 tonnes was extrapolated.

Ice VI (ISIS Neutron Laboratory)		
Load (tonnes)	Pressure (GPa)	Bulk Moduli (GPa)
22.5	1.290	15.071
25	1.533	21.342
27.5	1.871	26.476
30	2.062	30.257
32.5	2.068	30.028
Ice VII (ISIS Neutron Laboratory)		
35	2.068	22.934
37.5	2.210	25.576
40	2.772	28.336
45	3.475	33.088
50	4.124	37.181
55	4.775	40.881
60	5.380	44.326
75	6.439	50.898
80	6.704	52.119

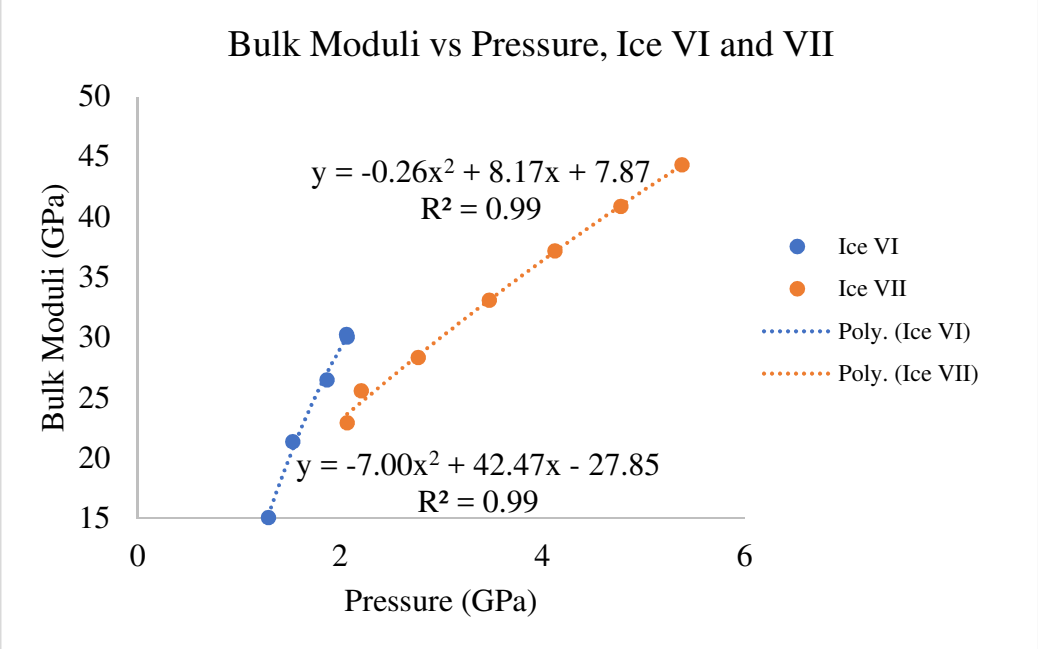

Figure A1-6. Ice VI and VII bulk moduli vs pressure, obtained from equations A1-7, A1-9 and Table A1-6. Curves plotted are useful for interpolation and extrapolation of data.

A1-4 Water Multilinear Isotropic Hardening

In FEA simulations, it was noticed how the inclusion of an isotropic multilinear hardening curve is useful in the obtaining accurate results. This feature available in ANSYS engineering data is used for simulations with large strain rates or proportional loading[311] (principal stresses maintain constant directions and constant ratios of their values[312]).

To add a stress (sample pressure, GPa) vs plastic strain (m/m), volumetric strain values were calculated from literature, while neutron data is available for this thesis. Bulk modulus can also be defined in terms of volume[313]:

$$B = V\frac{dP}{dV} \qquad \text{Equation A1-10}$$

Furthermore, compressibility (K) is the inverse of bulk modulus:

$$K = \frac{1}{B} = \frac{1}{V}\frac{dV}{dP} \qquad \text{Equation A1-11}$$

By integrating both sides of Equation A1-11 at a determined pressure interval, it is possible to obtain the change in volume:

$$\int_0^P K * V = \int_0^P \frac{dV}{dP}$$

$$V * \int_0^P K = \Delta V \qquad \text{Equation A1-12}$$

The term ΔV/V can be considered as volumetric strain, linked with plastic strain for the FEA simulations purpose. To find these values, the inverse of the equations of state for each water phase (Equations A1-5, A1-7 and A1-9) was integrated for each pressure step. Progressively adding each plastic strain step, along with its corresponding pressure value, generated the multilinear isotropic hardening curve introduced in this thesis.

Table A1-8. Multilinear isotropic hardening curve introduced for the water sample in the FEA models.

Multilinear Isotropic Hardening	
Pressure (GPa)	Plastic Strain (m^3/m^3)
0	0
0.20	0.07
0.34	0.11
0.49	0.14
0.59	0.16
1.29	0.25
1.53	0.26
1.87	0.28
2.06	0.28
2.07	0.28
2.21	0.29
2.77	0.31
3.48	0.33
4.12	0.35
4.78	0.37
5.38	0.38
6.43	0.42
6.70	0.42

Appendix 2

Lateral Pre-stress Analysis

A2-1 Stress Analysis of Binding Ring Pre-stress on ZTA Anvils

This Appendix provides complementary information about the lateral pre-stress effect of the binding ring in standard ZTA anvils, and how it is distributed. Comparative insights of the standard ZTA anvil with and without binding ring are also included. This thesis has mentioned how this method has been widely implemented in multiple high pressure devices such as gem and other toroidal anvil cells.

Information provided by ISIS Neutron Laboratory stated that the anvil sits proud 2.45 mm on the binding ring before press-fitting (this is the remaining length for the anvil to reach the bottom of the ring). Considering the 1.5º lateral angle in both anvil and binding ring, an interference of 0.124 mm can be calculated. Section 3.3.7 mentioned how the introduction of an offset value of 0.0642 mm from the binding ring to the anvil was simulated in ANSYS. Figure A2-1 illustrates the current configuration and binding effect on ZTA anvils.

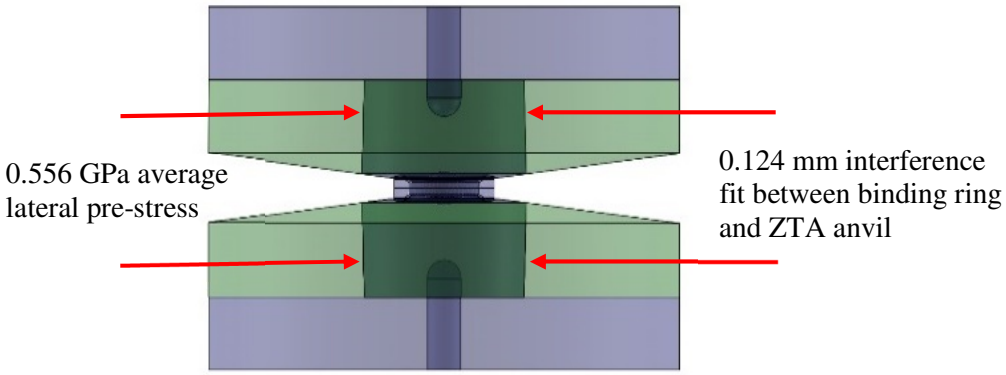

Figure A2-1. Schematic representation of the binding ring's effect on ZTA anvils produced by a 0.124 mm interference fit. The arrows indicate how lateral compressive pre-stress is offered by the maraging steel binding effect to the anvils. This method has been successfully implemented in high pressure apparatuses, increasing its operational load range by counteracting anvil's bending and lateral expansion.

To quantify the lateral pre-stress impact in standard ZTA anvils, the FEA model produced in this thesis was solved without axial (operative) load. Figures A2-2 and A2-3 present a general overview on principals and maximum shear stresses at 0 tonnes load. It is possible to notice that the beam aperture area is being exposed to initial stress concentrations, compressive stress values of 1.55 and 2.11 GPa can be noticed in this critical area. A top

compressive stress value of 6.98 GPa is visible at the chamfer area, also discussed in Chapter 5. Section 5.6 discussed how the anvil's lateral angle (1.5º) and its wedge effect cause larger compressive stress values at the bottom of the anvil. With respect to the anvil's core, it is possible to observe a progressive increase in compressive stress, from 0.34 GPa to 1.10 GPa.

Regarding tensile stress, values in the order of 100 MPa are present at the toroid area and beam aperture. A value of 730 MPa is reached at the chamfer area. These stresses are introduced in the system due to bending in the anvil. However, it is believed that this initial bending occurs with opposite direction than bending caused by the axial force, counteracting its effect to benefit the anvils' mechanical resistance. These stresses are minimal in comparison with compressive stresses and not linked with any kind of initial damages in the anvils.

It is useful to understand the initial stress situation in critical areas of the anvil. As exposed in Section 5.5, the initial stress accumulation at the beam aperture can introduce micro-fractures and initial damages in the anvil, weakening its structure.

In a more detailed analysis, it is possible to study the total amount of FEA nodes available in the ZTA anvil model. Figure A2-4 shows the minimum principal stress values across the anvil's body. The entire ZTA anvil has an initial average compressive stress value of 0.6 GPa. This result is similar when compared with the lateral pre-stress at the anvil-binding ring interface studied in Section 5.6 (0.55 GPa). Peak compressive stresses available in this graph are present at the chamfer area as studied in this thesis.

Meanwhile, Figure A2-5 shows the tensile stress accumulation in the standard ZTA anvil. As mentioned, tensile stress is minimal at 0 tonnes axial load. In fact the maximum principle stress has an average negative value, -12.8 MPa, having a 730 MPa peak at the chamfer region. Considered in Chapters 5 and 6, the chamfer area has characteristics of a stress concentrator.

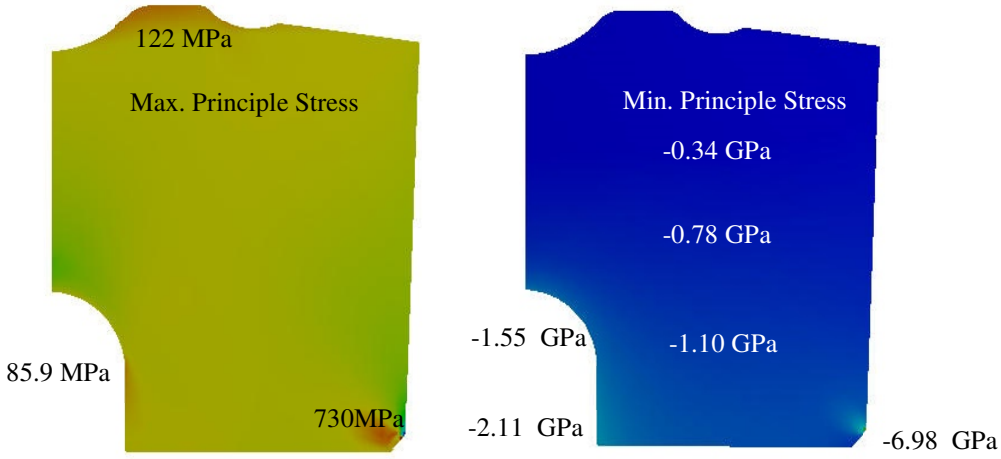

Figure A2-2. Maximum and minimum principal stress FEA results for a ZTA anvil with no axial (operational) load. Lateral pre-stress due to the binding ring causes compressive stress across the entire anvil, inducing tensile stresses due to bending.

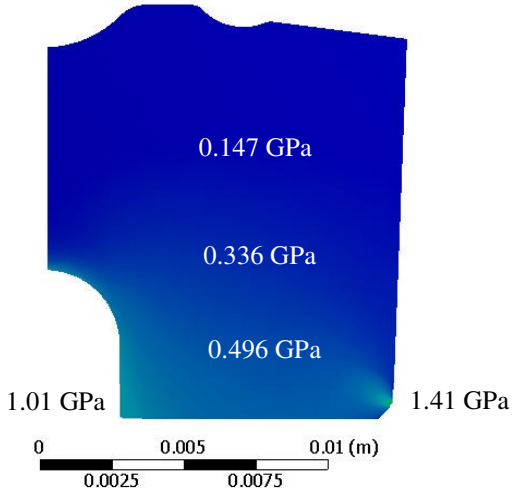

Figure A2-3. Maximum shear stress FEA results for a ZTA anvil with no axial load. Internal shear can be caused by bending of the anvil and helps to counteract bending caused by axial load when the anvil is in operation.

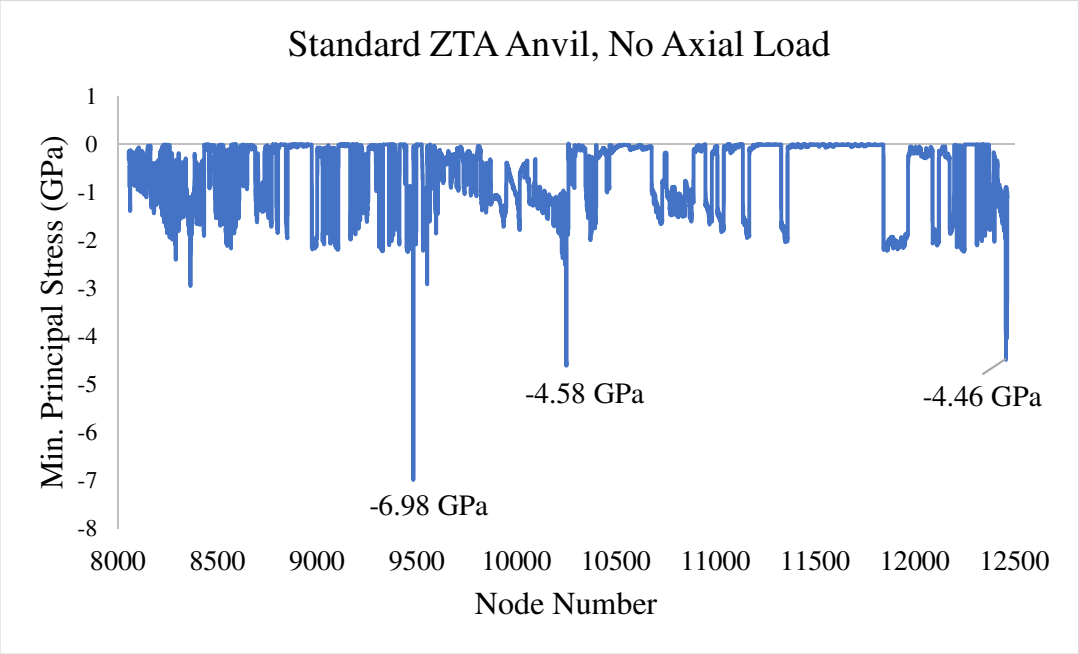

Figure A2-4. Minimum principle stress in the totality of the ZTA anvil nodes at 0 tonnes axial load. Peak values correspond to the chamfer area (Section 5.6). Discarding these peak values most of the anvil has an average pre-stress of 0.6 GPa.

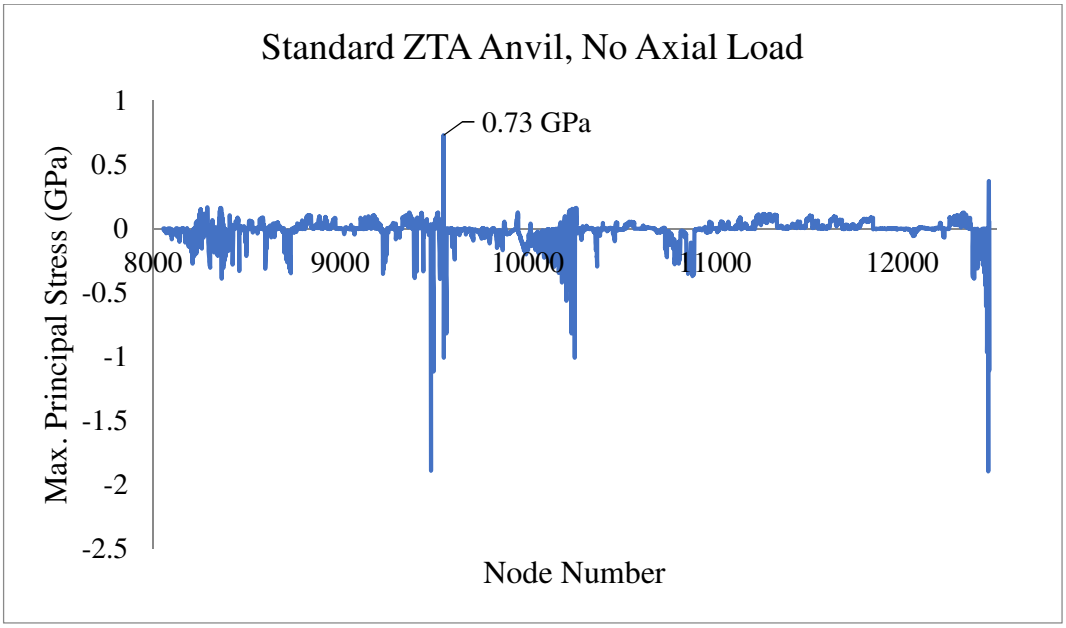

Figure A2-5. Maximum principle stress in the totality of the ZTA anvil nodes at 0 tonnes axial load. Peak values correspond to the chamfer area (Section 5.6). The anvil has an average maximum principle stress of -12.8 MPa.

Having evaluated the binding ring impact in a ZTA anvil with no axial load, it is interesting to observe its influence when the anvil reaches the load limit established in this project (75 tonnes). For this purpose, principals and maximum shear stress values were extracted from the nodes of a standard ZTA anvil model and compared with a configuration which excludes the binding ring. In this regard, Figure A2-6 presents how minimum principal stress has a similar pattern and magnitudes across the anvils in both scenarios. As explained in multiple sections of this PhD thesis, compressive stress values surpass ZTA limit due to the massive support, reporting top values of -14 GPa.

On the other hand, Figure A2-7 displays a dramatic variance between models when dealing with tensile stress accumulation. The model without binding ring is subject to tensile stress practically across the entire anvil's body when compared with its counterpart. Tensile stresses reach values up to 3.1 GPa, thrice as high as the top value registered in a standard ZTA anvil model. This plot is fundamental to recognise the key function of the binding ring, reducing potential damaging tensile stresses at the anvil's core.

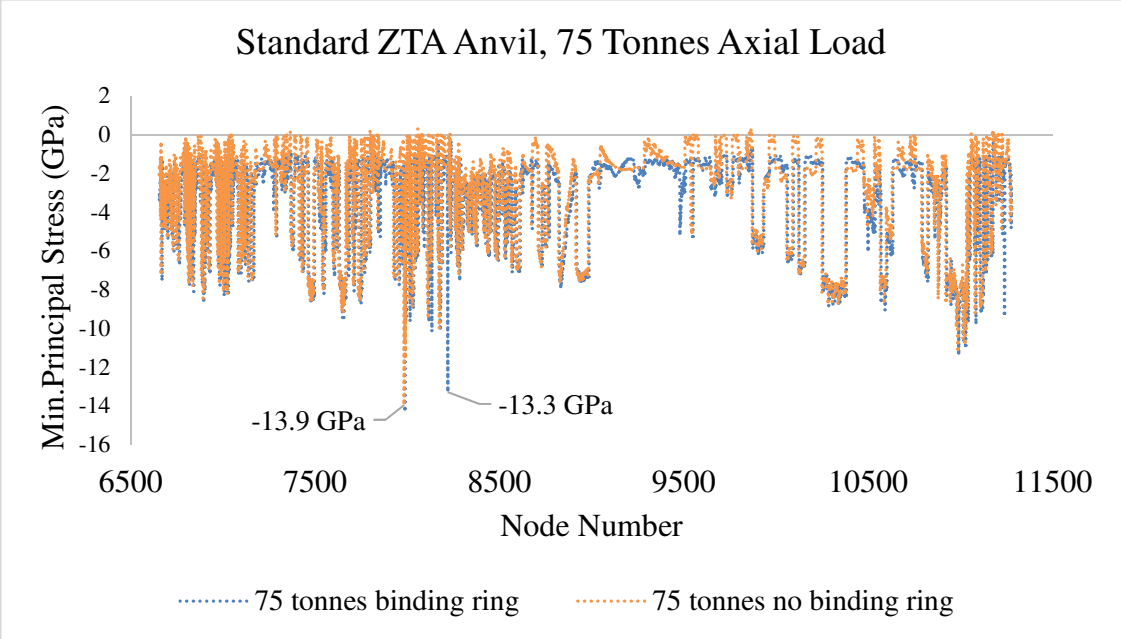

Figure A2-6. FEA minimum principal stress results comparison between a ZTA anvil (75 tonnes axial load) standard and without binding ring. This graph includes the totality of the anvil's nodes; it is possible to see how both cases present similar results due to the axial force applied.

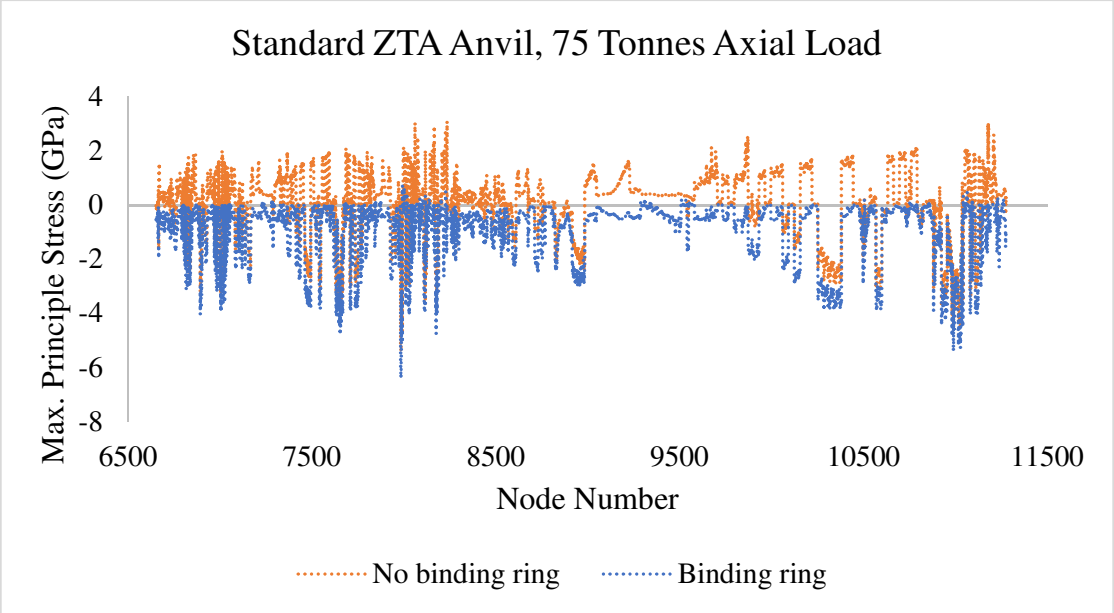

Figure A2-7. FEA maximum principal stress results comparison between a ZTA anvil (75 tonnes axial load) with and without binding ring. It is clear how the anvil without a binding ring displays a large amount of nodes under tension, with values up to 3 GPa. In contrast, most of the nodes examined in the anvil, with a binding ring installed, remain under compression, presenting few nodes under moderate tension.

From Figures A2-6 and A2-7, it is expected that the model with larger values of tensile and compressive stress will show higher shear stress regions as well. This is evident for the numerical model with no binding ring in Figure A2-8, where it is possible to benchmark its shear stress condition with the standard model.

Although the model without a binding ring has higher shear stress in general, the top value of 4.27 GPa corresponds to the toroid region due to gasket shear, being independent of the binding ring (as seen in Section 5.4). The shear stress peak value of 5.33 GPa corresponds to the chamfer at the anvil's back due to the binding ring (examined in section 5.6).

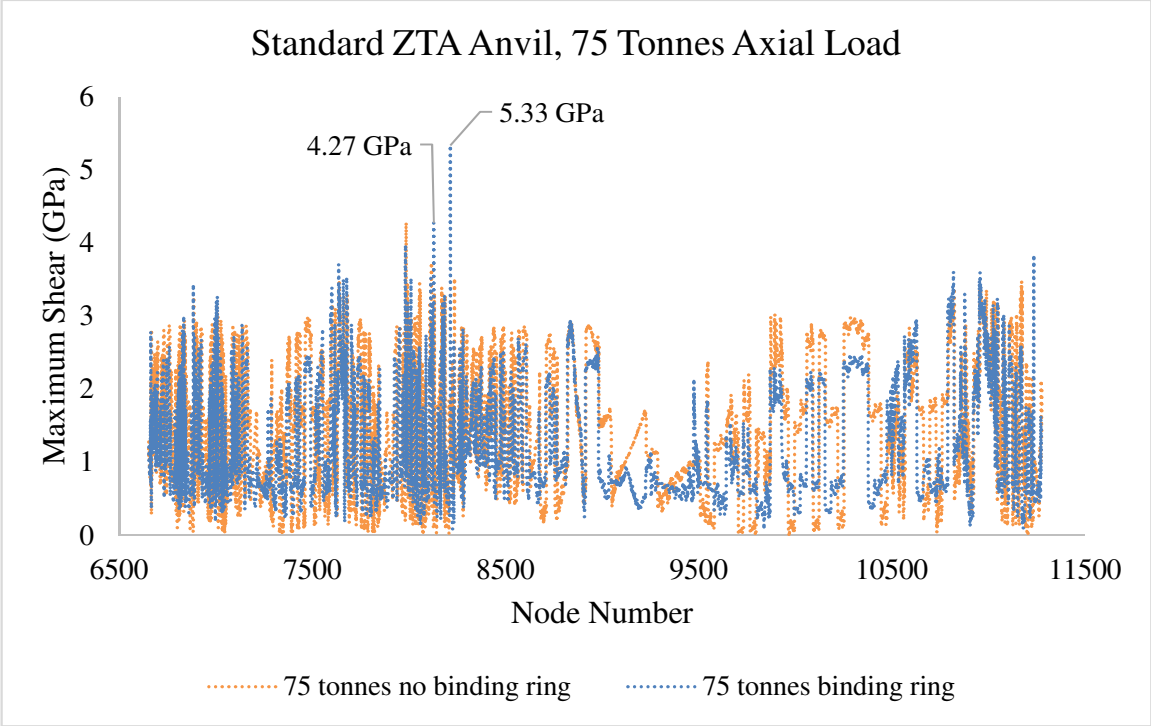

Figure A2-8. FEA maximum shear results comparison between a ZTA anvil (75 tonnes axial load) with and without binding ring. As a consequence of the large tensile stress accumulation at the anvil without binding ring, it is possible to identify larger shear stress values than in the case with a binding ring.

In synthesis, it is evident how the presence of a binding ring prevents accumulation of tensile stresses across the ZTA anvil's body introduced by bending and Poisson's effect, reducing internal shear as well. Ceramic anvils have a reduced tensile strength, making clear how the binding ring is vital for an appropriated operation. While benefits of having a binding ring are known from laboratory experience, the FEA results collected in this PhD thesis quantify the binding ring impact and establish a method for future analysis.

Finally, an interesting detail emerges when the direction of lateral stress is analysed. It is possible to visualise how, during an axial load increase from 0 to 75 tonnes, a deviation on its horizontal compressive nature is produced. At 75 tonnes, pre-stress acts in an almost 45° direction. This behaviour is a result of local bending on the anvil, which might not be perceptible due to minimal effect but which is noticed in this type of analysis.

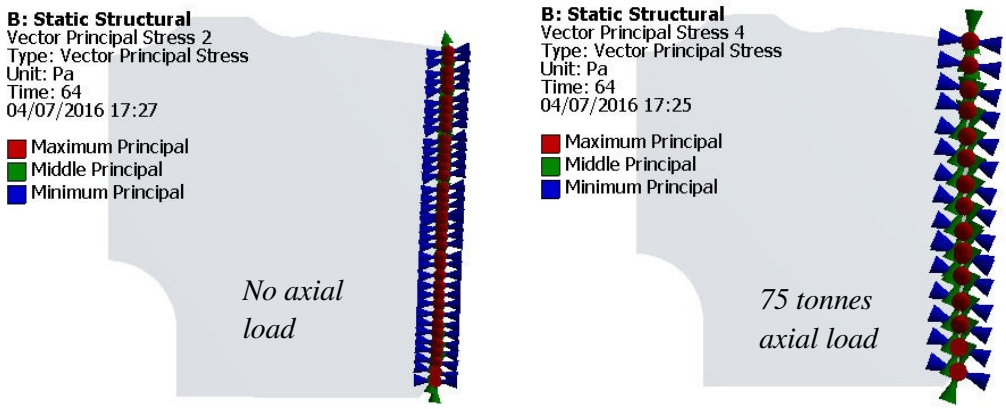

Figure A2-9. Comparison between ZTA anvils at 0 and 75 tonnes axial load. It becomes visible that the minimum principal stress direction changes when the anvil is loaded. This parameter is directly correlated with the lateral pre-stress effect. This thesis has proven the effectiveness of using a binding ring. Anvil's failure cannot be linked to this phenomenon, however it provides good insights into understanding lateral pre-stress behaviour and how anvil's bending is transferred to the binding ring.

Appendix 3

Technical Drawings of ZTA Anvils: Standard Toroidal Anvil, Optimised Toroidal Anvil and Toroidless Anvil Version

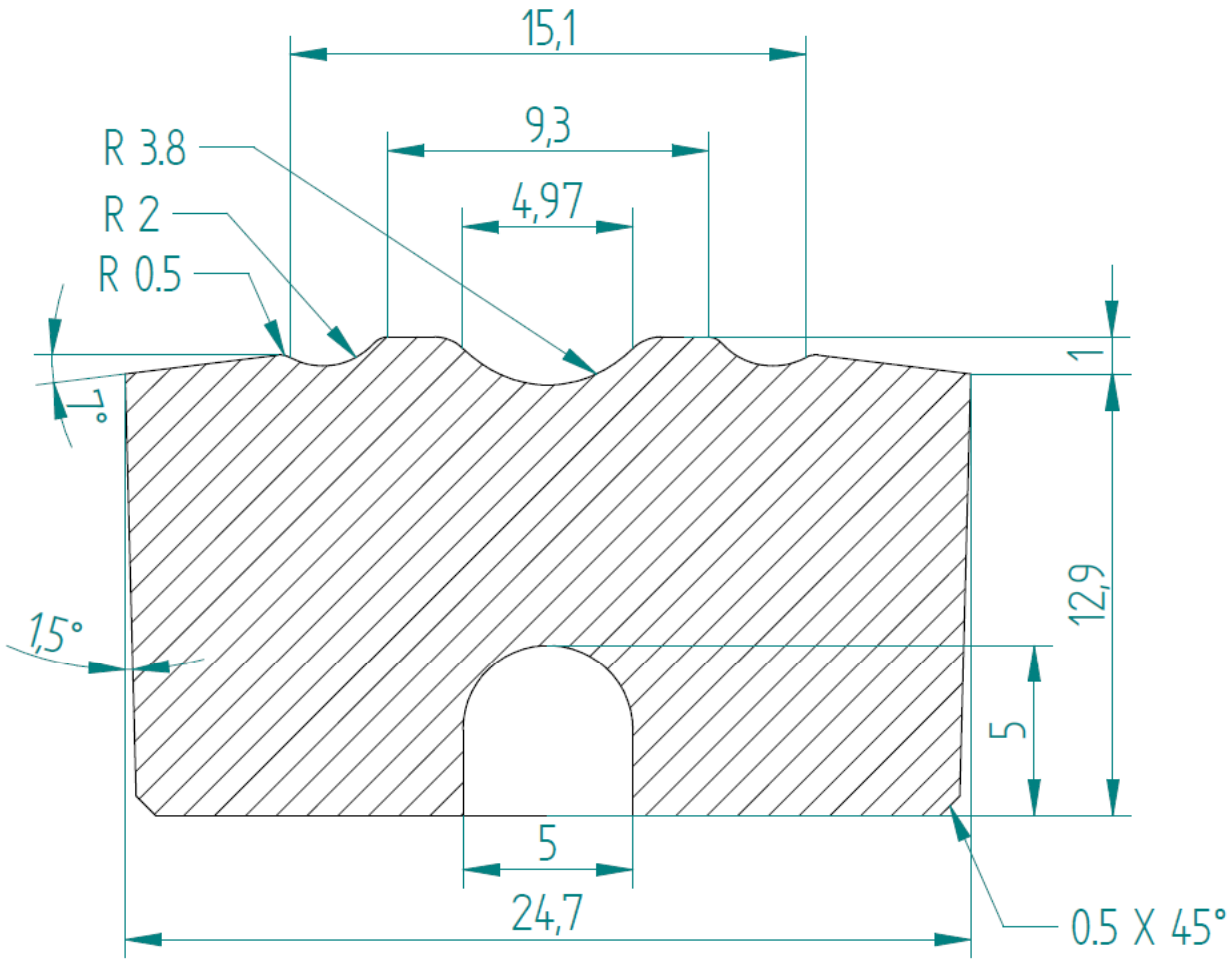

SECTION A-A
Scale 10:1

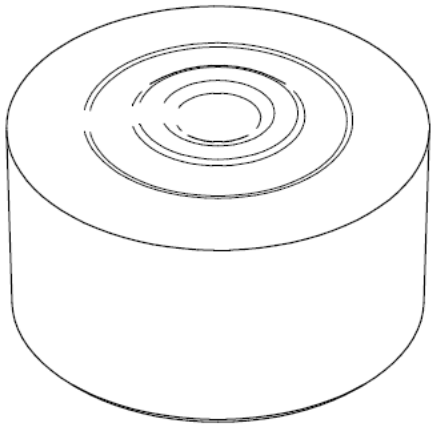

Scale 5:1

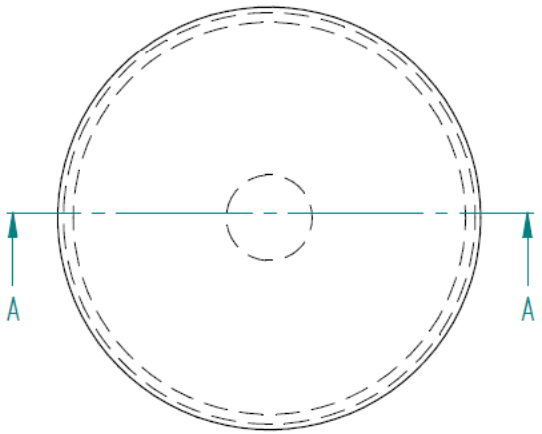

Scale 5:1

STANDARD ZTA TOROIDAL ANVIL
DIMENSIONS IN MM

REVISION HISTORY			
REV	DESCRIPTION	DATE	APPROVED

	NAME	DATE
DRAWN	JCF	02/10/17
CHECKED	KVK	
ENG APPR		
MGR APPR		

UNLESS OTHERWISE SPECIFIED DIMENSIONS ARE IN MILLIMETERS

Solid Edge

TITLE: ZTA toroidal anvil (standard)

SIZE A2 | DWG NO 1/3 | REV

FILE NAME: zta standard anvil draft.dft

SCALE: Indicated | WEIGHT: | SHEET 1 OF 3

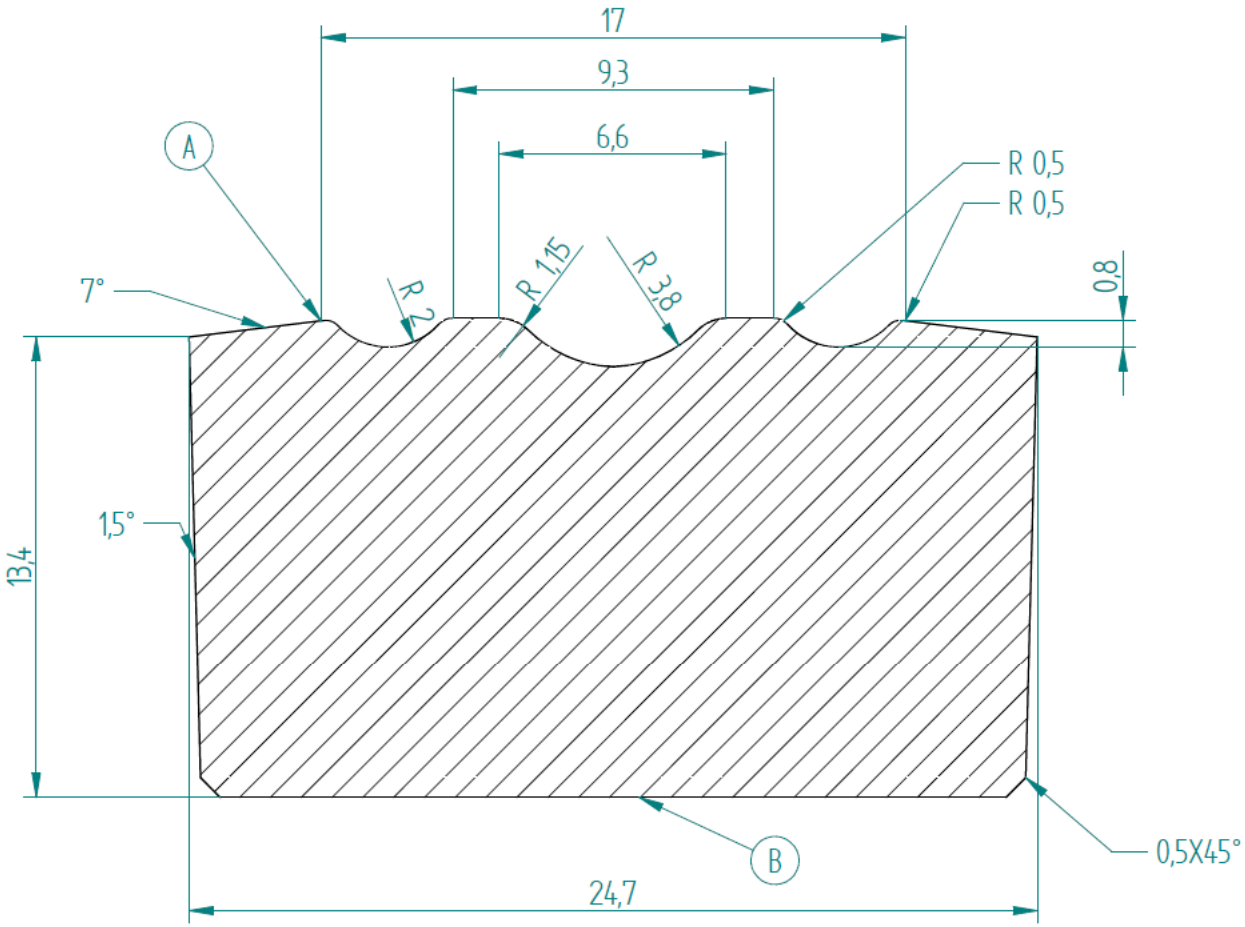

SECTION A-A

Scale 10:1

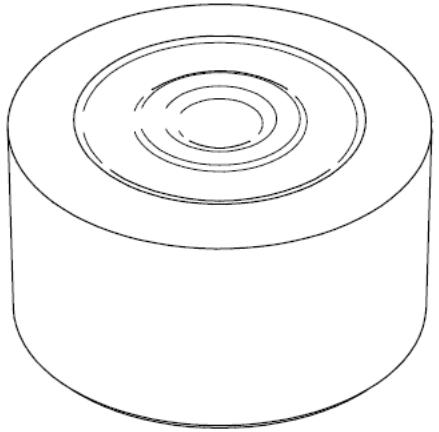

Scale 5:1

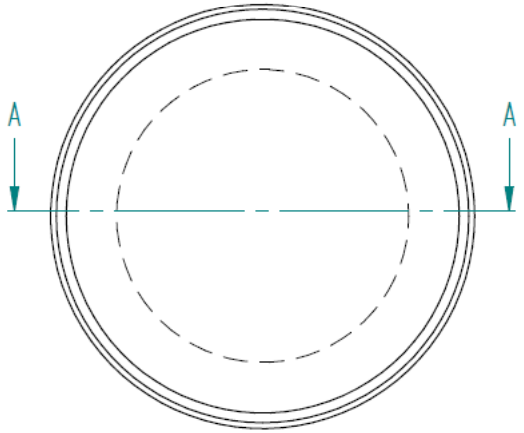

Scale 5:1

ZTA toroidal anvil optimised after stress and failure analysis.
Modifications with respect to standard ZTA toroidal anvil:
A- Toroid shoulder higher B- Beam apperture suppressed.

Dimensions in mm

REVISION HISTORY			
REV	DESCRIPTION	DATE	APPROVED

	NAME	DATE
DRAWN	JCF	02/14/17
CHECKED	KVK	
ENG APPR		
MGR APPR		

UNLESS OTHERWISE SPECIFIED DIMENSIONS ARE IN MILLIMETERS

Solid Edge

TITLE: ZTA toroidal anvil (optimised)

SIZE A2 | DWG NO 2/3 | REV

FILE NAME: zta anvil optimised - shoulder 7 deg.dft

SCALE: indicated | WEIGHT: | CSE - Univ. of Edinburgh

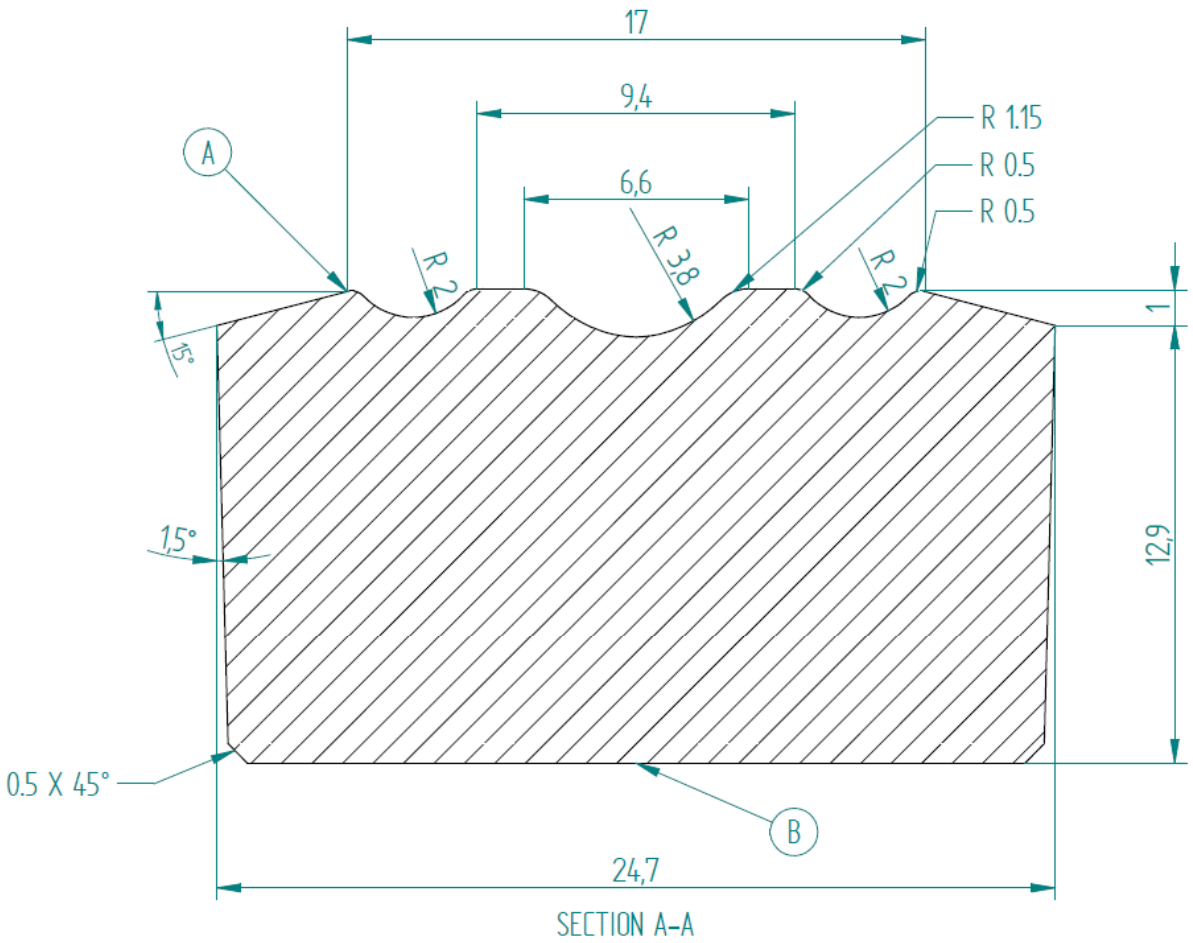

SECTION A-A

Scale 10:1

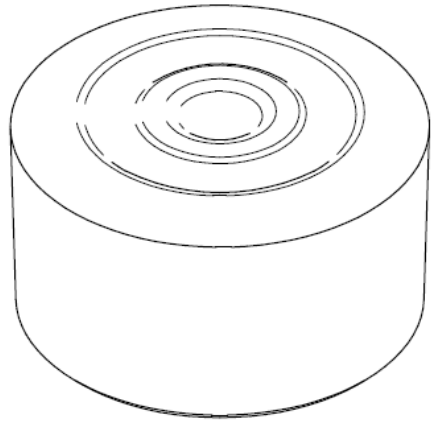

Scale 5:1

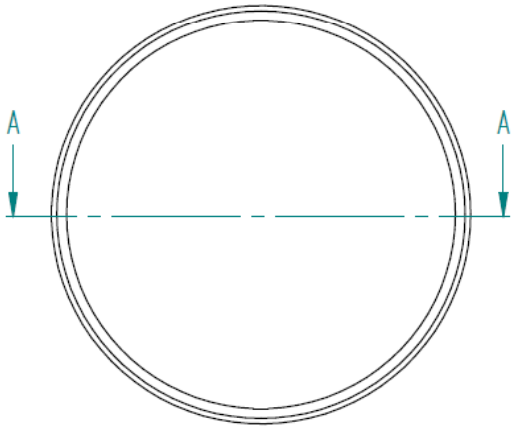

Scale 5:1

ZTA toroidal anvil optimised after stress and failure analysis.
Modifications with respect to standard model:
A- Higher toroid shoulder and greater angular access.
B- Beam aperture suppressed.

Dimensions in mm

REVISION HISTORY			
REV	DESCRIPTION	DATE	APPROVED

	NAME	DATE
DRAWN	JCF	02/13/17
CHECKED	KVK	
ENG APPR		
MGR APPR		

UNLESS OTHERWISE SPECIFIED DIMENSIONS ARE IN MILLIMETERS

Solid Edge

TITLE: ZTA toroidal anvil optimised

SIZE A2 | DWG NO 3/3 | REV

FILE NAME: zta anvil optimised - shoulder 15 deg.dft

SCALE: indicated | WEIGHT: | SHEET 3 OF 3

REVISION HISTORY			
REV	DESCRIPTION	DATE	APPROVED

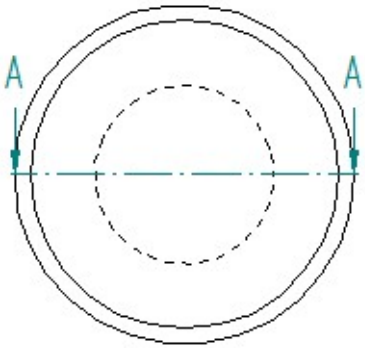

Scale 10:1

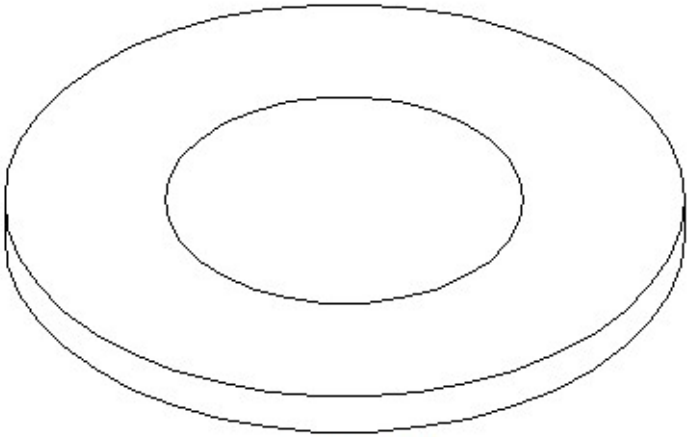

Scale 20:1

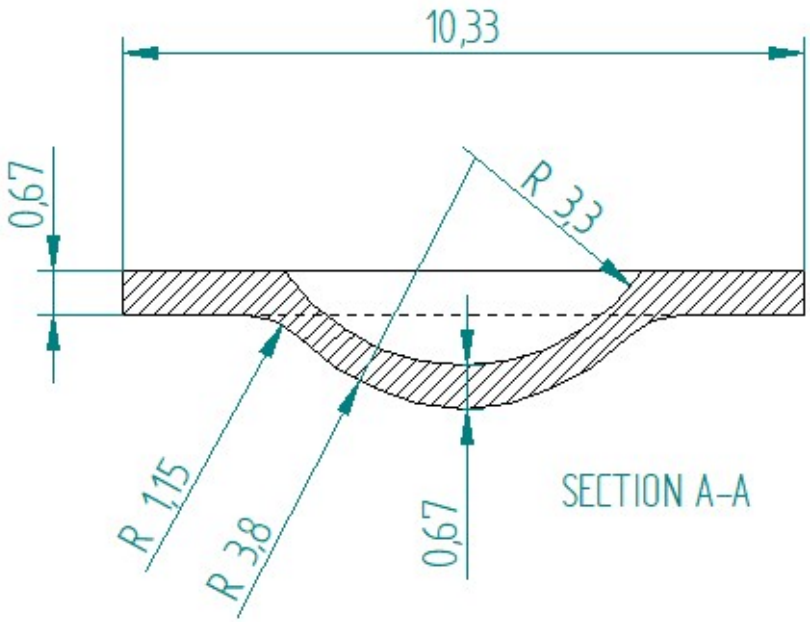

TiZr gasket for standard ZTA anvil
Dimensions in mm

	NAME	DATE
DRAWN	JCF	03/23/17
CHECKED	KVK	
ENG APPR.		
MGR APPR.		

UNLESS OTHERWISE SPECIFIED
DIMENSIONS ARE IN MILLIMETERS

Solid Edge

TITLE: TiZr gasket for standard ZTA anvil

SIZE: A2 | DWG NO: V1 | REV

FILE NAME: gasketdft

SCALE: 1.000 | WEIGHT:

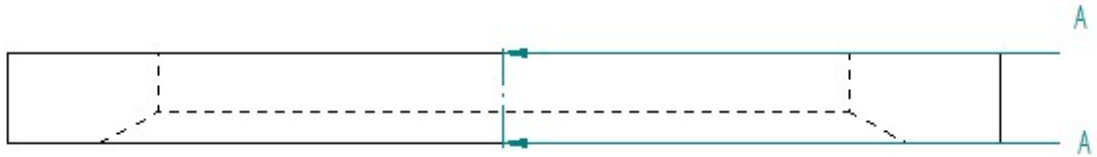

Scale 20:1

SECTION A-A

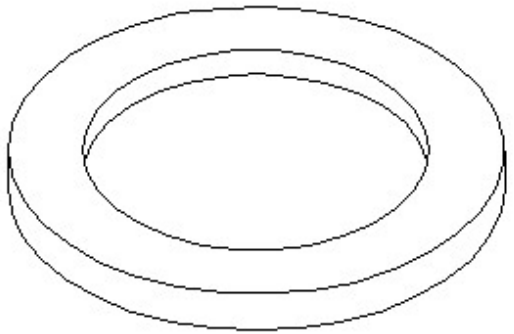

Scale 10:1

TiZr gasket ring for standard ZTA anvils

Dimensions in mm

REVISION HISTORY			
REV	DESCRIPTION	DATE	APPROVED

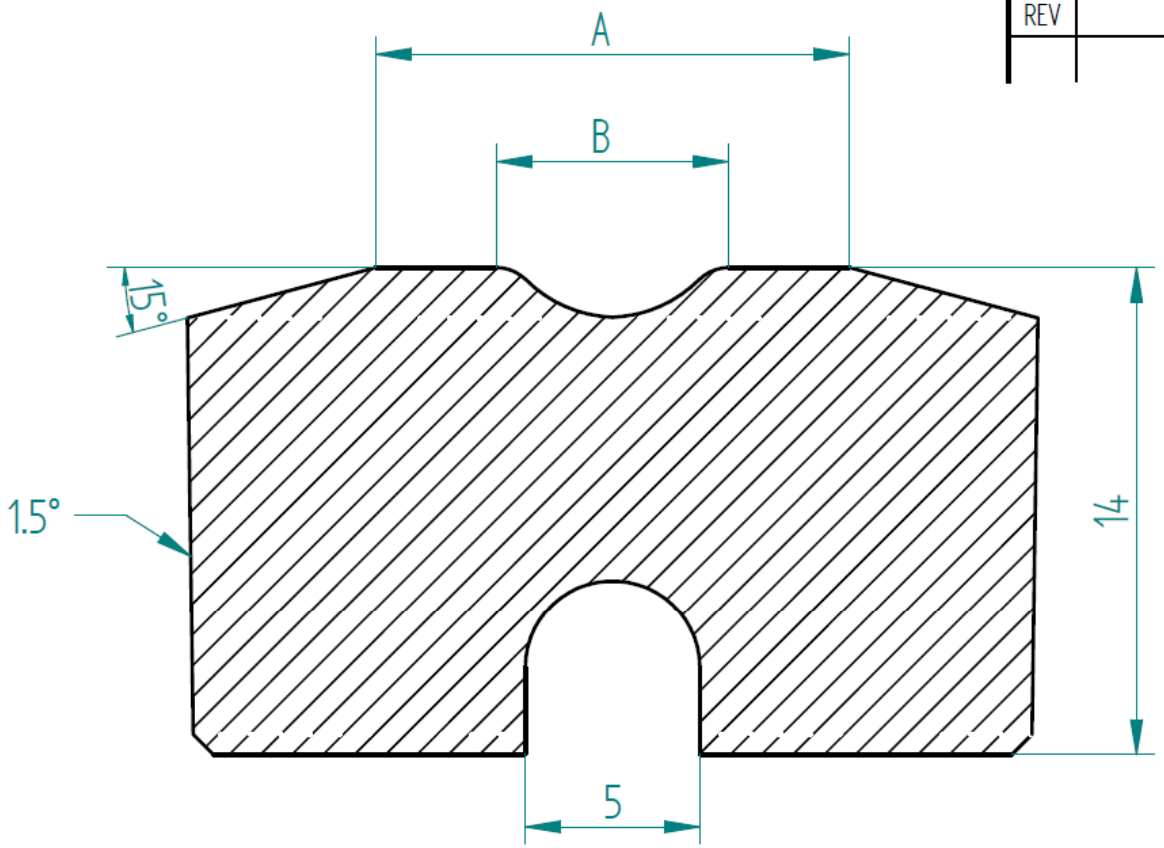

SECTION A–A

Scale 5:1

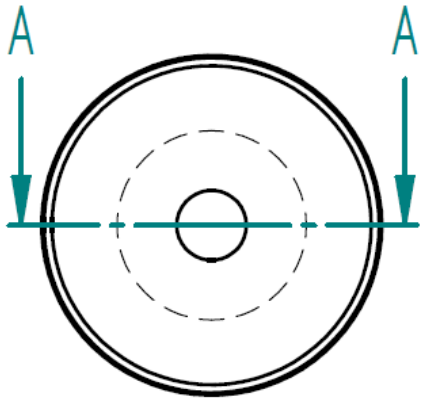

Komatsu investigated the influence of the A/B ratio in anvils for high pressure neutron scattering made of different materials. For ZTA, an A/B ratio of 8 / 4 mm was used, resulting in a peak sample pressure of 12 GPa approx.

	NAME	DATE
DRAWN	JCF	02/18/17
CHECKED	KVK	
ENG APPR		
MGR APPR		

UNLESS OTHERWISE SPECIFIED DIMENSIONS ARE IN MILLIMETERS

Solid Edge

TITLE: ZTA high pressure neutron anvil (Komatsu, 2014)

SIZE	DWG NO	REV
A4		

FILE NAME: klotz zta anvil.dft

SCALE: indicated	WEIGHT:	SHEET 1 OF 1

References

1. Bridgman, P. W. The measurement of high hydrostatic pressure. II. A secondary mercury resistance gauge. in *Proceedings of the American Academy of Arts and Sciences* **44,** 221–251 (JSTOR, 1909).

2. Bridgman, P. W. An experimental determination of certain compressibilities. in *Proceedings of the American Academy of Arts and Sciences* **44,** 255–279 (JSTOR, 1909).

3. Bridgman, P. W. The measurement of high hydrostatic pressure. I. A simple primary gauge. in *Proceedings of the American Academy of Arts and Sciences* **44,** 201–217 (JSTOR, 1909).

4. Jayaraman, A. Diamond anvil cell and high-pressure physical investigations. *Rev. Mod. Phys.* **55,** 65–108 (1983).

5. Bridgman, P. W. The technique of high pressure experimenting. in *Proceedings of the American Academy of Arts and Sciences* **49,** 627–643 (JSTOR, 1914).

6. Eremets, M. *High Pressure Experimental Methods*. (Oxford University Press, 1996).

7. Dubrovinsky, L., Dubrovinskaia, N., Prakapenka, V. B. & Abakumov, A. M. Implementation of micro-ball nanodiamond anvils for high-pressure studies above 6 [thinsp] Mbar. *Nat. Commun.* **3,** 1163 (2012).

8. C. E. Weir, E. R. Lippincott, A. V. Valkenberg, and E. N. B. Infrared studies in the 1- to 15-micron region to 30,000 atmospheres. *J. Res. Natl. Bur. Stand.* **63A,** (1959).

9. J. C. Jamieson, A. W. Lawson, and N. D. N. New device for obtaining x-ray diffraction patterns from substances exposed to high pressure. *Rev. Sci. Instrum.* **30,** 1016–1019 (1959).

10. Hemley, R. J. & Ashcroft, N. W. The revealing role of pressure in the condensed matter sciences. *Phys. Today* **51,** 26 (1998).

11. Block, S. & Piermarini, G. The diamond cell stimulates high-pressure research. *Phys. Today* **29,** 44 (1976).

12. Bassett, W. A. Diamond anvil cell, 50th birthday. *High Press. Res.* **29,** 163–186 (2009).

13. Xu, J. *et al.* Ultrahigh pressures in gem anvil cells. *High Press. Res.* **15,** 127–134 (1996).

14. Goncharenko, I. N. Neutron diffraction experiments in diamond and sapphire anvil cells. *High Press. Res.* **24,** 193–204 (2004).

15. Nellis, W. J. Dynamic experiments: An overview. Proceedings - International School of Physics Enrico Fermi **147,** 109–126 (IOS Press; Ohmsha; 1999, 2002).

16. Chhabildas, L. C., Davison, L. & Horie, Y. *High-pressure shock compression of solids VIII: The science and technology of high-velocity impact*. **8,** (Springer Science & Business Media, 2005).

17. Nellis, W. J. Dynamic high pressure: Why it makes metallic fluid hydrogen. *J. Phys. Chem. Solids* **84,** 49–56 (2015).

18. Thiot Ingenierie. Light gas guns. (2013). Available at: http://www.thiot-ingenierie.com/products/launchers/two-stage-light-gas-guns/. (Accessed: 17th January 2017)

19. Young, D. A. *Phase diagram of the elements*. (University of California Press, 1991).

20. Chandra, D, Reilly J, C. R. Metal Hydrides for Vehicular Applications: The State of the Art. *JOM* **58,** 26–32 (2006).

21. Dmitriev, V. *et al.* Pressure-temperature phase diagram of $LiBH_4$: Synchrotron x-ray diffraction experiments and theoretical analysis. *Phys. Rev. B* **77,** 174112 (2008).

22. Lide, D. R. *CRC handbook of chemistry and physics*. (Taylor & Francis, 2006).

23. Nakamura, T. Scientists recreate ultra-high pressure and temperature of innermost Earth - allowing synthesis of mantle and core materials . (2007). Available at: http://www.jamstec.go.jp/e/about/press_release/20100405/. (Accessed: 17th January 2017).

24. Balny, C., Masson, P. & Heremans, K. High pressure effects on biological macromolecules: from structural changes to alteration of cellular processes. *Biochim. Biophys. Acta - Protein Struct. Mol. Enzymol.* **1595,** 3–10 (2002).

25. Basset, J., Wollman, E. & Macheboeuf, M. Etudes sur les effets biologiques des ultrapressions. Action des pressions très élevées sur les bactériophages des spores et sur les autolysines. *CR Acad. Sci* **200,** 1072 (1935).

26. Suzuki, K. Studies on the kinetics of protein denaturation under high pressure. *Rev. Phys. Chem. Japan* **29,** 91–98 (1960).

27. Wu, H. Studies on denaturation of proteins. XIII. A theory of denaturation. *Chin J Physiol* **5,** 321–344 (1931).

28. Knorr, D. Novel approaches in food-processing technology: new technologies for preserving foods and modifying function. *Curr. Opin. Biotechnol.* **10,** 485–491 (1999).

29. Gaspar, L. P. *et al.* Hydrostatic pressure induces the fusion-active state of enveloped viruses. *J. Biol. Chem.* **277,** 8433–8439 (2002).

30. Fabbiani, F. P. A. & Pulham, C. R. High-pressure studies of pharmaceutical compounds and energetic materials. *Chem. Soc. Rev.* **35,** 932–942 (2006).

31. Y. B. Zel'dovich and Y. B. Raizer. *Physics of Shock Waves and High-Temperature Hydrodynamic Phenomena*. (Dover, Mineola, 2002).

32. Millett, J. C. F., Bourne, N. K. & GrayIII, G. T. The response of polyether ether ketone to one-dimensional shock loading. *J. Phys. D. Appl. Phys.* **37,** 942 (2004).

33. Bourne, N. K., Millett, J. C. F., Brown, E. N. & Gray III, G. T. Effect of halogenation on the shock properties of semicrystalline thermoplastics. *J. Appl. Phys.* **102,** 63510 (2007).

34. Millett, J. C. F., Bourne, N. K. & Akhavan, J. The response of hydroxy-terminated polybutadiene to one-dimensional shock loading. *J. Appl. Phys.* **95,** 4722–4727 (2004).

35. Hori, K., Iwama, A. & Fukuda, T. On the adhesion between Hydroxyl-Terminated Polybutadiene Fuel-Binder and Ammonium Perchlorate. Performance of bonding agents. *Propellants, Explos. Pyrotech.* **10,** 176–180 (1985).

36. Moore, D. S. & McGrane, S. D. Comparative infrared and Raman spectroscopy of energetic polymers. *J. Mol. Struct.* **661,** 561–566 (2003).

37. Sands, D. E. *Introduction to Crystallography*. (Dover Publications, 2012).

38. Fang, J. Instrumentation Development for Neutron Scattering at High Pressure. (University of Edinburgh, 2012).

39. AB, N. M. Wilhelm Conrad Röntgen - Facts. (2014). Available at: https://www.nobelprize.org/nobel_prizes/physics/laureates/1901/rontgen-facts.html. (Accessed: 21st January 2017)

40. Nobel Media AB. Max von Laue - Facts. (2014). Available at: http://www.nobelprize.org/nobel_prizes/physics/laureates/1914/laue-facts.html. (Accessed: 21st January 2017)

41. Nobel Media AB. The Nobel Prize in Physics 1915. (2014). Available at: https://www.nobelprize.org/nobel_prizes/physics/laureates/1915/.

42. U.S. National Library of Medicine. The Rosalind Franklin papers, biographical information. Available at: https://profiles.nlm.nih.gov/ps/retrieve/Narrative/KR/p-nid/183. (Accessed: 21st January 2017)

43. The Open University - University of Reading. PHYS 7.1: The atomic basis of matter. *PPLATO / FLAP (Flexible Learning Approach To Physics)* (1996). Available at: http://www.met.reading.ac.uk/pplato2/h-flap/phys7_1.html. (Accessed: 11th May 2017)

44. Giacovazzo, C. *Fundamentals of Crystallography*. (Oxford University Press, 2002).

45. Hammond, C. *The Basics of Crystallography and Diffraction*. (OUP Oxford, 2009).

46. Christine Clark, B. D. Single-crystal x-ray diffraction. (2017). Available at: http://serc.carleton.edu/research_education/geochemsheets/techniques/SXD.html. (Accessed: 23rd January 2017)

47. McMillan, P. F. New materials from high-pressure experiments. *Nat Mater* **1,** 19–25 (2002).

48. Diamond Light Source. X ray diffraction. (2016). Available at: http://www.diamond.ac.uk/Beamlines/Engineering-and-Environment/I12/applications/diffraction.html. (Accessed: 23rd January 2017)

49. Science and Technology Facilities Council, UK. Neutron training course. (2016). Available at: http://www.isis.stfc.ac.uk/learning/neutron-training-course/downloads/general/neutron-training-course---manual13577.pdf. (Accessed: 23rd January 2017)

50. The Institute of Physics. Neutron scattering. (2010). Available at: https://www.iop.org/publications/iop/2011/file_47455.pdf. (Accessed: 21st July 2017)

51. Eriksson, R. The European Spallation Source. Available at: https://europeanspallationsource.se/european-spallation-source. (Accessed: 17th January 2017)

52. Klotz, S. *Techniques in High Pressure Neutron Scattering*. (CRC Press, 2013).

53. Kuwayama, Y., Hirose, K., Sata, N. & Ohishi, Y. Phase relations of iron and iron–nickel alloys up to 300 GPa: Implications for composition and structure of the Earth's inner core. *Earth Planet. Sci. Lett.* **273,** 379–385 (2008).

54. Klotz, S. *et al.* High pressure neutron diffraction using the Paris-Edinburgh cell: Experimental possibilities and future prospects. *High Press. Res.* **14,** 249–255 (1996).

55. Klotz, S. *et al.* Neutron powder diffraction at pressures beyond 25 GPa. *Appl. Phys. Lett.* **66,** 1735 (1995).

56. Bull, C. L. *et al.* Toroidal anvils for single-crystal neutron studies. *High Press. Res.* **25,** 229–231 (2005).

57. Khvostantsev, L. G., Slesarev, V. N. & Brazhkin, V. V. Toroid type high-pressure device: history and prospects. *High Press. Res.* **24,** 371–383 (2004).

58. Thomasnet. Zirconia Toughened Alumina. (2015). Available at: http://www.thomasnet.com/articles/metals-metal-products/ziconia-alumina. (Accessed: 10th April 2015)

59. CAE Associates. Heat Exchanger Cooling Analysis. Available at: https://caeai.com/resources/heat-exchanger-cooling-analysis. (Accessed 17

February 2016).

60. Finite Element Analysis (FEA). *Finite Engineering* Available at: http://www.fea3d.com/services/fea/. (Accessed: 27th January 2017)

61. *Cadstan.* A Gallery of Cadstan works. Available at: http://cadstan.com/gallery-2/. (Accessed: 27th January 2017)

62. Budynas, R. G. & Nisbett, J. K. *Shigley's Mechanical Engineering Design*. (McGraw-Hill, 2011).

63. Konecranes Inc. Crane Parts. (2017). Available at: http://www.craneproparts.com/konecranes.html. (Accessed: 20th January 2017)

64. Irgens, F. *Continuum Mechanics*. (Springer Berlin Heidelberg, 2008).

65. Beer, F. P., Johnston, E. R. & DeWolf, J. T. *Mechanics of Materials*. (Cengage Learning, 2002).

66. Gere, J. M. & Goodno, B. J. *Mechanics of Materials*. (Cengage Learning, 2012).

67. Beer, F., Jr. Johnston, E. R., DeWolf, J. & Mazurek, D. *Mechanics of Materials*. (McGraw-Hill Companies Incorporated, 2012).

68. Carter, C. B. & Norton, M. G. *Ceramic Materials: Science and Engineering*. (Springer New York, 2013).

69. First Year Engineering. Crystal Structure. Available at: https://firstyearengineer.com/material-science/introduction/crystal-structure/. (Accessed: 20th April 2017)

70. Somiya, S. *et al. Handbook of Advanced Ceramics: Materials, Applications, Processing and Properties*. (Elsevier Science, 2003).

71. Bridgman, P. W. *The Physics of High Pressure*. (Bell and Sons, London, 1952).

72. Wentorf, R. H. *Modern very high pressure techniques*. (Butterworths, 1962).

73. Klement, W. & Jayaraman, A. Phase relations and structures of solids at high pressures. *Prog. Solid State Chem.* **3,** 289–376 (1967).

74. Spain, I. L. & Paauwe, J. *High Pressure Technology: Volume 1: Equipment Design, Materials, and Properties*. (Taylor & Francis, 1977).

75. McWhan, D. B., Bloch, D. & Parisot, G. Apparatus for neutron diffraction at high pressure. *Rev. Sci. Instrum.* **45,** 643–646 (1974).

76. Besson, J. M. *et al.* Neutron powder diffraction above 10 GPa. *Phys. B Condens. Matter* **180–181,** 907–910 (1992).

77. Bundy, F. P. Ultrahigh pressure apparatus using cemented tungsten carbide pistons with sintered diamond tips. *Rev. Sci. Instrum.* **46,** 1318–1324 (1975).

78. Besson, J. M. *et al.* High pressure neutron diffraction. Present and future possibilities using the Paris-Edinburgh cell. *High Press. Res.* **14,** 1–6 (1995).

79. Besson, J. M. *et al.* A large volume pressure cell for high temperatures. *Int. J. High Press. Res.* **8,** 625–630 (1992).

80. Loveday, J. S. *et al.* High pressure neutron diffraction studies using the Paris-Edinburgh cell. *Int. J. High Press. Res.* **14,** 303–309 (1996).

81. Ivanov, A. N. *et al.* Ceramic high pressure cell with profiled anvils for neutron diffraction investigations (up to 7 GPa). *High Press. Res.* **14,** 203–208 (1995).

82. Komatsu, K. *et al.* Performance of ceramic anvils for high pressure neutron scattering. *High Press. Res.* **34,** 494–499 (2014).

83. Tang, D., Lim, H.-B., Lee, K.-J., Lee, C.-H. & Cho, W.-S. Evaluation of mechanical reliability of zirconia-toughened alumina composites for dental implants. *Ceram. Int.* **38,** 2429–2436 (2012).

84. Douillard, T. *et al.* Comparative ageing behaviour of commercial, unworn and worn 3Y-TZP and zirconia-toughened alumina hip joint heads. *J. Eur. Ceram. Soc.* **32,** 1529–1540 (2012).

85. Pires, L. F. S., Tandler, B., Bissada, N. & Duarte Jr, S. Comparison of heat generated by alumina-toughened zirconia and stainless steel burs for implant placement. *Int. J. Oral Maxillofac. Implants* **27,** (2012).

86. Kim, S. *et al.* Clinical use of alumina-toughened zirconia abutments for implant-supported restoration: prospective cohort study of survival analysis. *Clin. Oral Implants Res.* **24,** 517–522 (2013).

87. Zhang, X. F. & Li, Y. C. On the comparison of the ballistic performance of 10% zirconia toughened alumina and 95% alumina ceramic target. *Mater. Des.* **31,** 1945–1952 (2010).

88. Wang, J. & Stevens, R. Zirconia-Toughened Alumina (ZTA) ceramics. *J. Mater. Sci.* **24,** 3421–3440 (1989).

89. Monteiro, S. N., Skury, A. L. D., de Azevedo, M. G. & Bobrovnitchii, G. S. Cubic boron nitride competing with diamond as a superhard engineering material – an overview. *J. Mater. Res. Technol.* **2,** 68–74 (2013).

90. Klotz, S., Strassle, T., Rousse, G., Hamel, G. & Pomjakushin, V. Angle-dispersive neutron diffraction under high pressure to 10 GPa. *Appl. Phys. Lett.* **86,** 31917–32100 (2005).

91. Funamori, N. & Sato, T. A Cubic Boron Nitride gasket for diamond-anvil experiments. *Rev. Sci. Instrum.* **79,** 53903 (2008).

92. Wang, L. *et al.* Application of a new composite cubic-boron nitride gasket assembly for high pressure inelastic x-ray scattering studies of carbon related materials. *Rev. Sci. Instrum.* **82,** 73902 (2011).

93. Kobayashi, E. *et al.* Influence of aging heat treatment on mechanical properties of biomedical Ti–Zr based ternary alloys containing niobium. *J. Mater. Sci. Mater. Med.* **9,** 625–630 (1998).

94. Wilkinson, M. K. Early history of neutron scattering at oak ridge. *Phys. B+ C* **137,** 3–16 (1986).

95. Lechner, R. High pressure vessel for measurement of pressure induced phonon energy shifts by inelastic scattering of neutrons. *Rev. Sci. Instrum.* **37,** 1534–1537 (1966).

96. Umebayashi, H., Shirane, G., C. Frazer, B. & B. Daniels, W. Neutron diffraction study of Cr under high pressure. *J. Phys. Soc. Japan* **24,** 368–372 (1968).

97. Smith, F. A. & Sparks, J. T. Neutron diffraction study of NiS under pressure. *J. Appl. Phys.* **40,** 1332–1333 (1969).

98. Sirota, N. N., Vasilev, E. A. & Govor, G. A. Neutron diffraction study of magnetic and chrystallographic phase transformation in Manganese Arsenide as a function of temperature and pressure. *Le J. Phys. Colloq.* **32,** C1-987 (1971).

99. Brugger, R. M., Bennion, R. B., Worlton, T. G. & Myers, W. R. Neutron diffraction at high pressures. *Trans. Am. Crystallogr. Assoc* **5,** 141–154 (1969).

100. Bloch, D., Paureau, J., Voiron, J. & Parisot, G. Neutron scattering at high pressure. *Rev. Sci. Instrum.* **47,** 296–298 (1976).

101. McWhan, D. B. & Vettier, C. Neutron scattering studies at high pressure on rare earth intermetallic compounds. *Le J. Phys. Colloq.* **40,** C5-107 (1979).

102. McWhan, D. B., Vettier, C., Youngblood, R. & Shirane, G. Neutron scattering study of pressure-induced antiferromagnetism in PrSb. *Phys. Rev. B* **20,** 4612 (1979).

103. Sammis, C. G. & Henyey, T. L. *Geophysics Laboratory Measurements*. (Elsevier Science, 1987).

104. Gerard, G. Investigations of massive support principle for ultra high pressure anvils. (DTIC Document, 1962).

105. Bradley, R. S. *Advances in High Pressure Research.* (Academic Press, 1966).

106. Dunstan, D. J. Theory of the gasket in diamond anvil high-pressure cells. *Rev. Sci. Instrum.* **60,** 3789–3795 (1989).

107. Yousuf, M. & Rajan, K. G. Principle of massive support in the opposed anvil high pressure apparatus. *Pramana* **18,** 1–15 (1982).

108. Dunstan, D. J. & Spain, I. L. Technology of diamond anvil high-pressure cells: I. Principles, design and construction. *J. Phys. E.* **22,** 913 (1989).

109. Besson, J. M. *et al.* Equation of state of lithium deuteride from neutron diffraction

under high pressure. *Phys. Rev. B* **45,** 2613–2619 (1992).

110. Nelmes, R. J. *et al.* Neutron- and x-ray-diffraction measurements of the bulk modulus of boron. *Phys. Rev. B* **47,** 7668–7673 (1993).

111. Nelmes, R. J. *et al.* Neutron diffraction study of the structure of deuterated ice VIII to 10 GPa. *Phys. Rev. Lett.* **71,** 1192–1195 (1993).

112. Klotz, S. *et al.* Crystal structure studies to 10 GPa with the Paris-Edinburgh cell: High pressure aspects. *High-pressure science and technology—1993* **309,** 1577–1580 (AIP Publishing, 1994).

113. Besson, J. M. & Nelmes, R. J. New developments in neutron-scattering methods under high pressure with the Paris—Edinburgh cells. *Phys. B Condens. Matter* **213–214,** 31–36 (1995).

114. Von Dreele, R. B. High pressure neutron powder diffraction at LANSCE. *High Press. Res.* **14,** 13–19 (1995).

115. Catti, M., Ferraris, G., Hull, S. & Pavese, A. Static compression and H disorder in brucite, Mg(OH)2, to 11 GPa: a powder neutron diffraction study. *Phys. Chem. Miner.* **22,** 200–206 (1995).

116. Besson, J. S. L. and W. G. M. and R. J. N. and S. K. and G. H. and J. M. The structure and structural pressure dependence of sodium deuteroxide-V by neutron powder diffraction. *J. Phys. Condens. Matter* **8,** L597 (1996).

117. Loveday, J. S. *et al.* High pressure neutron powder diffraction: The neutron scattering aspects of work with the Paris-Edinburgh cell. *High Press. Res.* **14,** 7–12 (1995).

118. Nelmes, R. J. *et al.* Observation of inverted-molecular compression in Boron Carbide. *Phys. Rev. Lett.* **74,** 2268–2271 (1995).

119. Loveday, J. S. *et al.* Structure of deuterated ammonia IV. *Phys. Rev. Lett.* **76,** 74–77 (1996).

120. Klotz, S. *et al.* Transverse acoustic phonons of Germanium up to 9.7 GPa by neutron inelastic scattering. *Phys. status solidi* **198,** 105–113 (1996).

121. Klotz, S., Hamel, G. & Frelat, J. A new type of compact large-capacity press for neutron and x-ray scattering. *High Press. Res.* **24,** 219–223 (2004).

122. Stishov, S. M. & Sadkov, Y. A. A compact hydraulic press to use with high-pressure devices for neutron scattering studies. *Instruments Exp. Tech.* **45,** 573–575 (2002).

123. Besson, J. M. *et al.* Variation of interatomic distances in ice VIII to 10 GPa. *Phys. Rev. B* **49,** 12540–12550 (1994).

124. Klotz, S. *et al.* Phonon dispersion measurements at high pressures to 7 GPa by inelastic neutron scattering. *Appl. Phys. Lett.* **66,** 1557–1559 (1995).

125. Bocian, A. *et al.* Gas loading apparatus for the Paris-Edinburgh press. *Rev. Sci. Instrum.* **81,** 93904 (2010).

126. Mezouar, M., Le Bihan, T., Libotte, H., Le Godec, Y. & Hausermann, D. Paris-Edinburgh large-volume cell coupled with a fast imaging-plate system for structural investigation at high pressure and high temperature. *J. Synchrotron Radiat.* **6,** 1115–1119 (1999).

127. Morard, G. *et al.* Optimization of Paris–Edinburgh press cell assemblies for in situ monochromatic X-ray diffraction and X-ray absorption. *High Press. Res.* **27,** 223–233 (2007).

128. Jacobsen, M. K. & Velisavljevic, N. Containment system for experiments on radioactive and other hazardous materials in a Paris-Edinburgh press. *Rev. Sci. Instrum.* **86,** 113904 (2015).

129. Matityahu, S., Emuna, M., Yahel, E., Makov, G. & Greenberg, Y. Novel experimental design for high pressure-high temperature electrical resistance measurements in a 'Paris-Edinburgh' large volume press. *Rev. Sci. Instrum.* **86,** 43902 (2015).

130. Playford, H. Y., Tucker, M. G. & Bull, C. L. Neutron total scattering of crystalline materials in the gigapascal regime. *J. Appl. Crystallogr.* **50,** (2017).

131. Utsumi, W. *et al.* Neutron powder diffraction under high pressure at J-PARC. *Nucl. Instruments Methods Phys. Res. Sect. A Accel. Spectrometers, Detect. Assoc. Equip.* **600,** 50–52 (2009).

132. Tulk, C. A. *et al.* Cage occupancies in the high pressure structure H methane hydrate: A neutron diffraction study. *J. Chem. Phys.* **136,** 54502 (2012).

133. Bove, L. E. *et al.* Translational and rotational diffusion in water in the Gigapascal range. *Phys. Rev. Lett.* **111,** 185901 (2013).

134. Lheureux, D. *et al.* Ultrasonics and X-ray diffraction under pressure in the Paris–Edinburgh cell. *Ultrasonics* **38,** 247–251 (2000).

135. Yamada, A. *et al.* High-pressure x-ray diffraction studies on the structure of liquid silicate using a Paris–Edinburgh type large volume press. *Rev. Sci. Instrum.* **82,** 15103 (2011).

136. Katayama, Y. *et al.* Density measurements of liquid under high pressure and high temperature. *J. Synchrotron Radiat.* **5,** 1023–1025 (1998).

137. Morard, G. *et al.* Structure of eutectic Fe–FeS melts to pressures up to 17 GPa: Implications for planetary cores. *Earth and Planetary Science Letters* **263,** (2007).

138. Kono, Y., Park, C., Kenney-Benson, C., Shen, G. & Wang, Y. Toward comprehensive studies of liquids at high pressures and high temperatures: Combined structure, elastic wave velocity, and viscosity measurements in the Paris–Edinburgh cell. *Phys. Earth Planet. Inter.* **228,** 269–280 (2014).

139. Katayama, Y. *et al.* EXAFS Study on Tellurium under high pressure and temperature. *Rev. HIGH Press. Sci. Technol.* **7,** 251–253 (1998).

140. Vaccari, M., Aquilanti, G., Pascarelli, S. & Mathon, O. A new EXAFS investigation of local structural changes in amorphous and crystalline GeO(2) at high pressure. *J. Phys. Condens. Matter* **21,** 145403 (2009).

141. Perrillat, J.-P., Mezouar, M., Garbarino, G. & Bauchau, S. In situ viscometry of high-pressure melts in the Paris–Edinburgh cell: application to liquid FeS. *High Press. Res.* **30,** 415–423 (2010).

142. Hall, H. T. Some High-Pressure, High-Temperature apparatus design considerations: equipment for use at 100 000 atmospheres and 3000° C. *Rev. Sci. Instrum.* **29,** 267–275 (1958).

143. Khvostantsev, L. G., Vereshchagin, L. F. & Novikov, A. P. Device of toroid type for high pressure generation. *High Temp.-High Press.* **9,** 637–639 (1977).

144. Khvostantsev, L. G. & Sidorov, V. A. Influence of pressure up to 90 kbar on the thermoelectric properties of antimony. *Phys. status solidi* **46,** 305–309 (1978).

145. Khvostantsev, L. G., Orlov, A. I., Abrikosov, N. K. & Ivanova, L. D. Thermoelectric properties and phase transition in Sb2Te3 under hydrostatic pressure up to 9 GPa. *Phys. status solidi* **58,** 37–40 (1980).

146. Bashkin, I. O., Dymova, T. N. & Ponyatovskii, E. G. On the structural transition from NaCl to CsCl type in alkali hydrides. *Phys. status solidi* **100,** 87–92 (1980).

147. Tsidil'kovsloT, I. M., Shchennikov, V. V & Gluzman, N. G. Metallization of mercury chalcogenides under ultrahigh pressures. *Fiz. Tverd. Tela {Leningrad}* **24,** 2658–2662 (1982).

148. Kechin, V. V & Likhter, A. I. Hall effect and magnetoresistance of antimony up to 5 G Pa. *Phys. status solidi* **117,** K13–K17 (1983).

149. Vlasov, A. V, Vinokurova, L. I., Pardavi-Horváth, M. & Lovas, A. Effects of pressure on amorphous Fe25Ni55Si10B10 alloys. *J. Magn. Magn. Mater.* **41,** 116–118 (1984).

150. Sadkov, Y. A. & Solodukhina, L. B. Calculation of pressure in solid-phase process vessels with shaped anvils. *J. Appl. Mech. Tech. Phys.* **33,** 903–910 (1992).

151. Wilding, M., Guthrie, M., Bull, C. L., Tucker, M. G. & McMillan, P. F. Feasibility of in situ neutron diffraction studies of non-crystalline silicates up to pressures of 25 GPa. *J. Phys. Condens. Matter* **20,** 244122 (2008).

152. Funnell, N. P., Marshall, W. G. & Parsons, S. Alanine at 13.6 GPa and its pressure-induced amorphisation at 15 GPa. *CrystEngComm* **13,** 5841–5848 (2011).

153. Fitzgibbons, T. C. *et al.* Benzene-derived carbon nanothreads. *Nat Mater* **14,** 43–47 (2015).

154. Fang, J., Bull, C. L., Loveday, J. S., Nelmes, R. J. & Kamenev, K. V. Strength analysis and optimisation of double-toroidal anvils for high-pressure research. *Rev. Sci. Instrum.* **83,** 93902 (2012).

155. Montagne, A., Pathak, S., Maeder, X. & Michler, J. Plasticity and fracture of sapphire at room temperature: load-controlled microcompression of four different orientations. *Ceram. Int.* **40,** 2083–2090 (2014).

156. Bundy, F. P. Designing tapered anvil apparatus for achieving higher pressures. *Rev. Sci. Instrum.* **48,** 591–596 (1977).

157. Dunn, K. The yield stress of opposed anvils. *J. Appl. Phys.* **48,** 1829–1832 (1977).

158. Adams, D. M. & Shaw, A. C. A computer-aided design study of the behaviour of diamond anvils under stress. *J. Phys. D. Appl. Phys.* **15,** 1609 (1982).

159. Adams, D. M., Christy, A. G. & Norman, A. J. Optimization of diamond anvil cell performance by finite element analysis. *Meas. Sci. Technol.* **4,** 422 (1993).

160. Bruno, M. S. & Dunn, K. J. Stress analysis of a beveled diamond anvil. *Rev. Sci. Instrum.* **55,** 940–943 (1984).

161. Moss, W. C., Hallquist, J. O., Reichlin, R., Goettel, K. A. & Martin, S. Finite element analysis of the diamond anvil cell: Achieving 4.6 Mbar. *Appl. Phys. Lett.* **48,** 1258–1260 (1986).

162. Moss, W. C. & Goettel, K. A. Finite element design of diamond anvils. *Appl. Phys. Lett.* **50,** 25–27 (1987).

163. Hemley, R. J. *et al.* X-ray imaging of stress and strain of diamond, iron, and tungsten at megabar pressures. *Science (80-.).* **276,** 1242–1245 (1997).

164. Moss, W. C. & Goettel, K. A. The stability of a sample in a diamond anvil cell. *J. Appl. Phys.* **61,** 4951–4954 (1987).

165. Novikov, N. V, Levitas, V. I. & Shestakov, S. I. Fundamentals of strength and durability calculations for high-pressure apparatus elements. *Phys. B+ C* **139,** 782–784 (1986).

166. Novikov, N. V & Polotnyak, S. B. The numerical modelling of the stress-strained state of diamond anvil cell components. *High Press. Sci. Technol.* **5,** 865–867 (1990).

167. Novikov, N. V, Levitas, V. I., Polotnyak, S. B. & Potyomkin, M. M. Numerical optimization of diamond anvil cell design. *Int. J. High Press. Res.* **8,** 507–509 (1992).

168. Levitas, V. I., Polotnyak, S. B. & Idesman, A. V. Large elastoplastic strains and the stressed state of a deformable gasket in high pressure equipment with diamond anvils. *Strength Mater.* **28,** 221–227 (1996).

169. Merkel, S., Hemley, R. J. & Mao, H. Finite-element modeling of diamond

deformation at multimegabar pressures. *Appl. Phys. Lett.* **74,** 656–658 (1999).

170. Vignes, R. M., Becker, R., Stölken, J. & Kumar, M. An assessment of diamond anvil cell measurements on material strength. *J. Appl. Phys.* **113,** 213503 (2013).

171. Huang, X. *et al.* Finite element analysis of resistivity measurement with four point probe in a diamond anvil cell. *J. Appl. Phys.* **101,** 64904 (2007).

172. Huang, X. *et al.* Finite element analysis of resistivity measurement with van der Pauw method in a diamond anvil cell. *Appl. Phys. Lett.* **90,** 242102 (2007).

173. Kiefer, B. & Duffy, T. S. Finite element simulations of the laser-heated diamond-anvil cell. *J. Appl. Phys.* **97,** 114902 (2005).

174. Montoya, J. A. & Goncharov, A. F. Finite element calculations of the time dependent thermal fluxes in the laser-heated diamond anvil cell. *J. Appl. Phys.* **111,** 112617 (2012).

175. Lobanov, S. S. *et al.* Pressure, stress, and strain distribution in the double-stage diamond anvil cell. *J. Appl. Phys.* **118,** 35905 (2015).

176. Wei, F. W. Y. D. L. & Yuning, G. Numerical simulation of laser induced ultrasonic in a diamond anvil cell by Finite Element Method. *Chinese J. Lasers* **8,** 20 (2011).

177. Feng, W., Yang, D., Guo, Y. & Chang, Y. Finite element modeling of bulk ultrasonic waves generated by ring-shaped laser illumination in a diamond anvil cell. *Opt. Express* **20,** 6429–6438 (2012).

178. Feng, B., Levitas, V. I. & Hemley, R. J. Large elastoplasticity under static megabar pressures: Formulation and application to compression of samples in diamond anvil cells. *Int. J. Plast.* (2016).

179. Conil, N. & Kavner, A. Numerical study of pressure relationships between sample and calibrant inside the diamond anvil cell. *J. Phys. Condens. Matter* **18,** S1039 (2006).

180. Tempere, J. & Silvera, I. F. Pressure distribution in a quasi-hydrostatic pressure medium: A finite element analysis. *J. Appl. Phys.* **110,** 113523 (2011).

181. Giriat, G. Instrumentation development for magnetic and structural studies under extremes of pressure and temperature. (2012).

182. Kepa, M., Huxley, A. & Kamenev, K. New pressure cell for ultrasonic measurements. in *APS Shock Compression of Condensed Matter Meeting Abstracts* **1,** 1004 (2013).

183. Binns, J., Kamenev, K. V, McIntyre, G. J., Moggach, S. A. & Parsons, S. Use of a miniature diamond-anvil cell in high-pressure single-crystal neutron Laue diffraction. *IUCrJ* **3,** 168–179 (2016).

184. Rainey, E. S. G., Hernlund, J. W. & Kavner, A. Temperature distributions in the laser-heated diamond anvil cell from 3-D numerical modeling. *J. Appl. Phys.* **114,**

204905 (2013).

185. Xu, J. & Mao, H. Moissanite: a window for high-pressure experiments. *Science* **290,** 783–785 (2000).

186. Ji-an Xu, Ho-kwang Mao, R. J. H. and E. H. The moissanite anvil cell : a new tool for high-pressure. *J. Physics Condensed Matter.* **14,** 11543–11548 (2002).

187. Del Corro, E., de la Roza, A. O., Taravillo, M. & Baonza, V. G. Raman modes and Grüneisen parameters of graphite under compressive biaxial stress. *Carbon N. Y.* **50,** 4600–4606 (2012).

188. Del Corro, E., González, J., Taravillo, M., Flahaut, E. & Baonza, V. G. Raman spectra of double-wall carbon nanotubes under extreme uniaxial stress. *Nano Lett.* **8,** 2215–8 (2008).

189. Snow, C. S., Karpus, J. F., Cooper, S. L., Kidd, T. E. & Chiang, T.-C. Quantum melting of the charge-density-wave state in 1T-TiSe2. *Phys. Rev. Lett.* **91,** 136402 (2003).

190. Kim, M. *et al.* Magnetic-field- and pressure-induced quantum phases in complex materials. *Adv. Mater.* **22,** 1148–1155 (2010).

191. Xu, J. *et al.* Powder neutron diffraction of WU ($Fe_{0.93}O$) to 12 GPa using large moissanite anvils. **24,** 247–253 (2004).

192. Kamitani, K. *et al.* The elastic constants of silicon carbide: A Brillouin-scattering study of 4H and 6H SiC single crystals. *J. Appl. Phys.* **82,** 3152 (1997).

193. Ji, V., Zhang, J.-M., Zhang, Y. & Xu, K.-W. Anisotropic elasticity in hexagonal crystals. *Thin Solid Films* **515,** 7020–7024 (2007).

194. Hang, J. I. Z., Ang, L. I. W., Eidner, D. O. J. W. & Chida, T. A. U. The strength of moissanite. **87,** 1005–1008 (2002).

195. J. Qian, L.L. Daemen, Y. Z. Hardness and fracture toughness of moissanite. *Diam. Relat. Mater.* **14,** 1669–1672 (2005).

196. Del Corro, E., Izquierdo, J. G., González, J., Taravillo, M. & Baonza, V. G. 3D Raman mapping of uniaxially loaded 6H-SiC crystals. *J. Raman Spectrosc.* **44,** 758–762 (2013).

197. Ridley, C. J., Jacobsen, M. K. & Kamenev, K. V. A finite-element study of sapphire anvils for increased sample volumes. *High Press. Res.* 1–14 (2015).

198. Han, Q.-G., Li, M.-Z., Jia, X.-P., Ma, H.-A. & Li, Y. Modeling of effective design of high pressure anvils used for large scale commercial production of gem quality large single crystal diamond. *Diam. Relat. Mater.* **20,** 969–973 (2011).

199. Han, Q.-G., Li, M.-Z., Jia, X.-P. & Ma, H.-A. Finite element analysis and design of cubic high-pressure anvils based on the principle of lateral support. *Rev. Sci. Instrum.* **81,** 123901 (2010).

200. Han, Q. *et al.* Finite element design of double bevel anvils of large volume cubic high pressure apparatus. *Rev. Sci. Instrum.* **78,** 113906 (2007).

201. Han, Q. *et al.* Finite element analysis of high-pressure anvils according to the principle of lateral support. *J. Appl. Phys.* **102,** 84504 (2007).

202. Han, Q.-G., Ban, Q.-C. & Zhu, P.-W. Design of a novel large volume cubic high pressure apparatus for raising the yield and quality of synthetic diamond. *J. Cryst. Growth* **422,** 29–35 (2015).

203. Han, Q.-G. *et al.* Finite-element analysis on performance and shear stress of cemented tungsten carbide anvils used in the China-type cubic-anvil high-pressure apparatus. *High Press. Res.* **29,** 457–465 (2009).

204. Li, R. *et al.* Finite element design of a temperature field for high-pressure diamond synthesis. *Diam. Relat. Mater.* **69,** 133–137 (2016).

205. Polotnyak, S. B. & Borimskii, O. I. Numerical simulation of the mechanical state of the two-stage multi-anvil high pressure apparatus. *J. Superhard Mater.* **38,** 91–102 (2016).

206. Feng, B., Zarechnyy, O. M. & Levitas, V. I. Strain-induced phase transformations under compression, unloading, and reloading in a diamond anvil cell. *J. Appl. Phys.* **113,** 173514–173519 (2013).

207. Feng, B. & Levitas, V. I. Plastic flows and strain-induced alpha to omega phase transformation in zirconium during compression in a diamond anvil cell: Finite element simulations. *Mater. Sci. Eng. A* **680,** 130–140 (2017).

208. Jacobsen, M. K. *et al.* High-pressure cell for neutron diffraction with in situ pressure control at cryogenic temperatures. *Rev. Sci. Instrum.* **85,** 43904 (2014).

209. Escobedo, J. P., Field, D. P., LeBlanc, M. M., Florando, J. N. & Lassila, D. H. The trianvil test apparatus: Measurement of shear strength under pressure. *Rev. Sci. Instrum.* **81,** 13908 (2010).

210. Solozhenko, V. L. *et al.* In situ studies of boron nitride crystallization from BN solutions in supercritical N–H fluid at high pressures and temperatures. *Phys. Chem. Chem. Phys.* **4,** 5386–5393 (2002).

211. Debord, R., Leguillon, D., Syfosse, G. & Fischer, M. A finite element study of a high-pressure/high-temperature cell for simultaneous X-ray and ultrasonic measurement. *High Press. Res.* **23,** 451–463 (2003).

212. Klotz, S., Philippe, J., Bull, C. L., Loveday, J. S. & Nelmes, R. J. A 3 kbar hydrogen-compatible gas loader for Paris–Edinburgh presses. *High Press. Res.* **33,** 214–220 (2013).

213. Klotz, S., Le Godec, Y., Strässle, T. & Stuhr, U. The α− γ− ε triple point of iron investigated by high pressure–high temperature neutron scattering. *Appl. Phys. Lett.* **93,** 91904 (2008).

214. Wang, W., Sokolov, D. A., Huxley, A. D. & Kamenev, K. V. Large volume high-pressure cell for inelastic neutron scattering. *Rev. Sci. Instrum.* **82,** 73903 (2011).

215. Wang, W. Instrumentation development for magneto-transport and neutron scattering measurements at high pressure and low temperature. (2013).

216. Chen, Q. *et al.* High-temperature high pressure cell for neutron-scattering studies. *High Press. Res.* **32,** 471–481 (2012).

217. Bridgman, P. W. Thermodynamic Properties of Liquid Water to 80 ºC and 12000 Kgm. *Proc. Am. Acad. Arts Sci.* **48,** 309–362 (1912).

218. Eisenberg, D. & Kauzmann, W. *The Structure and Properties of Water*. (OUP Oxford, 2005).

219. Guillot, B. A reappraisal of what we have learnt during three decades of computer simulations on water. *J. Mol. Liq.* **101,** 219–260 (2002).

220. Petrenko, V. F. & Whitworth, R. W. *Physics of Ice*. (OUP Oxford, 1999).

221. Fortes, A. D. & Choukroun, M. Phase Behaviour of Ices and Hydrates. *Space Sci. Rev.* **153,** 185–218 (2010).

222. Bocquillon, G., Léger, J.-M. & Bogicevic, C. Large-volume device for pressures of 20 GPA. *High Temp. High Press.* **35,** 355–370 (2003).

223. Sohl, F. *et al.* Subsurface Water Oceans on Icy Satellites: Chemical Composition and Exchange Processes. *Space Sci. Rev.* **153,** 485–510 (2010).

224. Dolan, D. H. & Gupta, Y. M. Nanosecond freezing of water under multiple shock wave compression: Optical transmission and imaging measurements. *J. Chem. Phys.* **121,** 9050–9057 (2004).

225. Walsh, J. M. & Rice, M. H. Dynamic compression of liquids from measurements on strong shock waves. *J. Chem. Phys.* **26,** 815–823 (1957).

226. Lyzenga, G. A., Ahrens, T. J., Nellis, W. J. & Mitchell, A. C. The temperature of shock-compressed water. *J. Chem. Phys.* **76,** 6282–6286 (1982).

227. Chau, R., Mitchell, A. C., Minich, R. W. & Nellis, W. J. Electrical conductivity of water compressed dynamically to pressures of 70–180 GPa (0.7–1.8 Mbar). *J. Chem. Phys.* **114,** 1361–1365 (2001).

228. Abramson, E. H. & Brown, J. M. Equation of state of water based on speeds of sound measured in the diamond-anvil cell. *Geochim. Cosmochim. Acta* **68,** 1827–1835 (2004).

229. Schwager, B., Chudinovskikh, L., Gavriliuk, A. & Boehler, R. Melting curve of H2O to 90 GPa measured in a laser-heated diamond cell. *J. Phys. Condens. Matter* **16,** S1177 (2004).

230. Dubrovinskaia, N. & Dubrovinsky, L. Melting curve of water studied in externally

heated diamond-anvil cell. *High Press. Res.* **23,** 307–311 (2003).

231. Smith, R. L. & Fang, Z. Techniques, applications and future prospects of diamond anvil cells for studying supercritical water systems. *J. Supercrit. Fluids* **47,** 431–446 (2009).

232. Chaplin, M. Water Phase Diagram. (2015). Available at: http://www1.lsbu.ac.uk/water/water_phase_diagram.html. (Accessed: 13th May 2015)

233. Cengel, Y. A. & Boles, M. A. *Thermodynamics: An Engineering Approach with Student Resource DVD*. (McGraw-Hill Higher Education, 2006).

234. Bridgman, P. W. The Pressure-Volume-Temperature Relations of the Liquid, and the Phase Diagram of Heavy Water. *J. Chem. Phys.* **3,** 597–605 (1935).

235. Grindley, T. & Lind Jr, J. E. PVT properties of water and mercury. *J. Chem. Phys.* **54,** 3983–3989 (1971).

236. Kamb, B. Structure of ice VI. *Science* **150,** 205–209 (1965).

237. Kamb, B. Structures of Forms of Ice. in *Acta Chrystallographica Section A-Crystal Physics Diffration Theoretical and General Chrystallography* S117 (Munksgaard Int. Publ. Ltd. Copenhagen, Denmerk, 1969).

238. Block, S., Weir, C. W. & Piermarini, G. J. High-pressure single-crystal studies of ice VI. *Science* **148,** 947–948 (1965).

239. Kamb, B. & Davis, B. L. Ice VII, the densest form of ice. *Proc. Natl. Acad. Sci. U. S. A.* **52,** 1433 (1964).

240. Bezacier, L. *et al.* Equations of state of ice VI and ice VII at high pressure and high temperature. *J. Chem. Phys.* **141,** 104505 (2014).

241. Bridgman, P. W. The phase diagram of water to 45,000 kg/cm^2. *J. Chem. Phys.* **5,** 964–966 (1937).

242. Baer, B. J., Brown, J. M., Zaug, J. M., Schiferl, D. & Chronister, E. L. Impulsive stimulated scattering in ice VI and ice VII. *J. Chem. Phys.* **108,** 4540–4544 (1998).

243. Somayazulu, M. *et al.* In situ high-pressure x-ray diffraction study of H_2O ice VII. *J. Chem. Phys.* **128,** 64510 (2008).

244. Polian, A. & Grimsditch, M. Brillouin scattering from H_2O: Liquid, ice VI, and ice VII. *Phys. Rev. B* **27,** 6409 (1983).

245. Chiu, J., Starr, F. W. & Giovambattista, N. Pressure-induced transformations in computer simulations of glassy water. *J. Chem. Phys.* **139,** 184504 (2013).

246. Sanz, E., Vega, C., Abascal, J. L. F. & MacDowell, L. G. Phase diagram of water from computer simulation. *Phys. Rev. Lett.* **92,** 255701 (2004).

247. Choukroun, M. & Grasset, O. Thermodynamic model for water and high-pressure ices up to 2.2 GPa and down to the metastable domain. *J. Chem. Phys.* **127,** 124506 (2007).

248. Sugimura, E. *et al.* Compression of H_2O ice to 126 GPa and implications for hydrogen-bond symmetrization: Synchrotron x-ray diffraction measurements and density-functional calculations. *Phys. Rev. B* **77,** 214103 (2008).

249. Fei, Y., Mao, H. & Hemley, R. J. Thermal expansivity, bulk modulus, and melting curve of H_2O–ice VII to 20 GPa. *J. Chem. Phys.* **99,** 5369–5373 (1993).

250. Shimizu, H., Nabetani, T., Nishiba, T. & Sasaki, S. High-pressure elastic properties of the VI and VII phase of ice in dense H_2O and D_2O. *Phys. Rev. B* **53,** 6107 (1996).

251. Chen, J.-Y., Kim, M., Yoo, C.-S., Liermann, H.-P. & Evans, W. J. Time-resolved x-ray diffraction across water-ice-VI/VII transformations using the dynamic-DAC. in *Journal of Physics: Conference Series* **500,** 142006 (IOP Publishing, 2014).

252. Lawrence, K. L. *ANSYS Workbench Tutorial Release 14*. (Schroff Development Corporation, 2012).

253. Lee, H. H. *Finite Element Simulations with ANSYS Workbench 16:* (SDC Publications, 2015).

254. ANSYS Inc. ANSYS R.15 User's Manual. (2013).

255. ANSYS Inc. Customer Training Material R13. Lecture 3. Introduction to contact. ANSYS Mechanical Structural Nonlinearities. (2010).

256. Moaveni, S. *Finite Element Analysis: Theory and Application with ANSYS*. (Pearson Prentice Hall, 2008).

257. ANSYS Inc. Workbench - Mechanical Introduction 12.0. Chapter 4, Static Structural Analysis. (2009).

258. Kress, R. *Numerical Analysis*. (Springer New York, 2012).

259. Von Neumann, J. & Goldstine, H. H. Numerical inverting of matrices of high order. *Bull. Am. Math. Soc.* **53,** 1021–1099 (1947).

260. Bathe, K. *Finite Element Procedures*. (Prentice-Hall, 2014).

261. Stoer, J., Bartels, R., Gautschi, W., Bulirsch, R. & Witzgall, C. *Introduction to Numerical Analysis*. (Springer New York, 2013).

262. Mei, C. C. *Mathematical Analysis in Engineering: How to Use the Basic Tools*. (Cambridge University Press, 1997).

263. Hamming, R. *Numerical Methods for Scientists and Engineers*. (Dover Publications, 2012).

264. Jin, L. Simulation of Coupled Electrostatic Mechanical Behavior with the Finite

Element Method. (Swansea University, 2010).

265. ANSYS Inc. ANSYS Multiphysics Solutions. (2010). Available at: http://www.ansys.com/-/media/Ansys/corporate/resourcelibrary/brochure/multiphysics-solutions-brochure.pdf. (Accessed: 10th April 2017)

266. Bathe, K.-J. Advances in the multiphysics analysis of structures. *Topping BHV, Ed.* (2012).

267. ADINA. Multiphysics capabilities of ADINA. Available at: http://www.adina.com/multiphysics.shtml. (Accessed: 10th April 2017)

268. Hrennikoff, A. Solution of problems of elasticity by the framework method. *J. Appl. Mech.* **8,** 169–175 (1941).

269. Courant, R. Variational methods for the solution of problems of equilibrium and vibrations. *Bull. Amer. Math. Soc* **49,** 1–23 (1943).

270. Strang, W. G. & Fix, G. J. *An analysis of the finite element method*. (Prentice-Hall, 1973).

271. Clough, R. W. The finite element method in plane stress analysis. Proceedings of American Society of Civil Engineers **23,** 345-37 (1960).

272. Akin, J. E. *Finite Element Analysis Concepts: Via SolidWorks*. (World Scientific, 2010).

273. Brauer, J. *What Every Engineer Should Know about Finite Element Analysis, Second Edition,*. (Taylor & Francis, 1993).

274. Ramamurty, G. *Applied Finite Element Analysis*. (I.K. International Publishing House Pvt. Limited, 2010).

275. Predictive Engineering. FEA Structural Analysis of Commercial Aircraft Landing Gear. (2016). Available at: http://www.predictiveengineering.com/consulting/fea/fea-structural-analysis-commercial-aircraft-landing-gear. (Accessed: 27th January 2017)

276. Comsol Inc. Keeping Track of Element Order in Multiphysics Models (2016). Available at: https://www.comsol.com/blogs/keeping-track-of-element-order-in-multiphysics-models/. (Accessed: 27th January 2017)

277. Dean, J. Introduction to the Finite Element (FEM). Lecture 2: First and Second Order One Dimensional Shape Functions. Cambridge University. Available at: http://www.ccg.msm.cam.ac.uk/images/FEMOR_Lecture_2.pdf. (Accessed 18 January 2017).

278. Comsol Inc. Finite Element Mesh Refinement. (2017). Available at: https://www.comsol.com/multiphysics/mesh-refinement. (Accessed: 27th January 2017)

279. CAE Associates. How Do I Know If My Mesh is Good Enough? (2016). Available at: https://caeai.com/blog/how-do-i-know-if-my-mesh-good-enough.

280. Adams, V. & Askenazi, A. *Building Better Products with Finite Element Analysis*. (OnWord Press, 1999).

281. Block, T. B. *Analysis of the mechanical response of impact loaded composite sandwich structures with focus on foam core shear failure:* . (Logos Verlag Berlin, 2014).

282. Christensen, J. & Bastien, C. *Nonlinear Optimization of Vehicle Safety Structures: Modeling of Structures Subjected to Large Deformations*. (Elsevier Science, 2015).

283. Livermore Software Technology Corporation. LS-DYNA. (2011). Available at: http://www.lstc.com/products/ls-dyna. (Accessed: 24th April 2017)

284. ANSYS Inc. ANSYS LS-DYNA Simulate the response of materials to short periods of severe loading. (2017). Available at: http://www.ansys.com/products/structures/ansys-ls-dyna. (Accessed: 24th April 2017)

285. Thieffry, P. Best of Both Worlds: Combining APDL with ANSYS Workbench for Structural Simulations. *ANSYS Advantage* 48–50 (2010).

286. Lin, J (ANSYS Inc.). Personal communication. (2017).

287. Bohler-Uddeholm Corporation. Maraging high strength steel. (2013). Available at: http://www.bucorp.com/media/Bohler_Special_Steels_Tools_for_Tube_Rod_Extr_Feb_2013.pdf. (Accessed: 3rd August 2015)

288. Done, R. *Safety Report - Titanium/Zirconium null matrix alloy. Internal safety report*. ISIS Neutron Facility.

289. Tulk, C. A., Gagnon, R. E., Kiefte, H. & Clouter, M. J. The pressure dependence of the elastic constants of ice III and ice VI. *J. Chem. Phys.* **107,** 10684–10690 (1997).

290. Johari, G. P., Lavergne, A. & Whalley, E. Dielectric properties of ice VII and VIII and the phase boundary between ice VI and VII. *J. Chem. Phys.* **61,** 4292–4300 (1974).

291. Hemley, R. J. *et al.* Static compression of H_2O-ice to 128 GPa (1.28 Mbar). *Nature* **330**, 737 - 740 (1987).

292. Munro, R. G., Block, S., Mauer, F. A. & Piermarini, G. Isothermal equations of state for H2O-VII and D2O-VII. *J. Appl. Phys.* **53,** 6174–6178 (1982).

293. Klotz, S. *et al.* Metastable ice VII at low temperature and ambient pressure. *Nature* **398,** 681–684 (1999).

294. Yoshimura, Y., Stewart, S. T., Somayazulu, M., Mao, H. & Hemley, R. J. High-pressure x-ray diffraction and Raman spectroscopy of ice VIII. *J. Chem. Phys.* **124,**

24502 (2006).

295. Antsyshkin, D. V, Dunaeva, A. N. & Kuskov, O. L. Thermodynamics of phase transitions in the system ice VI-ice VII-water. *Geochemistry Int.* **48,** 633–642 (2010).

296. Wang, E (CAD-FEM GmbH, Germany). ANSYS Contacts: Penalty vs. Lagrange. How to make it converge. Available at: http://www.civ.cvut.cz. (Accessed 23 June 2015).

297. ANSYS Inc. Customer Training Material R.13. Chapter 4: Advanced Contact. Workbench - Mechanical Structural Non-linearities (2009).

298. Lin, J (ANSYS Inc.). Customer Training Material R.15. Workbench Mechanical Contact Best Practices. (2014).

299. Mansour, J. M. Biomechanics of cartilage. *Kinesiol. Mech. pathomechanics Hum. Mov.* 66–79 (2003).

300. Mott, P. H., Dorgan, J. R. & Roland, C. M. The bulk modulus and Poisson's ratio of 'incompressible' materials. *J. Sound Vib.* **312,** 572–575 (2008).

301. Lees, C., Vincent, J. F. V & Hillerton, J. E. Poisson's ratio in skin. *Biomed. Mater. Eng.* **1,** 19–23 (1991).

302. Beatty, M. F. & Stalnaker, D. O. The Poisson function of finite elasticity. *J. Appl. Mech* **53,** 807–813 (1986).

303. Palmeri, M. L., Sharma, A. C., Bouchard, R. R., Nightingale, R. W. & Nightingale, K. R. A finite-element method model of soft tissue response to impulsive acoustic radiation force. *IEEE Trans. Ultrason. Ferroelectr. Freq. Control* **52,** 1699–1712 (2005).

304. Easwaran, V. & Munjal, M. L. Analysis of reflection characteristics of a normal incidence plane wave on resonant sound absorbers: A finite element approach. *J. Acoust. Soc. Am.* **93,** 1308–1318 (1993).

305. Ahart, M. *et al.* High-pressure Brillouin scattering of amorphous Be H 2. *J. Chem. Phys.* **124,** 14502 (2006).

306. Buch, V. & Devlin, J. P. *Water in Confining Geometries*. (Springer Berlin Heidelberg, 2013).

307. Rao, Y. V. C. *An introduction to thermodynamics*. (Universities Press, 2004).

308. Fok, S. L., Mitchell, B. C., Smart, J. & Marsden, B. J. A numerical study on the application of the Weibull theory to brittle materials. *Eng. Fract. Mech.* **68,** 1171–1179 (2001).

309. Danzer, R., Supancic, P., Pascual, J. & Lube, T. Fracture statistics of ceramics–Weibull statistics and deviations from Weibull statistics. *Eng. Fract. Mech.* **74,** 2919–2932 (2007).

310. Iizuka, R., Yagi, T., Gotou, H., Komatsu, K. & Kagi, H. An opposed-anvil-type apparatus with an optical window and a wide-angle aperture for neutron diffraction. *High Press. Res.* **32,** 430–441 (2012).

311. ANSYS Inc. Customer Training Material R.13. Lecture 5: Rate Independent Plasticity. ANSYS Mechanical ANSYS Mechanical Structural Nonlinearities. (2010).

312. Chattopadhyay, S. Investigation of Proportional and Non-Proportional Loadings Using Mohr's Circle. in *American Society for Engineering Education* (American Society for Engineering Education, 2012).

313. Achuthan, M. *Engineering Thermodynamics 2nd Ed.* (Prentice-Hall Of India Pvt. Limited, 2009).

314. Nikishov, GP. Introduction to the Finite Element Method. University of Wisconsin, Madison (USA). Available at: http://homepages.cae.wisc.edu/~suresh/ME964Website/M964Notes/Notes/introfem.pdf. (Accessed: 17th February 2018).

315. Rao, S.S. *The Finite Element Method in Engineering*. (Butterwoth-Heinemann, 2005).

316. University of Colorado, Boulder (USA). Advanced Finite Element Methods (ASEN 6367). Department of Aerospace Engineering Sciences. Available at: https://www.colorado.edu/engineering/CAS/courses.d/AFEM.d/. (Accessed: 17th February 2018).

317. Dean, J. Introduction to the Finite Element Method (FEM). Lecture 2. First and Second Order Dimensional Shape Functions. Available at: https://www.ccg.msm.cam.ac.uk/images/FEMOR_Lecture_2.pdf. (Accessed: 17th February 2018).

318. Greaves, G. N., Greer, A. L., Lakes, R. S., & Rouxel, T. Poisson's ratio and modern materials. Nature materials. **10**, 823 - 837 (2011).

319. Mott, P. H., Roland, C. M. Limits to Poisson's ratio in isotropic materials - general result for arbitrary deformation. Physica Scripta. **87**, 055404. (2013).

320. Regmi, S. Why normally Poisson's Ratio can't exceed 0.5?. Available at: http://avidsuraj.blogspot.co.uk/2015/10/why-normally-poisson-ratio-cant-exceed.html. (Accessed: 17th February 2018).

321. Liss, K.D., Qu, D., Yan, K., Reid, M. Variability of Poisson's Ratio and enhanced Ductility in Amorphous Metal. 15, 347 – 351. (2013).

322. Miller, E. HSFLD241/242: Modelling Enclosed Liquids. Available at: http://www.padtinc.com/blog/the-focus/hsfld241242-modeling-enclosed-liquids. (Accessed: 17th February 2018).